Harnessing Bayesian Optimisation for Quantum Information Processing

Swansea University
Prifysgol Abertawe

Fernando Martínez García

Department of Physics

Swansea University

Submitted to Swansea University in fulfilment
of the requirements for the degree of

Doctor of Philosophy

2021

Abstract

Achieving precise control over quantum systems has groundbreaking applications, such as simulating complex quantum systems, or implementing quantum algorithms with an improved efficiency over classical algorithms. Quantum computing has been under development for the last decades, resulting in the so-called Noisy Intermediate-Scale Quantum (NISQ) devices with about 50 qubits. While these devices are built with the purpose of achieving practical advantages over classical processors, they are vulnerable to noise sources. In order to account for error sources, one needs to implement Quantum Error Correction (QEC) techniques. These techniques protect quantum information by encoding a logical qubit into several physical ones. For the implementation of NISQ devices and QEC techniques, it is vital to keep improving the quantum operations and states involved. Here we develop calibration protocols based on the application of Bayesian inference. We show their advantages compared to the more traditional frequentist approaches, such as their ability to maximise the information gained with each measurement, or their straightforward automation. In our first line of research, we develop a Bayesian protocol for the correction of unwanted phases appearing in the experimental preparation of Steane code states. This protocol requires 13 times less measurements than the frequentist approach. In our second line of research, we develop a protocol for locking a laser to the qubit transition frequency in a trapped-ion architecture. This calibration is vital, since the correct implementation of single-qubit gates depends on it. In our final line of research, we study the Mølmer-Sørensen entangling gate, used in trapped-ion systems. First we introduce the calibration parameters, and derive a semianalytical model of the effects of one of them, for which there was no previous analytical understanding. Finally, we develop a Bayesian protocol for the calibration of these parameters, which was successfully implemented and tested in an experimental trapped-ion quantum processor.

Authorship Declaration

The following people and institutions contributed to the publication of work undertaken as part of this thesis:

	Name	Institutions
Candidate	Fernando Martínez-García	Department of Physics, Swansea University, Singleton Park, Swansea SA2 8PP, United Kingdom
Author 1 (PhD supervisor)	Markus Müller	Department of Physics, Swansea University, Singleton Park, Swansea SA2 8PP, United Kingdom Institute for Quantum Information, RWTH Aachen University, D-52056 Aachen, Germany Peter Grünberg Institute, Theoretical Nanoelectronics, Forschungszentrum Jülich, D-52425 Jülich, Germany
Author 2	Davide Vodola	Department of Physics, Swansea University, Singleton Park, Swansea SA2 8PP, United Kingdom Dipartimento di Fisica e Astronomia "Augusto Righi", Via Irnerio 46, Bologna, Italy INFN, Sezione di Bologna, I-40127 Bologna, Italy
Author 3	Lukas Gerster	Institut für Experimentalphysik, Universität Innsbruck, Technikerstraße 25/4, 6020 Innsbruck, Austria

	Name	Institutions
Author 4	Pavel Hrmo	Institut für Experimentalphysik, Universität Innsbruck, Technikerstraße 25/4, 6020 Innsbruck, Austria Since 17/06/2021 at Institute for Quantum Electronics, ETH Zurich, 8093 Zurich, Switzerland
Author 5	Martin van Mourik	Institut für Experimentalphysik, Universität Innsbruck, Technikerstraße 25/4, 6020 Innsbruck, Austria
Author 6	Benjamin Wilhelm	Institut für Experimentalphysik, Universität Innsbruck, Technikerstraße 25/4, 6020 Innsbruck, Austria
Author 7	Philipp Schindler	Institut für Experimentalphysik, Universität Innsbruck, Technikerstraße 25/4, 6020 Innsbruck, Austria
Author 8	Thomas Monz	Institut für Experimentalphysik, Universität Innsbruck, Technikerstraße 25/4, 6020 Innsbruck, Austria AQT, Technikerstraße 17, 6020 Innsbruck, Austria
Author 9	Rainer Blatt	Institut für Experimentalphysik, Universität Innsbruck, Technikerstraße 25/4, 6020 Innsbruck, Austria Institut für Quantenoptik und Quanteninformation, Österreichische Akademie der Wissenschaften, Technikerstraße 21a, 6020 Innsbruck, Austria

"Adaptive bayesian phase estimation for quantum error correcting codes", F. Martínez-García, D. Vodola, and M. Müller, *New Journal of Physics* **21** no. 12, 123027 (2019) [1].

- Located in Chapter 3.
- Candidate contributions (75%): derivation of the Bayesian inference algorithms and adaptive measurement rules; development and implementation of the numerical code; analysis, interpretation and visualization of obtained numerical data; main contribution to writing of the manuscript.
- Author 1 contributions (10%): original idea; supervision; revision of the manuscript.
- Author 2 contributions (15%): co-supervision; feedback on the numerical code and adaptation for the execution on the HPC cluster; revision of the manuscript.
- We the undersigned agree with the above stated "proportion of work undertaken" for the above published peer-reviewed manuscript contributing to this thesis:

Signed Candidate .....

Author 1 .....

Author 2 .....

"Analytical and experimental study of center line miscalibrations in Mølmer-Sørensen gates", F. Martínez-García, L. Gerster, D. Vodola, P. Hrmo, T. Monz, P. Schindler, and M. Müller *arXiv* (2021) [2].

- Located in Chapter 5.
- Candidate contributions (50%): derivation of the results from the Magnus expansion model; calculation of the numerical coefficients of the model; validation of the model results through numerical simulation; main contribution to writing of the manuscript.
- Author 1 contributions (5%): project supervision; revision of the manuscript.
- Author 2 contributions (10%): co-supervision; revision of the manuscript; polishing of the numerical calculation code for supplementary material for the publication.
- Author 3 contributions (20%): experimental measurements and writing of experimental section of the manuscript.
- Author 4 contributions (5%): revision of the manuscript.
- Author 7 contributions (5%): co-supervision, in particular with regard to experimental aspects; revision of the manuscript.
- Author 8 contributions (5%): revision of the manuscript.
- We the undersigned agree with the above stated "proportion of work undertaken" for the above published manuscript (currently under peer-review) contributing to this thesis:

Signed Candidate [redacted] .....

Author 1 [redacted] .....

Author 2 [redacted] .....

Author 3 .....

Author 4 .....

~~Author 5~~ .....

~~Author 6~~ .....

Author 7 .....

Author 8 .....

~~Author 9~~ .....

"Experimental Bayesian calibration of trapped ion entangling operations", L. Gerster, F. Martínez-García, P. Hrmo, M. van Mourik, B. Wilhelm, D. Vodola, M. Müller, R. Blatt, P. Schindler, and T. Monz, *arXiv* (2021) [3].

- Located in Chapter 6.
- Candidate contributions (25%): development of the theoretical model of the miscalibrated gate and numerical simulations of the gate; numerical benchmarking of the algorithm; contribution to writing of the manuscript.
- Author 1 contributions (5%): co-supervision; revision of the manuscript;
- Author 2 contributions (5%): revision of the manuscript;
- Author 3 contributions (35%): numerical and experimental implementation of the Bayesian calibration algorithm; numerical benchmarking of the algorithm; analysis of experimental data; main contribution to writing of the manuscript.
- Author 4 contributions (10%): numerical simulations of gates and the Bayesian calibration algorithm; numerical benchmarking of the algorithm; contribution to writing of the manuscript; revision of the manuscript.
- Author 5 contributions (5%): involvement in experimental implementation and analysis.
- Author 6 contributions (5%): involvement in experimental implementation and analysis.
- Author 7 contributions (5%): supervision; revision of the manuscript
- Author 8 contributions (2.5%): revision of the manuscript.
- Author 9 contributions (2.5%): revision of the manuscript.
- We the undersigned agree with the above stated "proportion of work undertaken" for the above published manuscript (currently under peer-review) contributing to this thesis:

Signed Candidate 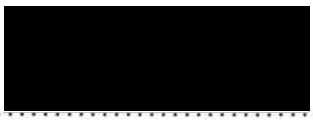 .....

Author 1 ..... [redacted]

Author 2 ..... [redacted]

Author 3 ..... [redacted]

Author 4 ..... [redacted]

Author 5 ..... [redacted]

Author 6 ..... [redacted]

Author 7 ..... [redacted]

Author 8 ..... [redacted]

Author 9 ..... [redacted]

Declaration

This work has not previously been accepted in substance for any degree and is not being concurrently submitted in candidature for any degree.

Signed: [redacted] (candidate)

Date: 22/12/2021

Statement 1

This thesis is the result of my own investigations, except where otherwise stated. Other sources are acknowledged by footnotes giving explicit references. A bibliography is appended.

Signed: [redacted] (candidate)

Date: 22/12/2021

Statement 2

I hereby give consent for my thesis, if accepted, to be available for photocopying and for inter-library loan, and for the title and summary to be made available to outside organisations.

Signed: [redacted] (candidate)

Date: 22/12/2021

Statement 3

The University's ethical procedures have been followed and, where appropriate, that ethical approval has been granted.

Signed: [redacted] (candidate)

Date: 22/12/2021

Contents

List of Figures **xvii**

List of Tables **xix**

1 Introduction **1**

I Background **11**

2 Introduction to qubit systems **13**

2.1 Qubits 13

2.2 Multi-qubit states and entanglement 17

2.3 Quantum gates 18

2.4 Noise processes 19

2.4.1 Bit-flip and dephasing channels 20

2.4.2 Depolarising channel 21

2.4.3 Amplitude damping channel 22

2.5 State and process characterisation 23

2.5.1 Quantum state tomography 23

2.5.2 Quantum process tomography 24

2.5.3 Randomised Benchmarking 26

3 Quantum harmonic oscillator **29**

3.1 1D and 3D Quantum harmonic oscillator 29

3.2 Coupled quantum harmonic oscillators 35

3.3 Coherent and thermal states 39

3.3.1 Coherent states 39

3.3.2 Thermal states 40

4 Ion traps **43**

4.1 Trapping the ions 44

4.2 Energy levels of the ion 48

4.3 Single-qubit gates 50

4.4 Entangling gates 53

5 Quantum Error Correction **57**

5.1 Stabiliser formalism 59

5.2 Steane code 60

6 Bayesian formalism **63**

6.1 Bayes theorem and Bayesian inference 63

6.2 Shannon's entropy and adaptiveness 65

6.3 Particle filtering algorithm 67

6.3.1 Importance sampling (IS) 68

6.3.2 Sampling importance resampling (SIR) 69

6.3.3 Bayesian parameter estimation 70

II Research results **75**

7 Adaptive Bayesian phase estimation for quantum error correcting codes **77**

7.1 Background 78

7.2 Single-qubit phase estimation example 80

7.2.1 Frequentist approach 80

7.2.2 Bayesian inference approach 82

7.2.2.1 Efficiency of the parameter learning process 83

7.3 Two-plaquette case 85

7.3.1 Phase Optimisation Method 88

7.3.1.1 Constant cosine PHOM 89

7.3.2 Bayesian inference approach 90

7.3.2.1 Direct Bayesian inference method 90

7.3.2.2 Marginal likelihood method 92
7.4 Correction of the full Steane code 97
7.4.1 PHOM simulations 98
7.4.2 Marginal likelihood Bayes simulations 100
7.5 Summary 101

8 Bayesian laser frequency locking **103**
8.1 Laser frequency locking 104
8.2 Frequentist Ramsey spectroscopy 106
8.3 Bayesian Ramsey spectroscopy 109
8.4 Experimental results 115
8.5 Summary 116

9 Miscalibrations in the Mølmer-Sørensen gate **119**
9.1 Mølmer-Sørensen gate 120
9.1.1 Center line detuned MS gate 126
9.2 Perturbative study of the center line detuned MS gate 128
9.2.1 Magnus expansion 129
9.2.2 First order Magnus expansion 131
9.2.3 Second order Magnus expansion 134
9.3 Predictions of the model 135
9.3.1 Relative phase 135
9.3.2 Populations 137
9.3.3 Fidelity 139
9.3.4 Purity 140
9.4 Experimental validation 141
9.5 Summary 144

10 Bayesian calibration of the Mølmer–Sørensen gate **147**
10.1 Parameters of the calibration 148
10.2 Experimental control parameters 150
10.3 Bayesian inference protocol 152
10.3.1 Measurement settings 152
10.3.2 Interpolator 153

10.3.3 Implementation of the particle filter 154
10.3.4 Stopping criterion 155
10.4 Results of the Bayesian calibration 157
10.5 Summary 160

11 Conclusions and Outlook **161**

A Appendices **167**
A.1 Generalisation for the three-plaquette case 167
A.2 Analytical study of the variance scaling for the phase measurement case 170
A.3 Analytical study of the variance scaling for the Ramsey cycle case . . . 173
A.4 Numerical coefficients 174

References **179**

Acknowledgements

Firstly, I would like to express my gratitude to my supervisor Markus Müller for his support, encouragement, and patience. His guidance was a decisive factor through all the stages of this project. I could not have imagined having a better mentor for my PhD studies.

Secondly, I would like to thank the present and past members of our group: Amit Kumar Pal, Mauricio Gutiérrez, Ciaran Ryan-Anderson, David Amaro, Jemma Bennett, Thomas Botzung, Eliana Fiorelli, Lorenzo Cardarelli, Sascha Heußen, Manuel Rispler, David Locher, and Lukas Bödeker. The productive discussions with all of them have made me a better scientist. Special thanks go to Davide Vodola for his constant help and guidance during all the projects in this thesis, and Pedro Parrado who I could always count on for talking about work and non-work-related problems. In the same line, I would like to thank the PhD students and postdocs in the Physics Department for their friendship.

Gracias, Paloma, por estar siempre ahí para alegrarme el día. Tu apoyo también ha sido vital, tanto para este proyecto como para todo lo demás. Gracias a mis padres, hermano, y al resto de mi familia por su apoyo incondicional. Finalmente, agradezco a todos mis amigos por estar siempre cerca, a pesar de la distancia, especialmente a los miembros de El Comando[1].

[1] Al final no me sobré, Nacho

List of Figures

2.1 Bloch sphere 15
2.2 Entangling circuit example 19
2.3 Noise channels 22
2.4 Quantum process tomography example 26
2.5 Randomised benchmarking example 27

3.1 Harmonic oscillator 30
3.2 QHO wave functions 33
3.3 Pair of classical coupled harmonic oscillators 37
3.4 Coherent states in (dimensionless) phase space 40

4.1 Linear Paul trap 44
4.2 Energy levels of the $^{40}Ca^{+}$ ion 49
4.3 Trapped ion transitions 53
4.4 Sideband cooling 54

5.1 Steane code 61

6.1 Bayesian inference example 64
6.2 Adaptive measurement example 66
6.3 Bayesian particle filtering algorithm 71

7.1 Frequentist phase estimation scan 81
7.2 Bayesian phase estimation 84
7.3 Adaptiveness of the phase measurement settings 86
7.4 One and two-plaquette cases 87

7.5 Constant cosine PHOM and Bayesian inference efficiencies 92
7.6 Marginal likelihood Bayesian inference pseudocode 95
7.7 Adaptiveness of the marginal likelihood Bayesian protocol 96
7.8 Efficiency of the PHOM (original and constant cosine versions) and marginal likelihood Bayesian protocol 99
7.9 Convergence of the PHOM 100
7.10 Efficiency comparison 102

8.1 Ramsey sequences 107
8.2 Ramsey fringes 108
8.3 Bayesian inference updates 110
8.4 Optimal measurement setup 113
8.5 Experimental Bayesian Ramsey protocol 114

9.1 Mølmer-Sørensen gate resonant paths 122
9.2 Single-loop MS gate 125
9.3 Center line detuned MS gate 127
9.4 Representation of the first order Magnus expansion coefficients 132
9.5 Representation of the final states obtained from first order Magnus expansion 134
9.6 Relative phase predicted by the Magnus expansion model 136
9.7 Populations predicted by the Magnus expansion model 138
9.8 Infidelities predicted by the Magnus expansion model 140
9.9 Purities predicted by the Magnus expansion model 141
9.10 Cycle for the experimental phase measurement of the center line detuned MS gate 142
9.11 Experimental results for the phase error introduced by a center line detuned gate 144
9.12 Experimental results for the populations after a center line detuned gate 145

10.1 Scans of Mølmer-Sørensen gate sequences 153
10.2 Randomised benchmarking stopping criterion 156
10.3 Example of a simulated MS gate Bayesian calibration 158
10.4 Capture range of the Bayesian protocol 159

List of Tables

8.1 Experimental results of the Bayesian Ramsey protocol 116

LIST OF TABLES

Chapter 1

Introduction

The creation and development of computers has been a milestone in the history of humanity. Their scientific and technological applications increased extensively with the development of more complex and powerful computer implementations. However, it was the proposal by Alan Turing [4] of a universal computing machine capable of computing general programmable instructions that paved the way for the current importance of computers. The development of computers, allowing more and more individuals to have access to one, along with the creation, development, and growth of the internet, did not only expand the scientific and technological applications of computers but also introduced them as a pillar of modern society. Moreover, the importance of computers keeps increasing by either the improvement of the hardware as noted, for example, by Moore's law [5] related to the almost exponential growth of the computational power of processors, or by the development of more advanced technologies implemented on computers, such as neural networks [6].

While computers have a vast number of applications, with more yet to be discovered and developed, they cannot efficiently solve certain problems. This is due to the limited tools that a computer has at its disposal to manipulate the information stored in bits. However, as noted by Feynman in 1982 [7], properties exclusive of quantum systems, such as state superposition and entanglement, can be used as additional tools for information processing. This is the idea behind quantum computers, which use quantum two-level systems generalising classical bits, known as *qubits*, allowing for the incorporation of these quantum properties to the set of tools available to a computer.

1. INTRODUCTION

The field of quantum computation gained considerable attention with the proposal of groundbreaking quantum algorithms such as Shor's algorithm [8] in 1994, and Grover's algorithm [9] in 1996. The former can be used for integer factorisation, a problem that, since there is no efficient classical algorithm to solve it, makes it the core of a wide variety of cryptographic algorithms such as RSA [10], and the latter being able to solve a database search problem with a quadratic speed-up compared to classical computers. While these are really interesting examples of quantum algorithms that can be performed on a quantum computer, there are other rich fields based on quantum protocols. This is the case of quantum cryptography [11–13], which uses properties of quantum systems such as the no-cloning theorem [14] to detect the presence of an eavesdropper during the transfer of a message, or quantum metrology [15], which uses characteristics of quantum systems such as entanglement and squeezed states to get access to more sensitive and precise measurements than those obtainable with a classical approach. Moreover, quantum computers could be used to simulate quantum systems, such as those appearing in chemistry or quantum materials [16, 17] that are impossible to simulate efficiently in a classical computer.

While these applications have great importance, to have access to them one first needs the ability to perform quantum information processing. This involves building a system of qubits and a set of operations with which one can modify the quantum information of individual qubits as well as their interaction with other qubits. These operations are called *quantum gates*, and by doing an appropriate selection of these gates one can build a discrete set, known as a *universal gate set*, which can then be used to approximate, up to arbitrary precision, any quantum operation [18]. Different physical implementations of quantum computers have been in constant development, with examples being based on trapped ions [19–27] superconductors [28–30], quantum dots [31, 32], photons [33], and Rydberg atoms [34–37] in optical lattices [38–40] or tweezer arrays [41, 42]. Any physical platform to be used for building a quantum computer must satisfy a set of conditions called Divincenzo's criteria [43], for which we will briefly mention trapped ions as an example. In the trapped-ion implementation, a qubit is encoded by using two electronic states of an ion in a trap, with gates being applied by using the interaction of laser light or microwave radiation and the Coulomb interaction between the trapped ions. This interaction can also be used to initialise the state of the qubits. Once the desired operations have been carried out, one can perform

a readout of the state of each qubit by using laser light that couples one of the binary states to a short-lived state [19]. This drives cycles of excitation followed by decay onto the original state while not affecting the other state of the binary basis. This process can be used to distinguish the state of the qubit by detecting the fluorescence and position of the qubit with a photomultiplier tube and a camera [44].

While there are several different approaches to implement a quantum computer, it should be taken into account that qubits are quantum systems and, as such, they are highly vulnerable to noise. This noise can result in the loss of their quantum information. These errors can appear due to a faulty initial state preparation of the qubits, or imperfect gates or state measurement. Additional errors might also appear due to the decay of the qubit state or the loss of the physical system used to encode the qubit. Moreover, the description of a complex physical system as a two-level system, encoding the qubit, is only an approximation of an ideal qubit, which can lead to the population of states outside of the binary states used for encoding the qubit. These mentioned noise processes are an evident problem for quantum information processing, which only grows larger with the number of qubits in the register. Since the application of interesting quantum computing protocols depends on having access to big enough qubit registers, this scalability problem supposes one of the main problems in quantum computing. As an example, an estimate of around 6000 noiseless qubits would be needed to break RSA keys of 2048 bits [45]. In order to overcome this scalability problem, it is necessary to introduce techniques to correct the errors that might appear during the computations.

Quantum Error Correction (QEC) is a field of quantum computing aimed at developing techniques to correct these errors. The idea behind QEC is to encode the information of a logical qubit into several physical qubits. This number of physical qubits can be increased to reduce the probability of a logical error arbitrarily, as long as the error probability is below a certain threshold [46, 47]. Small scale implementations of QEC protocols have been performed in the experiment [48–56] and developments in various quantum computing platforms [57–61] have pushed the fidelities of fundamental gate operations and the number of qubits available closer to the values needed for further QEC implementations, such as *fault-tolerant* QEC codes [62–64], which are protected against errors occurring during the QEC process itself. The implementation of fault-tolerant QEC has seen exciting progress, by the very recent breakthrough experiments

of Refs. [65–68]. However, the application of QEC for a useful quantum computation, which requires several logical qubits, is not expected in the immediate future due to the large number of physical qubits required. The aforementioned 6000 logical qubits needed to break RSA keys of 2048 bits would require about 20 million physical qubits considering the current noise and quantum computing platforms [45].

Since longer-term developments are needed to achieve fault-tolerant quantum computation, it is interesting to look at possible applications of current and near-term quantum processors. These processors, called Noisy Intermediate-Scale Quantum (NISQ) devices [69, 70], consist of a register of roughly 50 to 100 noisy qubits. This number is small enough to be implemented in the current experiments or in the near future, but large enough to demonstrate basic, but interesting, applications of quantum computers. In this line, Google developed its Sycamore quantum processor composed of 53 superconducting qubits and claimed its quantum supremacy [71] in 2019, and as of November of 2021, IBM unveiled their quantum processor with 127 qubits [72]. Moreover, the important advances made by NISQ devices are not related only to improvements in the hardware and its applications. Access to some of these NISQ devices has been made available for anyone online [73–75]. Hybrid algorithms [76], which consist of parametrised quantum circuits that are optimised by a classical computer to improve their efficiency for a given problem, are being developed. Examples of these hybrid algorithms are the Variational Quantum Eigensolver (VQE) [77] or the Quantum Approximate Optimisation Algorithm (QAOA) [78]. The open access to some NISQ devices, combined with the efficiency advantages of hybrid algorithms, has motivated investigations backed by experimental results [79–84] without needing to be part of the group implementing the NISQ device itself, or having to coordinate the experiments with them. Moreover, this open access to NISQ devices is currently motivating the creation and development of several start-ups [85] aiming at using these devices to solve problems related to fields such as finance and industry [86–94].

Whether the interest lies on near-term NISQ devices, or longer-term quantum computers with QEC, the importance of improving the fidelity of the qubits and quantum gates implemented in the experiments is evident. For NISQ devices, a higher fidelity of these components translates into a higher probability of achieving the correct result in a near-term quantum computation. For QEC this means, first, reaching an error probability below the threshold for which a given QEC code is useful, and second, once

the threshold has been reached, increasing these fidelities means requiring fewer physical qubits to build a logical one. Therefore, correct calibration of all the parameters related to the experimental implementation of qubits and quantum gates is vital for the experimental quantum information processing to have a high fidelity with respect to the ideal case.

From a general point of view, a calibration protocol consists of obtaining information about the parameters of a system, quantum or classical, by performing measurements. With this information about the current parameters, one can tune them to reach a value close enough to their ideal value. When considering the measurements that can be performed in a system, one can distinguish between two cases: probabilistic measurements, with a simple example being a coin toss, or deterministic measurements, such as measuring the weight of that coin (up to the precision of the weighing machine). In the case of quantum systems, measurements, in general, are probabilistic and have to be performed several times to get a picture of the statistics, which can then be associated with the most probable value of the parameters. This last point is where an important decision has to be made: how do we interpret the information obtained from the measurements to estimate a value for our parameters? From the *frequentist* approach, one can decide to repeat the same experiment several times to obtain the statistics associated, where the more measurements performed results in a better estimate. While frequentism is the most traditional approach, there is another way to interpret the outcomes of measurements to gain information, the *Bayesian* approach [95–97], based on the application of Bayes' theorem to update our knowledge with each measurement.

Bayes' theorem was first formulated by Thomas Bayes and published in 1763, two years after his death [98]. It prescribes how to update the prior knowledge of a system using an outcome of an experiment and the likelihood of that outcome in order to update our knowledge. In this approach, the parameters to be learnt are treated as variables, and their knowledge is modelled as a probability distribution. This will narrow down to the true values as more information is gained. This general definition can be used to model several cases, from simple ones such as asking an everyday question (e.g., asking for the time) and updating our knowledge after receiving an answer, to more complex cases such as measuring a quantum system (which can also be seen as asking a question) to infer the values of some parameters. While Bayes' theorem has been postulated for

over two centuries now, its application to inference processes was restricted to simple cases which allowed for an analytical solution. For more interesting cases, the study of more difficult probability distributions, with as many dimensions as parameters that one wants to learn, was not viable. However, the creation and evolution of classical computers proved again its importance, in this case, by allowing numerical calculations which permit the implementation of complex Bayesian inference processes.

Nowadays, it is possible to choose which kind of calibration protocol one wants to implement. On the one hand, a frequentist approach usually has an easier and less numerically intensive implementation but depends on performing the same measurements several times, which can lead to a suboptimal information gain. Moreover, a frequentist approach can find difficulties when performing a multi-parameter calibration, due to possible correlations between the parameters. This complicates the calibration process, which would consist of repeating iterations where each parameter is calibrated individually. These single parameter scans for a multi-parameter calibration can result in a slow convergence to the optimal value of the parameters, or even fail to find them. The Bayesian approach can avoid these problems since it works with a probability distribution of all the parameters at the same time, which accounts for possible correlations between them. Additionally, in the frequentist approach, obtaining the error of the estimates could not have an analytical formula, which leads to a dependence on numerical simulations for obtaining these errors. On the other hand, the Bayesian approach has built-in error estimates, since it works with probability distributions that have an associated variance. Finally, the Bayesian approach does not need to perform the same measurements several times, allowing for the selection of adaptive measurement settings. As a result, a Bayesian protocol can define the optimal measurements and how to update the knowledge about the parameters, allowing for a straightforward implementation into a computer program, therefore achieving a complete automation of the calibration protocol.

The work of this thesis is developed in this context. We focused on the implementation of Bayesian inference protocols in order to substitute other frequentist approaches, traditionally used for the calibration of quantum systems. In this thesis, we will present the advantages of these protocols compared to the frequentist approaches. Some of the protocols that we will develop have been implemented for the calibration of gates in

trapped-ion quantum devices, although the ideas explained can be generalised to other physical implementations.

This thesis is structured as follows: In the first part of this thesis, we introduce the background concepts necessary to understand the contents of this thesis. These concepts include qubit systems and quantum gates, noise processes, quantum harmonic oscillators, trapped-ion quantum computers, quantum error correction, and Bayesian formalism. Bayes' theorem is the central part of this thesis and will be used to build calibration protocols to improve the fidelities of quantum gates and QEC codes states. After this introduction, we then explain our original research results.

In Chapter 7 we present a protocol that can be used to measure and correct unwanted phases appearing after the preparation of a Steane quantum error correcting code. This Bayesian protocol is compared to another proposed frequentist protocol, and we show that it is more efficient, since our approach allows for the selection of adaptive measurement settings. Due to this adaptive selection, our Bayesian protocol optimises the information gained by each measurement, allowing it to require fewer measurements to obtain the same precision as the frequentist approach. The work presented in this chapter is included in reference

- "Adaptive Bayesian phase estimation for quantum error correcting codes", F. Martínez-García, D. Vodola, and M. Müller, *New Journal of Physics* **21** no. 12, 123027 (2019) [1].

In Chapter 8 we study the calibration of a laser to the transition frequency between two internal levels of a trapped ion. A correct calibration of the laser frequency is vital for the correct behaviour of trapped-ion operations. For example, the correct application of single-qubit gates depends on having a laser tuned to the transition frequency of the levels used to encode the qubit. We introduce a protocol based on Bayesian Ramsey spectroscopy to, not only tune the laser frequency at a given time but lock the laser to the transition frequency over time. This is done by estimating drifts that this frequency might suffer due to small changes over time of the laser frequency or in the magnetic field. This protocol shows advantages compared to the frequentist approach to Ramsey spectroscopy such as returning the error of the obtained estimate, having a simple rule for the selection of optimal measurements, being invulnerable to

fringe-hopping errors appearing in the frequentist approach, and being straightforward to automate by implementing the protocol in a computer program.

As a natural follow-up of this Bayesian calibration of single-qubit gates, we move on to the study and calibration of an entangling gate. In Chapter 9 we present the idea behind the Mølmer-Sørensen gate, which can be used to create entanglement in trapped-ion systems. We focus on the effects that the miscalibration of some of the parameters of this gate has on its performance. Particularly, we take a closer look at the effect that an asymmetry between the two laser frequencies has on this gate. Since there was no analytical understanding of the effects of this miscalibration, this imperfection could only be accounted for by performing numerical calculations. We derive a semi-analytical model based on a perturbative Magnus expansion to obtain an understanding of the error introduced by this miscalibration, without requiring numerical calculations or fitting procedures. We then compare the results from our model to those obtained by simulations, and even experimental results, concluding that our semi-analytical model manages to correctly account for the effects of that miscalibration. This model can then be used during the experimental calibration of the gate to identify and compensate for the effect of gate miscalibrations. The work presented in this chapter is included in reference [1]

- "Analytical and experimental study of center line miscalibrations in Mølmer-Sørensen gates", F. Martínez-García, L. Gerster, D. Vodola, P. Hrmo, T. Monz, P. Schindler, and M. Müller, *Physical Review A* **105** no. 3, 032437 (2022) [2].

After having explained the Mølmer-Sørensen gate and the experimental parameters that we want to optimise, we develop and investigate a new Bayesian protocol to estimate and correct these parameters in Chapter 10. For this purpose, we make use of a particle-filter algorithm to avoid the dimensionality problem that Bayesian inference processes suffer when estimating several parameters at the same time. Additionally, due to the lack of analytical likelihood functions for the possible outcomes of the experiments, we introduce the concept of an *interpolator*. This allows us to precalculate the values of the likelihoods for the points in a grid in parameter space. This can then be used to interpolate the values of the likelihoods without the need to calculate them by

[1] This work was accepted in a journal after the PhD viva and the reference has been changed accordingly.

numerical integration of the Hamiltonian. Thanks to the particle-filter algorithm and the interpolator, our Bayesian protocol manages to calibrate four different parameters, both in the simulations and in the experimental, in a completely automated way. The work presented in this chapter is included in reference [1]

- "Experimental Bayesian calibration of trapped-ion entangling operations", L. Gerster, F. Martínez-García, P. Hrmo, M. van Mourik, B. Wilhelm, D. Vodola, M. Müller, R. Blatt, P. Schindler, and T. Monz, *PRX Quantum* **3** no. 2, 020350 (2022) [3].

Finally, in Chapter 11 we summarise the results presented in the thesis, discuss the possible applications in the near and long term given the current status of quantum computation, and mention how these results could be generalised to other calibration protocols or quantum information processing architectures.

[1] This work was accepted in a journal after the PhD viva and the reference has been changed accordingly.

Part I

Background

Chapter 2

Introduction to qubit systems

In this chapter, we define the qubit and the quantum operations that can be performed on them. We will also elaborate on entanglement, a feature of quantum mechanics with no counterpart in classical mechanics. Finally, we will explain how to model noise processes and the concepts of state and process tomography used to characterise quantum states and operations. The book in Ref. [18] can be consulted by the reader interested in a more detailed introduction.

2.1 Qubits

A qubit is a quantum two-level system that is used as the quantum counterpart of a classical bit. Therefore, it is the basic unit of information in a quantum computer. Since a qubit is a quantum two-level system, its state belongs to a two-dimensional Hilbert space, $\mathcal{H}$, which is a complex vector space with an inner product. For representing a state in this Hilbert space we use the Dirac notation, which represents every state as a ket, $|\cdot\rangle$, while an element of the dual space is represented by a bra, $\langle\cdot|$, which is the conjugate transpose (or adjoint) of a ket: $\langle\cdot| = |\cdot\rangle^\dagger$, where we use the $\dagger$ symbol to represent the adjoint. We can select a basis for this two-dimensional Hilbert space. Let us consider the basis $\{|u_i\rangle\}$, $i = 1, 2$. This basis is orthonormal if it satisfies $\langle u_i|u_j\rangle = \delta_{ij}$ (Kronecker delta) and the closure relation

$$\sum_{i=1}^{2} |u_i\rangle\langle u_i| = \mathbb{1}. \tag{2.1}$$

An example of an orthonormal basis would be the one given by

$$|0\rangle = \begin{pmatrix} 1 \\ 0 \end{pmatrix}, \quad |1\rangle = \begin{pmatrix} 0 \\ 1 \end{pmatrix}. \tag{2.2}$$

Any general state $|\psi\rangle$ can be written on this basis by projecting the state into its components

$$\begin{aligned} \alpha &= \langle 0|\psi\rangle \\ \beta &= \langle 1|\psi\rangle \end{aligned} \tag{2.3}$$

from which we obtain that, in this basis, $|\psi\rangle$ can be written as

$$|\psi\rangle = \begin{pmatrix} \alpha \\ \beta \end{pmatrix} = \alpha\,|0\rangle + \beta\,|1\rangle\,. \tag{2.4}$$

A physical state must be normalised, $|\alpha|^2 + |\beta|^2 = 1$, and a global phase is undetectable, making the state $|\psi\rangle$ equivalent to $e^{i\phi}\,|\psi\rangle$ for any real phase ϕ. By using these properties, we obtain that any qubit state can be written as

$$|\psi\rangle = \cos\frac{\theta}{2}\,|0\rangle + e^{i\phi}\sin\frac{\theta}{2}\,|1\rangle\,, \tag{2.5}$$

where $\theta \in [0, \pi]$ and $\phi \in [0, 2\pi]$. Due to this general form, every state of a qubit can be parametrised by these two angles, θ and ϕ, which allows it to be represented in the surface of the Bloch sphere (see Fig. 2.1). In our case we have selected the basis $|0\rangle$ and $|1\rangle$, which we will call computational basis, to be contained in the Z-axis and we will consider them to be the eigenvectors of the Pauli operator Z, which in this basis is represented by

$$Z = \begin{pmatrix} 1 & 0 \\ 0 & -1 \end{pmatrix}. \tag{2.6}$$

As we can see from this form, the eigenvalues associated are $\langle 0|\,Z\,|0\rangle = 1$ for $|0\rangle$ and $\langle 1|\,Z\,|1\rangle = -1$ for $|1\rangle$. There are also X and Y Pauli operators, which will be represented on the computational basis by

$$X = \begin{pmatrix} 0 & 1 \\ 1 & 0 \end{pmatrix}, \quad Y = \begin{pmatrix} 0 & -i \\ i & 0 \end{pmatrix}. \tag{2.7}$$

Similar to the Z operator, the X and Y operators can define their own basis of $\mathcal{H}$, given by their eigenvectors, with associated eigenvalues $+1$ and -1: $\{|+\rangle_x\,, |-\rangle_x\}$ for

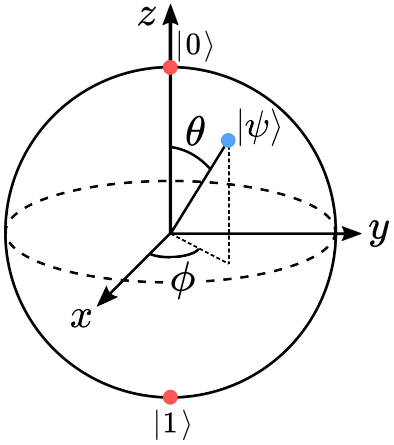

Figure 2.1: Bloch sphere. A pure state of a two-level system, e.g. a qubit, can be represented as a unit vector in the Bloch sphere, that is, a point in the surface parametrised by the angles θ and ϕ. The states that compose the computational basis, $|0\rangle$ and $|1\rangle$, are selected to be in the intersections of the Z-axis with the Bloch sphere.

X and $\{|+\rangle_y, |-\rangle_y\}$ for Y

$$\begin{aligned} |+\rangle_x &= \frac{1}{\sqrt{2}}(|0\rangle + |1\rangle), \quad |-\rangle_x = \frac{1}{\sqrt{2}}(|0\rangle - |1\rangle) \\ |+\rangle_y &= \frac{1}{\sqrt{2}}(|0\rangle + i\,|1\rangle), \quad |-\rangle_y = \frac{1}{\sqrt{2}}(|0\rangle - i\,|1\rangle) \end{aligned} \tag{2.8}$$

Due to a lack of information on the state of our qubit, it could be that the best knowledge that we have about it is described by a probabilistic ensemble $\{|\psi_i\rangle\}$ with probabilities p_i, with i being an index running over all the possible components of the ensemble. In this case, we have what is called a *mixed state*, instead of a pure state. This means that we can no longer describe it as a ket, and we have to use the density matrix formalism, which describes our state as a matrix defined by a statistical mixture given by

$$\rho = \sum_i p_i \,|\psi_i\rangle \,\langle\psi_i|\,. \tag{2.9}$$

This is easily generalisable to the case of a probabilistic ensemble distributed according to a continuous variable, x, for example. In this case, we have an ensemble $\{|\psi(x)\rangle\}$ with probabilities $p(x)$, and the density matrix would be

$$\rho = \int p(x)\,|\psi(x)\rangle\,\langle\psi(x)|\,dx. \tag{2.10}$$

For the case of a qubit, any density matrix can be written as

$$\rho = \frac{1}{2}(1 + \vec{n} \cdot \vec{\sigma}), \tag{2.11}$$

with $\vec{n}$ being a vector describing the position of the state in the Bloch sphere with $|\vec{n}| \leq 1$ and $\vec{\sigma} = (X, Y, Z)$ being a vector composed of the Pauli matrices. One of the extremal cases, $|\vec{n}| = 1$, corresponds to a state in the surface of the Bloch sphere, that is, a pure state. The other extremal case, $|\vec{n}| = 0$, also called a *completely mixed state*, corresponds to a state with no information, located at the center of the Bloch sphere.

In order to quantify how much a given quantum state is mixed, we can introduce the concept of *purity*, defined as

$$\chi(\rho) = \mathrm{Tr}\left(\rho^2\right). \tag{2.12}$$

The purity of a given state is a scalar that takes values between $1/d$ for a completely mixed state, where d is the dimension of the Hilbert space of the quantum system considered, and 1 for a pure state.

Finally, we also introduce the concept of *fidelity* [99], which can be interpreted as a way of quantifying how close a quantum state, ρ, is to another one, ρ'. The fidelity is defined as

$$F(\rho, \rho') = \left[\mathrm{Tr}\left(\sqrt{\sqrt{\rho}\,\rho'\sqrt{\rho}}\right)\right]^2. \tag{2.13}$$

This definition can be simplified for the case in which one of the states is a pure state to obtain:

$$F\left(|\psi\rangle, \rho'\right) = \langle\psi|\,\rho'\,|\psi\rangle\,. \tag{2.14}$$

Furthermore, for the case of both states being pure, i.e., $|\psi\rangle$ and $|\psi'\rangle$, the definition can be reduced to the following

$$F\left(|\psi\rangle, |\psi'\rangle\right) = \left|\langle\psi'|\psi\rangle\right|^2. \tag{2.15}$$

The fidelity is a scalar that satisfies $F(\rho, \rho') \in [0, 1]$, which only takes the value 1 when both states are the same.

Now that we have defined the basics of a qubit, we can move to systems that contain more than one qubit, which will allow us to explore concepts such as entanglement.

2.2 Multi-qubit states and entanglement

The state of a system of n qubits will be described by a vector in a 2^n-dimensional Hilbert space, obtained by the tensor product of n of the single-qubit Hilbert spaces, $\mathcal{H}^{\otimes n}$. A basis of this Hilbert space can be defined by all the possible combinations of tensor products of the basis of each two-dimensional Hilbert space, for example, $\{|i_1\rangle \otimes ... \otimes |i_n\rangle\}$ with $i_1, ..., i_n = 0, 1$. Therefore, a state in this expanded space will have the form

$$|\psi\rangle = \sum_{i_1,...,i_n} c_{i_1,...,i_n} |i_1\rangle \otimes ... \otimes |i_n\rangle = \sum_{i_1,...,i_n} c_{i_1,...,i_n} |i_1, ..., i_n\rangle \,, \tag{2.16}$$

where we simplified the notation by defining $|a\rangle \otimes |b\rangle \equiv |a, b\rangle$, although we will also use the notation $|a\, b\rangle \equiv |a, b\rangle$. Consequently, all the possible states of this multi-qubit system can be represented as a superposition of states of the form $|i_1, ..., i_n\rangle$ with coefficients $c_{i_1,...,i_n}$.

By looking at the general form of Eq. (2.16), we can introduce a classification based on the form of each specific state. If a state can be written as

$$|\psi\rangle = |\psi_1\rangle \otimes |\psi_2\rangle \otimes ... \otimes |\psi_n\rangle \,, \tag{2.17}$$

it is said to be separable, when this is not the case, it is said to be entangled. There are some important examples of entangled states such as the Bell states [100]

$$\begin{aligned} \left|\Phi^+\right\rangle &= \frac{1}{\sqrt{2}}(|00\rangle + |11\rangle), \qquad \left|\Phi^-\right\rangle = \frac{1}{\sqrt{2}}(|00\rangle - |11\rangle), \\ \left|\Psi^+\right\rangle &= \frac{1}{\sqrt{2}}(|01\rangle + |10\rangle), \qquad \left|\Psi^-\right\rangle = \frac{1}{\sqrt{2}}(|01\rangle - |10\rangle), \end{aligned} \tag{2.18}$$

or the Greenberger-Horne-Zeilinger (GHZ) state [101] of n qubits

$$|\mathrm{GHZ}\rangle = \frac{1}{\sqrt{2}}(|00\ldots0\rangle + |11\ldots1\rangle). \tag{2.19}$$

As superposition states, entangled states are a particularity of quantum mechanics with no classical counterpart. This makes them an important additional resource available for quantum information processing. Now that we have explained the basic concepts of qubit states, we can introduce the ideas behind quantum gates.

2.3 Quantum gates

While qubits are the basic components of a quantum computer with the purpose of storing quantum information, we need the ability to manipulate this information. Up to now, we have seen some examples of operators such as the X, Y, and Z, which perform single-qubit rotations of an angle π around their respective axis. These operators are just examples of general single-qubit rotations of arbitrary angle, ϕ, and rotation axis, $\vec{\sigma}$

$$R_{\vec{n}}(\phi) = e^{i\frac{\phi}{2}\vec{n}\cdot\vec{\sigma}} = \cos\frac{\phi}{2}\cdot\mathbb{1} + i\sin\frac{\phi}{2}(\vec{n}\cdot\vec{\sigma}). \tag{2.20}$$

Unitary operators such as these, when used as basic elements of the quantum information processing in a quantum computer, are called *quantum gates*. Other important examples of single-qubit gates are the Hadamard gate H, the phase gate S, and the T gate:

$$H = \frac{1}{\sqrt{2}}\begin{pmatrix}1 & 1\\ 1 & -1\end{pmatrix}, \quad S = \begin{pmatrix}1 & 0\\ 0 & e^{i\pi/2}\end{pmatrix}, \quad T = \begin{pmatrix}1 & 0\\ 0 & e^{i\pi/4}\end{pmatrix} \tag{2.21}$$

where the Hadamard gate has the effect of rotating the computational basis into the X-basis and vice versa

$$H|0\rangle = |+_x\rangle, \quad H|1\rangle = |-_x\rangle, \quad H|+_x\rangle = |0\rangle, \quad H|-_x\rangle = |1\rangle, \tag{2.22}$$

and the S and T gates are Z rotations of angles $\pi/2$ and $\pi/4$ respectively, that is, they introduce a phase to the state.

Although the previous gates can be used to manipulate the state of a single-qubit, we need the ability to create entanglement between different qubits. An important example of an entangling gate is the controlled-NOT (or CNOT) gate, which is a two-qubit gate that takes the state of a *control qubit* and performs an operation on a *target qubit*, defined as

$$\text{CNOT} = \begin{pmatrix}1 & 0 & 0 & 0\\ 0 & 1 & 0 & 0\\ 0 & 0 & 0 & 1\\ 0 & 0 & 1 & 0\end{pmatrix} = \frac{1}{2}\left[(\mathbb{1}_c + Z_c)\,\mathbb{1}_t + (\mathbb{1}_c - Z_c)\,X_t\right], \tag{2.23}$$

with c and t used to specify that the operators act on the control and target qubits, respectively. Therefore, the action of this gate is to apply an X operation on the target

qubit if the control is in the state $|1\rangle$ and leaves the target unchanged otherwise:

$$\begin{aligned} \text{CNOT}\,|0_c\,0_t\rangle &= |0_c\,0_t\rangle\,, \quad \text{CNOT}\,|1_c\,0_t\rangle = |1_c\,1_t\rangle\,, \\ \text{CNOT}\,|0_c\,1_t\rangle &= |0_c\,1_t\rangle\,, \quad \text{CNOT}\,|1_c\,1_t\rangle = |1_c\,0_t\rangle\,. \end{aligned} \tag{2.24}$$

It is simple to verify that this two-qubit operation can be used to create entanglement, where an example is shown in Fig. 2.2.

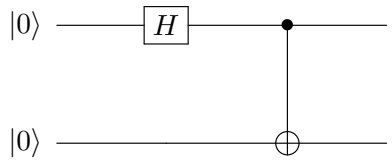

Figure 2.2: Entangling circuit example. An entangled state can be obtained by applying a Hadamard gate to a qubit, which will then be used as the control for a CNOT gate acting on a second qubit. The state obtained at the end of the circuit is the Bell state $|\Phi^+\rangle = 1/\sqrt{2}(|00\rangle + |11\rangle)$.

While these are examples of single-qubit and entangling gates, we need to be able to process quantum information in a general manner. Because of this, one could ask whether it is possible to perform any arbitrary operation on a set of qubits by using just a discrete set of gates. This is the idea behind the Solovay-Kitaev theorem [18], which proves that a *universal set of quantum gates*, composed of a discrete set of gates, can be used to build any general unitary operation, up to an arbitrary error. An example of such a universal set of quantum gates is composed of the H, T, and CNOT gates, where one can use these first two gates to approximate any single-qubit unitary, and the CNOT can be used to introduce the entanglement between different qubits.

2.4 Noise processes

Up to this point, we have introduced qubits and the operations that can be performed over them to manipulate their quantum information. However, all that has been introduced so far is an idealisation. A quantum computer, like any quantum system, will be affected by noise due to unwanted effects, such as a coupling of the qubits with the environment. In this case, we should consider on top of the state of our qubits, ρ, the state of the environment, ρ_E, and the interactions between these two subsystems. Without loss of generality, we can consider the state of the environment to be a pure state $\rho_E = |e_0\rangle\langle e_0|$, with $|e_0\rangle$ being an element of the Hilbert space of the environment,

spanned by $\{|e_k\rangle\}$. The final state after a general evolution, U, acting on this complete system will be $U\rho \otimes |e_0\rangle \langle e_0| U^\dagger$. However, the only system that will be measured is the one formed by the qubits, leaving all the information in the environment unused. Because of this, we have to trace over the environment to obtain the state of the qubits after the evolution, ρ':

$$\rho' = \sum_k \langle e_k| U \left(\rho \otimes |e_0\rangle \langle e_0|\right) U^\dagger |e_k\rangle = \sum_k E_k \rho E_k^\dagger, \tag{2.25}$$

where we have defined a set of *Kraus operators* [102], $\{E_k\}$, given by

$$E_k \equiv \langle e_k| U |e_0\rangle , \tag{2.26}$$

which satisfy

$$\sum_k E_k^\dagger E_k = \mathbb{1}. \tag{2.27}$$

Therefore, these effects can be modelled as *quantum channels* which take as input an initial quantum state, ρ, and output the noisy state, ρ':

$$\mathcal{E}(\rho) = \rho' = \sum_k E_k \rho E_k^\dagger, \tag{2.28}$$

where both ρ and ρ' are density matrices of a subsystem, in our case the qubit system.

An interpretation of Eq. (2.28) can be obtained if we consider the quantum channel as a process that substitutes the initial state ρ for the normalised state $E_k \rho E_k^\dagger / \operatorname{Tr}\left(E_k \rho E_k^\dagger\right)$ with a probability $p(k) = \operatorname{Tr}\left(E_k \rho E_k^\dagger\right)$. This leaves us with the statistical mixture, ρ', as the state after applying the quantum channel. Using this interpretation, it is easy to model some simple, yet important, single-qubit error models.

2.4.1 Bit-flip and dephasing channels

The *bit-flip channel* considers the possibility of having a bit-flip error, which performs the transformation $|0\rangle \leftrightarrow |1\rangle$, with a probability p. The operators associated with this channel are

$$E_0 = \sqrt{1-p}\,\mathbb{1}, \quad E_1 = \sqrt{p}\,X, \tag{2.29}$$

that is, the bit-flip channel is defined as

$$\mathcal{E}(\rho) = (1-p)\,\rho + p\,X\rho X, \tag{2.30}$$

which produces a statistical mixture composed of a $(1-p)$ probability of leaving the state unchanged and p of introducing a bit-flip error.

Similarly, one can define the *dephasing or phase-flip channel* by introducing the possibility of having an error of the form $|1\rangle \leftrightarrow -|1\rangle$. The operators associated to this channel are

$$E_0 = \sqrt{1-p}\,\mathbb{1}, \quad E_1 = \sqrt{p}\,Z, \tag{2.31}$$

where now p is the probability of the phase-flip error happening. In this case, the channel is

$$\mathcal{E}(\rho) = (1-p)\,\rho + p\,Z\rho Z. \tag{2.32}$$

The statistical mixture resulting from this channel accounts for a coherence loss in the state, with the limiting case of $p = 1/2$. This case would transform the state into a completely classical statistical mixture, that is, a diagonal density matrix, which keeps the same probabilities of measuring $|0\rangle$ or $|1\rangle$, but has no quantum coherences. A representation on the Bloch sphere of the effect of this channel, as well as for the following examples of noise channels, is shown in Fig. 2.3.

2.4.2 Depolarising channel

Another important example is the *depolarising channel*, which can be used to model the complete loss of quantum information with a probability p'. Such a channel can be written as:

$$\mathcal{E}(\rho) = (1-p')\,\rho + \frac{p'}{2}\,\mathbb{1}, \tag{2.33}$$

which either keeps the state unchanged with probability $1-p'$, or substitutes it for a completely mixed state with probability p', which accounts for losing all the information about the state. Using that for an arbitrary density matrix, ρ, the identity operator can be written as:

$$\frac{\mathbb{1}}{2} = \frac{\rho + X\rho X + Y\rho Y + Z\rho Z}{4}, \tag{2.34}$$

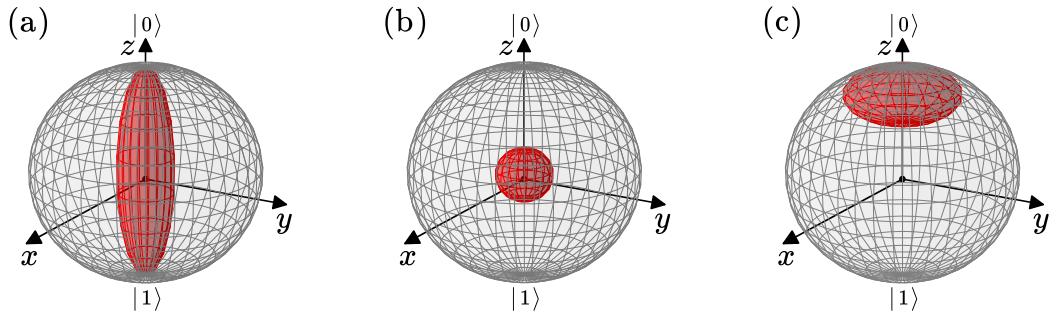

Figure 2.3: Noise channels. Representations of how different noise channels affect an initial state. This is shown by how all the possible initial states, represented by the Bloch sphere in grey, are contracted to the final ones shown in red. (a) Dephasing channel: This channel causes a decoherence of the state while leaving the populations unchanged. The case shown is for $p = 3/8$, as a consequence, the final state has some coherence. (b) Depolarising channel: This channel accounts for the loss of information of both the phase and the population of the qubit. As a result, the Bloch sphere is contracted to the center. The case shown is for $p = 3/8$. (c) Amplitude damping channel: This channel models the decay of one state, in this case, $|1\rangle$, into another, $|0\rangle$, with probability p. As a consequence, the Bloch sphere is contracted to the state $|0\rangle$. The case shown is for $p = 3/4$.

and defining $p \equiv 3p'/4$, one can rewrite the depolarising channel as

$$\mathcal{E}(\rho) = (1-p)\,\rho + \frac{p}{3}\,(X\rho X + Y\rho Y + Z\rho Z), \tag{2.35}$$

with operators

$$E_0 = \sqrt{1-p}\,\mathbb{1}, \quad E_1 = \sqrt{\frac{p}{3}}\,X, \quad E_2 = \sqrt{\frac{p}{3}}\,Y, \quad E_3 = \sqrt{\frac{p}{3}}\,Z \tag{2.36}$$

2.4.3 Amplitude damping channel

The *amplitude damping channel* can be used to describe an error that causes a decay of one state to another. As such, it can be used to model energy dissipation in a quantum system. The operators that define this model are

$$\begin{aligned} E_0 &= \begin{pmatrix} 1 & 0 \\ 0 & \sqrt{1-p} \end{pmatrix}, \\ E_1 &= \begin{pmatrix} 0 & \sqrt{p} \\ 0 & 0 \end{pmatrix}, \end{aligned} \tag{2.37}$$

with p being the probability of the state to decay. The action of the E_0 operator is to decrease the amplitude of the decaying state while leaving the non-decaying one unchanged. As for E_1, it changes the decaying state into the non-decaying one.

2.5 State and process characterisation

As explained, when studying a non-ideal quantum system one has to account for possible error sources that might affect the quantum state or even the performance of the quantum gates. In order to see how damaging these effects are, we need a method for estimating the form of our quantum states, or the true operations that our non-ideal quantum gates are performing. To do this, one can perform *quantum state tomography* (QST), *quantum process tomography* (QPT), and *randomised benchmarking* (RB).

2.5.1 Quantum state tomography

Quantum state tomography [18] is a method used to estimate the form of a state ρ. In the following, we will consider it to be the state of a qubit, but this method can be easily generalised for any quantum state. We know that the state ρ will be represented by a 2x2 matrix and as such, it can be expanded in, for example, the Pauli basis as we saw in Eq. (2.11). The X component can be obtained as $\mathrm{Tr}(X\rho)$, and similar expressions for the other elements. This leaves us with

$$\rho = \frac{\mathrm{Tr}(\rho)\,\mathbb{1} + \mathrm{Tr}(X\rho)\,X + \mathrm{Tr}(Y\rho)\,Y + \mathrm{Tr}(Z\rho)\,Z}{2}. \tag{2.38}$$

Therefore, we can reconstruct the form of the state by obtaining the expected values of each of these operators on the state ρ. However, since the information about an unknown quantum state is obtained by measuring it, and this process depends on the statistics associated with that state, we will need to have access to several copies to obtain the expected values.

A similar process can be performed for a general quantum state with a Hilbert space of dimension higher than two. However, it is straightforward to see that the number of expected values to be measured increases with the dimensionality of the quantum system and, with it, the number of measurements of the state ρ required. As a consequence, if we consider a multi-qubit state, the dimensionality scales exponentially with the number of qubits. This makes it not viable to perform quantum state tomography

in a system of more than a few qubits since one should measure 2^{2n} expected values, where we denote the number of qubits as n. However, it is noteworthy to mention that the number of expected values to be measured can be decreased if we already know some characteristics of the state. This is the case discussed in Chapter 7, where we aim to estimate the errors appearing in a seven-qubit state due to an imperfect state preparation, but thanks to the error model that we consider in that chapter, we will only need to measure seven parameters.

2.5.2 Quantum process tomography

While quantum state tomography is used to reconstruct the form of a state ρ, quantum process tomography [103] can be used to reconstruct the form of a quantum operation, such as a quantum gate. The basic idea behind this process is straightforward: Assuming a Hilbert space of dimension d, we can use a set $\{|\psi_i\rangle\langle\psi_i|\}_{i=1}^{d^2}$ that forms a basis of the matrices of this Hilbert space. If we want to obtain the form of a process, $\mathcal{E}$, we can apply it to each of the elements of this basis and perform quantum state tomography over each of the final states $\mathcal{E}(|\psi_i\rangle\langle\psi_i|), i = 1, ..., d$.

In principle, obtaining how $\mathcal{E}$ transforms each of these states is enough to characterise the process since, by linearity, we can obtain how it acts over any arbitrary state. However, we can go further by expressing the operation in the form:

$$\mathcal{E}(\rho) = \sum_k E_k \rho E_k^\dagger, \tag{2.39}$$

as in Sec. 2.4. While this is the diagonalised expression of the channel, it might be convenient to obtain its form given by a set of fixed operators that are easy to measure for a given experimental setup, $\{\tilde{E}_k\}$, which can be written as

$$\tilde{E}_i = \sum_m e_{i\,m} E_m, \tag{2.40}$$

from which it can be written

$$\mathcal{E}(\rho) = \sum_k \chi_{mn} \tilde{E}_m \rho \tilde{E}_n^\dagger, \tag{2.41}$$

$$\chi_{mn} = \sum_i e_{im} e_{in}^*. \tag{2.42}$$

Therefore, the process will be characterised in this operator basis if we obtain the matrix χ. In order to do this, we need to study the effect that this quantum channel has on every element of a matrix basis, $\{\rho_j\}_{j=1}^{d^2}$, which can be used to construct the density matrices of the system. We can learn this by doing quantum state tomography, and the results can be written as

$$\mathcal{E}(\rho_j) = \sum_k \lambda_{jk}\rho_k. \tag{2.43}$$

By using this λ matrix, defining the β matrices as

$$\tilde{E}_m\rho_j\tilde{E}_n^\dagger = \sum_k \beta_{jk}^{mn}\rho_k, \tag{2.44}$$

and using Eq. (2.41), one can obtain

$$\chi_{mn} = \sum_{jk} \kappa_{jk}^{mn}\lambda_{jk}, \tag{2.45}$$

where κ is the generalised inverse of β

$$\beta_{jk}^{mn} = \sum_{st,xy} \beta_{jk}^{st}\kappa_{st}^{xy}\beta_{xy}^{mn}. \tag{2.46}$$

Therefore, by measuring the effect of the process over the elements of the $\{\rho_j\}_{j=1}^{d^2}$ basis, one can obtain the coefficients of the λ matrix by using Eq. (2.43). One can use then Eq. (2.44) to Eq. (2.46) as well as λ to obtain the values of χ. This characterises $\mathcal{E}$ in terms of $\{\tilde{E}_k\}$. Examples of the final result of a quantum process tomography process for a simple single-qubit operation are shown in Fig. 2.4.

While quantum process tomography is a complete method for obtaining the form of an unknown quantum channel, it also has, in the same way as the quantum state tomography, an undesirable exponential scaling with the size of the system. This makes this method inefficient for estimating the fidelity of quantum operations as the size of the system increases. Additionally, this method is vulnerable to State Preparation And Measurement (SPAM) errors. However, one can use a Randomised Benchmarking process to obtain just the fidelity of the gate, with the benefit of requiring fewer measurements while not being affected by SPAM errors.

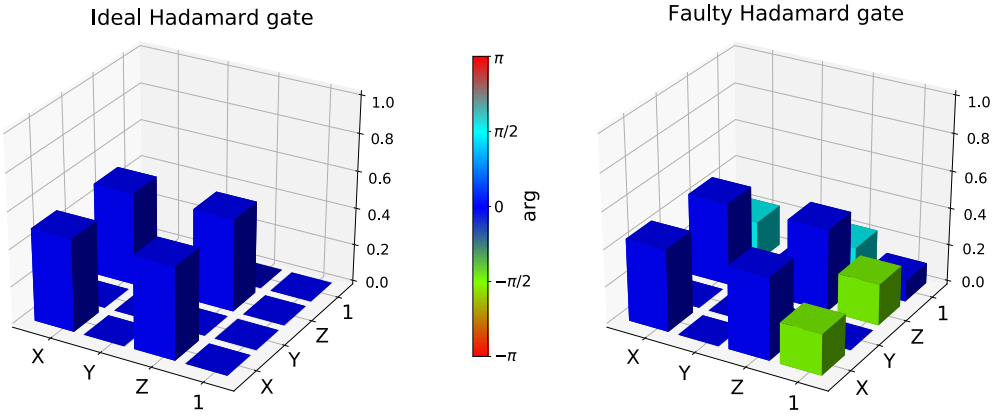

Figure 2.4: Quantum process tomography example. Values of the χ matrix obtained from quantum process tomography to characterise two processes. For this case we have used the $\{\tilde{E}_k\} = \{X, Y, Z, \mathbb{1}\}$ operators. Left: The process, in this case, is the Hadamard gate, $H = 1/\sqrt{2}(X + Z)$, defined in Eq. (2.21). The effect of this gate is $\mathcal{E}(\rho) = H\rho H = 1/2(X\rho X + Z\rho X + X\rho Z + Z\rho Z)$, which agrees with the result obtained. Right: Similar study for a faulty Hadamard gate with a large error, $H = 1/\sqrt{5}(2X + 2Z + i\mathbb{1})$.

2.5.3 Randomised Benchmarking

As we have explained, quantum process tomography has an exponential scaling with the size of the system, while also being vulnerable to SPAM errors. Due to this, other techniques have been developed to estimate the quality of a quantum operation while avoiding these problems. Randomised Benchmarking (RB) [104–106] and Gate Set Tomography (GST) [107, 108] are examples of such techniques. For the purposes of this thesis, we will explain how a Randomised Benchmarking process works.

Randomised Benchmarking is a technique that can be used to estimate the fidelity of the gate implemented with respect to the ideal gate. This method has the important advantage of having a better scaling with the size of the system than process tomography. However, this method does not give the complete form of the operation introduced by the gate, but rather an estimation of the error per gate.

The idea behind RB is to concatenate m repetitions of the gate that we want an estimate of the fidelity per gate with a random *Clifford operation* [109] in between each of these gates. A Clifford operation is an element of the Clifford group, which is the group that maps the Pauli group into itself. Considering that the Pauli group on n qubits is given by $\mathbf{P}_n = \{e^{i\theta\pi/2}\sigma_{j_1,1} \otimes ... \otimes \sigma_{j_n,n} \,|\, \theta = 0, 1, 2, 3,\ j_k = 0, 1, 2, 3\}$

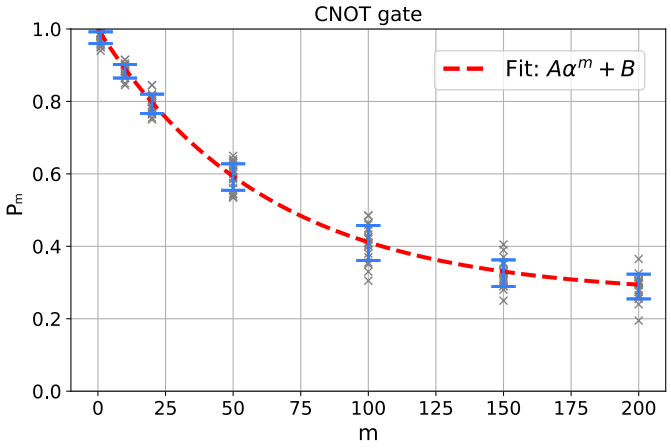

Figure 2.5: Randomised benchmarking example. Results from the simulation of a randomised benchmarking process applied to a CNOT gate with depolarising noise. A total of 20 different sequences of Clifford gates are applied and measured at different circuit depths, m, for 200 measurements each. Each outcome is represented by a cross. From these results, we can obtain an estimate of P_m and perform a fit as given by Eq. (2.48). From the resulting estimate of α, one can evaluate the quality of the implemented CNOT gate.

and $\vec{\sigma}_k = (\mathbb{1}_k, X_k, Y_k, Z_k)$ then, given an element of the Pauli group P and a Clifford operator C, they satisfy $CPC \in \mathbf{P}_n$.

After performing the concatenation of gates explained, we can model the resulting state by using a depolarising channel:

$$\rho_f^{(m)} = \alpha^m \cdot \rho_{f,\text{ideal}}^{(m)} + \frac{1-\alpha^m}{2^n} \cdot \mathbb{1}, \tag{2.47}$$

with n being the number of qubits involved in the gate, α the parameter of the depolarising channel, and $\rho_{f,\text{ideal}}^{(m)}$ being the ideal target state if the gate had no errors. The effect of the random gates applied allows us to consider this depolarising channel since their purpose is to transform the coherent error introduced by the gate into an incoherent error. Therefore, one can perform measurements for a given m to obtain the probability of success, i.e., that the state measured at the end is the initial state. This probability, P_m, is given by Eq. (2.47) as

$$P_m = \alpha^m + \frac{1-\alpha^m}{2^n} = A\,\alpha^m + B \tag{2.48}$$

where the A and B parameters absorb possible unwanted errors unrelated to the gate,

such as SPAM errors. This can be repeated for different values of m to obtain estimates of A, B, and α. An example is shown in Fig. 2.5. After this process, one can then use the parameter α as a measure of the quality of the gate.

Chapter 3

Quantum harmonic oscillator

In this chapter, we introduce the quantisation of one of the most important models in physics: the harmonic oscillator. The concept of Quantum Harmonic Oscillator (QHO) appears in several cases during the study of quantum systems and, in our case, it will be needed to understand how an ion is trapped in the realisation of an ion trap in Chapter 4. We will start by explaining the basic concepts of the one-dimensional and three-dimensional QHO. We will follow by deriving the behaviour of coupled QHOs. Finally, we explain some important states derived from the QHO and their physical interpretation.

3.1 1D and 3D Quantum harmonic oscillator

The quantum harmonic oscillator is obtained by quantisation of the classical harmonic oscillator. Thus, we will begin with the derivation of the classical case. We will start considering a one-dimensional case for simplicity.

The classical harmonic oscillator is described by a quadratic potential, $V(x)$, centered on x_0

$$V(x) = \frac{k}{2}(x - x_0)^2. \tag{3.1}$$

For a potential of this form, the motion of a particle will be given by the dynamical equation:

$$m\frac{d^2x}{dt^2} = -\frac{dV(x)}{dx} = -k(x - x_0), \tag{3.2}$$

with solution

$$x(t) = x_0 + A\sin(\omega t + \phi), \tag{3.3}$$

which is a sinusoidal oscillation around x_0 with amplitude A and phase ϕ defined by the initial conditions, and frequency ω defined as

$$\omega = \sqrt{\frac{k}{m}}\,. \tag{3.4}$$

Of course, this solution is obtained assuming that the potential has the form of Eq. (3.1). However, there are several cases in physics in which we will have a potential of this form, especially when we consider the expansion of a confining potential around a minimum x_0 in a Taylor's series, to obtain an approximation:

$$V(x) \approx V(x_0) + \frac{1}{2}\left(\frac{d^2V(x)}{dx^2}\right)(x - x_0)^2, \tag{3.5}$$

which will be valid as long as the motion is restricted to a small interval around x_0, see Fig. 3.1.

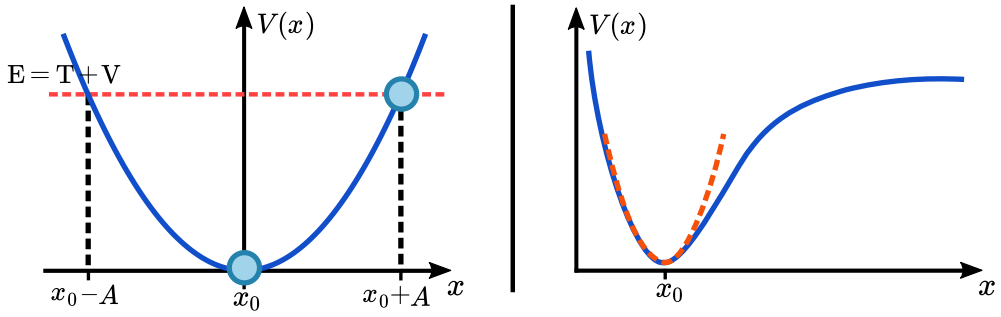

Figure 3.1: Harmonic oscillator. Left: Ideal harmonic oscillator. The quadratic potential, $V(x)$, traps a particle of total energy, E, in the interval $[x_0 - A, x_0 + A]$. In the limits of this interval, all the energy is in the form of potential energy, while at the bottom of the potential all the energy is in the form of kinetic energy, T. Right: Any confining potential (solid line) can be approximated by a quadratic potential (dashed line) in the region close to a minimum x_0. The motion of the particle can be treated as that of a harmonic oscillator when this approximation is valid.

The kinetic energy, T, and the potential energy are given as

$$\begin{aligned} T &= \frac{p^2}{2m}, \\ V &= \frac{1}{2}m\omega^2 x^2, \end{aligned} \tag{3.6}$$

where we assumed that the potential is centered around $x = 0$. This can be done by a simple change of coordinates if it is not the case. Therefore, the total energy of the harmonic oscillator is

$$E = \frac{p^2}{2m} + \frac{1}{2}m\omega^2 x^2 \,. \tag{3.7}$$

Now we are in the position to perform the quantisation of the harmonic oscillator. For this, we will use the position and momentum operators, X and P. Since they are canonical conjugates, they satisfy the canonical commutation relation [110]

$$[X, P] = i\hbar. \tag{3.8}$$

Using Eq. (3.7) and substituting x and p for X and P we obtain the Hamiltonian that describes the quantum harmonic oscillator

$$H = \frac{P^2}{2m} + \frac{1}{2}m\omega^2 X^2 \,. \tag{3.9}$$

We can diagonalise this Hamiltonian by introducing the operators a and $a^\dagger$ defined as

$$\begin{aligned} a &= \sqrt{\frac{m\omega}{2\hbar}} \left(X + \frac{i}{m\omega} P \right), \\ a^\dagger &= \sqrt{\frac{m\omega}{2\hbar}} \left(X - \frac{i}{m\omega} P \right). \end{aligned} \tag{3.10}$$

From Eq. (3.8), it follows

$$[a, a^\dagger] = 1 \,. \tag{3.11}$$

By using the inverted relations

$$\begin{aligned} X &= \sqrt{\frac{\hbar}{2m\omega}} \left(a^\dagger + a \right), \\ P &= i\sqrt{\frac{\hbar m\omega}{2}} \left(a^\dagger - a \right), \end{aligned} \tag{3.12}$$

we can transform the Hamiltonian in Eq. (3.9) into

$$H = \hbar\omega \left(a^\dagger a + \frac{1}{2} \right). \tag{3.13}$$

Solving the Hamiltonian is equivalent to finding the eigenvalues and eigenvectors of the operator $N \equiv a^\dagger a$. The eigenvectors of this operator are called Fock states, $|n\rangle$, with eigenvalues n, that is

$$N\,|n\rangle = n\,|n\rangle\,, \quad n \in \mathbb{N}_0\,. \tag{3.14}$$

Thus, the energies of H are discretised with a uniform separation $\hbar\omega$ between adjacent levels.

The operators $a^\dagger$ and a are the so-called *creation* and *destruction operators*, respectively. This is because they satisfy the following

$$\begin{aligned} a^\dagger\,|n\rangle &= \sqrt{n+1}\,|n+1\rangle\,, \\ a\,|n\rangle &= \sqrt{n}\,|n-1\rangle\,, \end{aligned} \tag{3.15}$$

that is, their action is to increase or decrease by one the eigenstate over which they act. Similarly, the operator N is called the number operator, since it just returns the number n related to the eigenstate over which it acts. We can calculate the form of the ground state in the $\{|x\rangle\}$ representation.

From Eq. (3.15), we know that

$$a\,|0\rangle = \sqrt{\frac{m\omega}{2\hbar}} \left(X + \frac{i}{m\omega} P \right) |0\rangle = 0\,. \tag{3.16}$$

Projecting onto $|x\rangle$, and using the position representation of the canonical operators

$$\begin{aligned} X &\to x, \\ P &\to -i\hbar \frac{d}{dx}, \end{aligned} \tag{3.17}$$

yields the differential equation

$$\left(\frac{m\omega}{\hbar} x + \frac{d}{dx} \right) \Psi_0(x) = 0, \tag{3.18}$$

with $\Psi_n(x) = \langle x|n\rangle$. The solution of this differential equation, when considering that

the wave function must be normalised, is:

$$\Psi_0(x) = \left(\frac{m\omega}{\pi\hbar}\right)^{1/4} e^{-\frac{m\omega}{2\hbar}x^2}, \tag{3.19}$$

which is a Gaussian probability distribution centered at $x = 0$ with variance $\sigma^2 = \hbar/m\omega$. Similar differential equations can be solved for higher Fock states, which yields the general solution for $\Psi_n(x)$ (see Fig. 3.2):

$$\Psi_n(x) = \frac{1}{\sqrt{2^n n!}} \left(\frac{m\omega}{\pi\hbar}\right)^{\frac{1}{4}} H_n\left(\sqrt{\frac{m\omega}{\hbar}}x\right) e^{-\frac{m\omega}{2\hbar}x^2}, \tag{3.20}$$

with $H_n(y)$ being the Hermite polynomials [111]

$$H_n(y) = (-1)^n e^{y^2} \frac{d}{dy}\left(e^{-y^2}\right) \tag{3.21}$$

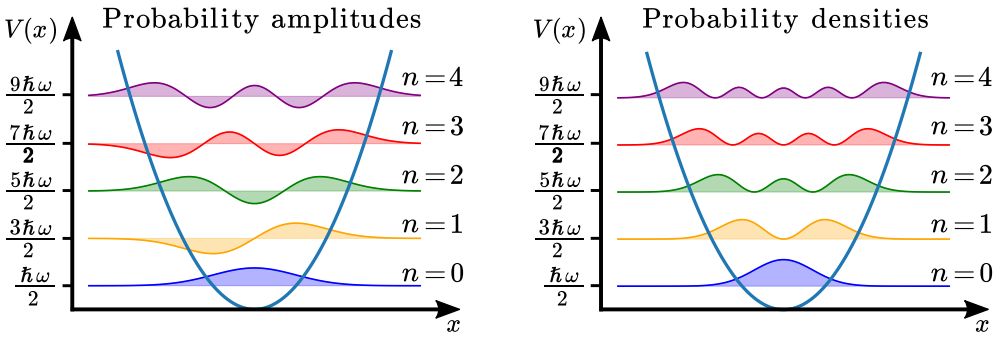

Figure 3.2: QHO wave functions. Left: Wave functions, $\Psi_n(x)$, of the ground state and first four excited states of the quantum harmonic oscillator as obtained in Eq. (3.20). The ground state has an energy $E = \hbar\omega/2$ and each increase of n involves an increase in the energy of $\hbar\omega$. Right: Equivalent plot showing the probability densities, $|\Psi_n(x)|^2$.

Now that we are familiarised with the quantum harmonic oscillator in one dimension, we can generalise it for the case of a particle trapped in a three-dimensional harmonic potential. In this case, the potential will have the form

$$V(\vec{r}) = \sum_{i=1}^{3} \frac{k_i}{2} r_i^2 = \sum_{i=1}^{3} \frac{1}{2} m\omega_i^2 r_i^2, \tag{3.22}$$

where

$$\omega_i = \sqrt{\frac{k_i}{m}}, \qquad i = 1, 2, 3, \tag{3.23}$$

and $\vec{r} = (x, y, z)$[1]. For this case, the quantised Hamiltonian is given by

$$H = H_x + H_y + H_z, \tag{3.24}$$

with

$$\begin{aligned} H_x &= \frac{1}{2m} P_x^2 + \frac{1}{2} m\omega_x^2 X^2, \\ H_y &= \frac{1}{2m} P_y^2 + \frac{1}{2} m\omega_y^2 Y^2, \\ H_z &= \frac{1}{2m} P_z^2 + \frac{1}{2} m\omega_z^2 Z^2. \end{aligned} \tag{3.25}$$

Since H_x, H_y, and H_z commute, finding the eigenvectors and eigenvalues of H reduces to finding the eigenvectors and eigenvalues of each component, H_x, H_y, and H_z. From Sec. 3.1 we know that these components of the Hamiltonian can be written as

$$H_i = \hbar\omega_i \left(a_i^\dagger a_i + \frac{1}{2} \right), \qquad i = x, y, z, \tag{3.26}$$

with a_x, a_y, and a_z being straightforward generalisations of the creation operator defined in Eq. (3.10). These components of the Hamiltonian satisfy

$$H_i \left| n_i \right\rangle_i = n_i \left| n_i \right\rangle_i, \qquad i = x, y, z. \tag{3.27}$$

Thus, the eigenvectors and eigenvalues of the complete Hamiltonian are all the possible combinations of the form $\left|n_x\right\rangle_x \otimes \left|n_y\right\rangle_y \otimes \left|n_z\right\rangle_z$ or, for simplicity, $\left|n_x, n_y, n_z\right\rangle$, which satisfy

$$H \left| n_x, n_y, n_z \right\rangle = \hbar \left[\omega_x \left(n_x + \frac{1}{2} \right) + \omega_y \left(n_y + \frac{1}{2} \right) + \omega_z \left(n_z + \frac{1}{2} \right) \right] \left| n_x, n_y, n_z \right\rangle. \tag{3.28}$$

Finally, since the eigenstates of the three-dimensional QHO are the tensor product of three one-dimensional QHOs, the eigenvectors in the $\{|\vec{r}\rangle = |x, y, z\rangle\}$ representation will be given by the product

$$\Psi_{n_x, n_y, n_z}(\vec{r}) = \langle x, y, z | n_x, n_y, n_z \rangle = \Psi_{n_x}(x) \Psi_{n_y}(y) \Psi_{n_z}(z), \tag{3.29}$$

[1] We are also considering, for simplicity, that the minimum of the potential is located at the origin, $\vec{r}_0 = (0, 0, 0)$.

with $\Psi_{n_x}(x)$, $\Psi_{n_y}(y)$, and $\Psi_{n_z}(z)$ defined as in Eq. (3.20).

3.2 Coupled quantum harmonic oscillators

Here we will derive the results for a system of coupled QHO. We will begin, in a similar way as in QHO derivation, with the calculations of a classical system of coupled harmonic oscillators. Then we will continue by quantising the results. The calculations shown will be done, for simplicity, for the particular case of a system of two coupled harmonic oscillators. The calculation for a bigger system of harmonic oscillators is just a generalisation of the calculations shown below. Similarly, we will consider the motion to be restricted to a single dimension, also for simplicity.

Let us assume a system of two particles, (1) and (2), where each particle is affected by a similar harmonic potential, where the potential acting on the first particle is centered at distance $-d$ from the origin and the one acting on the second particle is centered at $+d$. We will also consider that the potential has an additional term proportional to the square of the distance between particles (1) and (2). The potential is then

$$V(x_1, x_2) = \frac{1}{2}m\omega^2(x_1 - d)^2 + \frac{1}{2}m\omega^2(x_2 + d)^2 - \frac{1}{2}\alpha m\omega^2(x_1 - x_2)^2, \tag{3.30}$$

where α is a coupling constant. The equations of motion obtained from this potential are

$$\begin{aligned} m\frac{d^2}{dt^2}x_1 &= -m\omega^2(x_1 - d) + \alpha m\omega^2(x_1 - x_2), \\ m\frac{d^2}{dt^2}x_2 &= -m\omega^2(x_2 + d) - \alpha m\omega^2(x_1 - x_2). \end{aligned} \tag{3.31}$$

From this, we can see that the effect of the coupling term is a repulsive force between the particles when $\alpha > 0$, or an attractive one when $\alpha < 0$. The system in Eq. (3.31) represents two coupled differential equations, which can be written as

$$m\frac{d^2}{dt^2}\vec{x} = -m\omega^2 K\,\vec{x} - m\omega^2\vec{d}, \tag{3.32}$$

with $\vec{x}$ being the vector with components x_1 and x_2, and K and $\vec{d}$ being

$$K = \begin{pmatrix} 1-\alpha & \alpha \\ \alpha & 1-\alpha \end{pmatrix}, \qquad \vec{d} = \begin{pmatrix} -d \\ d \end{pmatrix}. \tag{3.33}$$

It is important to note that, for a general system of N coupled harmonic oscillators, Eq. (3.32) can be generalised by using the corresponding form of K and $\vec{d}$, which are now an $N \times N$ matrix and an N-dimensional vector, respectively. The system of differential equations in Eq. (3.32) can be decoupled by diagonalising K. In the following, we show how this is done for $N = 2$, which will be the relevant case for the results shown in this thesis. For $N = 2$, the basis that diagonalises K is given by

$$\begin{aligned} x_{\mathrm{COM}} &= \frac{x_1 + x_2}{2}, \\ x_{\mathrm{B}} &= x_1 - x_2, \end{aligned} \tag{3.34}$$

where COM stands for *center-of-mass* since x_{COM} denotes the position of the center of mass, and B stands for *breathing* since x_{B} denotes the distance between the particles for which the solution, as we will see below, is a sinusoidal expansion and contraction. With this change of variables, we obtain a system of decoupled differential equations

$$\begin{aligned} \frac{d^2}{dt^2} x_{\mathrm{COM}} &= -\omega^2 x_{\mathrm{COM}}, \\ \frac{d^2}{dt^2} x_{\mathrm{B}} &= -\omega^2 (1 - 2\alpha) x_{\mathrm{B}} + 2\omega^2 d, \end{aligned} \tag{3.35}$$

with solution

$$\begin{aligned} x_{\mathrm{COM}}(t) &= A_{\mathrm{COM}} \sin(\omega_{\mathrm{COM}} t + \phi_{\mathrm{COM}}), \\ x_{\mathrm{B}}(t) &= \frac{2d}{1 - 2\alpha} + A_{\mathrm{B}} \sin(\omega_{\mathrm{B}} t + \phi_{\mathrm{B}}). \end{aligned} \tag{3.36}$$

Here A_{COM}, A_{B}, ϕ_{COM}, and ϕ_{B} are constants obtained from the initial conditions and ω_{COM} and ω_{B} are given by

$$\begin{aligned} \omega_{\mathrm{COM}} &= \omega, \\ \omega_{\mathrm{B}} &= \omega\sqrt{1 - 2\alpha}. \end{aligned} \tag{3.37}$$

With this solution, obtained for the uncoupled reference system, we can predict the motion of particles (1) and (2) by inverting Eq. (3.34). An example of the motion due to the center of mass mode and the breathing mode can be seen in Fig. 3.3.

Now that we know the solution of this classical system, we can quantise it. We start by writing the classical Hamiltonian

$$H = \frac{p_1^2}{2m} + \frac{p_2^2}{2m} + \frac{1}{2} m\omega^2 (x_1 - d)^2 + \frac{1}{2} m\omega^2 (x_2 + d)^2 - \frac{1}{2} \alpha m\omega^2 (x_1 - x_2)^2. \tag{3.38}$$

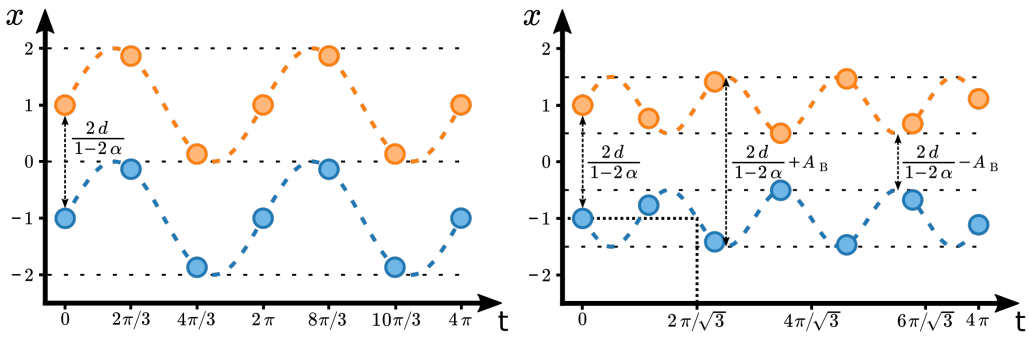

Figure 3.3: Pair of classical coupled harmonic oscillators. Left: Motion of the coupled particles, $x_1(t)$ and $x_2(t)$, for $\omega = 1$, $\alpha = -1$, $A_{\mathrm{COM}} = 1$, $A_{\mathrm{B}} = 0$, $\phi_{\mathrm{COM}} = \phi_{\mathrm{B}} = 0$ and $d = 3$. For this choice of parameters, the whole motion is due to the center of mass mode, while there is no motion due to the breathing mode. We can see that for this case, the two particles are always moving in the same direction, keeping the distance between them constant and equal to $2d/(1-2\alpha) = 2$. Right: Similar plot but for the parameters $\omega = 1$, $\alpha = -1$, $A_{\mathrm{COM}} = 0$, $A_{\mathrm{B}} = 1$, $\phi_{\mathrm{COM}} = \phi_{\mathrm{B}} = 0$ and $d = 3$. In this case, there is no motion due to the center of mass mode and all the motion is due to the breathing mode. The middle point between the particles is constant, but the relative distance between the particles changes. As we can see, the frequency for this case is $\omega_{\mathrm{B}} = \omega\sqrt{1-2\alpha} = \sqrt{3}$.

By introducing

$$\begin{aligned} p_{\mathrm{COM}} &= p_1 + p_2, \\ p_{\mathrm{B}} &= \frac{p_1 - p_2}{2}, \end{aligned} \tag{3.39}$$

and

$$\begin{aligned} \mu_{\mathrm{COM}} &= 2m, \\ \mu_{\mathrm{B}} &= \frac{m}{2}, \end{aligned} \tag{3.40}$$

we obtain that — up to a constant factor, which is equivalent to a global energy offset — the Hamiltonian can be written as

$$H = \frac{p_{\mathrm{COM}}^2}{2\mu_{\mathrm{COM}}} + \frac{p_{\mathrm{B}}^2}{2\mu_{\mathrm{B}}} + \frac{1}{2}\mu_{\mathrm{COM}}\omega_{\mathrm{COM}}^2 x_{\mathrm{COM}}^2 + \frac{1}{2}\mu_{\mathrm{B}}\omega_{\mathrm{B}}^2\left(x_{\mathrm{B}} - \frac{2d}{1-2\alpha}\right)^2. \tag{3.41}$$

With the change of variable

$$x'_{\mathrm{B}} = x_{\mathrm{B}} - \frac{2d}{1-2\alpha}, \tag{3.42}$$

it simplifies to

$$H = \frac{p_{\mathrm{COM}}^2}{2\mu_{\mathrm{COM}}} + \frac{p_{\mathrm{B}}^2}{2\mu_{\mathrm{B}}} + \frac{1}{2}\mu_{\mathrm{COM}}\omega_{\mathrm{COM}}^2 x_{\mathrm{COM}}^2 + \frac{1}{2}\mu_{\mathrm{B}}\omega_{\mathrm{B}}^2 x_{\mathrm{B}}'^2. \tag{3.43}$$

Now that we have the form of the Hamiltonian, we can quantise it. For this, we will use the operators

$$\begin{aligned} X_{\mathrm{COM}} &= \frac{X_1 + X_2}{2}, & P_{\mathrm{COM}} &= P_1 + P_2, \\ X'_{\mathrm{B}} &= X_1 - X_2 - \frac{2d}{1-2\alpha}, & P_{\mathrm{B}} &= \frac{P_1 + P_2}{2}. \end{aligned} \tag{3.44}$$

These operators satisfy the canonical commutation relations, for which the only commutators that are not 0 are $[X_{\mathrm{COM}}, P_{\mathrm{COM}}]$ and $[X_{\mathrm{B}}, P_{\mathrm{B}}]$, which are equal to $i\hbar$. Thus, these operators can be interpreted as position and momentum operators of two independent particles, which we can use to quantise the Hamiltonian in Eq. (3.43) to obtain

$$H = \frac{P_{\mathrm{COM}}^2}{2\mu_{\mathrm{COM}}} + \frac{P_{\mathrm{B}}^2}{2\mu_{\mathrm{B}}} + \frac{1}{2}\mu_{\mathrm{COM}}\omega_{\mathrm{COM}}^2 X_{\mathrm{COM}}^2 + \frac{1}{2}\mu_{\mathrm{B}}\omega_{\mathrm{B}}^2 X_{\mathrm{B}}'^2. \tag{3.45}$$

In a similar way as in the previous cases, we will introduce the creation and destruction operators, which in this case are defined as

$$\begin{aligned} a_{\mathrm{COM}} &= \sqrt{\frac{\mu_{\mathrm{COM}}\omega_{\mathrm{COM}}}{2\hbar}}\left(X_{\mathrm{COM}} + \frac{i}{\mu_{\mathrm{COM}}\omega_{\mathrm{COM}}}P_{\mathrm{COM}}\right), \\ a_{\mathrm{B}} &= \sqrt{\frac{\mu_{\mathrm{B}}\omega_{\mathrm{B}}}{2\hbar}}\left(X'_{\mathrm{B}} + \frac{i}{\mu_{\mathrm{B}}\omega_{\mathrm{B}}}P_{\mathrm{B}}\right), \end{aligned} \tag{3.46}$$

with which we can write the Hamiltonian as

$$H = \hbar\omega_{\mathrm{COM}}\left(a_{\mathrm{COM}}^\dagger a_{\mathrm{COM}} + \frac{1}{2}\right) + \hbar\omega_{\mathrm{B}}\left(a_{\mathrm{B}}^\dagger a_{\mathrm{B}} + \frac{1}{2}\right). \tag{3.47}$$

Thus, this Hamiltonian is equivalent to two independent QHO. In the same way as for the three-dimensional QHO in Sec. 3.1, the eigenstates of this Hamiltonian can be written as the tensor product of the eigenstates of each individual QHO. Therefore, the basis of eigenstates Eq. (3.47) will be given by all the possible combinations $|n_{\mathrm{COM}}, n_{\mathrm{B}}\rangle \equiv |n_{\mathrm{COM}}\rangle \otimes |n_{\mathrm{B}}\rangle$ with eigenvalues of the form

$$H\,|n_{\mathrm{COM}}, n_{\mathrm{B}}\rangle = \left[\hbar\omega_{\mathrm{COM}}\left(n_{\mathrm{COM}} + \frac{1}{2}\right) + \hbar\omega_{\mathrm{B}}\left(n_{\mathrm{B}} + \frac{1}{2}\right)\right]|n_{\mathrm{COM}}, n_{\mathrm{B}}\rangle \tag{3.48}$$

3.3 Coherent and thermal states

While the Fock states introduced in Sec. 3.1 are important due to their role as eigenstates of the QHO, there are other important states that must be introduced. This is the case of *coherent states* and *thermal states*.

3.3.1 Coherent states

Coherent states, $|\alpha\rangle$ with $\alpha \in \mathbb{C}$, can be defined as eigenstates of the destruction operator, a, that is

$$a\,|\alpha\rangle = \alpha\,|\alpha\rangle\,. \tag{3.49}$$

Using this definition, one can find that they have the following form

$$|\alpha\rangle = e^{-\frac{|\alpha|^2}{2}} \sum_{n=0} \frac{\alpha^n}{\sqrt{n!}}\,|n\rangle\,. \tag{3.50}$$

The physical relevance of coherent states stems from their properties in phase space. Their mean position and momentum are given by the eigenvalue α

$$\langle X\rangle_\alpha = \langle\alpha|\,X\,|\alpha\rangle = \sqrt{\frac{2\hbar}{m\omega}}\,\mathrm{Re}(\alpha), \tag{3.51}$$

$$\langle P\rangle_\alpha = \langle\alpha|\,P\,|\alpha\rangle = \sqrt{2\hbar m\omega}\,\mathrm{Im}(\alpha). \tag{3.52}$$

Their variances

$$\Delta X^2 = \langle\alpha|\,X^2\,|\alpha\rangle - \langle\alpha|\,X\,|\alpha\rangle^2 = \frac{\hbar}{2m\omega}, \tag{3.53}$$

$$\Delta P^2 = \langle\alpha|\,P^2\,|\alpha\rangle - \langle\alpha|\,P\,|\alpha\rangle^2 = \frac{\hbar m\omega}{2}, \tag{3.54}$$

saturate the lower limit of the uncertainty principle

$$\Delta X\,\Delta P = \frac{\hbar}{2}, \tag{3.55}$$

Finally, one can study the evolution of a coherent state, $|\alpha_0\rangle$, under the QHO Hamiltonian, to obtain:

$$|\alpha(t)\rangle = \left|\alpha_0 e^{i\omega t}\right\rangle. \tag{3.56}$$

Therefore, the state at any time under this evolution is also a coherent state, where the argument of the state differs from the initial one, α_0, by a time-dependent phase. Since the state at all times will be also a coherent state, we can use Eq. (3.51) to Eq. (3.53) to obtain the evolution of a coherent state over time in phase space. Finally, one can define the displacement operator, $D(\alpha)$, as the operator that creates the coherent state, $|\alpha\rangle$, when applied to the vacuum state, $|0\rangle$, (which is also a coherent state), that is

$$D(\alpha)\,|0\rangle = |\alpha\rangle\,, \tag{3.57}$$

which has the form

$$D(\alpha) = \exp\Big(\alpha a^\dagger - \alpha^* a\Big). \tag{3.58}$$

After obtaining the properties and evolution of the coherent states in phase space, one can understand their importance, since they are the closest quantum analog to a classical harmonic oscillator. An example of a coherent state in phase space and the application of a displacement operator can be seen in Fig. 3.4.

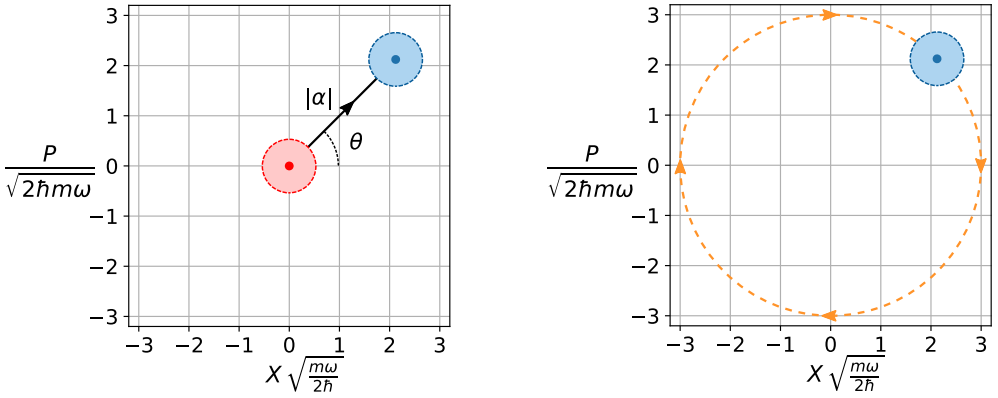

Figure 3.4: Coherent states in (dimensionless) phase space. Left: The displacement operator, $D(\alpha)$ (in this case $\alpha = 3e^{i\pi/4} = |\alpha|e^{i\theta}$), moves the initial state $|0\rangle$ (shown in red) in phase space to obtain the state $|\alpha\rangle$ (in blue). The circles represent the standard deviations associated to these states. Right: The obtained coherent state then evolves under the QHO Hamiltonian following the trajectory in orange.

3.3.2 Thermal states

A thermal state describes a QHO in thermodynamic equilibrium with a reservoir at temperature T. The density operator of a single-mode QHO (as in Eq. (3.13)) is given

by [110]

$$\rho = \frac{e^{-H/kT}}{Z}, \tag{3.59}$$

where k is the Boltzmann constant and Z is a normalisation coefficient given by

$$Z = \mathrm{Tr}\left(e^{-H/kT}\right) = \frac{e^{\hbar\omega/2kT}}{e^{\hbar\omega/kT} - 1}, \tag{3.60}$$

The populations of the thermal state in Eq. (3.59) are given by

$$p_{\bar{n}}(n) = e^{-\hbar\omega(n+1)/kT}\left(e^{\hbar\omega/kT} - 1\right). \tag{3.61}$$

which means that the populations decay exponentially as a function of n. The subindex $\bar{n}$ represents the mean phonon number, given by

$$\bar{n} = \frac{1}{e^{\hbar\omega/kT} - 1}. \tag{3.62}$$

The value $\bar{n}$ is enough to characterise the thermal state since it is possible to write the populations as

$$p_{\bar{n}}(n) = \frac{\bar{n}^n}{(\bar{n}+1)^{n+1}}. \tag{3.63}$$

Finally, one can prove that the coherences of a thermal state are all zero. Therefore, a thermal state is a completely statistical mixture. Thermal states are useful when modeling an experimental preparation of a QHO, such as the one describing the motional states of trapped ions, where imperfections on the preparation can cause the appearance of this kind of states.

Chapter 4

Ion traps

Up to this point, we have introduced some basic theoretical concepts of quantum mechanics that will be useful for the understanding of this thesis. However, we still have to understand how a quantum computation can be achieved experimentally.

There are different architectures for implementing quantum computers that use different physical systems to encode qubits and perform quantum information processing. Some of these implementations are based on superconductors [28, 29], quantum dots [31, 32], Rydberg atoms [34–36] in optical lattices [38–40] or tweezer arrays [41, 42], or trapped ions [19–27]. In this thesis, we will focus on the latter implementation, where trapped ions are used to encode qubits. We do this since some of the results of the Bayesian techniques presented in this thesis are particularised to calibrate trapped-ion experiments. However, we note that generalisations of these techniques can be applied to other architectures.

The application of trapped-ion systems for quantum computation was first introduced by Cirac and Zoller [19]. In this implementation, trapped ions are used to approximate qubits, with the motional state shared by these ions being used to create entanglement. Since this initial proposal, trapped-ion technology has developed rapidly, achieving high-fidelity single-qubit operations [112], qubit state preparation and readout [113], entangling operations [114], and even quantum error correction [48, 49, 51]. Additionally, the different ions and their respective internal levels provide a rich variety of levels to encode the qubits or to use as auxiliary levels, as well as different approaches for performing quantum gates. However, while trapped-ion systems are successful in

this sense, they show problems such as relatively slow operations compared to other qubit implementations.

In the following we provide an introduction to the basics of trapped-ions systems, giving a brief overview of how the ions are trapped, how the qubits are encoded in the energy levels of the ions, and what are the basic quantum operations that can be applied to the ions.

4.1 Trapping the ions

To perform quantum operations on ions, one first needs to trap them. In order to do this, one can use Penning traps [115–117], which are based on the application of an electric and magnetic field. Another option is to use Paul traps [27, 118], which combines oscillating and static electric fields. The latter is the case that we will study here.

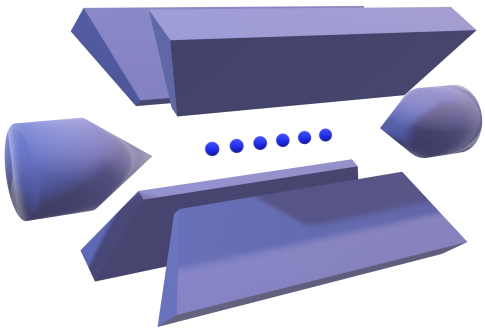

Figure 4.1: Linear Paul trap. A linear Paul trap can be obtained by using two opposing end-cap electrodes and four blades. A DC voltage is applied to the two end-cap electrodes, which creates a confining potential along the longitudinal axis. Additionally, a radial confinement is obtained by applying an oscillating voltage to two of the four blades, while setting the other two to ground. By setting the trap parameters correctly, one can obtain an effective confining potential in which the trapped ions are positioned in the spatial direction defined by the end-cap electrodes (see Eq. (4.7)).

In order to trap the ions, we need to create a confining potential. An initial idea would be to use an electric potential of the form

$$V(x, y, z) = \frac{1}{2}(\alpha x^2 + \beta y^2 + \gamma z^2), \tag{4.1}$$

which would be confining in the three spatial directions. However, due to Earnshaw's theorem, an electrostatic potential of this form cannot exist. Since it must satisfy Laplace's equation

$$\nabla^2 V(x,y,z) = \alpha + \beta + \gamma = 0, \tag{4.2}$$

the potential would be non-confining in at least one of the spatial directions. In order to circumvent this problem, one can use a time-dependent potential of the form [119]

$$V(x,y,z,t) = V_0 \cos(\omega_T t)(x^2 - y^2) + U_0 \left(z^2 - \frac{1}{2}(x^2 + y^2) \right). \tag{4.3}$$

This yields the equations of motion

$$\begin{aligned} &\frac{d^2x}{dt^2} + \left[\frac{qV_0}{m} \cos(\omega_T t) + \frac{qU_0}{m} \right] x = 0, \\ &\frac{d^2y}{dt^2} + \left[-\frac{qV_0}{m} \cos(\omega_T t) + \frac{qU_0}{m} \right] y = 0, \\ &\frac{d^2z}{dt^2} + \frac{2qU_0}{m} z = 0, \end{aligned} \tag{4.4}$$

with m and q being the mass and charge of the ion, respectively. These are Mathieu equations [120] and can be written as

$$\frac{d^2 r_i}{d\tau^2} + (a_i - 2q_i \cos(2\tau)) r_i = 0, \tag{4.5}$$

with $\vec{r} = (x, y, z)$ being the position vector with $i = x, y, z$, $2\tau = \omega_T t$, and

$$\begin{aligned} a_x = a_y = -\frac{1}{2} a_z = \frac{4qU_0}{m\omega_T^2} \\ q_x = -q_y = \frac{4qV_0}{m\omega_T^2}, \quad q_z = 0. \end{aligned} \tag{4.6}$$

For $|a_i| \ll 1$ and $|q_i| \ll 1$, the approximate solutions of Eq. (4.5) are given by

$$r_i(t) \approx A_i \cos(\nu_i t + \phi_i) \left[1 + \frac{q_i}{2} \cos(\omega_T t) \right], \tag{4.7}$$

where

$$\nu_i = \frac{\omega_T}{2} \sqrt{a_i + \frac{q_i^2}{2}}. \tag{4.8}$$

We have also introduced A_i, which are the amplitudes of the movement, and ϕ_i, which

are the phases. Each of them is determined by the initial conditions.

There are two different terms in Eq. (4.7). The first one is the oscillation described by ν_i, which is called the *secular motion*. The second one is the term dependent on ω_T which, since we are considering $|q_i| \ll 1$, is usually called *micromotion*. If we ignore the micromotion, we can see that the ion is trapped in the three spatial directions by an effective harmonic potential, which can be quantised. Additionally, if the parameters are selected such as $\nu_x, \nu_y \gg \nu_z$, then the motion of the ion can be considered to be restricted to one spatial dimension.

The previous derivation was performed for a single ion in the trap. In order to obtain the behaviour for N ions, one must consider the potential, which accounts for both the harmonic potential and the Coulomb interaction between ions

$$V = \frac{1}{2}\sum_{n=1}^{N} m\nu^2 z_n(t)^2 + \sum_{n,m=1,n\neq m}^{N} \frac{q^2}{8\pi\epsilon_0}\frac{1}{|z_n(t) - z_m(t)|}, \tag{4.9}$$

with $\nu \equiv \nu_z$, since we are considering that the movement is restricted to the z-direction, ϵ_0 being the vacuum permittivity and $z_n(t)$ being the position of the n^{th} ion. Assuming that the system is sufficiently cold, the motion can be approximated as a small movement, $q_n(t)$, around an equilibrium position, z_n^0:

$$z_n(t) \approx z_n^0 + q_n(t).$$

With this, one can calculate the equilibrium positions by solving

$$\left(\frac{\partial V}{\partial z_n}\right)_{z_n = z_n^0} = 0. \tag{4.10}$$

Using the length scale, l

$$l = \left(\frac{q^2}{4\pi\epsilon_0 m\nu^2}\right), \tag{4.11}$$

and the dimensionless equilibrium position, $u_n = z_n^0/l$, Eq. (4.10) can be written as

$$u_m - \sum_{n=1}^{m-1}\frac{1}{(u_m - u_n)^2} + \sum_{n=m+1}^{N}\frac{1}{(u_n - u_m)^2} = 0, \quad m = 1, ..., N. \tag{4.12}$$

Solving this equation for $N = 2$ ions in the trap, one can obtain

$$u_1 = -\left(\frac{1}{2}\right)^{2/3}, \quad u_2 = \left(\frac{1}{2}\right)^{2/3}. \tag{4.13}$$

As for the normal modes of the coupled oscillator, to obtain them one has to write the Hamiltonian

$$H = \frac{m}{2}\sum_{n=1}^{N}(\dot{q}_n)^2 + \frac{1}{2}\sum_{n,m=1}^{N} q_n q_m K_{nm}, \tag{4.14}$$

with K_{nm} being the matrix defined by

$$K_{nm} = \left(\frac{\partial V}{\partial q_n \partial q_m}\right)_{q_n=q_m=0} = \begin{cases} 1 + 2\sum_{\substack{k=1 \\ k\neq m}}^{N} \frac{1}{|u_m - u_k|^3} & \text{if} \quad n = m \\ -\frac{2}{|u_m - u_n|^3} & \text{if} \quad n \neq m \end{cases}. \tag{4.15}$$

As in Sec. 3.2, one can obtain the eigenvectors and eigenvalues of K_{nm} to solve this problem. For $N = 2$ one finds the center-of-mass and breathing modes

$$v_{\text{COM}} = \frac{1}{\sqrt{2}}(1, 1), \quad v_B = \frac{1}{\sqrt{2}}(-1, 1), \tag{4.16}$$

with eigenvalues $\lambda_{\text{COM}} = 1$ and $\lambda_B = 3$, which results in a frequency for these modes of $\nu_{\text{COM}} = \nu_z$ and $\nu_{\text{B}} = \sqrt{3}\nu_z$. For bigger values of N, one can also calculate the normal modes [121]. For any number of ions, the least energetic mode is always the COM mode, with the frequency of the second most energetic state always being $\sqrt{3}$ times that of the COM mode. Thanks to this energy gap between the COM mode and the others, we will be able to consider only the COM mode.

In this thesis, we will focus on linear Paul traps like the one that we just explained. However, it is important to mention that, for the particular case of qubits based on trapped ions in Paul traps, as the number of qubits increases the distance between ions is reduced. Solving Eq. (4.12) for different values of N, one can find that the minimum distance between ions is given, approximately, by the following formula [121]

$$z_{\min}(N) = l \cdot \frac{2.018}{N^{0.559}}, \tag{4.17}$$

which can be used to estimate the ion-storing capabilities of the trap. This scaling effect is a problem since having closer ions increases the errors appearing due to *cross-talk* effects [44], which appears due to the laser fields used to manipulate the quantum

information of some qubits, which we will explain in the next sections, affecting neighbour qubits. However, this can be accounted for by using methods aimed to correct these errors [122–124]. Another option is to use a so-called *shuttling* ion trap [125–129]. Within this approach, when one needs to manipulate a set of qubits, they are moved from a storage zone to a manipulation zone. In this zone, they are subjected to the desired operations, and then they are moved back to the storage zone. However, this approach introduces more complicated techniques, such as moving the ions to different zones, that are not required to understand the results obtained in this thesis since we use at most two trapped-ions, which will not be affected by cross-talk errors.

4.2 Energy levels of the ion

The choice of the ion used to approximate a two-level system is vital, since the $|0\rangle$ and $|1\rangle$ states, as well as the operations performed on the system, will depend on the energy levels of the ion, which results in different categories of trapped-ion qubits. First, there are *hyperfine qubits*, which encode the qubit levels in hyperfine levels of the ion, with a transition frequency on the order of the gigahertzs. Second, there are *Zeeman qubits* that use magnetic fields to encode the qubits in the appearing Zeeman splittings, yielding qubits with a transition frequency on the order of tens of megahertzs. Another case is that of *fine structure qubits* that use fine structure levels with transition frequencies of the order of tens of terahertzs to encode the qubit. Finally, there are *optical qubits* that use states separated by optical transitions, that is, of the order of hundreds of terahertzs, to encode the qubits.

For this thesis, we will consider optical qubits encoded in the $^{40}Ca^{+}$ ion [44]. Using the ground state $4S_{1/2}$ and the metastable excited state $3D_{5/2}$ with a lifetime of 1.1s. The $4S_{1/2}$ has two Zeeman sublevels ($m = \pm 1/2$) while the $3D_{5/2}$ state has six ($m = \pm 1/2, \pm 3/2, \pm 5/2$). A uniform magnetic field in the position of the ion causes a Zeeman shift of the energies of the levels given by

$$\Delta\omega_Z(m, B) = m\, g_j \frac{\mu_B B}{\hbar} \tag{4.18}$$

where B is the magnetic field, μ_B is the Bohr magneton and g_j is the Landé g-factor, which for the state $4S_{1/2}$ is $g_S \approx 2$ and for the $3D_{5/2}$ state is $g_D \approx 1.2$. Due to this effect of the magnetic field, the states used for the qubit are the $4S_{1/2}(m = -1/2) \equiv |1\rangle \equiv |g\rangle$

and $3D_{5/2}(m = -1/2) \equiv |0\rangle \equiv |e\rangle$ states, since their transition frequency will be the least sensitive to fluctuations in the magnetic field. In the following, we will use the notation $|e\rangle$ and $|g\rangle$ over $|0\rangle$ and $|1\rangle$ when considering trapped-ion qubits to avoid confusion between their internal and motional state.

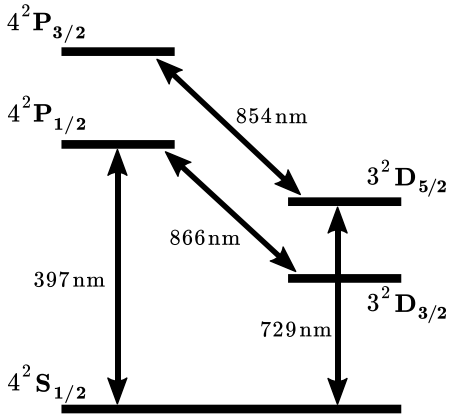

Figure 4.2: Energy levels of the $^{40}Ca^+$ ion. A qubit can be encoded by using the ground state $4S_{1/2}(m_j = -1/2) \equiv |1\rangle \equiv |g\rangle$ and the metastable excited state $3D_{5/2}(m_j = -1/2) \equiv |0\rangle \equiv |e\rangle$.

Using laser light with a frequency of 729nm we can drive resonant transitions between the $|g\rangle$ and $|e\rangle$ levels (see Sec. 4.3), which will be needed for performing single-qubit gates. The measurement of the qubit state is performed by electron shelving, which takes advantage of the $4S_{1/2} \leftrightarrow 4P_{1/2}$ transition, where the ion is illuminated with a laser of frequency 397nm. This will either project the state of the qubit to the $4S_{1/2}$ or the $3D_{5/2}$ state. First, if the qubit is projected to the ground state $4S_{1/2}$, it will go through a cycle of getting excited to the $4P_{1/2}$ state and decaying to the original $4S_{1/2}$ state. This cycle will emit photons that can be measured and interpreted as a measurement of the $|g\rangle$ state. However, it is also possible for the $4P_{1/2}$ state to decay to the $3D_{3/2}$. In order to solve this problem, an additional 866nm laser can be used to pump this unwanted population back to the $4P_{1/2}$ level. Second, if the state is projected to the excited state, $3D_{5/2}$, this state will not be affected by the laser, and no photons will be measured. The energy levels of the $^{40}Ca^+$ ion and the laser frequencies involved in these operations are shown in Fig. 4.2.

4.3 Single-qubit gates

Now that we know how to approximate a two-level system by using an ion, we need to explain how to perform quantum operations on this system. We will begin by explaining the single-qubit operations since they are simpler than the entangling operations.

The Hamiltonian describing an ion in the trap is given by

$$H_0 = H_{\text{ion}} + H_{\text{trap}}. \tag{4.19}$$

Here H_{trap} represents the part of the Hamiltonian appearing due to the harmonic potential of the trap, given by

$$H_{\text{trap}} = \hbar\nu(a^\dagger a + 1/2), \tag{4.20}$$

where $a^\dagger$ and a are the creation and annihilation operators related to the vibrational state of the ion, respectively. The part appearing due to our approximated two-level system is

$$H_{\text{ion}} = \hbar\frac{\omega_{eg}}{2}\sigma_z, \tag{4.21}$$

with ω_{eg} being the energy difference between the ground and excited levels, $|g\rangle$ and $|e\rangle$. The eigenstates of H_0 are of the form $|g, n\rangle$ and $|e, n\rangle$ where n is an integer that indicates the excitation state of the harmonic Hamiltonian.

In order to interact with this system, we will use a laser with an electric field described by

$$E(x,t) = E_0 e^{i(kx-\omega t+\phi)} + E_0 e^{-i(kx-\omega t+\phi)}, \tag{4.22}$$

with E_0 being the amplitude of the electric field, k the wavenumber, ω the frequency of the laser, and ϕ the phase. This interaction is modelled by a new term in the Hamiltonian, $H_{\text{int}}(t)$, given by

$$H_{\text{int}}(t) = \hbar\frac{\Omega}{2}\left(e^{i(kx-\omega t+\phi)} + e^{-i(kx-\omega t+\phi)}\right)\left(|e\rangle\langle g| + |g\rangle\langle e|\right), \tag{4.23}$$

where Ω is the Rabi frequency, which depends on the interaction of the laser with the dipole moment of the ion (or the quadrupole in the case of the ground and excited levels that we defined in Sec. 4.2 since for this case the transition is dipole-forbidden).

Defining $\sigma^+ = |e\rangle\langle g|$ and $\sigma^- = |g\rangle\langle e|$ we have the complete Hamiltonian

$$H(t) = \hbar\frac{\omega_{eg}}{2}\sigma_z + \hbar\nu(a^\dagger a + 1/2) + \hbar\frac{\Omega}{2}\left(e^{i(kx-\omega t+\phi)} + e^{-i(kx-\omega t+\phi)}\right)\left(\sigma^+ + \sigma^-\right). \quad (4.24)$$

Since the ion is trapped in the harmonic potential of the trap, it is convenient to replace the position operator by the a and $a^\dagger$ operators. By making this change we obtain

$$H(t) = H_0 + \hbar\frac{\Omega}{2}\left(e^{i(\eta(a+a^\dagger)-\omega t+\phi)} + e^{-i(\eta(a+a^\dagger)-\omega t+\phi)}\right)\left(\sigma^+ + \sigma^-\right). \quad (4.25)$$

We have introduced the Lamb-Dicke parameter [27]

$$\eta = k\sqrt{\frac{\hbar}{2m\nu}}, \quad (4.26)$$

which relates the recoil energy due to the ion absorbing a photon to the energy spacing of the quantised levels of the harmonic oscillator. In the Lamb-Dicke regime, the Lamb-Dicke parameter and the motional state of the ion, $|n\rangle$, satisfy $\eta\sqrt{n} \ll 1$, and we can approximate the Hamiltonian as

$$H(t) \approx H_0 + \hbar\frac{\Omega}{2}\left[(1 + i\eta(a + a^\dagger))e^{-i(\omega t-\phi)} + (1 - i\eta(a + a^\dagger))e^{i(\omega t-\phi)}\right]\left(\sigma^+ + \sigma^-\right). \quad (4.27)$$

We can change this Hamiltonian to the interaction picture, defined as

$$\hat{H}(t) = U(t)H(t)U^\dagger(t) + i\left(\frac{d}{dt}U(t)\right)U^\dagger(t), \quad (4.28)$$

with

$$U(t) = e^{iH_0 t}. \quad (4.29)$$

The interaction Hamiltonian is approximately

$$\begin{aligned}\hat{H}(t) \approx{}& \frac{\hbar\Omega}{2}\left(\sigma^+ e^{i(\omega_{eg}-\omega)t}e^{-i\phi} + \sigma^- e^{-i(\omega_{eg}-\omega)t}e^{i\phi}\right)\\ &+ \frac{i\hbar\Omega\eta}{2}\left(a\sigma^+ e^{i(\omega_{eg}-\omega-\nu)t}e^{-i\phi} + a^\dagger\sigma^- e^{-i(\omega_{eg}-\omega-\nu)t}e^{i\phi}\right)\\ &+ \frac{i\hbar\Omega\eta}{2}\left(a^\dagger\sigma^+ e^{i(\omega_{eg}-\omega+\nu)t}e^{-i\phi} + a\sigma^- e^{-i(\omega_{eg}-\omega+\nu)t}e^{i\phi}\right),\end{aligned} \quad (4.30)$$

where we have used the rotating wave approximation (RWA) to ignore the fast rotating

terms.

We can further simplify this Hamiltonian, for example, by considering that the frequency of the laser is resonant with the qubit transition, $\omega = \omega_{eg}$. In this case, the only resonant terms would be those that have a $\omega_{eg} - \omega$ in the exponential. The resulting Hamiltonian is

$$\hat{H}(t) \approx \frac{\hbar\Omega}{2}\left(\sigma^+ e^{-i\phi} + \sigma^- e^{i\phi}\right) = \frac{\hbar\Omega}{2}\sigma_\phi \tag{4.31}$$

with

$$\sigma_\phi = \sigma_x \cos(\phi) + \sigma_y \sin(\phi). \tag{4.32}$$

Using that $\sigma_\phi^2 = \mathbb{1}$, one can check that the evolution introduced by this Hamiltonian is

$$\hat{U}(t) = e^{-iHt/\hbar} = \mathbb{1}\cos\left(\frac{\Omega}{2}t\right) - i\sigma_\phi \sin\left(\frac{\Omega}{2}t\right). \tag{4.33}$$

This evolution is a rotation on the Bloch sphere around a rotating axis defined by σ_ϕ, while keeping the motional state of the ion unchanged. Therefore, the interaction of a laser of this frequency introduces Rabi oscillations between $|g, n\rangle$ and $|e, n\rangle$, which is also referred to as *carrier transition*. For a given Ω one can tune the time of the gate to obtain the desired rotation angle, with especially important cases being the $\pi/2$-pulses ($\Omega \cdot t = \pi/2$), which introduce a rotation of $\pi/2$, and the π-pulses ($\Omega \cdot t = \pi$), of rotation angle π, effectively swapping the population of $|g\rangle$ and $|e\rangle$.

A different case happens when the frequency of the laser is $\omega_{eg} - \nu$. For this case, the Hamiltonian is

$$\hat{H}(t) \approx \frac{i\hbar\Omega\eta}{2}\Big(a\sigma^+ e^{i(\omega_{eg}-\omega-\nu)t}e^{-i\phi} + a^\dagger\sigma^- e^{-i(\omega_{eg}-\omega-\nu)t}e^{i\phi}\Big), \tag{4.34}$$

which introduces Rabi oscillations of the form $|g, n\rangle \leftrightarrow |e, n-1\rangle$, also called *red sideband transition*. Finally, if the frequency of the laser is $\omega_{eg} + \nu$, the Hamiltonian is

$$\hat{H}(t) \approx \frac{i\hbar\Omega\eta}{2}\Big(a^\dagger\sigma^+ e^{i(\omega_{eg}-\omega+\nu)t}e^{-i\phi} + a\sigma^- e^{-i(\omega_{eg}-\omega+\nu)t}e^{i\phi}\Big), \tag{4.35}$$

which introduces Rabi oscillations of the form $|g, n\rangle \leftrightarrow |e, n+1\rangle$, also called *blue sideband transition*. A schematic of these processes is shown in Fig. 4.3.

From this interaction of the trapped ion with laser light of the appropriate frequency, it is possible to use the carrier transition to perform single-qubit rotations around an

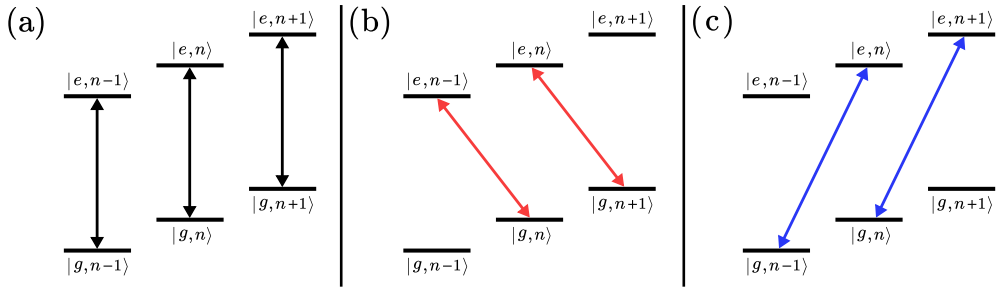

Figure 4.3: Trapped ion transitions. Ladder energy levels of the trapped ion. We show only the motional level $|n\rangle$ and its neighbours. (a) Illuminating the ion with a laser of frequency $\omega = \omega_{eg}$ introduces Rabi oscillations corresponding to the carrier transitions, $|g, n\rangle \leftrightarrow |e, n\rangle$. (b) When the frequency of the laser is $\omega = \omega_{eg} - \nu$, the red sideband transitions ($|g, n\rangle \leftrightarrow |e, n-1\rangle$) are the resonant ones. (c) Otherwise, if the frequency is $\omega = \omega_{eg} + \nu$ the resonant transitions are the blue sideband ones, $|g, n\rangle \leftrightarrow |e, n+1\rangle$.

axis located in the equator of the Bloch sphere, with this rotation axis being selected by the phase of the laser, ϕ. Additionally, the red sideband transition can be used to decrease the motional state of the ion by following a process called *sideband cooling*. This process consists in using a laser resonant to the red sideband to couple an ion in the $|g, n\rangle$ state to the $|e, n-1\rangle$ state. The population transferred to the $|e, n-1\rangle$ can in turn decay to the $|g, n-1\rangle$, effectively reducing the motional state. Repeating this cycle effectively reduces the motional state of the ion. However, since an advantage of using the state $3D_{5/2}$ for encoding the $|e\rangle$ state was its relatively long lifetime, the decay part would require considerable time. In order to speed up this process, one can couple the metastable state $3D_{5/2}$ to the short-lived $4P_{3/2}$ state by using laser light of 854nm. The population transferred to this state decays to the state $|g, n-1\rangle$ faster, thus reducing the time required for the sideband cooling process. A representation of these processes is shown in Fig. 4.4.

4.4 Entangling gates

In order to perform any unitary quantum operation on a qubit register, we need what is called a universal set of gates. Up to this point, we have explained how to perform single-qubit operations, but to complete our universal set of gates, we need to perform entangling operations between different qubits. In the following, we will explain the

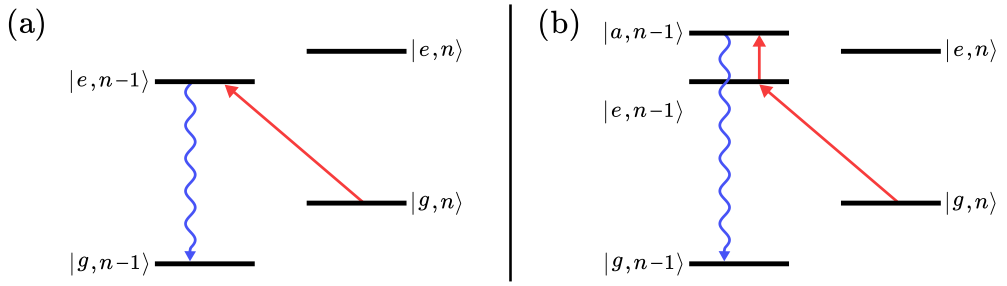

Figure 4.4: Sideband cooling. (a) The state $|g,n\rangle$ can be coupled to the $|e,n-1\rangle$ state by using a laser resonant to the red sideband transition. The population transferred can then decay to the $|g,n-1\rangle$ state, effectively decreasing the motional energy of the ion. (b) If the state used to define the $|e\rangle$ state of the qubit has a relatively long lifetime, an additional laser can be used to couple the state $|e,n-1\rangle$ to another auxiliary level $|a,n-1\rangle$ different from the ion levels used for defining the qubit and with a shorter lifetime. This state can then decay to the $|g,n-1\rangle$ state, achieving a decrease of the motional energy of the ion and requiring less time than by using a decay from $|e,n-1\rangle$.

Cirac-Zoller gate [19], which was the initial proposal for an entangling gate on a trapped-ion setup.

The Cirac-Zoller gate, which was first proposed in 1995 [19] and experimentally implemented in 2003 [130], consists in the application of three laser pulses applied to a pair of ions prepared in the ground motional state. The first one is a red sideband π-pulse acting on one of the qubits, let us call it A. This operation, U_A, has no effect if qubit A is in the ground state, but if it is in the excited state it will change the qubit to the ground state and the motional state from $|0\rangle$ to $|1\rangle$. The second pulse, U_B acts on the second qubit, B, and it is a red sideband 2π-pulse with respect to the ground state of the qubit and an auxiliary state of the ion, $|a\rangle_B$ (not necessarily the one mentioned for sideband cooling), such that if the qubit B is in the ground state of the qubit and the center-of-mass mode of the ions is in the $|1\rangle$ state, it gains a -1 phase, otherwise it is left unchanged. The final pulse is just a repetition of U_A. The states after the application of each pulse for each of the four possible initial states are

$$\begin{aligned}
|g_A,g_B,0\rangle &\xrightarrow{U_A} |g_A,g_B,0\rangle \xrightarrow{U_B} |g_A,g_B,0\rangle \xrightarrow{U_A} |g_A,g_B,0\rangle \\
|g_A,e_B,0\rangle &\xrightarrow{U_A} |g_A,e_B,0\rangle \xrightarrow{U_B} |g_A,e_B,0\rangle \xrightarrow{U_A} |g_A,e_B,0\rangle \\
|e_A,g_B,0\rangle &\xrightarrow{U_A} -i\,|g_A,g_B,1\rangle \xrightarrow{U_B} i\,|g_A,g_B,1\rangle \xrightarrow{U_A} |e_A,g_B,0\rangle \\
|e_A,e_B,0\rangle &\xrightarrow{U_A} -i\,|g_A,e_B,1\rangle \xrightarrow{U_B} -i\,|g_A,e_B,1\rangle \xrightarrow{U_A} -|e_A,e_B,0\rangle\,.
\end{aligned} \tag{4.36}$$

This gate, $U_{c-Z} \equiv U_A U_B U_A$, can be used to create entanglement. For example, combined with the Hadamard gate it creates a Bell state

$$H_B C_{c-Z} H_A H_B \left|e_A, e_B, 0\right\rangle = \frac{1}{\sqrt{2}}(\left|g_A, e_B, 0\right\rangle - \left|e_A, g_B, 0\right\rangle). \tag{4.37}$$

However, even if this gate can be used to create entanglement, it shows some problems in its experimental implementation. First, the correct behaviour of the gate depends on preparing the motional ground state. However, in the experiment, this will not be possible, since the ions will be in a thermal state that, even if it has a small value $\bar{n}$, will reduce the fidelity of the gate. Second, this gate can be applied only to a pair of ions, which is inconvenient since in the experiment there are situations where it is preferable to apply an entangling gate over more than two ions at the same time.

Thus, even though the Cirac-Zoller gate was the first proposal for an entangling gate in trapped ions, it is desirable to find an alternative that solves these problems, such as the Mølmer-Sørensen gate [131, 132], which is based on the application of a bichromatic laser beam that performs correlated spin flips. It has important advantages over the Cirac-Zoller gate, such as being able to create entanglement with more than two qubits, or being resilient, in first-order approximation, against imperfectly cooled ions. We will explain in detail the working principle and derivation of this gate, as well as different miscalibration errors that can appear in the experiment, in Chapter 9.

Chapter 5

Quantum Error Correction

Up to this point, we introduced the basic elements of a quantum computer: the qubits, the different operations that one can perform over them to process quantum information and perform quantum computations, and an example of a physical platform in which a quantum computer can be implemented. However, this implementation of a quantum computer will be subject to imperfections which introduce noise into the computation process. Of course, the existence of noise is not a problem appearing exclusively in quantum computation. Classical computers also suffer errors in the bits during a computation which are possible to correct by applying classical error correction protocols. However, the quantum nature of a quantum computer restricts the tools available for error correction. First of all, while creating copies of the information of a set of bits is an important tool for classical error correction, the no-cloning theorem [14] states that it is not possible to create copies of an arbitrary unknown quantum state. Second, while one can measure a set of bits without changing their state, one can not measure a set of qubits without projecting them into the eigenbasis of the measurement. Third, the nature of the errors appearing in a qubit is more complex than those appearing in a bit. Similar to a bit changing from state 0 to 1 or vice versa due to an error, a qubit can suffer a similar effect with its states $|0\rangle$ and $|1\rangle$, but on top of that, qubits can also lose the information inside the phase of a quantum superposition by either errors that change this phase, or by decoherent errors that destroy the superposition, an example being a trapped-ion qubit in a superposition decaying to the ground state.

In order to correctly perform quantum computations, one needs specific protocols to detect and correct quantum errors with the experimentally available tools. This is

where the field of Quantum Error Correction (QEC) appears. The main idea behind QEC is to encode the information of a logical qubit into a set of physical qubits. If an error happens in the qubit system then one can perform a set of measurement that yield no information about the logical state and, in consequence, it does not change the logical information. The outcomes from these measurements can then be associated with an error, which can then be corrected.

The most basic QEC code is the 3-qubit code, encoding one logical qubit into three physical ones. With this code, one can perform parity measurements to correct either single-qubit errors or bit-flip errors, but not both. In order to obtain a more useful QEC code, one has to introduce more physical qubits. This is the case of the Shor or 5-qubit codes, which can also correct phase-flip errors.

While QEC codes can correct errors that have happened in the physical qubits of the system, they are vulnerable to errors happening in the circuit that implements the QEC process itself. Due to this, one has to design QEC codes in such a way that they can also correct the errors that they introduce into the system. These are the so-called *fault-tolerant* circuit constructions. However, their application usually comes with an increase in the number of physical qubits needed. On top of this, the *threshold theorem* [46, 47, 63] establishes the existence of a critical error probability threshold for which, if the error probability is under the threshold, the application of QEC techniques reduces the probability of having a logical error. Moreover, below this threshold the probability for an error that the QEC code cannot correct can be arbitrarily decreased by increasing the code size.

A remarkable type of QEC codes, which can be made fault-tolerant, is the family of *topological codes* [133]. These codes are built in such a way that the physical qubits and the checks used to detect errors, called *stabilisers* (defined in detail in the next section), define a specific topology (e.g. a torus or a two-dimensional bounded array). By defining a code in this way, operators acting on the logical qubit are defined as chains of physical operations that complete a non-trivial cycle around the given topology, that is, they cannot be deformed into a single point. Due to this, for a logical error to happen, errors must appear on physical qubits such as they complete a non-trivial cycle. Additionally, one can perform measurements to infer a correction to the errors. It is important to note that, for long sequences of errors appearing in the code, this inference process can fail, introducing more errors to the code instead of correcting the

previously existing ones. In this case, the combination of previously existing errors and the new ones can complete a non-trivial cycle, resulting in a logical error. However, since in the experimental implementations the errors are usually assumed to be local and, as such, they are assumed to appear in random qubits, the probability of a logical error happening decreases exponentially with the size of the code.

Current important examples of topological codes are the surface code [134, 135] and the color code [136]. This is in part due to their high error thresholds for which current estimates are between 0.5% and 1.14% [137–139] for the surface code and 0.082% and 0.37% [140–142] for the color code, but also due to their syndrome extraction depending on gates applied between neighbouring qubits, that is, there is no need for interaction between qubits far apart, which otherwise would be difficult to implement on certain physical platforms. Additionally, these examples of topological codes can also implement some *transversal gates*, which means that the application of logical gates can be performed by applying single-qubit gates on all the physical qubits. However, the implementation of a universal gate set fault-tolerantly is known to be impossible by a no-go theorem by Eastin and Knill [143]. While first implementations of non-fault-tolerant surface and color codes have been implemented using different physical platforms [51–56], the increase in size of quantum processors along with the improvements on gate fidelities have been pushing closer to theoretical proposals of fault-tolerant implementations [68, 144–147], resulting in very recent and exciting breakthrough experiments [65–67].

While QEC is a large and active area of research, in this section we will build a brief and direct explanation of the basic ideas of QEC needed to understand an example of a QEC code, the Steane code, which is the target of the calibration protocol explained in Chapter 7. For a broader and more detailed introduction to QEC, the reader is referred to Refs. [18, 148, 149].

5.1 Stabiliser formalism

An important class of QEC codes are the *stabiliser codes* [150, 151]. The idea behind them is that, after encoding a logical qubit of possible states $|0\rangle_L$ and $|1\rangle_L$ into N physical qubits, it is possible to detect whether an error has happened in any of the physical qubits by measuring a set of operators called *stabilisers*. A specific result of this

set of measurements will reveal errors in the set of physical qubits without projecting the logical qubit into the zero or one state. Once the errors on the physical qubits are detected, they can be corrected to recover the correct logical state.

In order to understand these QEC codes, we begin by explaining the stabiliser formalism, which is a way to define a state using a set of operators. A state $|\psi\rangle$ is said to be stabilised by the operator S if it is a $+1$ eigenstate of S

$$S|\psi\rangle = |\psi\rangle . \tag{5.1}$$

Using this definition, one can define an N-qubit state, $|\psi\rangle$, by using a set of N linearly independent commuting stabilisers, $\{S_i\}_{i=1}^{N}$, that is

$$S_i|\psi\rangle = |\psi\rangle , \quad i = 1, ..., N. \tag{5.2}$$

The operators S_i may be elements of the extension of the Pauli group to a system of N qubits. To understand why this is enough to define a state, note that the Hilbert space of N qubits has dimension 2^N and each of these equations divides it by two, leaving just one possible state that has $+1$ eigenvalue for all of the N stabilisers.

In a QEC code of N qubits, one can define $N-1$ stabilisers, leaving a 2-dimensional Hilbert space spanned by the $+1$ eigenstates of these stabilisers. Of these states, one can define one of them as the logical zero state, $|0\rangle_L$, and the other as the logical one, $|1\rangle_L$. Finally, one can define an additional stabiliser that will be responsible for distinguishing which of these two logical states is the logical qubit, due to this, we call this final stabiliser the *logical operator*. Since all the stabilisers commute with the logical operator, one can measure all of them to obtain information about possible errors happening in the physical qubits without changing the logical state.

Now that we have introduced the main idea behind QEC codes, we will explain a simple but important example: the Steane code.

5.2 Steane code

The Steane code [152] is a stabiliser code that uses seven physical qubits to encode a logical qubit, and it is the smallest case of a color code [136]. The logical subspace of

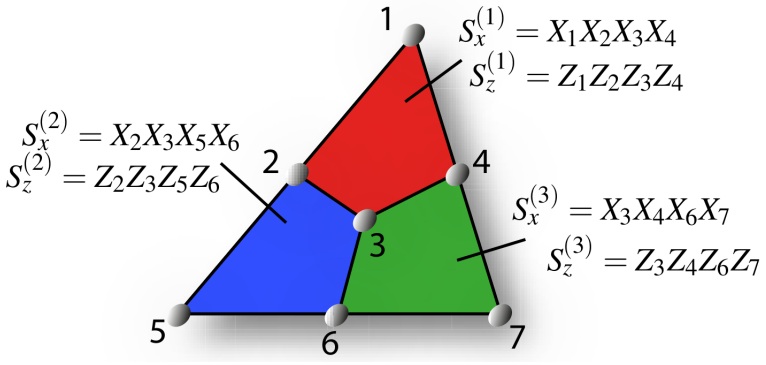

Figure 5.1: Steane code. Representation of the relation between the physical qubits and the stabilisers used for the Steane code. Seven physical qubits are used to encode a logical qubit in the two-dimensional +1 subeigenspace of six stabilisers: $S_x^{(i)}$ and $S_z^{(i)}$ with $i = 1, 2, 3$. An arbitrary single-qubit error can be detected by performing stabiliser measurements which can then be corrected.

the seven-qubit Hilbert space is defined by the following six stabilisers

$$\begin{aligned} S_x^{(1)} &= X_1X_2X_3X_4, \quad S_z^{(1)} = Z_1Z_2Z_3Z_4, \\ S_x^{(2)} &= X_2X_3X_5X_6, \quad S_z^{(2)} = Z_2Z_3Z_5Z_6, \\ S_x^{(3)} &= X_3X_4X_6X_7, \quad S_z^{(3)} = Z_3Z_4Z_6Z_7, \end{aligned} \tag{5.3}$$

which are tensor products of Pauli X or Z operators with the subindex indicating on which qubit each Pauli operator is applied. A representation of each of these stabilisers and the qubits over which they act is shown in Fig. 5.1. Finally, one can define the logical operator used to measure the state of the logical qubit, Z_L, given by

$$Z_L = Z_1Z_2Z_3Z_4Z_5Z_6Z_7. \tag{5.4}$$

Therefore, the logical zero state is the common +1 eigenstate of all the stabilisers as well as of Z_L, which is given by

$$\begin{aligned} |0\rangle_L = \frac{1}{2\sqrt{2}}(&|0000000\rangle + |0110110\rangle + |1111000\rangle + |1001110\rangle \\ &+ |0011011\rangle + |0101101\rangle + |1100011\rangle + |1010101\rangle). \end{aligned} \tag{5.5}$$

Similarly, one can find the form of the logical one state, $|1\rangle_L$. These states satisfy $Z_L|0\rangle_L = |0\rangle_L$ and $Z_L|1\rangle_L = -|1\rangle_L$. One can also define the logical X operator, X_L,

given by

$$X_L = X_1 X_2 X_3 X_4 X_5 X_6 X_7, \tag{5.6}$$

which flips the logical qubit, $X_L |0\rangle_L = |1\rangle_L$ and $X_L |1\rangle_L = |0\rangle_L$. Due to the form of this construction, one can apply logical bit-flip and phase-flip gates by simply using seven single qubit X or Z gates.

Now that we have defined the stabilisers and the logical states, let us assume that an error E of the form of a Pauli operator occurs on one of the physical qubits that encode the zero logical state. Since the error does not commute with all the stabilisers, the state will no longer be a $+1$ eigenstate for all of them and

$$S_\alpha^{(i)} E |0\rangle_L = -E |0\rangle_L , \quad i = 1, 2, 3, \quad \alpha = x, z \tag{5.7}$$

for those stabilisers $S_\alpha^{(i)}$ that anticommute with E. Once the measurement of the stabilisers has been performed, it is possible to obtain a one-to-one relation between the measurement outcomes, also called *syndrome*, and the error that happened and in which physical qubit it happened. One can then conclude which operation has to be applied to correct the code. As an example, let us assume that the code suffers an X_1 error. The measurement of the $S_z^{(1)}$ stabiliser would return a -1 while the outcome of all the other stabiliser measurements would be a $+1$. This syndrome would be associated to an X_1 error, which can then be corrected by applying X_1 on the first qubit.

The Steane code ensures the correction of single bit-flip and/or phase-flip errors. However, for some cases with more than one error of the same type, the result of the correction plus the original error might complete a stabiliser, which would effectively return the state to the correct logical state. An example of this would be when an X error appears on the first, second, and third qubit. When one measures the stabilisers for this case, the conclusion would be that an X error appeared on the fourth qubit, so the correction corresponds to apply an X_4 operator. For this case, the original error plus the correction corresponds to an stabiliser, which leaves the original state unchanged. Therefore, the Steane code can also correct these specific cases. However, in order to ensure that the code corrects more than single bit flips and phase flips, one has to increase the size of this code [136].

Chapter 6

Bayesian formalism

When learning statistics, one usually sees two different approaches on how to interpret sets of measured data, the common frequentist approach and the Bayesian approach. The frequentist approach consists in assuming a model given a prior knowledge and repeating the same experiment to estimate a set of probabilities based on the frequency of each of the outcomes. These probabilities can then be used to obtain information on the parameters of the model. Thus, a frequentist works by studying the frequency of experimental outcomes, which are more accurate the more the experiment is repeated. The Bayesian approach starts by modelling the prior knowledge by using a probability distribution of the parameters of the system. This prior knowledge is updated measurement after measurement, obtaining at the end a probability distribution that has more information about the parameters of the experiment than the prior knowledge.

In this chapter, we provide an introduction to Bayes' theorem and the concept of Bayesian inference, which will be the central part of the protocols derived in this thesis.

6.1 Bayes theorem and Bayesian inference

Bayes' theorem prescribes how to update the prior probability distribution $P(\mathbf{\Theta})$ of a set of parameters $\mathbf{\Theta}$ after a measurement outcome, m, by using the likelihood of that outcome given $\mathbf{\Theta}$, $P(m|\mathbf{\Theta})$. The final result is a posterior probability distribution, $P(\mathbf{\Theta}|m)$, with the form

$$P(\mathbf{\Theta}|m) \propto P(m|\mathbf{\Theta})P(\mathbf{\Theta}) \tag{6.1}$$

up to a normalisation factor. This posterior can then be used as a prior for the next update through an iterative process in which the probability distribution after T measurements is given by

$$p(\mathbf{\Theta}|m_1, ..., m_T) \propto p(\mathbf{\Theta}) \prod_{t=1}^{T} P(m_t|\mathbf{\Theta}), \tag{6.2}$$

provided that the measurements are independent of each other. For an increasing number of measurements, the degree of uncertainty of the parameters $\mathbf{\Theta}$ will decrease until we obtain a precise enough set of estimates for the parameters under study. An example of Bayesian inference is shown in Fig. 6.1.

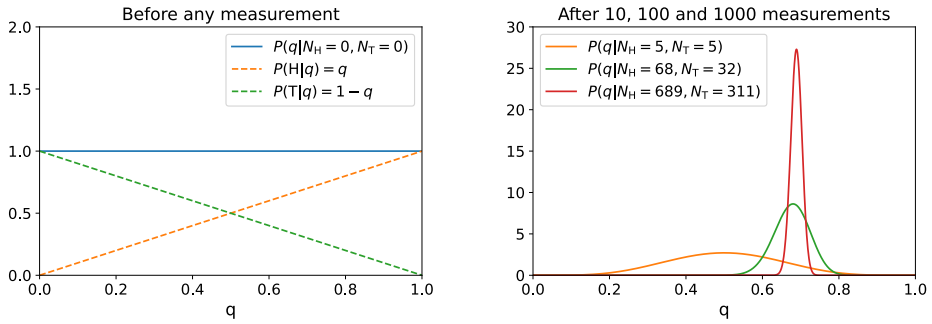

Figure 6.1: Bayesian inference example. A simple case of Bayesian inference can be applied to the problem of characterising a Bernouilli experiment, e.g., estimating the probability of obtaining tails or heads when tossing a coin [153]. If the probability of obtaining heads is $P(H|q) = q$ and for tails it is $P(T|q) = 1 - q$, the probability distribution obtained by applying Bayesian inference after obtaining N_H heads and N_T tails is $P(q|N_H, N_T) \propto q^{N_H}(1-q)^{N_T}$. Left: Prior probability distribution of the parameter q before tossing the coin, i.e., before measuring the system. Since nothing is known about the system, the prior is a uniform probability distribution. Right: Probability distributions of q after 10, 100, and 1000 measurements. The results are obtained by simulating a coin with a true value of the parameter q of 0.7 and the estimate obtained after 1000 measurements for the case shown is 0.69. Moreover, since we have access to the probability distribution, we can easily calculate the standard deviation of this estimate, which is $\sigma_q = 0.015$.

While, as explained, Eq. (6.2) defines how to perform Bayesian inference for estimating parameters, in some cases we will have a degree of freedom in the protocol in the form of the measurements that we can perform. In the next section, we give a brief explanation of how one can take advantage of this degree of freedom in order to select the measurements that provide the most information about the desired parameters.

6.2 Shannon's entropy and adaptiveness

In order to decide which are the most informative measurements that we can perform in a system, we will introduce a few basic concepts of information theory [153, 154]. In the following we will use discrete one-dimensional probability distributions and outcomes for simplicity, but the results shown are generalisable to other cases.

Shannon's entropy, introduced by Claude Shannon in his paper *"A Mathematical Theory of Communication"* in 1948 [155], quantifies the level of uncertainty of a random variable, Θ. It is defined as

$$H(\Theta) = -\sum_i p(\theta_i) \log_2(p(\theta_i)), \tag{6.3}$$

where θ_i represents each possible result of Θ, and we use base 2 logarithms, to express the result in bits of information. From this definition, we can get the intuitive idea that when the probability of a given outcome is much higher than the others, which is a case where we have a considerable amount of information about the system, the entropy is low, with the limiting case where one of the probabilities is one and the others zero having no entropy. Similarly, if all the probabilities are similar, that is, we do not know much about the system, then the entropy is high, with the limiting case of having equal probabilities for all outcomes maximising the entropy.

As we have seen from the Bayesian approach, our knowledge about a given parameter can be expressed as a probability distribution and, as such, we can directly use Shannon's entropy. In particular, in the Bayesian approach we work with prior and posterior distributions, where the posterior is obtained after performing a measurement on the system (which can be seen as asking a question) and obtaining an outcome (an answer). We will use $\{m_j^\alpha\}_{j=1}^J$ to denote the set of all J possible outcomes when the measurement settings used for obtaining that outcome (or the question asked) is α. If we were to obtain the outcome m_j^α, we can compare the entropy difference between the prior and the posterior

$$IG(\Theta, m_j^\alpha) = \sum_i p(\theta_i|m_j^\alpha) \log_2(p(\theta_i|m_j^\alpha)) - \sum_i p(\theta_i) \log_2(p(\theta_i)). \tag{6.4}$$

The interpretation of this result is that, thanks to the measurement performed on the system, we have gained information about the system, and this is given by $IG(\Theta, m_j^\alpha)$.

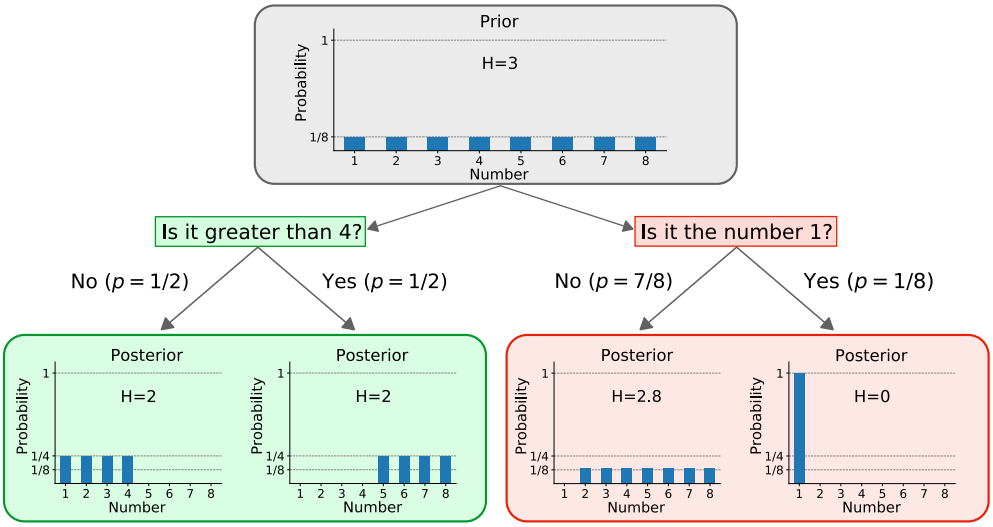

Figure 6.2: Adaptive measurement example. In this example, the goal is to guess an integer between 1 and 8 that another person has chosen. Unless we know that this person had some bias when choosing the number, our best prior is a discrete uniform distribution. This prior has an entropy of 3 that can be obtained by using Eq. (6.3), this means that there are 3 bits of information to be learnt since the distributions involved are uniform. In this example, we show two different measurement settings, i.e., questions that we can ask: the optimal approach (green) and the "bold" approach (red). In the optimal case, the questions are selected in such a way that for each possible answer the entropy of the posterior is 2, which means that the expected information gain with that measurement setting is 1 bit. Following this strategy, one will guess the correct number after three questions. In the "bold" approach, one tries to guess directly the number, this high-risk high-reward strategy is successful one out of eight times, in which case one learns 3 bits. However, the other times the information gain is only 0.2 bits. This results in an expected information gain of 0.55 bits for this measurement setting. This strategy guesses the correct number after 4.375 questions on average.

We ideally want to perform measurements that maximise this information gain. However, since we do not know what the outcome of our measurement will be, the best we can do is to use a measurement setting that maximises

$$\overline{IG}(\Theta, \alpha) = \sum_j IG(\Theta, m_j^\alpha) p(m_j^\alpha). \tag{6.5}$$

In other words, we look for the measurement setting that maximises the expected information gain based on our current knowledge about the system. It should be noted that this result for optimal experimental design can also be obtained by arguments of maximising the expected *Kullback-Leibler divergence* between the prior and the posterior

distribution [153, 156].

Bayesian updates and optimal measurement settings can be thought of as being at the core of how we, as humans, infer to reach a conclusion, where we can look around or ask questions (among other tools at our disposal) to update our knowledge about our surroundings. In this sense, it is intuitive that there are strategies to obtain information more efficiently, and the previous result for optimal measurement settings can be used to obtain the optimal strategy for simple cases, such as solving problems in game theory like the examples in Ref. [157] or Fig. 6.2. Unfortunately, even when finding an optimal measurement setting is possible, this might depend on numerical calculations that slow down a Bayesian inference process. However, as we will see in Chapters 7 and 8, one can use some approximations about the prior distribution to obtain an optimal measurement setting by using analytically obtained rules.

For more details about information theory and optimal measurement settings, the reader is referred to Refs. [158, 159]

6.3 Particle filtering algorithm

Using the results explained in Sec. 6.1 we can obtain a probability distribution for our unknown parameters based on the results of a set of measurements. However, obtaining interesting properties, such as the mean values or the variances, from the inferred probability distributions resulting from an inference process cannot be done analytically in general. Therefore, we depend on obtaining these values numerically. A simple way to perform this numerical process is to evaluate the probability distribution at a set of points to discretise it. However, the dimensionality of the probability distribution under study increases with the number of parameters that we want to estimate. If we were to discretise the probability distribution by evaluating it in points of a fixed grid in the parameter space, this increasing dimensionality would require an increasing number of evaluations of the distribution, otherwise, we could run into a discretisation error when calculating the estimates and variances of the distribution due to undersampling the probability distribution. Since for a higher number of parameters we would need a higher number of evaluations, this could make the process prohibitively slow. To circumvent this dimensionality problem we draw on the ideas of particle filtering

algorithms [160–164] with which we can obtain approximate samples from a given probability distribution, which can then be used to obtain an approximation of its estimates and variances. Obtaining approximate samples allows us to adapt the evaluations that we perform on the probability distribution so that they are located in more relevant points on the parameter space, therefore requiring fewer evaluations than a naive fixed grid approach as the one described before.

In the following, we introduce the basic methods that we will use for a particle filtering algorithm: The *importance sampling* and the *sampling importance resampling* methods. We will then explain how to use them for a Bayesian inference protocol for parameter estimation.

6.3.1 Importance sampling (IS)

Our goal is to obtain a set of samples from a target probability distribution, $p(\mathbf{\Theta})$, where $\mathbf{\Theta}$ is a vector composed by the parameters that we want to learn, and which we consider to be variables since we use a Bayesian approach. However, due to the form of $p(\mathbf{\Theta})$, there might not be a simple way to sample directly from it. Thus, we will use a sampling probability distribution, $s(\mathbf{\Theta})$, from which we assume that it is simple to obtain a set of N_p samples, $\{\widetilde{\mathbf{\Theta}}_i\}_{i=1}^{N_p}$, where $\widetilde{\mathbf{\Theta}}_i$ is a point in the parameter space that we will call *particle*. Since we can obtain perfect samples from $s(\mathbf{\Theta})$, we can approximate the probability in an infinitesimal interval as

$$s(\mathbf{\Theta})d\mathbf{\Theta} \approx \frac{1}{N_p}\sum_{i=1}^{N_p}\delta_{\widetilde{\mathbf{\Theta}}_i}(d\mathbf{\Theta}), \tag{6.6}$$

where we introduce the *Dirac measure*,

$$\delta_{\widetilde{\mathbf{\Theta}}_i}(A) \equiv \begin{cases} 1, & \text{if} \quad \widetilde{\mathbf{\Theta}}_i \in A \\ 0, & \text{otherwise} \end{cases} . \tag{6.7}$$

The expected value of a function $f(\mathbf{\Theta})$ under $p(\mathbf{\Theta})$ is

$$\begin{aligned}\overline{f(\mathbf{\Theta})} &= \int_{\mathbb{R}} f(\mathbf{\Theta})p(\mathbf{\Theta})d\mathbf{\Theta} = \int_{\mathbb{R}} f(\mathbf{\Theta})\frac{p(\mathbf{\Theta})}{s(\mathbf{\Theta})}s(\mathbf{\Theta})d\mathbf{\Theta} \\ &\approx \frac{1}{N_p}\sum_{i=1}^{N_p}\int_{\mathbb{R}} f(\mathbf{\Theta})\frac{p(\mathbf{\Theta})}{s(\mathbf{\Theta})}\delta_{\widetilde{\mathbf{\Theta}}_i}(d\mathbf{\Theta}) \\ &= \frac{1}{N_p}\sum_{i=1}^{N_p} f(\widetilde{\mathbf{\Theta}}_i)\frac{p(\widetilde{\mathbf{\Theta}}_i)}{s(\widetilde{\mathbf{\Theta}}_i)} = \sum_{i=1}^{N_p} f(\widetilde{\mathbf{\Theta}}_i)w^{(i)},\end{aligned} \tag{6.8}$$

where we have defined the *importance weights*, $w^{(i)}$, as

$$w^{(i)} \equiv \frac{1}{N_p}\frac{p(\widetilde{\mathbf{\Theta}}_i)}{s(\widetilde{\mathbf{\Theta}}_i)} \quad \text{for} \quad i = 1, ..., N_p, \tag{6.9}$$

which is the same result that we would obtain by using the following approximation for $p(\mathbf{\Theta})$:

$$p(\mathbf{\Theta})d\mathbf{\Theta} \approx \sum_{i=1}^{N_p} w^{(i)}\delta_{\widetilde{\mathbf{\Theta}}_i}(d\mathbf{\Theta}). \tag{6.10}$$

Therefore, the importance weights correspond to a correction applied to the samples obtained from $s(\mathbf{\Theta})$ so that the resulting weighted particle system represents an approximation of $p(\mathbf{\Theta})$.

By using IS one can obtain a set of weighted particles that discretise a complex probability distribution. However, IS can lead to many particles having small weights after multiple iterations, which would then have a small contribution to the probability distribution, the same problem that one would find when using a fixed grid approach. This problem can be solved by using the weighted particle system to obtain samples approximately distributed to the target distribution. In order to obtain these samples, we will use the *sampling importance resampling* method.

6.3.2 Sampling importance resampling (SIR)

The SIR method is an extension of the IS which complements it by following it with a resampling step, which generates samples approximately distributed according to the target probability distribution. The resampling is implemented as follows: After obtaining a set of weighted particles $\{\widetilde{\mathbf{\Theta}}_i, w^{(i)}\}_{i=1}^{N_p}$ by using IS, we define the normalised

weights

$$\tilde{w}^{(i)} \equiv \frac{w^{(i)}}{\sum_{i=1}^{N_p} w^{(i)}} \quad \text{for} \quad i = 1, ..., N_p, \tag{6.11}$$

allowing us to define the normalised particle system $\{\widetilde{\mathbf{\Theta}}_i, \tilde{w}^{(i)}\}_{i=1}^{N_p}$. We can then generate N_p approximate samples, $\{\widehat{\mathbf{\Theta}}_i\}_{i=1}^{N_p}$, by using the discrete probability distribution defined by $\{\widetilde{\mathbf{\Theta}}_i, \tilde{w}^{(i)}\}_{i=1}^{N_p}$

$$P(\widehat{\mathbf{\Theta}}_j = \widetilde{\mathbf{\Theta}}_i) = \tilde{w}^{(i)}, \quad \text{for} \quad i, j = 1, ..., N_p. \tag{6.12}$$

The resulting set of samples (or weightless particles), $\{\widehat{\mathbf{\Theta}}_i\}_{i=1}^{N_p}$, approximates the result of sampling the target probability distribution. By using these samples, we can approximate the target probability distribution as

$$p(\mathbf{\Theta})d\mathbf{\Theta} \approx \frac{1}{N_p} \sum_{i=1}^{N_p} \delta_{\widehat{\mathbf{\Theta}}_i}(d\mathbf{\Theta}). \tag{6.13}$$

Therefore, by using the SIR method we can obtain approximate samples from a posterior distribution by using samples from a prior. This can then be implemented into a Bayesian inference protocol as we will explain now.

6.3.3 Bayesian parameter estimation

Our Bayesian inference model will be represented by a state-space model (SSM) [165] characterised by a set of states $\mathbf{\Theta}_t$ at each inference step t. We can obtain information about the state $\mathbf{\Theta}_t$ by performing measurements, m_t, to obtain a probability distribution of $\mathbf{\Theta}_t$ based on the outcomes of these measurements. We assume that our process is a first-order Markov process, such as the state $\mathbf{\Theta}_t$ only depends on the previous state, $\mathbf{\Theta}_{t-1}$. Additionally, we assume our measurements to be dependent only on the current state $\mathbf{\Theta}_t$. A step-by-step representation of the following process can be found in Fig. 6.3. With these considerations, we can define the transition probability from the state $\mathbf{\Theta}_{t-1}$ to $\mathbf{\Theta}_t$, $T(\mathbf{\Theta}_t|\mathbf{\Theta}_{t-1})$, by

$$p(\mathbf{\Theta}_t|m_{1:t-1}) = \int T(\mathbf{\Theta}_t|\mathbf{\Theta}_{t-1}) p(\mathbf{\Theta}_{t-1}|m_{1:t-1}) d\mathbf{\Theta}_{t-1}. \tag{6.14}$$

The form of this transition probability depends on the system under consideration and can be used, for example, to model the introduction of noise into the system, which can be included on purpose to move the particles after each iteration to avoid having

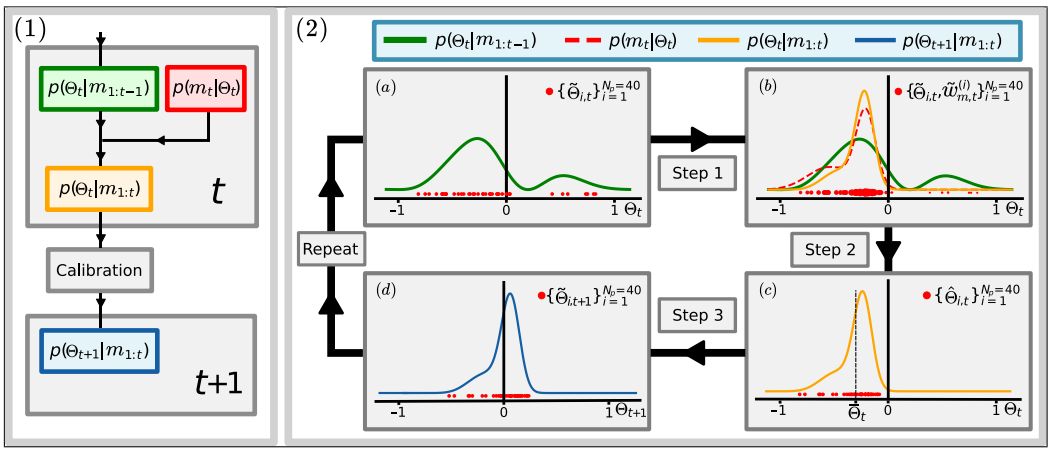

Figure 6.3: Bayesian particle filtering algorithm. (1) Representation of a cycle of the calibration process. The initial probability distribution at iteration t with $t-1$ measurements, $p(\boldsymbol{\Theta}_t|m_{1:t-1})$, is updated by performing a new set of measurements, m_t, to obtain $p(\boldsymbol{\Theta}_t|m_{1:t})$. The estimates obtained from this probability distribution can then be used to calibrate the parameters, obtaining the initial probability distribution for iteration $t+1$. (2) Steps followed to perform an iteration of the particle filtering algorithm for a simplified case with only one parameter, Θ. In (a) we have particles obtained from sampling the prior probability distribution $p(\Theta_t|m_{1:t-1})$. A new set of measurements is performed to obtain the posterior probability distribution in (b) by using the likelihood of the outcome obtained for the new measurement, $p(m_t|\Theta_t)$. The weights are obtained as prescribed by Eq. (6.18), where a bigger weight is visually represented by a bigger size of the particle. These weighted particles can then be used to obtain the estimate of the parameter at this iteration, $\bar{\Theta}_t$, by using Eq. (6.19). In (c), a resampling process is performed to obtain particles with equal weights that approximate particles from the posterior probability distribution. The previously obtained value $\bar{\Theta}_t$ is also shown here. Finally, in (d), $\bar{\Theta}_t$ has been used to calibrate the parameter Θ, where for this example we are assuming that the ideal value of Θ is zero, therefore, the correction applied is to change the value of the parameter by $-\bar{\Theta}_t$.

several particles in the same position as could happen when using Eq. (6.12), or to introduce corrections on the parameters based on the previous estimate of the state. With these definitions, our goal will consist in obtaining an estimate of $\boldsymbol{\Theta}_t$ from a set of measurements performed on the system $m_{1:t} = \{m_1, ..., m_t\}$.

Using Bayes' theorem, we find a relation between the states before and after the measurement

$$p(\boldsymbol{\Theta}_t|m_{1:t}) \propto p(m_t|\boldsymbol{\Theta}_t)p(\boldsymbol{\Theta}_t|m_{1:t-1}), \tag{6.15}$$

up to a normalisation factor. Thus, from $p(\boldsymbol{\Theta}_t|m_{1:t-1})$ and $p(m_t|\boldsymbol{\Theta}_t)$ we may infer $p(\boldsymbol{\Theta}_t|m_{1:t})$, which can then be used with $T(\boldsymbol{\Theta}_{t+1}|\boldsymbol{\Theta}_t)$ to obtain $p(\boldsymbol{\Theta}_{t+1}|m_{1:t})$ through Eq. (6.14). This defines an iterative process to estimate $\boldsymbol{\Theta}_t$ by performing measurements

and updating our knowledge based on the results.

In case the probability distribution $p(\mathbf{\Theta}_t|m_{1:t})$ becomes too complex, we can use the SIR method to obtain approximate samples of this distribution at each step. To this end, we will distinguish two sets of samples at step t. First, we have $\{\widetilde{\mathbf{\Theta}}_{i,t}\}_{i=1}^{N_p}$ that represents the positions of the particles at step t before the measurement and resampling, that is, the approximate samples from $p(\mathbf{\Theta}_t|m_{1:t-1})$. Second, we have $\{\widehat{\mathbf{\Theta}}_{i,t}\}_{i=1}^{N_p}$ that represents the positions of the particles at step t after the measurement and resampling, which are approximate samples of $p(\mathbf{\Theta}_{i,t}|m_{1:t})$. At iteration t we want to obtain $\{\widehat{\mathbf{\Theta}}_{i,t}\}_{i=1}^{N_p}$ from $\{\widetilde{\mathbf{\Theta}}_{i,t}\}_{i=1}^{N_p}$ and Eq. (6.15). To this end, we calculate the importance weights as defined in Eq. (6.9)

$$w_{m,t}^{(i)} = \frac{1}{N_p}\frac{p(\widetilde{\mathbf{\Theta}}_{i,t}|m_{1:t})}{p(\widetilde{\mathbf{\Theta}}_{i,t}|m_{1:t-1})}, \quad \text{for} \quad i = 1, ..., N_p, \tag{6.16}$$

where we have introduced the subindex m in $w_{m,t}^{(i)}$ to specify that the new weights are obtained after a measurement m_t. According to Eq. (6.15) we can rewrite Eq. (6.16) as

$$w_{m,t}^{(i)} \propto p(m_t|\widetilde{\mathbf{\Theta}}_{i,t}), \quad \text{for} \quad i = 1, ..., N_p, \tag{6.17}$$

from which we can obtain the normalised importance weights

$$\tilde{w}_{m,t}^{(i)} = \frac{p(m_t|\widetilde{\mathbf{\Theta}}_{i,t})}{\sum_{i=1}^{N_p} p(m_t|\widetilde{\mathbf{\Theta}}_{i,t})}, \quad \text{for} \quad i = 1, ..., N_p. \tag{6.18}$$

Using this set of weighted particles, $\{\widetilde{\mathbf{\Theta}}_{i,t}, \tilde{w}_{m,t}^{(i)}\}_{i=1}^{N_p}$, we can then obtain the estimates and variances at that iteration:

$$\overline{\mathbf{\Theta}}_t = \sum_{i=1}^{N_p} \tilde{w}_{m,t}^{(i)} \widetilde{\mathbf{\Theta}}_{i,t}, \tag{6.19}$$

$$\mathrm{Var}(\mathbf{\Theta}_t) = \sum_{i=1}^{N_p} \tilde{w}_{m,t}^{(i)} (\widetilde{\mathbf{\Theta}}_{i,t} - \overline{\mathbf{\Theta}}_t)^2. \tag{6.20}$$

These are the quantities of interest at each iteration of the Bayesian inference process.

Finally, we can use the SIR method with these weighted particles to obtain a new set of equally weighted particles, $\{\widehat{\mathbf{\Theta}}_{i,t}\}_{i=1}^{N_p}$. This allows us to correct the previously obtained estimates of the parameters, bringing them closer to their ideal value. The

form in which the correction moves our set of particles will be given by the transition function, $T(\boldsymbol{\Theta}_{t+1}|\boldsymbol{\Theta}_t)$, which we can use with $\{\widehat{\boldsymbol{\Theta}}_{i,t}\}_{i=1}^{N_p}$ and Eq. (6.14) to obtain the particles that will be used at the beginning of the next iteration: $\{\widetilde{\boldsymbol{\Theta}}_{i,t+1}\}_{i=1}^{N_p}$. This completes an iteration of a Bayesian protocol using a particle filter.

Part II

Research results

Chapter 7

Adaptive Bayesian phase estimation for quantum error correcting codes

In this chapter, we explain the work about phase estimation of quantum error correcting code states by application of Bayesian inference that we presented in Ref. [1]. In this work, we introduced an adaptive Bayesian method to measure systematic phase shift errors appearing in the experimental preparation of multi-qubit states. In particular, we used it for correcting the errors appearing in the logical states of the Steane code introduced in Sec. 5.2. Using this method one is capable of adapting the experimental configuration for each measurement based on the previous measurements in such a way that it optimises the information gained. Additionally, we derive a simple analytical rule for this adaptive selection, saving computational power that would be otherwise used in obtaining numerically the optimal measurement at each step of the process.

We compared our method to the Phase Optimisation Method (PHOM) proposed in Ref. [52], which is a frequentist and non-adaptive phase estimation method based on a generalization of a Ramsey experiment [166] for multi-qubit states that was realised in an experimental implementation of the Steane code. In order to compare both of these methods, we simulated them to estimate quantum phases appearing in the preparation of quantum states needed for the Steane code. The efficiency obtained by simulation of our method is in agreement with the efficiency derived from the theoretical calculations, and shows an improvement by reducing the number of measurements required by more

than one order of magnitude when compared to the PHOM.

In Sec. 7.1 we will explain the importance of correcting unwanted relative phases appearing during the initialisation of a code state for the correct performance of the QEC code. In Sec. 7.2 we explain a single-qubit state phase measurement as a toy model to introduce the concepts and notation required for this chapter. To this end we will also compare a frequentist approach to this problem, which consists in performing parameter scans, to a Bayesian inference approach. In Sec. 7.3 we introduce and compare the efficiencies of the PHOM and our Bayesian inference method to an intermediate quantum state obtained during the preparation of the logical states of the Steane code. This intermediate state has a less complex structure than the final states of the code but the generalisation of the protocol shown in this section to the final state of the code is straightforward. Finally, in Sec. 7.4 we generalise the previous results and present our Bayesian inference method to estimate the phase shifts on the fully encoded seven-qubit logical states and perform a comparison between the results obtained for the efficiency of our method with the PHOM.

7.1 Background

In Chapter 5 we saw that in quantum error correction quantum information is encoded in entangled many-qubit systems, in the form of a logical qubit. As shown in Sec. 5.2, the Steane code is obtained by restricting the Hilbert space of seven qubits to the subspace of states which are simultaneously +1 eigenstates of six commuting stabiliser operators $S_x^{(i)}$ and $S_z^{(i)}$, $i = 1, 2, 3$ (see Fig. 5.1). These stabilisers define a 2-dimensional subspace for this 7-qubit system that can be used to encode a logical qubit. However, due to imperfections during the initial state preparation of the $|0\rangle_L$ and $|1\rangle_L$ logical states in the experimental realisation of this code, the obtained state might differ from the expected ideal one [51]. Dynamical phase shifts during the encoding sequence can accumulate and give rise to unknown, although systematic, relative phases between the eight components of the expected ideal final state given in Eq. (5.5), resulting instead in the following state

$$\begin{aligned}|0'\rangle_L =& \frac{1}{2\sqrt{2}}(|0000000\rangle + e^{i\phi_1}|0110110\rangle + e^{i\phi_2}|1111000\rangle + e^{i\phi_3}|1001110\rangle \\ &+ e^{i\phi_4}|0011011\rangle + e^{i\phi_5}|0101101\rangle + e^{i\phi_6}|1100011\rangle + e^{i\phi_7}|1010101\rangle). \end{aligned} \quad (7.1)$$

Examples of errors that can introduce these phase shifts are magnetic shifts between the different electronic states used to define the computational subspace, or a slowly varying laser field frequency introducing a detuning with respect to the qubit transition, such as the case studied in Chapter 8.

Additionally, other errors and in particular incoherent processes can generate populations in other states. A simple one-parameter model of such errors is given by a Werner-state [167] of the form

$$\rho = \frac{p}{\dim}\mathbb{1} + (1-p)\left|0'\right\rangle_L \left\langle 0'\right|_L . \tag{7.2}$$

The first component represents a completely mixed state ($\dim = 2^7 = 128$ in our case) and the parameter $p \in [0, 1]$ quantifies the magnitude of this white-noise component. For more experimental details on the origin of these errors we refer the reader to Refs. [51, 52]. However, we note that incoherent errors such as the one described by the mixed-state contribution in the state in Eq. (7.2) cannot be corrected by the techniques we discuss here. Therefore, to keep notation simple, in what follows we will omit the mixed state component in state descriptions and only consider the part of the state containing the relative phases which can be detected and compensated by the methods discussed.

An error-free initialisation of the QEC states is vital for the correct performance of the QEC code. Thus, the experimental implementation of QEC needs a method to estimate unwanted phase shifts so it can be followed by the necessary corrections. Additionally, the experimental parameters might drift over time, requiring a periodic estimation of the phases. Due to this, the time required for the method is also an important factor. The less time it takes to produce an estimate, the more time is available to perform experiments with the logical qubit. In the next sections we will present our Bayesian inference method to estimate the phases and study the behaviour of the variance of the estimates as a function of the number of measures needed. This study will then prove that our method is superior to the usual frequentist approach to this problem.

7.2 Single-qubit phase estimation example

Before we start with the correction of multiple phase shifts in a multi-qubit state, it is recommendable to start with a simple toy model for the measurement of the phase of a single qubit so we can explain the basic elements of our method.

Suppose that we have a setup that is able to produce copies of qubits in a state with an unwanted relative phase ϕ due to some systematic error

$$|\psi\rangle = \frac{1}{\sqrt{2}}\left(|0\rangle + e^{i\phi}|1\rangle\right). \tag{7.3}$$

Our goal is to obtain an estimate of this phase from a finite set of data obtained from measurements performed on different copies of this state. Measuring the Z Pauli operator yields information about the populations of $|0\rangle$ and $|1\rangle$, but we already know that these populations are $1/2$. This measurement is uninformative with respect to the phase ϕ. Instead, we will perform measurements of the form

$$O_\theta = \cos(\theta)X + \sin(\theta)Y \tag{7.4}$$

on the XY plane of the Bloch sphere (see Fig. 7.1 (a)). The expected value of this operator for the state $|\psi\rangle$ is sensitive to ϕ

$$\langle\psi| O_\theta |\psi\rangle = \cos(\phi - \theta). \tag{7.5}$$

In the following subsections, we will study two different ways in which we can perform and interpret the outcomes of the measurements in order to obtain the value ϕ, one related to a frequentist approach and the other being a Bayesian inference approach.

7.2.1 Frequentist approach

The most intuitive approach to this problem is the frequentist one. In order to estimate ϕ, one can apply a Ramsey-type experiment that can be summarised as follows (see Fig. 7.1):

1. Divide the interval $[-\pi, \pi)$ in M equidistant points

$$\theta_m = m \cdot \frac{2\pi}{M} - \pi, \quad m = 0, 1, ..., M-1. \tag{7.6}$$

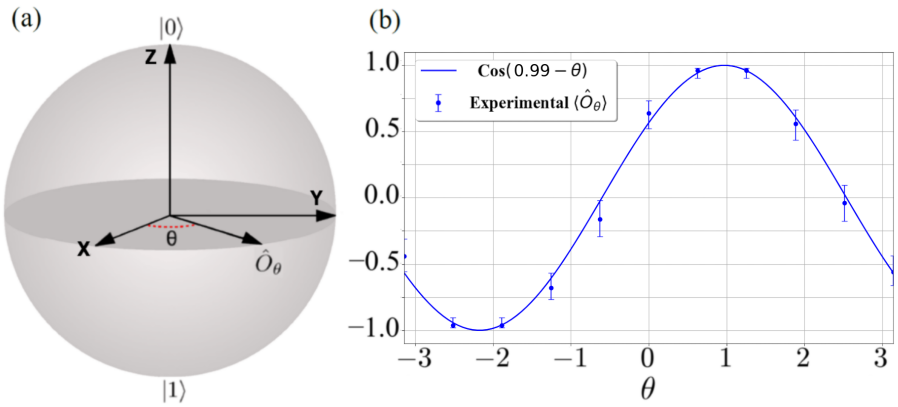

Figure 7.1: Frequentist phase estimation scan. (a) Bloch sphere representation of the measurements to be performed for estimating the phase ϕ of the quantum state of Eq. (7.3). The observables O_θ are obtained by rotating the observable X around the Z axis by an angle θ. The way O_θ is selected depends on the method used to estimate ϕ. In the Ramsey scan case different values of θ are selected and several measurements are performed for each of these values. This allows a reconstruction of the expected sinusoidal dependence of $\langle\psi| O_\theta |\psi\rangle$ with θ that yields an estimate for the phase ϕ (panel (b)). In the Bayes case, the outcomes of O_θ are used to update the probability distribution $P(\phi)$. In this case, the value θ for each measurement is different and it is selected in a way that maximises the information gain per measurement (See Sec. 7.2.2 and Fig. 7.2). (b) Scan simulation for the phase estimation of the state $|\psi\rangle$ in Eq. (7.3) with $\phi = 1$. The points represent the values O_{θ_m} where the θ_m are $M = 10$ equidistant points in the interval $[-\pi, \pi)$. The points are obtained by simulating $N = 50$ measurements of O_{θ_m} for each θ_m and they are used to fit a cosine whose phase A is the estimation obtained for ϕ and it is given by $A = 0.99 \pm 0.09$. The error of A is obtained by a bootstrap resampling [168].

2. For each of the values θ_m we perform N measurements of which $N_+^{(m)}$ will have outcome $+1$ and $N_-^{(m)}$ will have outcome -1. We estimate the expected value $\langle\psi| O_{\theta_m} |\psi\rangle$ as $(N_+^{(m)} - N_-^{(m)})/N$.

3. Using the estimates of $\langle\psi| O_{\theta_m} |\psi\rangle$ obtained for the different values of θ_m, we perform a least squares fit to a function of the form

$$f(\theta) = \cos(A - \theta). \tag{7.7}$$

4. By comparison of Eqs. (7.5) and (7.7), our estimate of ϕ is given by the fitted parameter A.

The more measurements we are able to perform, the more precise the estimates of $\langle\psi| O_{\theta_m} |\psi\rangle$ will be. As a consequence, we will be able to obtain a better fit that will yield a more precise estimate of the ϕ. However, this method has an important limitation: you must restrict your measurements to a set of values θ_m and perform several measurement for each of them. Additionally, these values are selected in a completely arbitrary way. Thus, we might wonder if there is a way to perform each measurement with a different value of θ in such a way that, based on the previous outcomes, it maximises the amount of information gained about ϕ. As we will see in the next subsection, this is the case with the Bayesian inference approach.

7.2.2 Bayesian inference approach

To perform a Bayesian inference process to estimate ϕ, we need to know the likelihoods of our measurements first. In our case we measure the operators O_θ (with different values of θ for each measurement) with possible outcomes $+_\theta$ and $-_\theta$. The likelihoods of these outcomes for the state given in Eq. (7.3) are

$$P(\pm_\theta|\phi) = \frac{1 \pm \cos(\phi - \theta)}{2}. \tag{7.8}$$

Assuming no prior knowledge about the value of ϕ, we start with a uniform probability distribution $P(\phi) = 1/2\pi$ defined in the interval $[-\pi, \pi)$ as a prior. From this prior we can start a Bayesian inference process as described in Sec. 6.1: After the first measurement, we will be able to update our prior to obtain a posterior by using the

likelihood of the outcome

$$P(\phi|\pm_{\theta_1}) \propto P(\phi) \cdot P(\pm_{\theta_1}|\phi). \tag{7.9}$$

This posterior can be used as a prior for the next measurement and so on, defining an iterative process. After N measurements, the probability distribution for ϕ will be given by

$$\begin{aligned} P(\phi|\pm_{\theta_1}, ..., \pm_{\theta_N}) \propto P(\phi)P(\pm_{\theta_1}|\phi) \cdot ... \cdot P(\pm_{\theta_N}|\phi) = \\ = \frac{1}{2\pi} \cdot \frac{1 \pm \cos(\phi - \theta_1)}{2} \cdot ... \cdot \frac{1 \pm \cos(\phi - \theta_N)}{2}. \end{aligned} \tag{7.10}$$

As the number of measurements increases, the posterior probability distribution can be approximated by a normal distribution with decreasing standard deviation. An example of this process is shown in Fig. 7.2

7.2.2.1 Efficiency of the parameter learning process

Now that we have defined the Bayesian inference process applied to the phase estimation of a single-qubit, we can study the accuracy of the estimate as a function of the number of measurements. While doing this, we will also prove that there is a way of selecting the value θ for each measurement based on the previous results which maximises the information gain of ϕ.

Let us suppose that, after a sufficiently large number n of measurements, the probability distribution $P_n(\phi) \equiv P(\phi|\pm_{\theta_1}, ..., \pm_{\theta_n})$ can be approximated by a Gaussian with mean $\bar{\phi}_n$ and standard deviation σ_n

$$P_n(\phi) \approx \frac{1}{\sqrt{2\pi\sigma_n^2}} \exp\left(-\frac{(\phi - \bar{\phi}_n)}{2\sigma_n^2}\right). \tag{7.11}$$

For the measurement $n+1$, the probability $p_{n+1}^{\pm}$ of measuring $\pm$ when the angle selected is θ_{n+1} is

$$p_{n+1}^{\pm} = \int_{-\pi}^{\pi} \frac{1 \pm \cos(\phi - \theta_{n+1})}{2} P_n(\phi) d\phi \ . \tag{7.12}$$

The probability distribution after having obtained $+$ or $-$ is updated as

$$P_{n+1}^{\pm}(\phi) = \frac{1}{p_{n+1}^{\pm}} \frac{1 \pm \cos(\phi - \theta_{n+1})}{2} P_n(\phi), \tag{7.13}$$

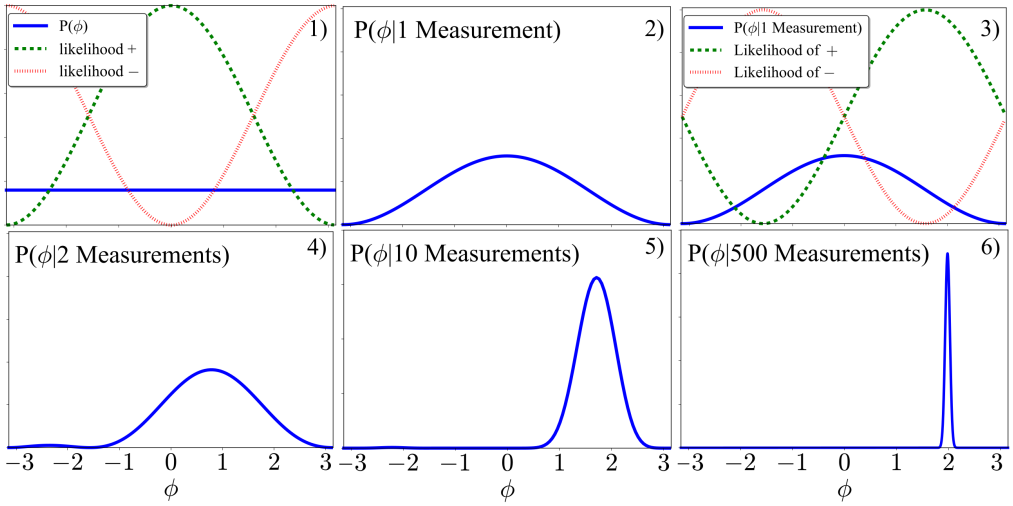

Figure 7.2: Bayesian phase estimation. Bayesian inference process for the phase estimation of the state $|\psi\rangle$ in Eq. (7.3) with $\phi = 2$. Each step of the inference process consists in performing a measurement of the operator $\hat{O}_{\theta_{n-1}}$, updating the probability distribution based on the result of the measurement and selecting an optimal angle θ_n for the next measurement. 1) One starts with a uniform probability distribution of ϕ. $\theta = 0$ is selected for the first measurement. 2) If the + outcome is obtained (as assumed here), the probability distribution is updated by multiplying the prior probability distribution by the likelihood of obtaining a + and renormalizing. The maximum of $P(\phi|1 \text{ measurement})$ is located at $\phi = 0$. 3) The optimal selection of θ will be given by Eq. (7.16). Thus, we select $\theta = \pi/2$ for the next measurement. 4) Assume + is obtained again. The probability distribution can be updated again based on this result. This process of measuring, updating and finding the next optimal θ can be performed iteratively. 5) After 10 measurements the probability distribution can be approximated by a normal distribution. 6) After 500 measurements we obtain a normal distribution centered near the value $\phi = 2$ used for the simulation.

where $p^{\pm}_{n+1}$ appears due to normalisation. These posterior probability distributions will have a standard deviation denoted by $\sigma^{\pm}_{n+1}$. The average decrease of the variance after performing measurement $n+1$ is given by (see Appendix A.2)

$$\overline{\sigma^2_{n+1} - \sigma^2_n} = -\alpha_{n+1}\sigma^4_n \tag{7.14}$$

with

$$\alpha_{n+1} \equiv \frac{e^{\sigma^2_n}\sin^2(\overline{\phi}_n - \theta_{n+1})}{1 - e^{\sigma^2_n}\cos^2(\overline{\phi}_n - \theta_{n+1})} \ . \tag{7.15}$$

From inspection of Eqs. (7.14) and (7.15), we conclude that the maximum decrease on average for the variance is obtained when we select a value of θ_{n+1} that maximizes the

value of α_{n+1}. This is achieved (see Fig. 7.3) for

$$\theta_{n+1} = \overline{\phi}_n \pm \frac{\pi}{2}. \tag{7.16}$$

Then, it can be proven that the succession in Eq. (7.14) has the following asymptotic solution:

$$\sigma_n^2 = \frac{1}{\alpha_n n}. \tag{7.17}$$

However, as the variance decreases, α_n approaches the constant value 1 (except for values close to $\theta_n = \overline{\phi}_{n-1} \pm k\pi$, $k \in \mathbb{N}$) as Fig. 7.3 shows. This means that after several measurements, the decrease of the variance will be independent on the value of θ we select for the next measurement and σ_n^2 will evolve as

$$\sigma_n^2 = \frac{1}{n}. \tag{7.18}$$

Similar results can be obtained by performing calculations involving Shannon's entropy as explained in Sec. 6.2 [169–171] for the selection of the optimal measurement. However, this approach requires numerical calculations to obtain the optimal measurement in each step of the iteration. This can lead to a slow evaluation by the classical computer of the optimal measurement settings, as compared to the simple rule governed by Eq. (7.16) of our method, leading to a slow-down of the calibration. In Figure 7.3 we show that, after several measurements, this adaptive way of selecting the next measurement becomes as efficient as a non-adaptive method for the one-qubit case. However, we stress that this is not a generic feature but specific to this simple example. We will show in the following sections that for the phase measurement of multi-qubit states an adaptive approach to the selection of the measurements yields an improvement in the efficiency as compared to the non-adaptive approach. It is worth mentioning that the result in Eq. (7.18) indicates that our increase in the knowledge of the system satisfies the Standard Quantum Limit (SQL).

7.3 Two-plaquette case

Now that we have explained the basic idea behind phase estimation of quantum states, we can move from the single-qubit toy model to a more complex case. This will be what we call the two-plaquette case, in which we will study a multi-qubit state appearing in

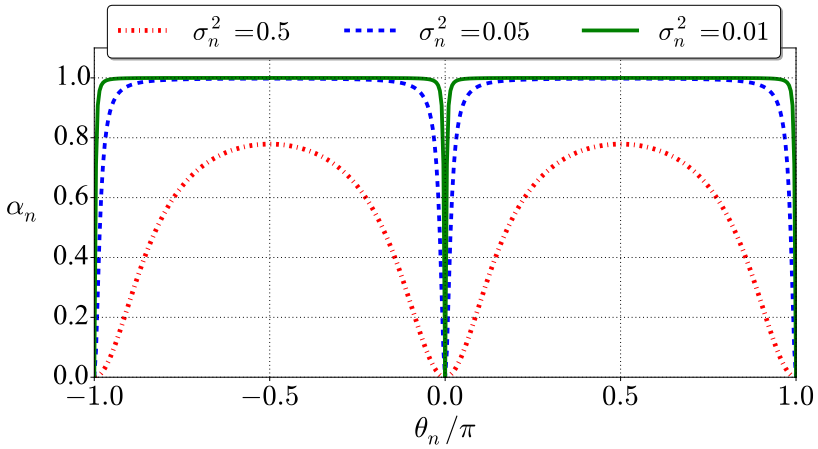

Figure 7.3: Adaptiveness of the phase measurement settings. The quantity α dictates the decrease of the variance $\overline{\sigma_{n+1}^2 - \sigma_n^2}$ after each measurement step. This figure shows the dependence of α with θ_n for the case $\bar{\phi}_n = 0$ and different values of σ_n^2. Other values of $\bar{\phi}_n$ produce the same plot with a translation on the horizontal axis. As σ_n^2 decreases α approaches 1 except for the values $\theta = \bar{\phi}_n \pm k\pi$.

an intermediate step during the preparation of the Steane code states. Thanks to this example we will be able to study a multi-qubit state which shows some complications that do not appear in the single-qubit case. From this case we will define a Bayesian inference process that will be easily generalisable to the phase estimation of the final states of the Steane code.

At the start of the preparation of the Steane code states, four-qubit entangling operations are applied to the first plaquette (Fig. 7.4 (a)). This yields the quantum state $|\psi_1\rangle \propto (1 + S_x^{(1)})\,|0\rangle^{\otimes 7}$composed by the superposition of two components in the computational basis which can have a relative phase due to systematic errors. This is equivalent to a single-qubit phase estimation, as the phase can be corrected by rotating one of the four qubits and performing measurements of the $S_x^{(1)}$ stabiliser.

We can increase the complexity of the problem by considering the state $|\psi_2\rangle$ obtained by application of four-qubit entangling operations to the first and second plaquettes (see Fig. 7.4 (b))

$$|\psi_2\rangle \propto \prod_{i=1}^{2}(\mathbb{1} + S_x^{(i)})\,|0\rangle^{\otimes 7} = |0000000\rangle + |0110110\rangle + |1111000\rangle + |1001110\rangle\,. \quad (7.19)$$

This state is a +1 eigenstate of the X-type stabilisers on the first and second plaquette,

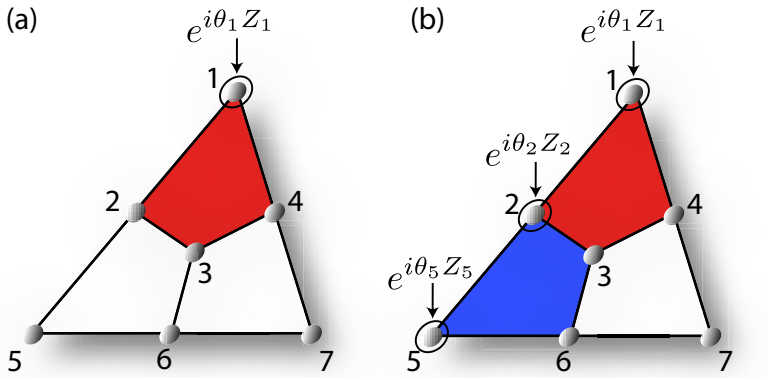

Figure 7.4: One and two-plaquette cases. (a) One-plaquette case. During the first step of the preparation of the seven-qubit error correcting code, four-qubit entangling operations are performed on qubits 1 to 4. A phase appearing in the resulting state due to systematic errors can be estimated by performing measurements of $S_x^{(1)}$ for different rotations on the first qubit. This is similar to the single-qubit phase estimation. (b) Two-plaquette case. After the manipulation of the first and second plaquettes, up to three relative phases can appear in quantum state obtained. To estimate these phases we can perform measurements of $S_x^{(1)}$, $S_x^{(2)}$ and $S_x^{(1)}S_x^{(2)}$ for different rotations on the first, second and fifth qubit.

$S_x^{(1)} = X_1X_2X_3X_4$, $S_x^{(2)} = X_2X_3X_5X_6$ and the product of both, $S_x^{(1)}S_x^{(2)} = X_1X_4X_5X_6$. As such, it maximises their mean value:

$$\langle\psi_2| S_x^{(1)} |\psi_2\rangle = \langle\psi_2| S_x^{(2)} |\psi_2\rangle = \langle\psi_2| S_x^{(1)}S_x^{(2)} |\psi_2\rangle = 1. \tag{7.20}$$

However, systematic phase shifts accumulate during the preparation of $|\psi_2\rangle$ due to experimental errors. The state $|\psi_2'\rangle$ containing these unknown phase shifts is

$$|\psi_2'\rangle \propto |0000000\rangle + e^{i\phi_1} |0110110\rangle + e^{i\phi_2} |1111000\rangle + e^{i\phi_3} |1001110\rangle . \tag{7.21}$$

In order to compensate these relative phase shifts we can apply single qubit Z rotations (see Fig. 7.4 (b)). For example, by rotating the first, second and fifth qubits by angles θ_1, θ_2 and θ_5 respectively we obtain

$$\begin{aligned} e^{i\theta_1 Z_1} e^{i\theta_2 Z_2} e^{i\theta_5 Z_5} |\psi_2'\rangle \propto |0000000\rangle &+ e^{i[\phi_1+2(\theta_2+\theta_5)]} |0110110\rangle \\ &+ e^{i[\phi_2+2(\theta_1+\theta_2)]} |1111000\rangle + e^{i[\phi_3+2(\theta_1+\theta_5)]} |1001110\rangle . \end{aligned} \tag{7.22}$$

The selection of qubits to be rotated is arbitrary as long as these three rotations do

not commute with $S_x^{(1)}$, $S_x^{(2)}$ and $S_x^{(1)}S_x^{(2)}$. The expected values of the stabilisers in the state Eq. (7.21) are given by

$$\langle S_x^{(1)}\rangle = \frac{\cos[\phi_2 + 2(\theta_2+\theta_1)] + \cos[\phi_1 - \phi_3 + 2(\theta_2-\theta_1)]}{2}, \tag{7.23}$$

$$\langle S_x^{(2)}\rangle = \frac{\cos[\phi_1 + 2(\theta_2+\theta_5)] + \cos[\phi_2 - \phi_3 + 2(\theta_2-\theta_5)]}{2}, \tag{7.24}$$

$$\langle S_x^{(1)}S_x^{(2)}\rangle = \frac{\cos[\phi_3 + 2(\theta_5+\theta_1)] + \cos[\phi_1 - \phi_2 + 2(\theta_5-\theta_1)]}{2}, \tag{7.25}$$

Therefore, for this case we are trying to estimate three phases, not one as in the single-qubit case. In order to obtain information about the unknown systematic phases, we can perform measurements of these stabilisers for different values of the rotation angles θ. Once the values of these phases are measured it is possible to perform single-qubit rotations to transform the state $|\psi_2'\rangle$ into the desired state $|\psi_2\rangle$.

In the following subsections, we will talk about two different approaches to this problem. The first one is the PHOM, based on a similar frequentist approach as the scans explained for the single-qubit case in Sec. 7.2.1, while the second one is our Bayesian inference method, which is similar to the one in Sec. 7.2.2 but with some additional difficulties due to the increased dimensionality of the problem. We will explain both and show how the Bayesian method can be performed in an adaptive way. Finally, we will compare both methods and demonstrate that ours is more efficient than the PHOM since it requires less measurements to obtain estimates of the phases with the same associated errors.

7.3.1 Phase Optimisation Method

The Phase Optimisation Method introduced in Ref. [52] is a frequentist approach that can be used to estimate phases of multi-qubit states appearing during the preparation of the Steane code. It consists in performing scans of the expected values of each stabiliser for different single-qubit rotation values to find the values of the rotations that optimise the expected value of each stabiliser. Once the expected values are optimised, it means that the found single-qubit rotations correct the unwanted phases. The PHOM is an iterative protocol. For concreteness, we review how it works for the the state in Eq. (7.21).

1. For each stabiliser, an associated rotation on a qubit i, θ_i, is chosen. The selection is arbitrary, but each stabiliser must not commute with its associated qubit rotation. We associate θ_2 with $S_x^{(1)}$, θ_5 with $S_x^{(2)}$ and θ_1 with $S_x^{(1)}S_x^{(2)}$.

2. Choose an initial configuration for the set of rotation parameters, which we will denote as $\boldsymbol{\theta}^{(0)} = \{\, \theta_1^{(0)}, \theta_2^{(0)}, \theta_5^{(0)} \,\}$.

3. Scan $\langle S_x^{(1)} \rangle$ in a similar way as in the single-qubit case (see Fig. 7.1 (b)) over its associated angle, θ_2, in the interval $[-\pi, \pi]$ while keeping $\theta_1 = \theta_1^{(0)}$ and $\theta_5 = \theta_5^{(0)}$ fixed. Determine and fix θ_2 to the value $\theta_2 = \theta_2^{(1)}$ for which $\langle S_x^{(1)} \rangle$ is maximized. Similarly perform scans of $\langle S_x^{(2)} \rangle$ over θ_5 to obtain $\theta_5^{(1)}$ and $\langle S_x^{(1)} S_x^{(2)} \rangle$ over θ_1 to obtain $\theta_1^{(1)}$. With these steps $\boldsymbol{\theta}^{(0)} = \{\, \theta_1^{(0)}, \theta_2^{(0)}, \theta_5^{(0)} \,\}$ has changed to $\boldsymbol{\theta}^{(1)} = \{\, \theta_1^{(1)}, \theta_2^{(1)}, \theta_5^{(1)} \,\}$. Performing this step completes one PHOM iteration.

4. The values of the angles $\boldsymbol{\theta}$ might not converge to the values that correct the phases after only one iteration. If necessary, repeat step (3) for a number of iterations I until the set of angles $\boldsymbol{\theta}$ converges to a desired precision.

After enough iterations have been performed, this method will converge to an estimate of the angles θ_1, θ_2 and θ_5 that correct the systematic phases ϕ_1, ϕ_2 and ϕ_3. The precision of this estimate will become better as the number of measurements used for the scans of each iteration increases.

The convergence of the original PHOM method depends on the number of iterations performed, which in turn depends on the value of the original phases that we want to correct. This makes the efficiency of the PHOM difficult to study, since there is no way to know from the start how many iterations will be needed. This can be avoided with a modified version of the PHOM that we also introduced in [1] and that we called constant cosine PHOM.

7.3.1.1 Constant cosine PHOM

The constant cosine PHOM is a similar method that also performs scans of the expected values of the stabilisers for different qubit rotations to obtain a correction for systematic phases. This process is closer to the scan method in Sec. 7.2.1. From Eq. (7.23) we can

see that if we keep the value $\theta_2 - \theta_1$ fixed and vary $\theta_2 + \theta_1$ the mean value of $\langle S_x^{(1)} \rangle$ will be given by

$$\langle S_x^{(1)} \rangle = \frac{\cos[\phi_2 + 2(\theta_2 + \theta_1)] + h}{2}, \quad h \equiv \cos[\phi_1 - \phi_3 + 2(\theta_2 - \theta_1)]. \tag{7.26}$$

The offset h is uniform for all measurements because the difference $\theta_2 - \theta_1$ is fixed. Thus the angle ϕ_2 that represents the phase shift to be corrected is the value of $-2(\theta_2 + \theta_1)$ for which a maximum in the mean value $\langle S_x^{(1)} \rangle$ is reached. A similar reasoning can be followed for $\langle S_x^{(2)} \rangle$ and $\langle S_x^{(1)} S_x^{(2)} \rangle$ to obtain ϕ_1 and ϕ_3. This method has the advantage of finding an estimate for the phases with only one round of scans, with the precision of the estimate increasing with the number of measurements used for each scan.

7.3.2 Bayesian inference approach

Now that we have introduced the more intuitive PHOM, let us explain and analyse the two Bayesian inference methods that we designed to measure the phases in the state $|\psi_2'\rangle$ of Eq. (7.21) of the two-plaquette case. The methods are (i) a Bayesian inference method by direct application of the likelihoods, and (ii) a Bayesian inference method using marginal likelihoods. We will first describe the direct Bayesian inference method and show that its complexity and non-adaptivity makes it almost equally efficient to the constant cosine PHOM. Next, we will explain the marginal likelihood method and show how, due to its simplicity, it is possible to find a rule to select adaptive measurements, allowing this method to be more efficient than the constant cosine PHOM.

7.3.2.1 Direct Bayesian inference method

For this method, the Bayesian estimation of the phases requires measuring the plaquettes and updating the probability distribution based on the outcomes. The likelihoods of each plaquette measurement is obtained from the expected values as

$$\begin{aligned} P_1(\pm_{\boldsymbol{\theta}}|\boldsymbol{\phi}) &= \frac{1 \pm \langle S_x^{(1)} \rangle}{2}, \\ P_2(\pm_{\boldsymbol{\theta}}|\boldsymbol{\phi}) &= \frac{1 \pm \langle S_x^{(2)} \rangle}{2}, \\ P_{12}(\pm_{\boldsymbol{\theta}}|\boldsymbol{\phi}) &= \frac{1 \pm \langle S_x^{(1)} S_x^{(2)} \rangle}{2}. \end{aligned} \tag{7.27}$$

Here $P_1(\pm_{\boldsymbol{\theta}}|\boldsymbol{\phi})$ is the likelihood of obtaining a + or a − outcome when measuring $S_x^{(1)}$ for $\boldsymbol{\theta} = \{\theta_1, \theta_2, \theta_5\}$ and $\boldsymbol{\phi} = \{\phi_1, \phi_2, \phi_3\}$. Similarly, $P_2(\pm_{\boldsymbol{\theta}}|\boldsymbol{\phi})$ is related to $S_x^{(2)}$ and $P_{12}(\pm_{\boldsymbol{\theta}}|\boldsymbol{\phi})$ to $S_x^{(1)}S_x^{(2)}$. For instance, the likelihood for $S_x^{(1)}$ is given by

$$P_1(\pm_{\boldsymbol{\theta}}|\boldsymbol{\phi}) = \frac{2 \pm \cos[\phi_2 + 2(\theta_2 + \theta_1)] \pm \cos[\phi_1 - \phi_3 + 2(\theta_2 - \theta_1)]}{4}. \tag{7.28}$$

Since the likelihoods are functions of three variables, the probability distribution is a three-dimensional function. As explained in Sec. 6.3, as the number of parameters increases, so does the dimensionality of the posterior distributions, which complicates finding the estimates of the desired parameters and their variance. While performing a Bayesian inference on the three-dimensional distribution case might be possible with a particle filtering algorithm, this will not be the case for the full Steane code preparation, where the seven parameters are too many for a particle filter. To avoid this dimensionality problem we can keep one of the cosines constant for each stabiliser measurement in a similar way as it is done for the constant cosine PHOM. This is done by keeping the value of $\theta_2 - \theta_1$ constant to ensure that one of the cosines has a constant value that we denote as h_2. This yields a likelihood given by (see also Eq.(7.26))

$$P_1(\pm_{\boldsymbol{\theta}}|\phi_2, h) = \frac{2 \pm h_2 \pm \cos[\phi_2 + 2(\theta_2 + \theta_1)]}{4} \tag{7.29}$$

for the first plaquette. Similar expressions can be obtained for the other stabilisers. This approach yields normal probability distributions defined on two variables, one being h_1, h_2 or h_3 and the other being ϕ_1, ϕ_2 or ϕ_3, depending on the stabiliser that is measured. The estimate for each phase is easily obtained from its corresponding probability distribution.

We performed a numerical study of the efficiencies of this method and the constant cosine PHOM protocol (see Fig. 7.5). The numerical fit of the data obtained with the PHOM showed that the scaling of the variance as a function of the number of measurements n is given by $\sigma_{i,n}^2 = (6.6 \pm 0.2)/n$ when estimating the single angle ϕ_i. Similarly, for the constant cosine Bayes we obtained $\sigma_{i,n}^2 = (6.2 \pm 0.6)/n$. However, in order to obtain an estimate of the other two phases, these processes must be repeated for each of the other stabilisers. This yields a scaling of the variance of $\sigma_n^2 = (19.8 \pm 0.4)/n$ for the PHOM and $\sigma_n^2 = (18.6 \pm 1.0)/n$ for the constant cosine Bayes method. This

provides an estimate of the efficiency of the PHOM and the direct Bayesian inference method for the intermediate state $|\psi_2'\rangle$.

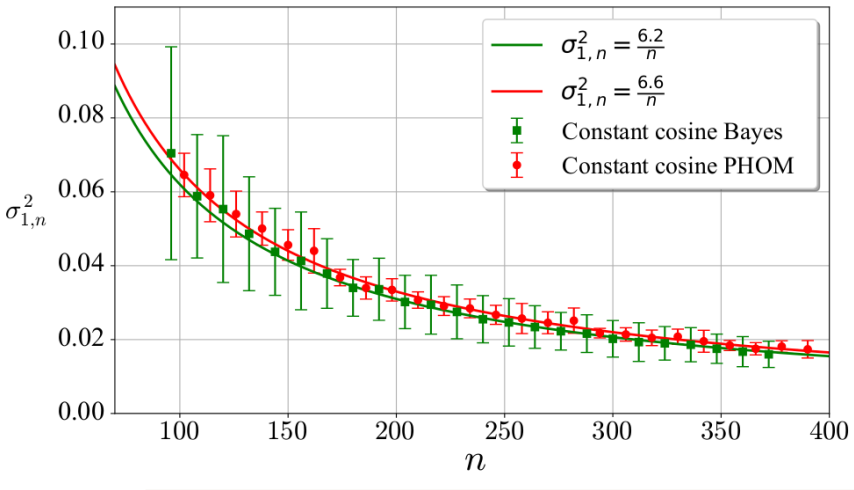

Figure 7.5: Constant cosine PHOM and Bayesian inference efficiencies. Behaviour of the variance of ϕ_1 obtained for the simulations of the constant cosine approach for both the PHOM (red circles) and the Bayesian inference (green squares) as a function of the number of measurements n. Solid lines represent fits of the numerical data obtained for both methods. The same behaviour is obtained for ϕ_2 and ϕ_3 (not shown).

From the results obtained, the Bayesian inference method as explained above does not offer much of an advantage as compared to the PHOM, since both have a similar efficiency with the number of measurements. In the end, this low efficiency is a consequence of both of these methods (i) being able only to scan one of the stabilisers at the same time and (ii) performing measurements in a non-adaptive way. In the following we will introduce and analyze the Bayesian marginal likelihood method, which provides an improvement in efficiency over both the PHOM and the constant cosine Bayesian inference method by solving both of these problems.

7.3.2.2 Marginal likelihood method

In this method, we select the control phases to obtain a likelihood that depends only on one of the phases that we want to estimate. Because of this, the probability distribution is a 1D function. We can follow this approach for each likelihood, updating three 1D probability distributions (one for each unknown phase) simultaneously with each measurement outcome.

Let us first consider measurements of the first stabiliser, whose likelihood is given by Eq. (7.28), focusing on the value of ϕ_2. To estimate this phase, we have two different control parameters, θ_1 and θ_2, that we can change before each measurement. We choose to perform a measurement under the constraint of keeping the value of $2(\theta_2 - \theta_1)$ fixed to a certain value θ_c while changing the value of $2(\theta_2 + \theta_1)$. With this choice, the containing $\phi_1 - \phi_3$ is fixed and assumes a constant value c_2. This yields the likelihood

$$P_1(\pm_{\boldsymbol{\theta}}|\phi_2) = \frac{2 \pm \cos[\phi_2 + 2(\theta_2 + \theta_1)] \pm c_2}{4}. \tag{7.30}$$

Now, for a second measurement we select θ_1 and θ_2 such that they fulfill the same constraint as before but shifted by $\pm\pi$, i.e. $2(\theta_2 - \theta_1) = \theta_c \pm \pi$. For this selection, the value of the second cosine term in Eq. (7.28) becomes $-c_2$ instead of c_2 and the likelihood is given by

$$P_1(\pm_{\boldsymbol{\theta}}|\phi_2) = \frac{2 \pm \cos[\phi_2 + 2(\theta_2 + \theta_1)] \mp c_2}{4}. \tag{7.31}$$

Therefore, if we fix $2(\theta_2+\theta_1)$ and perform such a combined pair of measurements under the discussed constraints, one with c_2 and another with $-c_2$, we can marginalize over c_2 to obtain the following marginal likelihood for each individual measurement

$$P_1(\pm_{\boldsymbol{\theta}}|\phi_2) = \frac{2 \pm \cos[\phi_2 + 2(\theta_2 + \theta_1)]}{4}, \tag{7.32}$$

which only depends on ϕ_2. After this pair of measurements, we then fix $2(\theta_2+\theta_1)$ to a new value and perform another pair of measurements in the same way as before. The key observation is that, as a result of this process, the likelihood obtained is similar to the one for the single-qubit case of Eq. (7.8). This allows one to directly generalise the analysis for the scaling of the variance from the single-qubit case (see Eq. (7.14) and 7.15) to ϕ_2 (see Appendix A.2) obtaining

$$\overline{\sigma^2_{2,n+1} - \sigma^2_{2,n}} = -\alpha_{2,n+1}\sigma^4_{2,n}, \tag{7.33}$$

where

$$\alpha_{2,n} \equiv \frac{\exp\left(\sigma^2_{2,n}\right)\sin^2(\overline{\phi}_{2,n} - \tilde{\theta}_{2,n+1})}{4 - \exp\left(\sigma^2_{2,n}\right)\cos^2(\overline{\phi}_{2,n} - \tilde{\theta}_{2,n+1})}, \tag{7.34}$$

and $\tilde{\theta}_{2,n} \equiv -2(\theta_{2,n} + \theta_{1,n})$. For small values of $\sigma^2_{2,n+1}$, $\alpha_{2,n+1}$ can be approximated by

(see Fig. 7.7)

$$\alpha_{2,n+1} \approx \frac{\sin^2(\bar{\phi}_{2,n} - \tilde{\theta}_{2,n+1})}{4 - \cos^2(\bar{\phi}_{2,n} - \tilde{\theta}_{2,n+1})}. \tag{7.35}$$

Note that in this two-plaquette case, in Eq. (7.35) a 4 appears in the denominator, as opposed to the 1 in the single-qubit case. Due to this, the quantity $\alpha_{2,n+1}$, which determines the decrease in the uncertainty, has a sinusoidal behaviour between 0 and 1/4. Note also that in constrast to the single-qubit case (cf. Fig. 7.3) this oscillatory behaviour does not disappear with an increasing number of measurements. Figure 7.7 shows that the decrease in the standard deviation is maximized if we choose $\tilde{\theta}_{2,n+1} = \bar{\phi}_{2,n} \pm \pi/2$, making this the optimal adaptive measurement selection. For this optimal choice the value of $\alpha_{2,n+1}$ is 1/4, for which the variance scales as $\sigma^2_{2,n} = 4/n$.

So far, in the explanation of the protocol we have focused on estimating ϕ_2. However, our protocol allows one to measure ϕ_1, ϕ_2 and ϕ_3 at the same time. Based on the adaptive way of selecting the measurements as explained above, we make the following selection,

$$\begin{cases} \tilde{\theta}_{1,n} \equiv -2(\theta_2 + \theta_5) = \bar{\phi}_1 + \beta_1 \\ \tilde{\theta}_{2,n} \equiv -2(\theta_2 + \theta_1) = \bar{\phi}_2 + \beta_2 \\ \tilde{\theta}_{3,n} \equiv -2(\theta_1 + \theta_5) = \bar{\phi}_3 + \beta_3 \end{cases} \tag{7.36}$$

where each β_j is either $\pi/2$ or $-\pi/2$. Making these selections fixes the following values

$$\begin{cases} 2(\theta_2 - \theta_5) = -\bar{\phi}_2 + \bar{\phi}_3 + \beta_3 - \beta_2 \\ 2(\theta_5 - \theta_1) = -\bar{\phi}_1 + \bar{\phi}_2 + \beta_2 - \beta_1 \\ 2(\theta_2 - \theta_1) = -\bar{\phi}_1 + \bar{\phi}_3 + \beta_3 - \beta_1 \end{cases} \tag{7.37}$$

Since the combinations of β_j appearing in Eq. (7.37) yield either $\pm\pi$ or 0, we choose the β-parameters in a way that we alternate between these values to marginalize over the value c_i appearing in each of the three likelihoods. This yields a likelihood equivalent to Eq. (7.32) for the measurement of each stabilizer. For the selection given by Eq. (7.36) it is guaranteed that our protocol realises adaptive optimal measurements while also having the benefit that in each measurement set one can use the measure obtained for each of the three stabilisers to update the corresponding probability distribution of each single phase at the same time, as opposed to the PHOM and the Bayesian inference with the constant cosine. Thus, the estimate of each phase will have a variance σ_n^2

Input: n copies of the state $|\psi'\rangle$
Output: List of estimated phases $\bar{\boldsymbol{\phi}} = \{\bar{\phi}_1, \bar{\phi}_2, \bar{\phi}_3\}$
and corresponding probability distributions $\mathcal{P} = \{P(\phi_1), P(\phi_2), P(\phi_3)\}$
• Define
$\boldsymbol{\theta} = \{\theta_1, \theta_2, \theta_5\}$ ▷ angles θ_k to perform rotations on qubit k
$\Pi = \{P_2(\pm_{\boldsymbol{\theta}}, \phi_1), P_1(\pm_{\boldsymbol{\theta}}, \phi_2), P_{12}(\pm_{\boldsymbol{\theta}}, \phi_3)\}$ ▷ likelihoods corresponding to ϕ_1, ϕ_2, ϕ_3
$\mathcal{S} = \{S_x^{(2)}, S_x^{(1)}, S_x^{(1)}S_x^{(2)}\}$ ▷ stabilizers corresponding to the likelihoods Π
• Set all probability distributions in $\mathcal{P}$ equal to $1/2\pi$
• Set all the angles in $\boldsymbol{\theta}$ equal to zero
for m **in** n **do**
• Rotate qubits $\mathcal{Q} = \{1, 2, 5\}$ along the Z axis by the angles in $\boldsymbol{\theta}$
• Measure the stabilizers in $\mathcal{S}$ and obtain the measurement set $\mathcal{M}$
for j in $J = 1, 2, 3$ **do** ▷ The set J corresponds to the indices of the phases in $\bar{\boldsymbol{\phi}}$
• Update the j-th probability in $\mathcal{P}$ with the j-th likelihood in Π
according to the j-th measurement in $\mathcal{M}$
• Compute the maximum of the j-th probability in $\mathcal{P}$ and denote it as $\bar{\phi}_j$
• Update the list of estimated phases with $\bar{\phi}_j$
end for
• Compute the new rotation angles in $\boldsymbol{\theta}$ by solving the linear system S

$$S = \begin{cases} 2(\theta_2 + \theta_5) = -\bar{\phi}_1 + \beta_1 \\ 2(\theta_2 + \theta_1) = -\bar{\phi}_2 + \beta_2 \\ 2(\theta_1 + \theta_5) = -\bar{\phi}_3 + \beta_3 \end{cases}$$

where each β_j is chosen alternately at each measurement between $\{+\pi/2, -\pi/2\}$
end for

Figure 7.6: Marginal likelihood Bayesian inference pseudocode. Pseudocode to determine the three phases, $\boldsymbol{\phi} = \{\phi_1, \phi_2, \phi_3\}$, appearing in the two-plaquette case of Sec. 7.3 by implementation of the marginal likelihood Bayesian inference method. This pseudocode can also be applied for estimating the seven phases appearing in the complete Steane code case of Sec. 7.4 after redefining $\boldsymbol{\phi}$, the list of unknown phases and their indices J; $\mathcal{P}$, their probability distributions; $\boldsymbol{\theta}$, the angles for the rotations of the measurements; Π, the likelihoods; $\mathcal{S}$ the list of stabilisers; $\mathcal{Q}$ the list of qubits to be rotated; the system of equations S according to Eq. (A.20) in Appendix A.1.

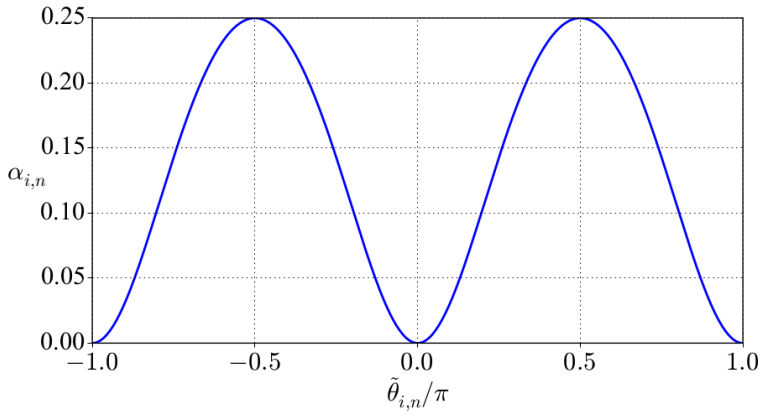

Figure 7.7: Adaptiveness of the marginal likelihood Bayesian protocol. Dependence of the factor $\alpha_{i,n}$ on $\tilde{\theta}_{i,n}$ for $i = 1, 2, 3$ (here $\bar{\phi}_{i,n-1} = 0$). $\alpha_{i,n}$ dictates the decrease of the variance step by step. $\alpha_{i,n}$ oscillates between 0 and 0.25 and its mean value is $(2 - \sqrt{3})/2 \approx 0.134$, with its maximum at $\tilde{\theta}_{i,n} = \bar{\phi}_{i,n-1} \pm \pi/2$. By Eq. (7.17), this is the optimal way of selecting $\tilde{\theta}_{i,n}$.

given by

$$\sigma_n^2 = \frac{4}{n}. \tag{7.38}$$

Finally, it is interesting to analyse by how much the efficiency of the protocol would decrease if one did not make an adaptive choice of the parameters. If one selected the values $\tilde{\theta}_{i,n}$ randomly, then $\alpha_{i,n}$ would have a mean value equal to $\overline{\alpha}_{i,n} = (2 - \sqrt{3})/2 \approx 0.134$, which is readily obtained by integrating Eq. (7.35) over a uniform probability distribution of $\tilde{\theta}_{i,n}$. Taking into consideration Eq. (7.17) the scaling of the variance in such a non-adaptive protocol would be given by

$$\sigma_{i,n}^2 \approx \frac{1}{0.134n} \approx \frac{7.5}{n}. \tag{7.39}$$

From these results we can see the reasons behind this marginal likelihood method having a better efficiency than the PHOM or direct Bayesian inference. First, the marginal likelihood method can update the information from each unknown phase by measuring the stabilisers in the same copy of the quantum state, while the other two methods can only measure one of the phases with each copy. Second, with the marginal likelihood method we found a rule to perform adaptive measurements, reduc-

ing even more the number of measurements needed as compared to the PHOM and direct Bayesian inference.

The marginal likelihood method, which is shown in this section for the two-plaquette intermediate case, can be directly generalised for the correction of the seven unwanted phases appearing in the Steane code logical states, as we will explain in the following.

7.4 Correction of the full Steane code

The correction of the unwanted phases in the Steane code logical states (see Eq. (7.1) for the $|0'\rangle_L$ case) can be done with a generalisation of the marginal likelihood method from Sec. 7.3.2.2. This is obtained directly by considering that now we have seven unwanted phases and that to estimate them we can perform measurements of different combinations of stabilisers: $S_x^{(1)}$, $S_x^{(2)}$, $S_x^{(3)}$, $S_x^{(1)}S_x^{(2)}$, $S_x^{(1)}S_x^{(3)}$, $S_x^{(2)}S_x^{(3)}$ and $S_x^{(1)}S_x^{(2)}S_x^{(3)}$. For example, the marginal likelihood for the measurement of the first stabiliser is

$$P_1(\pm_{\boldsymbol{\theta}}|\phi_2) = \frac{4 \pm \cos\Big(\phi_2 - \tilde{\theta}_2\Big)}{8}, \tag{7.40}$$

where $\tilde{\theta}_2 \equiv -2(\theta_1 + \theta_2 + \theta_3 + \theta_4)$. Similar expressions are obtained for the other six combinations of stabilisers (see A.1). From these likelihoods we can study the behaviour of the variance as a function of the measurements. The variance and the values of α for each angle ϕ_i for the next step $n+1$ ($\alpha_{i,n+1}$) are given by (see Appendix A.2)

$$\overline{\sigma_{i,n+1}^2 - \sigma_{i,n}^2} = -\alpha_{i,n+1}\sigma_{i,n}^4, \tag{7.41}$$

with

$$\alpha_{i,n+1} = \frac{e^{\sigma_{i,n}^2}\sin^2(\overline{\phi}_{i,n} - \tilde{\theta}_{i,n+1})}{16 - e^{\sigma_{i,n}^2}\cos^2(\overline{\phi}_{i,n} - \tilde{\theta}_{i,n+1})}. \tag{7.42}$$

For small values of $\sigma_{i,n}^2$ one finds

$$\alpha_{i,n+1} \approx \frac{\sin^2(\overline{\phi}_{i,n} - \tilde{\theta}_{i,n+1})}{16 - \cos^2(\overline{\phi}_{i,n} - \tilde{\theta}_{i,n+1})}. \tag{7.43}$$

The maximum value of each $\alpha_{i,n+1}$ is $1/16$ for $\tilde{\theta}_{i,n+1} = \bar{\phi}_{i,n} \pm \pi/2$. This rule ensures an adaptive way of selecting the measurements that yields more information than a

non-adaptive selection and gives the scaling

$$\sigma_n^2 = \frac{16}{n} \tag{7.44}$$

for the variance of the estimate for each phase measured.

Now that we have generalised the marginal likelihood method to the full Steane code case, we are only left with studying how much does our method improves the efficiency compared to the PHOM. For this we simulated several times a PHOM process for the Steane code $|0'\rangle_L$ state in Eq. (7.1). From the errors of these estimates we estimated the variance of the method. As for the variance of the marginal likelihood method, obtaining the variance is much simpler since an advantage of performing Bayesian inference is that the information of the unknown parameter is contained in a probability distribution from which one can directly obtain a variance.

7.4.1 PHOM simulations

For the numerical simulations of the PHOM, we initially fix the number of iterations I to be performed as explained in step (4) of Sec. 7.3.1 and we choose a number n of copies of the initial quantum state that we can measure. We then choose $\mathcal{N}$ different 7-dimensional vectors representing the seven initially unknown phases $\boldsymbol{\phi}^{(k)}$ $(k = 1, ..., \mathcal{N})$. We perform the PHOM following Sec. 7.3.1 and the expressions (A.4) to (A.11) in A.1 in order to obtain an estimate of the seven phases $\boldsymbol{\phi}_{\text{est}}^{(k)}$. For each of the vectors, we calculate the difference between the estimated phases and the phases chosen initially: $\boldsymbol{\phi}_{\text{est}}^{(k)} - \boldsymbol{\phi}^{(k)}$. We finally compute an estimate of the variance of the PHOM for a given n and a fixed number of iterations I as

$$\sigma_n^2 = \frac{1}{\mathcal{N}} \sum_{k=1}^{\mathcal{N}} (\boldsymbol{\phi}_{\text{est}}^{(k)} - \boldsymbol{\phi}^{(k)})^2, \tag{7.45}$$

where $\mathcal{N}$ is a large number to obtain a good estimate of σ_n^2, in our case $\mathcal{N} = 50000$. To perform the scans of each stabiliser we divide the intervals $[-\pi, \pi]$ of the angles θs into $M = 10$ points. Since we have to measure seven stabilisers, the number of measurements per point (mpp) we can perform is mpp $= n/(7MI)$. Repeating this process using a different n and $I = 1, \ldots, 4$ yields the data plotted with circles in Fig. 7.8.

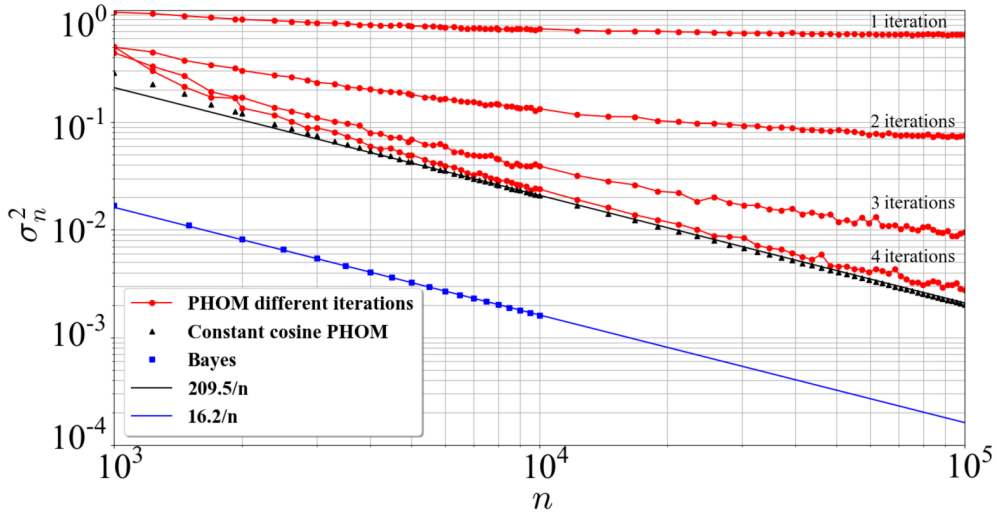

Figure 7.8: Efficiency of the PHOM (original and constant cosine versions) and marginal likelihood Bayesian protocol. Behaviour of the variance as a function of the total number of measurements n. Only for the PHOM, the total number of measurements is given by $n = 7 \cdot M \cdot I \cdot \text{mpp}$, where 7 corresponds to the number of phases to be estimated, M is the number of division of the interval $[-\pi, \pi]$ of each phase, I is the number of iterations used for the PHOM, and mpp is the number of measurement for each of the M divisions. For the PHOM using constant cosines a behaviour of $\sigma_n^2 = (209.5 \pm 0.5)/n$ is obtained. The PHOM shows a similar behaviour when using enough iterations for the method to converge. Finally, using marginal Bayes the performance is $\sigma_n^2 = (16.2 \pm 0.1)/n$. Error bars for results of the constant cosine PHOM and the Bayes method are smaller than the symbol size.

A similar process is done for the constant cosine PHOM, where in this case it is simpler because this method only requires one iteration (see Sec. 7.3.1). The results obtained for this case are represented by the triangles in Fig. 7.8, where performing a fit of the relation between the variance and the number of measurements for the constant cosine PHOM yields a behaviour of $\sigma_n^2 = (209.5 \pm 0.5)/n$.

From the results obtained, we can see that as the number of iterations used for the PHOM increases, the variance with the number of resources decreases until reaching a similar behaviour as that of the constant cosine PHOM. This is due to the PHOM having two limitations, one given by the number of iterations and another by the finite number of measurements used for each scan. If a small number of iterations is used, most of the PHOM simulations do not converge and the result is a wrong estimation

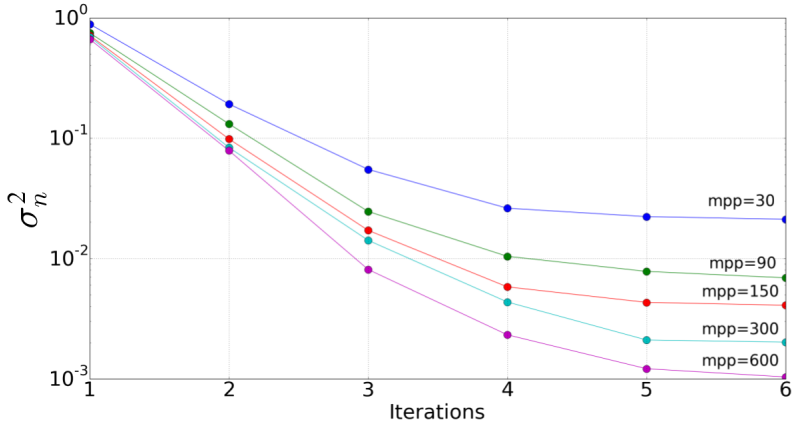

Figure 7.9: Convergence of the PHOM. Behaviour of the variance for increased number of iterations of the PHOM algorithm. In each iteration the mean values of each stabiliser combination are reconstructed by performing a scan measuring an interval of length π divided in ten points and performing a fixed amount of measurements per point (mpp) for each of these divisions. The variance approaches a constant value after several iterations. This is due to the finite number of mpp introducing a constant statistical noise. As the number of mpp increases this noise decreases.

for the phases which results in a big variance. As the number of iterations increases, more simulations converge to a correct phase and the variance obtained decreases. After performing enough iterations, all the simulations converge and the only source of error is the number of measurements used for each scan. As this number increases, the statistical error of each scan performed decreases yielding a better estimate of each phase. This behaviour is represented in Fig. 7.9. Thus, the constant cosine PHOM will always be the lower bound for the variances of the PHOM and we will focus on it for the comparison with the marginal likelihood method.

7.4.2 Marginal likelihood Bayes simulations

To obtain the behaviour of the variance with the number of measurements for the marginal likelihood Bayes inference method we apply a generalisation of the method shown in the pseudocode of Fig. 7.6 with the expressions (A.12) to (A.20) in Appendix A.1. After performing enough measurements ($n \approx 100$) the probability distribution obtained can be approximated by a normal probability distribution for each of the phases that is used for computing the variances and for estimating the error

of this adaptive technique. The results for the variances are shown in Fig. 7.8 where the data is plotted with squares. It can be seen that the variance decreases as the number of measurements used increases. A numerical fit of the data obtained reveals that the variance decreases as $\sigma_n^2 = (16.2 \pm 0.1)/n$, as was expected from the analytical derivation of the method in Sec. 7.4.

7.5 Summary

In this chapter we have explained our work on the derivation of an adaptive Bayesian protocol to measure systematic phase shift errors appearing in the experimental preparation of multi-qubit states. It is important to note that having modelled the errors appearing in these states as only unwanted relative phases allows us to focus on this type of errors instead of forcing us to do a complete state tomography (as explained in Sec. 2.5) that would require a considerable amount of measurements for obtaining information about both the phases and the populations. In our case, we have aimed the protocol at the correction of errors appearing in the logical states of the Steane code. This method is capable of finding, by a simple analytical rule, the measurement settings that maximise the information gained at each measurement step. The simplicity of this rule saves computational power that would otherwise be needed to estimate numerically the optimal measurement at each step of the protocol.

We compared our method to the PHOM, a non-adaptive phase estimation method based on a generalisation of a Ramsey experiment for multi-qubit states that was recently demonstrated for the Steane code [51]. We simulated both methods to measure quantum phases appearing in the preparation of quantum states needed for the Steane code. The efficiency obtained by simulation of our method is in agreement with the efficiency derived from the theoretical calculations. It shows a reduction of the measurement time by more than one order of magnitude when compared with the PHOM (see Fig. 7.10). We notice that although there are methods that yield a better efficiency than the Standard Quantum Limit (SQL) [172–175], these methods rely on the non-trivial implementation of multi-qubit gates which we do not consider here. However, it might be interesting to generalise our protocol to these kind of techniques.

A very important conclussion is that this type of Bayesian methods can be generalised to other systematic errors appearing in any kind of multi-qubit states, regardless

	PHOM	PHOM constant cosine	BAYES marginal likelihood
Variance σ^2	$\sim 224/n$	$(209.5 \pm 0.5)/n$	$(16.2 \pm 0.1)/n$
Efficiency relative to PHOM	1	$\sim$1	$\sim$13

Figure 7.10: Efficiency comparison. Comparison of the efficiencies among the different methods studied to measure phases for the three-plaquette case. For the PHOM case the results for the optimal selection of iterations have been used.

the physical platform used to create that quantum state such as, e.g. trapped ions, Rydberg atoms in optical lattices or tweezer arrays, and other AMO and solid-state architectures.

Given the success of this Bayesian approach for estimating and correcting unwanted phases, it is interesting to see how a similar approach can be used to calibrate quantum gates used in the experiment. This is the problem that we will study in Chapters 8 and 10, where we will respectively show advantages of using Bayesian protocols for calibrating single-qubit gates and entangling gates.

Chapter 8

Bayesian laser frequency locking

In this chapter we explain the derivation and the results from the experimental implementation of a Bayesian inference protocol aimed at the estimation of laser frequencies and magnetic fields in a trapped-ion architecture. A calibration of these parameters is vital for the correct implementation of operations in trapped-ion systems. In particular, the implementation of single-qubit operations depends on the application of a laser field with a frequency resonant to the qubit transition, as discussed in Sec. 4.3. It is also highly desirable to lock this frequency to the transition frequency not at a single point in time, but at all times [176, 177]. In order to achieve this, our protocol can be performed at different times in order to obtain an estimation of the drifts of these parameters over time. Using these estimates, one can compensate the drifts, thus obtaining a dynamic frequency lock of the laser to the transition frequency.

The Bayesian inference protocol that we show here can be completely automated, which allows a computer to perform the calibration of these experimental parameters without requiring supervision from personnel of the laboratory. On top of this, the protocol uses simple analytical rules to select optimal measurement settings that yield the most information about the desired parameters. Finally, since the Bayesian approach takes into account all the measurements performed, this protocol does not suffer from the so-called *fringe hopping errors* that can appear in a frequentist approach to Ramsey spectroscopy, and that we will explain in Sec. 8.2.

This work was performed during a visit to the University of Innsbruck, in collaboration with Marc Bußjäger, who was a master student at the time. A version of the

results of this work, more focused on the experimental details, can be found in his master thesis [178].

We begin this chapter by explaining our goal in Sec. 8.1, where we introduce the parameters to be calibrated, and highlight their importance for the experiment. In Sec. 8.2, we introduce the Ramsey cycle commonly employed for the calibration of these parameters, using a frequentist approach. We then explain its extension to a Bayesian inference protocol in Sec. 8.3. In Sec. 8.4 we show the results from the experimental implementation of our Bayesian protocol. Finally, in Sec. 8.5 we provide a summary of the results from this chapter.

8.1 Laser frequency locking

The correct performance of a trapped-ion quantum computer depends on tuning a laser field to a frequency that is resonant with the qubit transition. As can be seen from the results shown in Sec. 4.3, having a non-zero detuning of the laser's frequency ω_L with respect to the qubit transition ω_{eg}, that is

$$\Delta = \omega_{eg} - \omega_L \neq 0, \tag{8.1}$$

introduces errors in the quantum operations of trapped-ion qubits. Indeed, this non-resonant laser frequency introduces an unwanted σ_z component to the Hamiltonian describing the evolution of a trapped-ion qubit under the effect of the laser field. Due to this, it is important to realise a calibration process to reduce the detuning as much as possible. A Rabi spectroscopy [44, 178, 179] may provide an initial calibration of the laser's frequency, which can then be followed by a Ramsey spectroscopy process, which will be explained in detail in Sec. 8.2.

After the initial calibration, undesired time-dependent effects may still introduce a detuning. An example of this is a frequency drift due to the heating of the cavity of the laser over time. Due to this drift, which we will consider to be constant in time, the laser's frequency will grow linearly in time as

$$\omega_L(t) = \omega_{L,0} + \dot{\omega}_L \cdot t, \tag{8.2}$$

where $\omega_{L,0}$ is the initial frequency of the laser and $\dot{\omega}_L$ is the drift.

Another source of errors is a drift of the magnetic field $B(t)$ experienced by the qubits and which we consider to be given by

$$B(t) = B_0 + \dot{B} \cdot t. \tag{8.3}$$

Similarly to the previous case, B_0 is the initial magnetic field and $\dot{B}$ represents the constant drift. This causes a Zeeman shift of the levels of the ion, effectively changing the transition frequency of the qubit over time. The change in the transition frequency introduced by the Zeeman shift will be given by the difference between the shifts suffered by the excited state and the ground state (see Eq. (4.18)). In particular

$$\Delta\omega_{eg,Z}(t) = -\frac{1}{2}\frac{\mu_B\, B(t)}{\hbar}\left(g_D - g_S\right), \tag{8.4}$$

for the trapped-ion qubit transition $4S_{1/2}(m = -1/2) \leftrightarrow 3D_{5/2}(m = -1/2)$—which we denote as $(-1/2, -1/2)$ from now on. As a consequence, the qubit transition frequency will grow linearly in time

$$\omega_{eg}(t) = \omega_{eg,0} + \Delta\omega_{eg,Z}(t), \tag{8.5}$$

from the transition frequency of the qubit without Zeeman shifts $\omega_{eg,0}$.

In order to correct these drifts, one could periodically measure and correct the detunings. However, this requires a considerable amount of time and the detuning still accumulates between calibrations. In order to reduce the impact of these problems, one can obtain an estimate of the drifts and compensate for them over time. To do this, we can consider the auxiliary transition $4S_{1/2}(m = -1/2) \leftrightarrow 3D_{5/2}(m = -5/2)$, which we denote as $(-1/2, -5/2)$. This transition will suffer a Zeeman shift

$$\Delta\omega_{\mathrm{aux},Z}(t) = -\frac{\mu_B B(t)}{\hbar}\left(\frac{5}{2}g_D - \frac{1}{2}g_S\right), \tag{8.6}$$

which modifies the transition frequency

$$\omega_{\mathrm{aux}}(t) = \omega_{eg,0} + \Delta\omega_{\mathrm{aux},Z}(t). \tag{8.7}$$

The detuning of the laser with respect to these two transitions at a given time, $\Delta(t)$ and $\Delta_{\mathrm{aux}}(t)$, can be measured and, since each transition has a different sensitivity to

the magnetic field, one may obtain the detuning resulting from the laser's drift, and the one resulting from the Zeeman shift. These measurements can be repeated over time to obtain an estimate of the drifts, which can then be used to lock the laser frequency to the qubit transition.

As explained before, the detunings can be obtained from Ramsey spectroscopy, which is usually performed in a frequentist manner. However, in this work we integrate the Ramsey spectroscopy in a Bayesian inference process. In the following sections we explain the Ramsey spectroscopy process in the frequentist and the Bayesian approach.

8.2 Frequentist Ramsey spectroscopy

A Ramsey sequence consists in applying two $\pi/2$-pulses to a qubit, each of them around a rotation axis located on the equator of the Bloch sphere, separated by a waiting time τ_R. Assuming an initial state $|g\rangle$, and a detuning Δ between the laser and the qubit transition, which is much smaller than the Rabi frequency, $\Delta \ll \Omega$, the final state of the qubit will be

$$|\psi_f\rangle \approx U_{\phi_2}\left(\frac{\pi}{2}\right) e^{-i\Delta\cdot\tau_R\sigma_z} U_{\phi_1}\left(\frac{\pi}{2}\right)|g\rangle\,. \tag{8.8}$$

The angles ϕ_1 and ϕ_2 indicate the rotation axis of each of the $\pi/2$ pulses. If $\phi_1 = \phi_2$ and $\Delta = 0$, the final state would be $|e\rangle$. As we introduce some detuning, we will measure some population in the $|g\rangle$ state. It is therefore possible to extract information about a detuning by performing Ramsey sequences, as shown in Fig. 8.1.

For a more precise modeling of the calibration process, we have to consider situations in which the detuning is not small compared to the Rabi frequency. In this case the $\pi/2$-pulses will not be rotations around an axis in the equator of the Bloch sphere, since their rotation axis will have a Z component. Moreover, the duration of the gates, $\tau_{\pi/2}$, which was obtained assuming $\Delta = 0$, will not even be that of a correct $\pi/2$-pulse for this case. When including these effects into the sequence, one obtains that the likelihood of measuring the $|e\rangle$ state at the end is given by [119]

$$\begin{aligned} P\left(|e\rangle\,|\Delta,\tau_R,\phi\right) = \frac{4\Omega^2}{\tilde{\Omega}^2}\sin^2\left(\frac{\tilde{\Omega}\tau_{\pi/2}}{2}\right)\Bigg[\cos\left(\frac{\tilde{\Omega}\tau_{\pi/2}}{2}\right)\sin\left(\frac{\Delta\tau_R+\phi}{2}\right) \\ -\frac{\Delta}{\tilde{\Omega}}\sin\left(\frac{\tilde{\Omega}\tau_{\pi/2}}{2}\right)\cos\left(\frac{\Delta\tau_R+\phi}{2}\right)\Bigg]^2. \end{aligned} \tag{8.9}$$

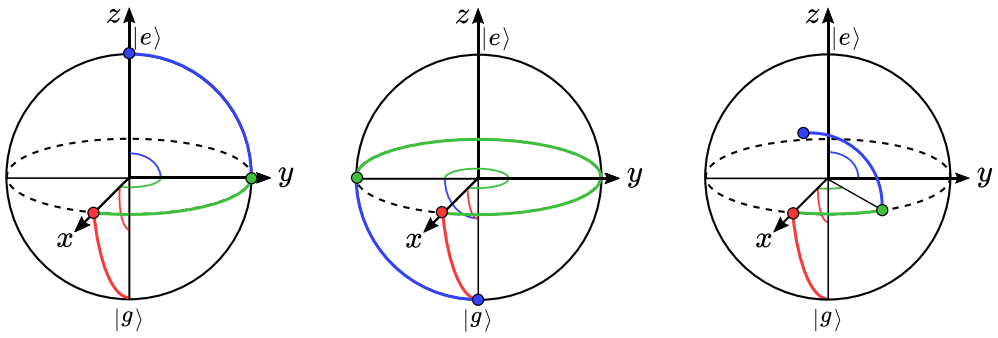

Figure 8.1: Ramsey sequences. In a Ramsey sequence, two $\pi/2$-pulses are applied with a waiting time τ_R in between them to obtain information about a detuning Δ. Left: The first rotation (red) is selected to be a $\pi/2$ rotation around the Y axis. This state then evolves by rotating around the Z axis by an angle $\Delta \cdot \tau_R$ (green), which in this case is $\pi/2$. Finally, a rotation around the X axis brings the qubit to the $|e\rangle$ state (blue). Middle: Similar case but with $\Delta \cdot \tau_R = 3\pi/2$, which causes the final rotation to bring the qubit to the initial state, $|g\rangle$. Right: An arbitrary waiting time for the sequence causes the final state to be in a superposition of $|g\rangle$ and $|e\rangle$.

where $\phi = \phi_2 - \phi_1$ and $\tilde{\Omega} = \sqrt{\Omega^2 + \Delta^2}$.

It is important to note that Eq. (8.9) is just an approximation. In the experiment, the qubit will be subject to amplitude and phase damping, each of them characterised by a relaxation (T_1) and coherence (T_2) time, respectively. In the experimental setup used, phase damping errors dominate the amplitude damping ones, that is $T_2 \ll T_1$. Therefore, we will only consider phase damping, although the amplitude damping could be included too. When one accounts for dephasing, the likelihood becomes

$$P_{T_2}\left(|e\rangle \,|\Delta, \tau_R, \phi\right) = \frac{1}{2} + \left(P\left(|e\rangle \,|\Delta, \tau_R, \phi\right) - \frac{1}{2}\right) e^{-\frac{\tau_R}{T_2}}. \tag{8.10}$$

However, if we limit the Ramsey sequences to waiting times $\tau_R \ll T_2$, we can work with Eq. (8.9).

A frequentist approach for using Ramsey sequences to estimate the detuning of the laser consists in performing a scan over the detuning, while measuring the expected populations of the qubit after a Ramsey sequence, for a fixed waiting time and phase $\phi = 0$ between the $\pi/2$-pulses. These results are fit to Eq. (8.9) in order to see when the probability of measuring the $|e\rangle$ state is maximised. The maximum corresponds to the situation where the detuning is zero.

It is important to explain the role of the waiting time during a Ramsey scan. As

can be seen in Fig. 8.2, a longer waiting time results in the appearance of more of the so-called Ramsey fringes in the scan. The zero detuning case will be related to the position of the maximum of one of these fringes (and the phase between the $\pi/2$-pulses), thus, if the range of detunings used for the scan is too small, it might not be possible to distinguish which one is the correct fringe. It is therefore important to select an appropriate waiting time for the range of frequencies under consideration.

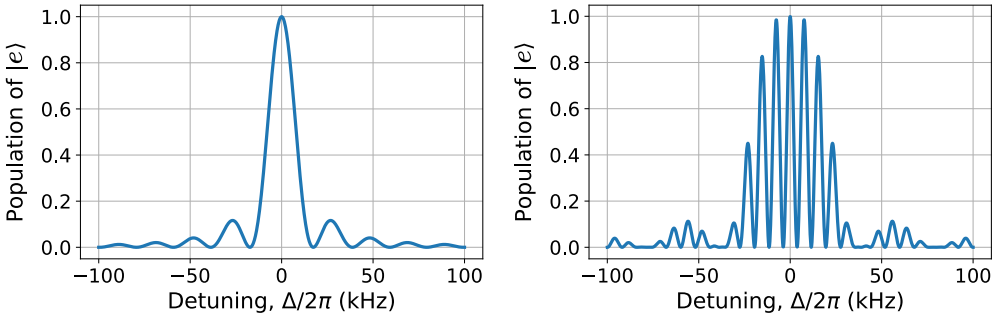

Figure 8.2: Ramsey fringes. Probability of measuring the state $|e\rangle$ after a Ramsey sequence obtained from Eq. (8.9) with $\Omega = 2\pi \cdot 10\text{kHz}$ and $\phi = 0$. Left: For this case the waiting time is zero, which makes the sequence equivalent to that of a Rabi scan. Right: In this case the waiting time is $\tau_R = 100\mu\text{s}$, and we can see the appearance of several Ramsey fringes.

While the previous method is valid for estimating and correcting the detuning, it can require a large amount of measurements. An alternative frequentist method for estimating the detuning can be realised when an initial, but perhaps not very precise, calibration has been performed. Here, even though the value of the detuning might be unknown, its range is established as $\Delta \ll \Omega$. In this case one can select an initial short waiting time and obtain two data points for the expected values of the populations with $\phi = \pm\pi/2$. Since the waiting time is small, this amounts to sampling two symmetric points around a unique Ramsey fringe. For zero detuning, the expected value of the populations are measured around symmetric points around the center of the Ramsey fringe, which results in 0.5 for both data points. However, if there is a detuning, this symmetry is broken, yielding different expected values for each point. This asymmetry can be used to correct the detuning, moving closer to the center of the Ramsey fringe. Once a first step is completed, one can repeat the process for a longer waiting time,

for which the central Ramsey fringe becomes narrower. This can be used for a more precise measurement of the detuning, but the increased waiting time has an upper limit in order to not overlap other non-central Ramsey fringes in the error interval of our detuning, which may result in the protocol using one of the non-central Ramsey fringes. This error in the calibration protocol is called *fringe hopping*, and leads to errors in the estimated detuning. Therefore, the final protocol consists in measuring two data points with $\phi = \pm\pi/2$ for an initially small waiting time, correcting the detuning according to the results, and repeat this process while slowly increasing the waiting time at each step. This ensures that we do not suffer from fringe hopping errors, while effectively increasing the precision of the measurements.

8.3 Bayesian Ramsey spectroscopy

The frequentist approach for the Ramsey spectroscopy is a relatively complex protocol in which one increases the waiting time after each step in an specific way in order to avoid fringe hopping. In contrast, the Bayesian inference protocol only depends on performing measurements and updating the prior distribution with the likelihood of the outcomes. To begin with the Bayesian inference protocol, we need a prior distribution of the detuning, $P(\Delta)$, which will model our knowledge of this parameter at the beginning of the protocol. In our case, we consider a rectangular prior distribution defining a range of possible values in the interval $[-\Delta_{\max}, \Delta_{\max}]$

$$P(\Delta) = \begin{cases} \frac{1}{2\Delta_{\max}}, & \Delta \in [-\Delta_{\max}, \Delta_{\max}] \\ 0, & \text{otherwise} \end{cases} . \tag{8.11}$$

However, the prior distribution can be adapted to other distributions, such as a normal distribution, depending on our prior knowledge. Once we have defined this prior, we just need to perform measurements and update it. This will be done by using the likelihood as defined by Eq. (8.9) (or Eq. (8.10)). Since the possible outcomes are binary, the associated likelihood for the outcome m is

$$P(m|\Delta, \tau_R, \phi) = \begin{cases} P\left(|e\rangle\,|\Delta, \tau_R, \phi\right), & m = |e\rangle \\ 1 - P\left(|e\rangle\,|\Delta, \tau_R, \phi\right), & m = |g\rangle \end{cases} . \tag{8.12}$$

While it is possible to select different parameters for each individual Ramsey cycle,

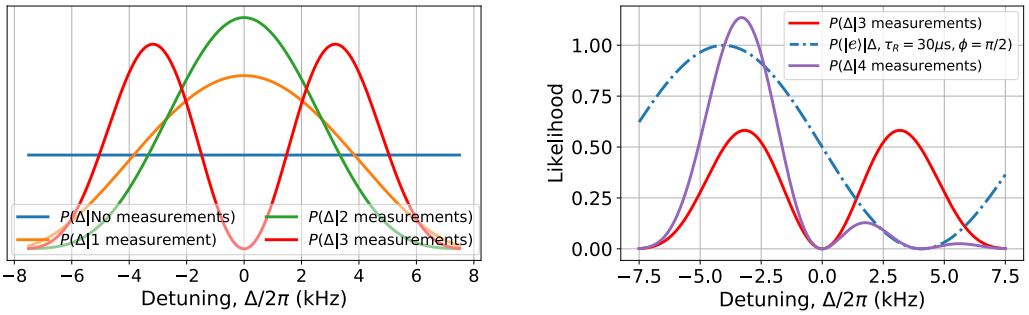

Figure 8.3: Bayesian inference updates. Example of how the information is updated after individual measurements performed with $\Omega = 2\pi \cdot 10\text{kHz}$, $\tau_R = 30\mu\text{s}$, and a detuning of $\Delta = -2\pi \cdot 2.5\text{kHz}$. The distributions shown are not normalised for clarity in the figure. Left: The distribution before any measurements is assumed to be a constant distribution defined in the interval shown. If the result of the first measurement, obtained for $\phi = 0$, is $|e\rangle$, the prior is updated by using the likelihood of that measurement to obtain the posterior (orange). If a second measurement returns the same outcome, the posterior is updated using the same likelihood as before (green). As a consequence, the posterior gets narrower. If for the third measurement a $|g\rangle$ state is measured, and since the likelihood associated to this outcome attributes a zero probability to the case of $\Delta = 0$, the posterior is divided into two peaks. Right: By changing ϕ to $\pi/2$, if the outcome of the next measurement is $|e\rangle$, we can update our posterior to distinguish which one of the two peaks is more probable.

changing the measurement settings requires time in the experiment, and doing this would considerably slow the calibration process. Therefore, we will consider the same configuration for n_{exp} measurements. In this case we will obtain n_g measurements of the $|g\rangle$ state and $n_e = n_{\text{exp}} - n_g$ measurements of $|e\rangle$. To avoid long notation, we introduce $\mathcal{M}_t = \{\tau_{R,t}, \phi_t, n_{g,t}, n_{e,t}\}$ in order to specify the experimental configuration and outcomes of a set of $n_{\text{exp}} = n_{g,t} + n_{e,t}$ measurements, where $t = 1, ..., T$ will be one of the total T sets of measurements. Consequently, the prior distribution after t sets of measurements, $P(\Delta|\mathcal{M}_{1:t})$, will be updated as

$$P(\Delta|\mathcal{M}_{1:t}) \propto P(|g\rangle\,|\Delta, \mathcal{M}_t)^{n_{g,t}} \cdot P(|e\rangle\,|\Delta, \mathcal{M}_t)^{n_{e,t}} \cdot P(\Delta|\mathcal{M}_{1:t-1}), \tag{8.13}$$

which defines the Bayesian inference process for the Ramsey spectroscopy. An example of this process with $n_{\text{exp}} = 1$ is shown in Fig. 8.3.

Until now we have explained how to measure and update a prior distribution based on an experimental setup consisting of a waiting time and a relative angle between the

$\pi/2$-pulses. Note that we have not commented yet upon how to select the measurement configurations. These are degrees of freedom of the protocol that we can take advantage of in order to obtain a more accurate estimate of the detuning, while requiring less measurements. In the following, we will study the adaptivity of our method by considering the total number of measurements n performed in the t sets of measurements, and finding the optimal measurement setting for the next single measurement update, $n+1$. We will then use this resulting measurement setting for the whole set of measurements $t+1$. This simplifies the study, since we will consider only binary outcomes of the $n+1$ measurement, instead of the $2^{n_{\text{exp}}}$ possible outcomes in the $t+1$ set of measurements.

After performing t sets of measurements, we can consider the probability distribution of the detuning to be approximated by a normal distribution

$$P_n(\Delta) = P(\Delta|\mathcal{M}_{1:t}) \approx \frac{1}{\sqrt{2\pi\sigma_n^2}} \cdot \exp\left(-\frac{\Delta^2}{2\sigma_n^2}\right), \tag{8.14}$$

where σ_n^2 is the variance after these n measurements. We consider this normal distribution to be centered around $\Delta = 0$, which can always be the case if after each set of measurements we correct the detuning by subtracting the estimated value of the detuning. Additionally, we assume that σ_n^2 is sufficiently small so that $\sigma_n \ll \Omega$, and that the waiting time selected for the next measurement satisfies $\tau_{R,n} \ll T_2$. In this case, the likelihood of a $|e\rangle$ measurement of the next set can be approximated by

$$P(|e\rangle\,|\Delta, \tau_{R,n+1}, \phi_{n+1}) \approx \frac{1+\cos\left(\Delta\cdot\tau_{R,n+1}+\phi_{n+1}\right)}{2}. \tag{8.15}$$

The expected decrease in the variance obtained from this likelihood, and the one corresponding to a $|g\rangle$ outcome, is given by (see Appendix A.3)

$$\overline{{\sigma^2}_{n+1} - {\sigma^2}_n} = -\frac{e^{-\sigma_n^2\tau_{R,n+1}^2}\sigma_n^4\tau_{R,n+1}^2\sin^2(\phi_{n+1})}{1-e^{-\sigma_n^2\tau_{R,n+1}^2}\cos^2(\phi_{n+1})}. \tag{8.16}$$

From the latter, one can obtain that the optimal measurement settings for the $n+1$ measurement are given by

$$\begin{aligned} \tau_{R,n+1}^{\text{opt}} &= 1/\sigma_n, \\ \phi_{n+1}^{\text{opt}} &= \pm\frac{\pi}{2}. \end{aligned} \tag{8.17}$$

By a closer inspection of the likelihood, one can get an intuitive understanding of why these measurement settings are optimal, and a representation of this is shown in Fig. 8.4: Choosing $\phi_{n+1} = \phi_{n+1}^{\text{opt}}$ ensures that the likelihood is asymmetric on the position of the maximum of the prior distribution. This is done to ensure that the posterior distribution is kept as a single located zone in the parameter space. If we were to use $\phi_{n+1} = 0$, then the minimum of the Ramsey fringe would be located at the position of the maximum of the prior, which could divide the distribution in two peaks in the posterior for a $|g\rangle$ outcome, which is an unwanted behaviour. In the case where the prior is not centered around zero, that is, $\overline{\Delta}_n \neq 0$, this condition would be given by (see Appendix A.3)

$$\phi_{n+1}^{\text{opt}} = \pm\frac{\pi}{2} - \overline{\Delta}_n \, \tau_{R,n+1}^{\text{opt}} = \pm\frac{\pi}{2} - \frac{\overline{\Delta}_n}{\sigma_n}. \tag{8.18}$$

As for the waiting time, if we were to choose $\tau_{R,n+1}$ too small then the update would not have a considerable effect on reducing the variance. If otherwise, the waiting time is too large, then the update would divide the prior normal distribution in several peaks, which is not a desired behaviour either. However, setting the waiting time to $\tau_{R,n+1}^{\text{opt}}$ we manage to set the periodicity of our likelihood to the scale of our prior, which minimises the standard deviation of the posterior.

As explained, these are the optimal measurement settings for the $n+1$ measurement. However, we will use these settings for all the measurements in the $t+1$ iteration of the algorithm, since changing them for each measurement in this iteration would be prohibitively slow in the experimental implementation. After the $t+1$ iteration is complete, we will then obtain a new set of measurement settings for the $t+2$ iteration and so on.

Since we just learnt how to select the parameters of the Ramsey sequence, we have now all the components to perform the Bayesian inference protocol, which will be as follows:

1. Define the initial prior distribution $P(\Delta)$ as in Eq. (8.11) or as another probability distribution that models the initial knowledge about the detuning.

2. Select a waiting time for the initial set of measurements, $\tau_{R,t}$ with $t = 1$, small enough so that the first posterior does not have several peaks.

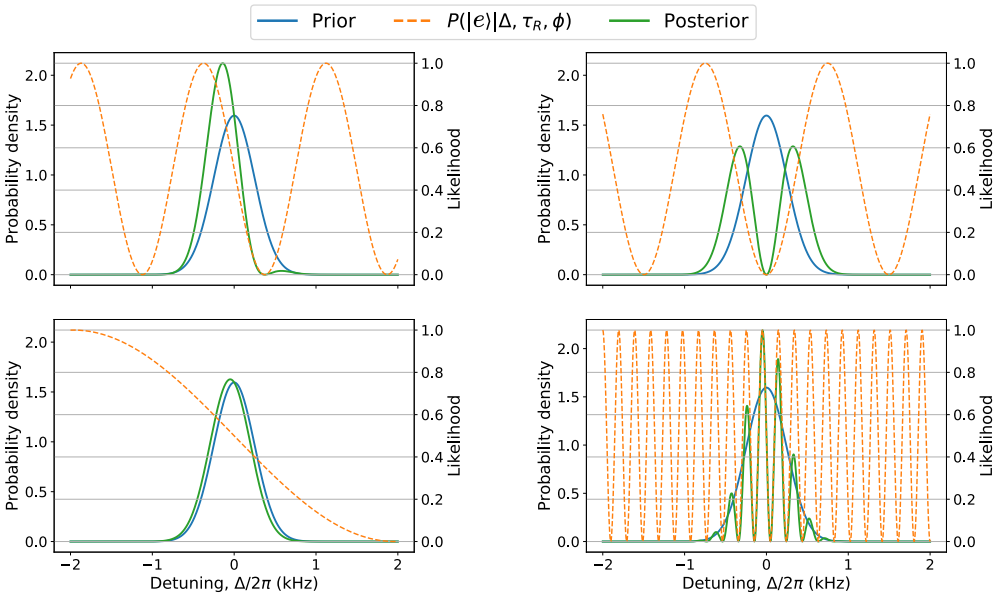

Figure 8.4: Optimal measurement setup. Different measurement settings for a Bayesian Ramsey cycle update with $\Omega = 2\pi \cdot 10$kHz and a Gaussian prior. Upper left: Example of optimised measurement settings. The likelihood is asymmetric in the position where the maximum of the prior is, and the waiting time is equal to the inverse of the standard deviation of the prior. As a result, part of the left side of the prior distribution is discarded in the posterior, minimising the posterior variance. Upper right: An incorrect selection of ϕ can cause the posterior to be divided into two peaks. In the case shown, this happens when measuring the outcome $|g\rangle$. In the case of a $|e\rangle$ measurement (not shown), the posterior would be a normal distribution with a higher standard deviation as the one obtained with the optimised settings. Lower left: A short waiting time causes the likelihood to be approximately constant in the interval of intererest of the prior distribution, causing the posterior to be almost the same as the prior. This leads to a small information gain. Lower right: A long waiting time causes the posterior to be divided into several peaks. Therefore, the reduction of the variance compared to the prior is small.

3. Perform n_{exp} measurements and obtain $n_{g,t}$ measurements of $|g\rangle$ and $n_{e,t}$ measurements of $|e\rangle$.

4. Update the prior by using the likelihood of obtaining those results given the selected experimental setup as in Eq. (8.13) to obtain the posterior distribution.

5. Correct the detuning by using the estimated value of the posterior distribution. This step is optional if the estimate of Δ, $\bar{\Delta}$, satisfies $\bar{\Delta} \ll \Omega$.

6. If the posterior distribution is approximately a normal distribution, obtain its variance and set the measurement settings for the next set of measurements to

the optimal values as in Eq. (8.17). If the detuning was not corrected in the previous step, the optimal phase has to be selected as in Eq. (8.18). However, if there is more than one peak in the posterior, select a different phase ϕ for the next measurements such as there is only one peak left after the next iteration (see Fig. 8.5).

7. Set the current posterior distribution as the prior for the next iteration.

8. Repeat from step 3 to 7 until the uncertainty of the detuning meets the desired threshold.

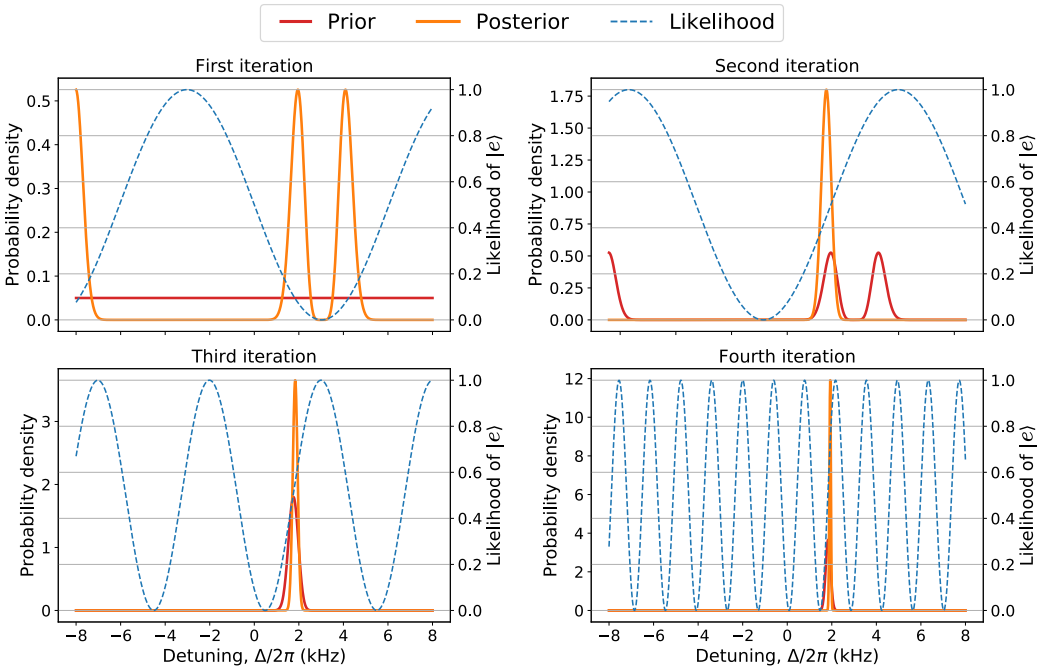

Figure 8.5: Experimental Bayesian Ramsey protocol. Bayesian inference updates for each iteration of the protocol with the experimental configurations and outcomes shown in table 8.1, for a detuning of $\Delta = 2\pi \cdot 2\text{kHz}$. Top left: After the first iteration, the prior is updated into a posterior with more than one peak. Top right: By selecting a phase ϕ for the second iteration such as the likelihood allows to distinguish which one is the correct peak, we can obtain a single peak in the posterior. Bottom left and right: With an approximate normal distribution as the prior, we can select the waiting time and the phase between pulses adaptively, achieving a fast convergence of the protocol to an estimate of the detuning after the fourth iteration of $1991 \pm 111\text{Hz}$.

8.4 Experimental results

The experimental implementation of the Bayesian Ramsey spectroscopy protocol was done in collaboration with Marc Bußjäger [178]. As preparation for the experiment, an initial calibration round over a wide detuning range was performed by using Rabi spectroscopy. With this initial calibration, rough estimates of the $(-1/2, -1/2)$ and $(-1/2, -5/2)$ transitions were obtained, with an error of the order of a few kilohertz, which was small enough to implement our Bayesian Ramsey spectroscopy.

In order to show that the Bayesian protocol works, a previously precisely calibrated $(-1/2, -1/2)$ transition was intentionally detuned to $\Delta = 2\pi \cdot 2\text{kHz}$. This is the value that the Bayesian protocol is expected to produce as an outcome. The experiment consisted of four ions manipulated by global beams, therefore each Ramsey cycle produced four independent outcomes. Ten repetitions were repeated for each experimental configuration of the Ramsey cycle, which means a total of 40 outcomes before updating the waiting time and phase between $\pi/2$-pulses for the next iteration. This is repeated for a total of $T = 4$ iterations.

The Ramsey experiments are done with a π-pulse time of $t_\pi = 19.6\mu\text{s}$ and a coherence time of $T_2 = 4\text{ms}$. The initial iteration of Ramsey cycles, $t = 1$, is performed with a waiting time of $\tau_R = 70.2\mu\text{s}$ and a phase between pulses of $\phi = 90°$. The posterior is a distribution with more than one peak (see Fig. 8.5), which can be effectively reduced to just one peak by changing the value of ϕ for the next iteration, $t = 2$, which then allows for the selection of adaptive measurements for the next iterations. The values used for each iteration and the results obtained are given in table 8.1. The result of the Bayesian protocol for these outcomes (see Fig. 8.5) is a detuning of $1991 \pm 111\text{Hz}$, in agreement with the intentionally introduced detuning of 2kHz, which indicates that the protocol works correctly.

After checking that the Bayesian protocol could be used to obtain the detuning of a laser with respect to a transition, it was used by Marc Bußjäger in Ref. [178] to estimate the drifts $\dot{\omega}_L$ and $\dot{B}$. In order to obtain these values, the Bayesian protocol was used to obtain an estimate of the detuning every two minutes. The configuration for this case was $T = 10$ iterations, each of them consisting on 20 cycles acting at the same time over two ions for the $(-1/2, -1/2)$ transition, and over the other two ions for the $(-1/2, -5/2)$ transition. A linear fit was performed by using these estimates,

t	$\tau_{R,t}(\mu s)$	ϕ_t	$n_{g,t}$	$n_{e,t}$
1	70.2	90°	37	3
2	70.2	211.7°	24	16
3	187.2	144.8°	17	23
4	707.8	157.8°	10	30

Table 8.1: Experimental results of the Bayesian Ramsey protocol. Using the adaptive Bayesian Ramsey spectroscopy as explained, we perform measurements, update our knowledge about the detuning, and obtain the optimal experimental configuration for the next set of measurements. The resulting probability distributions at each step are shown in Fig. 8.5

where a maximum look-back time of 1 hour for the magnetic field and 2 hours for the laser frequency is defined to only include recent enough data points, which results in better linear fits than using all the available data points. In order to characterise the quality of the laser stabilisation performed by the Bayesian protocol, frequentist Ramsey experiments were performed over the stabilised laser. One hundred experiments were performed every second, alternating between the $(-1/2, -1/2)$ and the $(-1/2, -5/2)$ transitions after every 10^4 experiments. The results of these experiments showed a mean detuning $\overline{\Delta}_{-1/2} = 32 \pm 36$ Hz for the $(-1/2, -1/2)$ transition and a $\overline{\Delta}_{-5/2} = 18 \pm 41$ Hz mean detuning for the $(-1/2, -5/2)$ transition. These errors in the stabilised laser frequencies are explained due to the deviations from the linear trend of $\omega_L(t)$ and $B(t)$. Therefore, the Bayesian protocol was able to stabilise the laser to the desired transitions, up to a few tens of Hertz.

8.5 Summary

In this chapter we have shown that the adaptive Bayesian Ramsey protocol is an improvement from the traditional frequentist approach to the Ramsey spectroscopy in different ways. First of all, it defines a simple rule for the optimal selection of the parameters for a Ramsey cycle in order to maximise the information gained by each outcome. This decreases the amount of measurements required to estimate the detuning of a laser from a given transition, meaning that less time must be lost in the calibration process. As a consequence, this time that is saved from the calibration of the system can be used for more relevant experiments. Second, the automation of the protocol is simple in the sense that the selection of experimental parameters for each

iteration, the update rules, and also obtaining the estimate of the detuning, are steps easily programmable in a computer. Third, beyond the estimate, it is straightforward to obtain the error associated to it. Finally, this protocol is less sensitive to errors such as fringe hopping, since it considers the previous measurements on top of the ones associated to the current iteration.

The experimental implementation of this protocol has been able to obtain the correct values of the detunings. Due to this, it was then used to perform laser frequency stabilisation [178], which required measuring the detuning of the laser from two transitions as a function of time, in order to estimate a frequency drift. The result of this process was a laser stabilised to the desired transitions with a detuning of the order of a few tens of Hertz, where this error comes mainly from the simple linear model used for the drift rather than due to any issue related to the Bayesian protocol itself.

Given the advantages that the Bayesian approach shows for the calibration of lasers, additional applications of Bayesian protocols for calibrating experimental setups can be thought of. In the following chapters, we will focus on the study of the Mølmer-Sørensen entangling gate in order to implement a Bayesian inference protocol for its calibration in the experiment. With this goal, in Chapter 9 we will derive the evolution introduced by this gate as well as possible miscalibrations that can appear in its experimental implementation. Particularly, we will focus on modeling the effect of one of these miscalibrations, known as *center line detuning*, for which there is no analytical derivation. After introducing these concepts, we will then introduce a Bayesian protocol for the calibration of this gate in Chapter 10.

Chapter 9

Miscalibrations in the Mølmer-Sørensen gate

In the previous chapter we explained the importance of the correct calibration of single-qubit gates and we developed a Bayesian protocol for their calibration in trapped-ion platforms. From that work, it is straightforward to think about designing a Bayesian protocol for the calibration of entangling gates. However, the implementation of entangling gates depends on more complex physical models than those used for single-qubit gates. Due to this, it is more challenging to achieve high fidelities in entangling gates than for single-qubit gates, since one needs a deep understanding of the gate and the effects that possible miscalibrations have on its performance. This complicates the implementation of not only Bayesian techniques but of any calibration protocol as compared to the calibration of single-qubit operations. Therefore, having access to an analytical understanding of these effects is desirable for the implementation and calibration of a quantum gate.

In this chapter, we will focus on the study of the Mølmer-Sørensen (MS) gate, which we briefly mentioned in Sec. 4.4, and the possible miscalibrations that can appear in its experimental implementation. The MS gate has some experimentally relevant properties, such as being able to create entanglement between more than two ions with a single application, and its independence on the initial vibrational state of the ions to first order. Moreover, its application, together with single-qubit rotations, is sufficient to obtain a CNOT gate [180]. As explained, the physical model of this entangling gate is more complex than those used for the implementation of the single-qubit gates that

we have seen. This higher degree of complexity increases the number of experimental parameters that need to be calibrated to obtain a high-fidelity gate. Additionally, for the miscalibration of some of these parameters there is no analytical model for the action of the gate on the quantum system. However, as we explained, it is helpful to understand the effects of these miscalibrations to determine if the gate is correctly calibrated or not. Specially, for understanding which miscalibration is limiting the fidelity of the gate.

After introducing the MS gate, we will focus on understanding the effect of one of these miscalibrations: the *center line detuning*. A center line detuning appears due to a miscalibration in the frequencies of the bichromatic laser used to implement the MS gate. Until recently there was no analytical derivation of the evolution introduced by the center line detuned MS gate. In this thesis, we introduce a semianalytical model that we developed in Ref. [2], based on a Magnus expansion [181]. This perturbative model provides physical and analytical insights into the final states obtained after the application of the MS gate with a center line detuning. This allows us to estimate key properties such as populations, relative phases, fidelities, or purities after the miscalibrated gate. After this study of the MS gate, we will then be in position to introduce in Chapter 10 the Bayesian protocol aimed at its calibration.

In Sec. 9.1, we introduce the derivation of the ideal MS gate, which we then generalise to consider different gate miscalibrations that allow for an analytical derivation. In Sec. 9.2, we introduce the derivation of a Magnus expansion applied to a center line detuned MS gate, which is used to obtain the form of the final states obtained from the application of the gate. In Sec. 9.3, we use these final states to obtain expressions for quantities of interest such as populations, relative phases, fidelities, and purities. We also compare these predictions with results obtained from numerical integration of the gate evolution. Finally, in Sec. 9.4 we show experimental results that further validate the results obtained from our model.

9.1 Mølmer-Sørensen gate

The Mølmer-Sørensen gate is based on the application of a force that is dependent on the internal state of the ions, and takes advantage of a common vibrational mode shared between the trapped ions [121]. This force induces a periodic movement of the

motional state of the ions in phase space. At the end of the gate the motion is returned to its original state with an accumulated relative phase in the internal states. The MS phase can be used to create entanglement between more than two ions with a single application and is independent of the initial vibrational state to first order [131, 132]. This last property provides the gate with a robustness when working with thermal states of the gate-mediating phonon mode, which can result from imperfect ground state cooling.

In order to derive the MS gate Hamiltonian, let us consider a system of N ions in a linear trap interacting with a bichromatic laser field of frequencies ω_1 and ω_2. We will focus on the lowest frequency center-of-mass (COM) mode of the ions and ignore the other more energetic modes, because the frequency difference between the COM mode and the other modes is much larger than the Rabi frequency of the driving laser field. This system may be described by the Hamiltonian

$$\begin{aligned} H(t) &= H_0 + H_{\text{int}}(t), \\ H_0 &= \sum_{j=1}^{N} \frac{\omega_{eg,0}}{2}\sigma_{z,j} + \nu(a^\dagger a + 1/2), \\ H_{\text{int}}(t) &= \sum_{j=1}^{N} \frac{\Omega(t)}{2}\left(\sigma_j^+ + \sigma_j^-\right)\left(e^{i(k_1 x_j - \omega_1 t + \varphi)} + e^{i(k_2 x_j - \omega_2 t + \varphi)} + h.c.\right), \end{aligned} \tag{9.1}$$

where $\omega_{eg,0}$ is the transition frequency between the internal states, $|e\rangle$ and $|g\rangle$, used to encode the qubit; ν is the trap frequency of the COM mode, which defines the distance of the motional sidebands (see Fig. 9.1) from the carrier; $a^\dagger$ and a are the Fock operators related to the COM mode; σ_j^+ and σ_j^- are the ladder operators acting on the internal states of the j^{th} ion and, similarly, $\sigma_{x,j}$, $\sigma_{y,j}$ and $\sigma_{z,j}$ represent the Pauli operators acting on the internal state of that ion; φ is the phase of the two laser tones of frequencies ω_1 and ω_2 - we will consider φ to be equal for both; $\vec{k}_1$ and $\vec{k}_2$ are the wavevectors of each laser tone; $\Omega(t)$ is the Rabi frequency, which is assumed to be equal for all ions and for both components of the laser field, and can be time-dependent for a general pulse-shape of the laser, $f(t)$,

$$\Omega(t) = \Omega\, f(t). \tag{9.2}$$

In order to implement the MS gate, the frequencies of the bichromatic laser must be

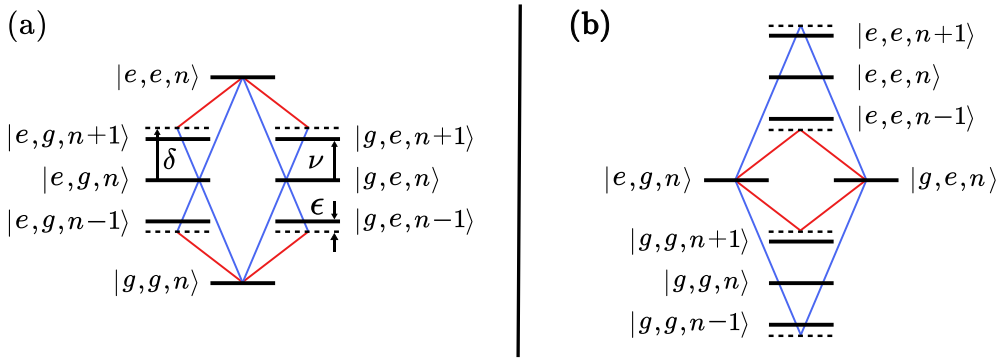

Figure 9.1: Mølmer-Sørensen gate resonant paths. (a) Energy diagram for two ions with quantised center of mass vibrational mode of frequency ν interacting with a bichromatic laser of frequencies $\omega_1 = \omega_{eg} + \delta$ and $\omega_2 = \omega_{eg} - \delta$. The bichromatic laser allows a resonant two-photon transition between $|g, g, n\rangle$ and $|e, e, n\rangle$. There are four different paths, each of them going through an intermediate virtual state separated by $\epsilon = \nu - \delta$ to one of the sidebands. (b) Similar diagram as before but for the transition $|e, g, n\rangle \leftrightarrow |g, e, n\rangle$ introduced by the MS gate.

centered around the carrier transition frequency and close to the sideband transition frequency, that is, $\omega_1 = \omega_{eg,0} + \delta$ and $\omega_2 = \omega_{eg,0} - \delta$, with a detuning δ close but not equal to ν, see Fig. 9.1. Introducing these values in the interaction term of the Hamiltonian we obtain

$$H_{\text{int}}(t) = \sum_{j=1}^{N} \frac{\Omega(t)}{2} \left(e^{i(\vec{k}_1 \vec{x}_j - (\omega_{eg,0}+\delta)t+\varphi)} + e^{i(\vec{k}_2 \vec{x}_j - (\omega_{eg,0}-\delta)t+\varphi)} + h.c. \right) \left(\sigma_j^+ + \sigma_j^- \right). \tag{9.3}$$

We can write $\vec{k}_i \vec{x} = \eta_i (a^\dagger + a)$ with $i = 1, 2$, where η_i is the Lamb-Dicke parameter (see Eq. (4.26)), and since $\delta \ll \omega_{eg,0}$ we can assume $\eta_1, \eta_2 \approx \eta$. We can simplify this Hamiltonian by assuming that we are in the Lamb-Dicke regime, $\eta\sqrt{n} \ll 1$, with n being the phonon number of the COM motional state, introducing the sideband detuning as $\epsilon = \nu - \delta$, transforming to the interaction picture defined by the evolution operator, $V(t) = e^{iH_0 t}$, that is

$$\hat{H}(t) = V(t)H(t)V^\dagger(t) + i \left(\frac{d}{dt} V(t) \right) V^\dagger(t). \tag{9.4}$$

Finally, applying the rotating wave approximation to keep only the terms rotating with ϵ and ignoring the other fast-rotating terms that go with $\nu + \delta$ or $\omega_{eg,0}$, we obtain the

following Hamiltonian

$$\hat{H}(t) = -\eta\,\Omega(t)\left(a^{\dagger}e^{i\epsilon t} + ae^{-i\epsilon t}\right)S_{\varphi}, \tag{9.5}$$

where we have defined

$$S_{\varphi} = S_y\cos(\varphi) + S_x\sin(\varphi), \tag{9.6}$$

and

$$S_{\alpha} = \frac{1}{2}\sum_{j=1}^{N}\sigma_{\alpha,j}, \quad \alpha = x, y, z. \tag{9.7}$$

The evolution introduced by the Hamiltonian in Eq. (9.5) can be solved by calculating the limit to infinity of a product of small evolution operators [132, 182]

$$\hat{U}(t) = \lim_{K\to\infty}\prod_{k=1}^{K}\exp\Big(-i\hat{H}(t_k)\Delta t\Big) = \lim_{K\to\infty}\prod_{k=1}^{K}\exp\Big[D(\gamma(t_k)S_{\varphi}\Delta t)\Big], \tag{9.8}$$

where $t = K\cdot\Delta t$, $D(\alpha)$ is the displacement operator as in Eq. (3.58), and we defined

$$\gamma(t) \equiv i\eta\Omega(t)e^{i\epsilon t}. \tag{9.9}$$

Using the Baker-Campbell-Hausdorff relation [183]

$$D(\alpha)D(\beta) = D(\alpha+\beta)\exp(i\,\mathrm{Im}(\alpha\beta^{*})), \tag{9.10}$$

we obtain

$$\begin{aligned}&\prod_{k=1}^{K}\exp\Big[D(\gamma(t_k)S_{\varphi}\Delta t)\Big]\\ &\qquad = D\left(\sum_{k=1}^{K}\gamma(t_k)S_{\varphi}\Delta t\right)\prod_{k=2}^{K}\exp\left(i\,\mathrm{Im}\left[\gamma(t_k)\sum_{j=1}^{K-1}\gamma^{*}(t_j)S_{\varphi}^{2}\right]\Delta t^{2}\right),\end{aligned} \tag{9.11}$$

for which in the limit $K\to\infty$ we obtain

$$\hat{U}(t) = D\left(\int_0^t\gamma(t')dt'S_{\varphi}\right)\exp\left(i\,\mathrm{Im}\int_0^t\gamma(t')dt'\int_0^{t'}\gamma^{*}(t'')dt''S_{\varphi}^{2}\right). \tag{9.12}$$

Therefore, the action of the gate can be expressed in terms of

$$\Gamma(t) = \int_0^t \gamma(t')dt', \tag{9.13}$$

$$\theta(t) = \mathrm{Im}\int_0^t \gamma(t')dt' \int_0^{t'} \gamma^*(t'')dt''. \tag{9.14}$$

For a simple case with a constant Rabi frequency, although these calculations can be performed for other pulse shapes, the time evolution introduced by the gate is given by

$$\hat{U}(t) = D\left(\frac{\eta\Omega}{\epsilon}(e^{i\epsilon t}-1)S_\varphi\right)\exp\left[i\left(\frac{(\eta\Omega)^2}{\epsilon}t - \left(\frac{\eta\Omega}{\epsilon}\right)^2\sin(\epsilon t)\right)S_\varphi^2\right]. \tag{9.15}$$

The parameters of the gate can be tuned to obtain the desired evolution

$$\mathrm{MS}_\varphi(\theta) = \exp\left(i\theta S_\varphi^2\right). \tag{9.16}$$

One typically aims to obtain $\theta = \pi/2$, for which the action of the gate on a state in the computational basis produces a maximally entangled state. In order to achieve this, there are two approaches. The first uses a gate in the *weak-field regime*, $\eta\Omega \ll \epsilon$, where the bichromatic laser has a small coupling to the sidebands, which makes the population transfered to them negligible. In this regime, we obtain

$$\hat{U}(t) \approx \exp\left(i\frac{(\eta\Omega)^2}{\epsilon}S_\varphi^2 t\right). \tag{9.17}$$

Within this approximation, the evolution operator does not change the motional state of the ions at any time, performing a Rabi oscillation between $|e,e,n\rangle \leftrightarrow |g,g,n\rangle$ and $|g,e,n\rangle \leftrightarrow |e,g,n\rangle$ with a rotating axis defined by S_φ in the equator of the Bloch sphere defined by these two states. However, restricting the gate to this regime causes it to be slow. To obtain a faster gate we can consider the MS gate where we set

$$t_g|\epsilon| = 2\pi, \tag{9.18}$$

with t_g being the gate time. With this condition the displacement operator in Eq. (9.15) becomes the identity (since $\Gamma(t_g) = 0$), and the argument in the exponential simplifies.

We then have to configure the gate in such a way that

$$\theta(t_g) = \frac{(\eta\Omega)^2}{\epsilon} t_g = \frac{\pi}{2}, \tag{9.19}$$

to obtain the evolution operator

$$\hat{U}(t_g) = \exp\left(i\frac{\pi}{2}S_\varphi^2\right) \tag{9.20}$$

For this case, the coupling of the bichromatic laser with the sidebands is not negligible, and the motional state at intermediate times between the beginning and the end of the gate will be different from the initial one. This can be seen since the displacement operator in Eq. (9.15) performs a loop in phase space, returning to the original point at the end of the gate (see Fig. 9.2 (b)). As for the entanglement introduced by the gate, given by $\theta(t_g)$, it is equal to the area enclosed by this loop. A similar explanation can be made for the gate in the weak-field regime. In this case the gate performs several loops in phase space of a much smaller size, making the population of the sidebands negligible at all times, and the rotation induced by the gate will be equal to the area enclosed by several small loops.

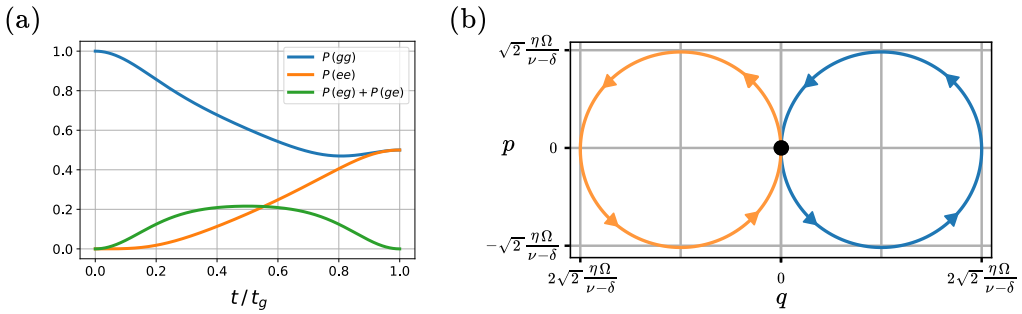

Figure 9.2: Single-loop MS gate. (a) Evolution of the populations of the internal states of two qubits for the initial state $|g, g, 0\rangle$ under the action of a single-loop MS gate with constant Rabi frequency. The states $|e, g\rangle$ and $|g, e\rangle$ have a finite population during the gate, but they return to zero after the gate is completed. At the end of the gate, the qubits are in a maximally entangled state. (b) Trajectory in phase space, defined by the, momentum, p, and position, q, induced by the MS gate with the ions on the $+1$ eigenstate of S_φ (in orange) and the -1 eigenstate (in blue), with the black circle indicating the initial position. The trajectory returns to the initial point in phase space after t_g. The rotation introduced by the gate is given by the area enclosed by the trajectory.

While the evolution shown in Eq. (9.20) would be the effect of the ideal MS gate, obtained by a perfect calibration of the parameters, it is important to understand what are the effects that a wrong calibration would introduce in the gate. One can see that if the relation in Eq. (9.19) is not satisfied, the entanglement between the internal state of the ions introduced by the gate would not be the desired one. Additionally, a miscalibration in the relation between the gate time and the sideband detuning shown in Eq. (9.18) can change the motional state of the ions and introduce entanglement between the internal and motional states. This can be understood in terms of the example shown in Fig. 9.2 as a loop in phase space that does not return the motional state to the initial one at the end of the gate due to an under or over-rotation. On top of this, this miscalibration would also introduce an error in the value of θ. All of these unwanted effects reduce the fidelity of the gate.

The previous examples of the effects that some miscalibrations have on the gate can be easily understood thanks to having access to a closed form of the evolution introduced by the gate. However, this will not be the case for a gate with a *center line detuning*. In the following we introduce what is a center line detuning, its sources and how this miscalibration affects the Hamiltonian of the MS gate.

9.1.1 Center line detuned MS gate

A center line detuning is a miscalibration appearing in the MS gate due to the frequencies of the bichromatic laser not being centered around the carrier. A center line detuning can appear due to two different contributions. First, the transition frequency between $|g\rangle$ and $|e\rangle$ can be affected by an AC-Stark shift $\lambda_{AC}(t) \propto \Omega(t)^2$ caused by the interaction of the laser with off-resonant atomic levels [184, 185], which will be time-dependent due to the pulse-shape of the laser, $f(t)$. Due to this, the transition frequency will have the form

$$\omega_{eg}(t) = \omega_{eg,0} + \lambda_{AC}\, f(t)^2. \tag{9.21}$$

Another contribution to the center line detuning that we consider is due to a shift, λ_l, of the bichromatic laser frequencies given by

$$\begin{aligned} \omega_1 &= \omega_{eg,0} + \omega_d + \lambda_l, \\ \omega_2 &= \omega_{eg,0} - \omega_d + \lambda_l. \end{aligned} \tag{9.22}$$

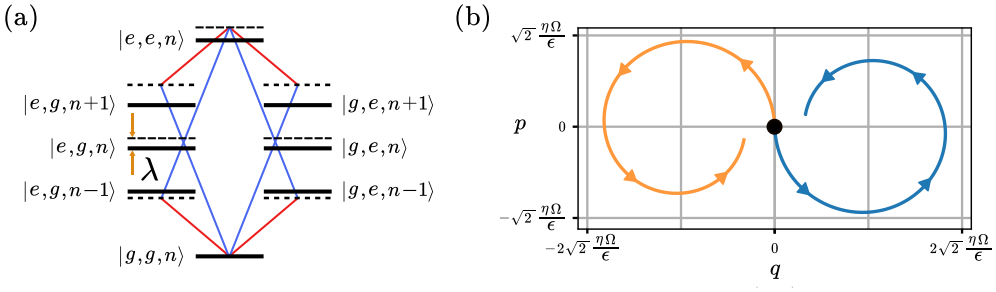

Figure 9.3: Center line detuned MS gate. (a) The existence of a center line detuning, λ, which appears due to the laser frequencies not being centered around the carrier, breaks the symmetry between the four paths and the two-photon resonance. (b) Similar phase space plot as in Fig. 9.2, but with a constant center line detuning $\lambda/\epsilon = 0.1$. The center line detuning miscalibration deforms the loop as compared to the ideal case, causing the final motional state to be different from the initial one, therefore introducing and entanglement between the motional states and the ionic states. Additionally, the trajectory in this case is dependent on the initial motional state, with the case shown being for initial $|n = 0\rangle$. This effect also causes the final internal state to be different from the ideal one (not shown).

Combined, these contributions cause a detuning of the mean value of the bichromatic frequencies from the carrier transition frequency, given by

$$\lambda(t) = \lambda_{AC}\, f(t)^2 - \lambda_l. \tag{9.23}$$

The effect of this miscalibration on the level structure of the MS gate at a given time is shown in Fig. 9.3 (a).

Introducing these changes into the model and following a similar derivation as for the ideal MS gate, where instead of changing into the interaction picture defined by the evolution operator generated by H_0, we change to the interaction picture defined by

$$W(t) = \exp\left[i \left(\sum_{j=1}^{N} \frac{\omega_{eg,0} - \lambda_l}{2} \sigma_{z,j} + \nu(a^\dagger a + 1/2) \right) t \right], \tag{9.24}$$

and obtain the Hamiltonian

$$\hat{H}(t) = \lambda(t)\, S_z - \eta\Omega(t)(a^\dagger e^{i\epsilon t} + a e^{-i\epsilon t})\, S_\varphi. \tag{9.25}$$

Therefore, the effect of the center line detuning miscalibrations is the appearance of an unwanted S_z term in the Hamiltonian. This term does not only cause the dynamics

to be different from the ideal gate (see for example Fig. 9.3 (b)), but also causes the evolution introduced by the gate to not have an analytical solution.

In the following section we present a perturbative study based on a Magnus expansion [181, 186], which we use to analyse the effect that the center line detuning has on the gate's performance.

9.2 Perturbative study of the center line detuned MS gate

As we saw in the previous section, the Hamiltonian with a center line detuning has the form of the ideal Hamiltonian of the MS gate plus an additional term accounting for the center line detuning miscalibration. In the following we will rescale the time as $\tau = \epsilon\, t$, which is dimensionless since ϵ is a frequency. This rescaling is convenient since it makes our study independent of specific choices for the gate parameters. The adimensional time-dependent Schrödinger equation becomes

$$i\epsilon \frac{d}{d\tau}\phi(\tau) = \hat{H}(\tau/\epsilon)\phi(\tau). \tag{9.26}$$

The evolution is ruled by a rescaled Hamiltonian, $\hat{\mathcal{H}}(\tau)$, given by

$$\hat{\mathcal{H}}(\tau) = \hat{\mathcal{H}}_{\text{ideal}}(\tau) + \tilde{\mathcal{H}}_{\text{cl}}(\tau), \tag{9.27}$$

where

$$\begin{aligned} \hat{\mathcal{H}}_{\text{ideal}}(\tau) &= -\tilde{\Omega}(\tau/\epsilon)(a^\dagger e^{i\tau} + a e^{-i\tau})\, S_\varphi, \\ \hat{\mathcal{H}}_{\text{cl}}(\tau) &= \tilde{\lambda}(\tau/\epsilon)\, S_z, \end{aligned} \tag{9.28}$$

with $\tilde{\Omega}(\tau/\epsilon) = \eta\Omega(\tau/\epsilon)/\epsilon$ and $\tilde{\lambda}(\tau/\epsilon) = \lambda(\tau/\epsilon)/\epsilon$.

In order to simplify the analysis, we will consider a square pulse-shape. In this case we can write $\tilde{\lambda}(\tau/\epsilon) = \tilde{\lambda} = (\lambda_{AC} - \lambda_l)/\epsilon$ and $\tilde{\Omega}(\tau/\epsilon) = \tilde{\Omega} = \eta\Omega/\epsilon$, which satisfies $\tilde{\Omega} = 1/2$ when we consider the conditions in Eq. (9.18) and Eq. (9.19). We note that for the study of a given time-dependent pulse shape, one can follow a similar derivation as the one that we will show, at the cost of introducing the pulse shape in the respective numerical integrals that will appear.

Our goal is to obtain the evolution operator, $\hat{\mathcal{U}}(\tau)$, associated to the Hamiltonian in Eq. (9.27). In the following we will study the effect of the center line detuning miscalibration by using a Magnus expansion approach where we consider this unwanted

term as a perturbation. This perturbative study is justified since typical values of the center line detuning miscalibration represent only a small fraction of the value of the sideband detuning. Without loss of generality, we will continue to assume that the common phase of both laser tones is $\varphi = 0$.

9.2.1 Magnus expansion

We already know the form of the evolution introduced by the unperturbed Hamiltonian, $\hat{\mathcal{H}}_{\text{ideal}}(\tau)$, given by the rescaled version of Eq. (9.15)

$$\hat{\mathcal{U}}_0(\tau) = D\Big[F(\tau)\, S_y\Big] \cdot \exp\left[iG(\tau)S_y^2\right], \tag{9.29}$$

where $F(\tau) = \tilde{\Omega}\left(e^{i\tau} - 1\right)$ and $G(\tau) = \tilde{\Omega}^2\Big(\tau - \sin(\tau)\Big)$. We can move to another rotating frame defined by this free evolution operator, $\hat{\mathcal{U}}_0(\tau)$. In this frame, the Hamiltonian of the system becomes

$$\tilde{\mathcal{H}}(\tau) = \hat{\mathcal{U}}_0^{\dagger}(\tau)\hat{\mathcal{H}}_{\text{cl}}\hat{\mathcal{U}}_0(\tau). \tag{9.30}$$

In this rotating frame, we separate the perturbation term due to the center line detuning of the initial Hamiltonian, $\hat{\mathcal{H}}(\tau)$, from the one that allows for an analytical solution. From now on, we will focus on studying the term arising from the center line detuning as a perturbation to the Hamiltonian of the ideal gate (with the perturbative parameter being $\tilde{\lambda}$) by using a Magnus expansion [181, 186], which has the advantage of producing a unitary perturbative evolution operator at any order. With this approach, we can represent the operator that describes the evolution due to this Hamiltonian, $\tilde{\mathcal{U}}(\tau)$, in exponential form:

$$\tilde{\mathcal{U}}(\tau) = \exp\Big[M(\tau)\Big]. \tag{9.31}$$

The Magnus exponent, $M(\tau)$, is given by a series

$$M(\tau) = \sum_{j=1} M_j(\tau), \tag{9.32}$$

with the first terms

$$M_1(\tau) = -i \int_0^\tau \tilde{\mathcal{H}}(t_1) dt_1, \tag{9.33}$$

$$M_2(\tau) = -\frac{1}{2} \int_0^\tau \int_0^{t_1} [\tilde{\mathcal{H}}(t_1), \tilde{\mathcal{H}}(t_2)] dt_2 dt_1. \tag{9.34}$$

Here, $M_1(\tau)$ and $M_2(\tau)$ have a first and second order dependence on $\tilde{\lambda}$, respectively. Considering only these terms and ignoring higher order dependences on the center line detuning, the evolution operator is approximated by

$$\tilde{\mathcal{U}}^{(2)}(\tau) \approx \mathbb{1} + M_1(\tau) + \Big(M_2(\tau) + M_1^2(\tau)/2 \Big). \tag{9.35}$$

We can now use this result with the free evolution operator to obtain an approximation up to second order in Magnus expansion, $\hat{\mathcal{U}}^{(2)}(\tau)$, of the evolution, $\hat{\mathcal{U}}(\tau)$, introduced by the Hamiltonian in Eq. (9.27)

$$\hat{\mathcal{U}}^{(2)}(\tau) \approx \hat{\mathcal{U}}_0(\tau) + \hat{\mathcal{U}}_0(\tau) M_1(\tau) + \hat{\mathcal{U}}_0(\tau) \Big(M_2(\tau) + M_1^2(\tau)/2 \Big). \tag{9.36}$$

One can use this second order evolution operator or, more generally, the corresponding evolution operator obtained by a perturbation expansion up to K^{th} order, to obtain the action that the gate has over an initial state after a normalised gate time τ_g. In the following we consider the initial states $|\sigma, \sigma', n\rangle$ in the computational basis where $\sigma, \sigma' \in \{g, e\}$, and study the action of the center line detuned gate on them in a sum over k^{th} order perturbative correction states $\left|\psi^{(k)}_{\sigma,\sigma',n}\right\rangle$ with coefficients $\tilde{\lambda}^k$. The resulting state $\left|\Psi^{(K)}_{\sigma,\sigma',n}\right\rangle$ can be written as:

$$\left|\Psi^{(K)}_{\sigma,\sigma',n}\right\rangle = \hat{\mathcal{U}}^{(K)}(\tau_g) \left|\sigma, \sigma', n\right\rangle = \left|\psi_{\sigma,\sigma',n}\right\rangle - \sum_{k=1}^{K} \tilde{\lambda}^k \left|\psi^{(k)}_{\sigma,\sigma',n}\right\rangle, \tag{9.37}$$

where $\left|\psi_{\sigma,\sigma',n}\right\rangle$ is the target state of the ideal gate.

We will begin by studying the first order Magnus expansion, from which we will be able to write the perturbed evolution as a unitary operator acting on the qubit space. From this we will see that the only linear effect that the center line detuning has on the gate is the appearance of an unwanted relative phase. In order to obtain further results, we will need to study the second order Magnus expansion, which will

allow us to capture more exactly the dependences of other key properties, namely the populations, fidelities, and purities, with the center line detuning.

9.2.2 First order Magnus expansion

In order to study the first order dependence of the MS gate on the center line detuning, we consider only the first two terms in Eq. (9.36)

$$\hat{\mathcal{U}}^{(1)}(\tau) \approx \hat{\mathcal{U}}_0(\tau) + \hat{\mathcal{U}}_0(\tau) M_1(\tau). \tag{9.38}$$

In the absence of any center line detuning, the final state after the application of the ideal MS gate for a normalised gate time, $\tau_g = 2\pi$ (see Eq. (9.18)), for each initial state would be given by

$$|\psi_{g,g,n}\rangle = \hat{\mathcal{U}}_0(\tau_g)\,|g,g,n\rangle = \frac{e^{i\pi/4}}{\sqrt{2}}\Big(\,|g,g,n\rangle - i\,|e,e,n\rangle\,\Big), \tag{9.39}$$

$$|\psi_{e,e,n}\rangle = \hat{\mathcal{U}}_0(\tau_g)\,|e,e,n\rangle = \frac{e^{i\pi/4}}{\sqrt{2}}\Big(-i\,|g,g,n\rangle + |e,e,n\rangle\,\Big), \tag{9.40}$$

$$|\psi_{g,e,n}\rangle = \hat{\mathcal{U}}_0(\tau_g)\,|g,e,n\rangle = \frac{e^{i\pi/4}}{\sqrt{2}}\Big(\,|g,e,n\rangle + i\,|e,g,n\rangle\,\Big), \tag{9.41}$$

$$|\psi_{e,g,n}\rangle = \hat{\mathcal{U}}_0(\tau_g)\,|e,g,n\rangle = \frac{e^{i\pi/4}}{\sqrt{2}}\Big(i\,|g,e,n\rangle + |e,g,n\rangle\,\Big). \tag{9.42}$$

One can then calculate the first order corrections to the final states (see Appendix A.4), given by

$$\begin{aligned}\Big|\psi^{(1)}_{g,g,n}\Big\rangle = \sum_{m\geq 0}\Big[&if^{\text{odd}}_{n,m} I^m_n\,(|e,g,m\rangle + |g,e,m\rangle)\\ &+ f^{\text{even}}_{n,m}\,((I^n_m + I^m_n)\,|g,g,m\rangle + (I^n_m - I^m_n)\,|e,e,m\rangle)\Big],\end{aligned} \tag{9.43}$$

$$\begin{aligned}\Big|\psi^{(1)}_{e,e,n}\Big\rangle = \sum_{m\geq 0}\Big[&-if^{\text{odd}}_{n,m} I^m_n\,(|e,g,m\rangle + |g,e,m\rangle)\\ &+ f^{\text{even}}_{n,m}\,((I^n_m + I^m_n)\,|g,g,m\rangle + (I^n_m - I^m_n)\,|e,e,m\rangle)\Big],\end{aligned} \tag{9.44}$$

$$\Big|\psi^{(1)}_{g,e,n}\Big\rangle = \Big|\psi^{(1)}_{e,g,n}\Big\rangle = i\sum_{m\geq 0} I^n_m f^{\text{odd}}_{n,m}\Big(\,|g,g,m\rangle + |e,e,m\rangle\,\Big), \tag{9.45}$$

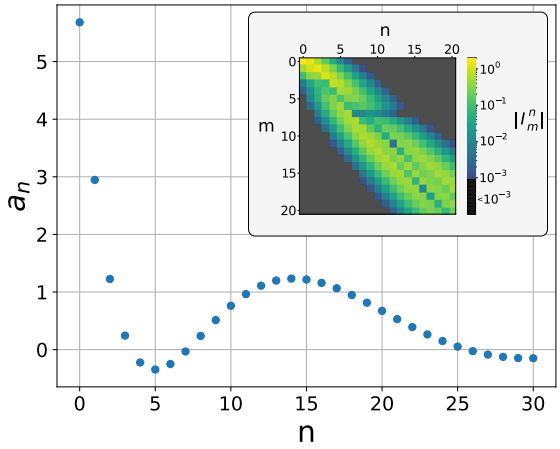

Figure 9.4: Representation of the first order Magnus expansion coefficients. Values of the numerical coefficients a_n, defined in Eq. (9.53). These values appear in the predictions of our model due to the first order corrections to the final state. Therefore, for the first values of n, the first order effects decrease as n increases (see, for example, Eq. (9.55), Fig. 9.5, and Fig. 9.6). These low values of n are the most relevant in the experiment since the initial motional state of the ions is cooled before the application of the gate. An inset is shown for the absolute values of the I^n_m coefficients, from which the a_n coefficients are obtained by using Eq. (9.53).

where we defined

$$f^{\text{even}}_{n,m} = \frac{(1+(-1)^{n-m})}{2}, \quad f^{\text{odd}}_{n,m} = \frac{(1-(-1)^{n-m})}{2}, \tag{9.46}$$

and I^n_m, which is a matrix (see Appendix A.4 and Fig. 9.4) obtained from numerical integrations of

$$I^n_m = \frac{i}{2}\int_0^{\tau_g} e^{iG(\tau)} \langle m| D[F(\tau)] |n\rangle \, d\tau. \tag{9.47}$$

While these coefficients depend on the pulse-shape and on the phonon motional states, they do not have any dependence on the center-line detuning. This implies that, for obtaining corrections to the final states, we only need to calculate I^n_m once for that given pulse-shape. The coefficients obtained can then be used with Eq. (9.37) for the calculation of the final state $\left|\Psi^{(1)}_{\sigma,\sigma',n}\right\rangle$ up to first order for any value of the center line detuning. In our constant pulse-shape case, all of these coefficients have the form of a real value multiplied by $(-1+i)$. The code that we developed to obtain these coefficients can be found in the GitHub repository in Ref. [187], which also includes the numerical calculation of the second order coefficients appearing in Sec. 9.2.3.

We can prove that, up to first order in $\tilde{\lambda}$, the center line detuning does not introduce

any unwanted entanglement between the internal and motional states. This can be shown by computing the density matrix of the state $\left|\Psi^{(1)}_{\sigma,\sigma',n}\right\rangle$ that from Eq. (9.37) takes the form:

$$\left|\Psi^{(1)}_{\sigma,\sigma',n}\right\rangle\left\langle\Psi^{(1)}_{\sigma,\sigma',n}\right| = \left|\Psi^{(1),tr}_{\sigma,\sigma',n}\right\rangle\left\langle\Psi^{(1),tr}_{\sigma,\sigma',n}\right| \otimes |n\rangle\langle n| + O(\tilde{\lambda}^2), \tag{9.48}$$

where the states $\left|\Psi^{(1),tr}_{\sigma,\sigma',n}\right\rangle$ are the following

$$\left|\Psi^{(1),tr}_{g,g,n}\right\rangle = \frac{1}{\sqrt{2}}\Big[(1 - ia_n\tilde{\lambda})\,|g,g\rangle - i\,|e,e\rangle\Big], \tag{9.49}$$

$$\left|\Psi^{(1),tr}_{e,e,n}\right\rangle = \frac{1}{\sqrt{2}}\Big[-i\,|g,g\rangle + (1 + ia_n\tilde{\lambda})\,|e,e\rangle\Big], \tag{9.50}$$

$$\left|\Psi^{(1),tr}_{g,e,n}\right\rangle = \frac{1}{\sqrt{2}}\Big(|g,e\rangle + i\,|e,g\rangle\Big), \tag{9.51}$$

$$\left|\Psi^{(1),tr}_{e,g,n}\right\rangle = \frac{1}{\sqrt{2}}\Big(|e,g\rangle + i\,|g,e\rangle\Big), \tag{9.52}$$

and we defined the real numbers a_n as

$$a_n = 4I_n^n/(-1+i). \tag{9.53}$$

A representation of the values a_n for different values of n is shown in Fig. 9.4.

From these results one can obtain that the action of the center line detuned MS gate over the qubits is, in the computational basis and up to first order, a unitary operator given by

$$\hat{\mathcal{U}}^{(1),tr}_n(\tau_g) = \frac{1}{\sqrt{2}}\begin{pmatrix} 1 - ia_n\tilde{\lambda} & 0 & 0 & -i \\ 0 & 1 & i & 0 \\ 0 & i & 1 & 0 \\ -i & 0 & 0 & 1 + ia_n\tilde{\lambda} \end{pmatrix}. \tag{9.54}$$

Therefore, the center line detuning does not introduce, up to first order, any unwanted entanglement between the internal and motional states. In order to compare this unitary with the one from the ideal MS gate we consider that $1 - ia_n\tilde{\lambda} \approx \exp\Big(-i\tilde{\lambda}a_n\Big)$, from which we can identify

$$\hat{\mathcal{U}}^{(1),tr}_n(\tau_g) = R_z(-a_n\tilde{\lambda})\hat{\mathcal{U}}_0(\tau_g)R_z(-a_n\tilde{\lambda}), \tag{9.55}$$

where

$$R_z(\phi) \equiv \exp\left(i\,\phi\,S_z/2\right). \tag{9.56}$$

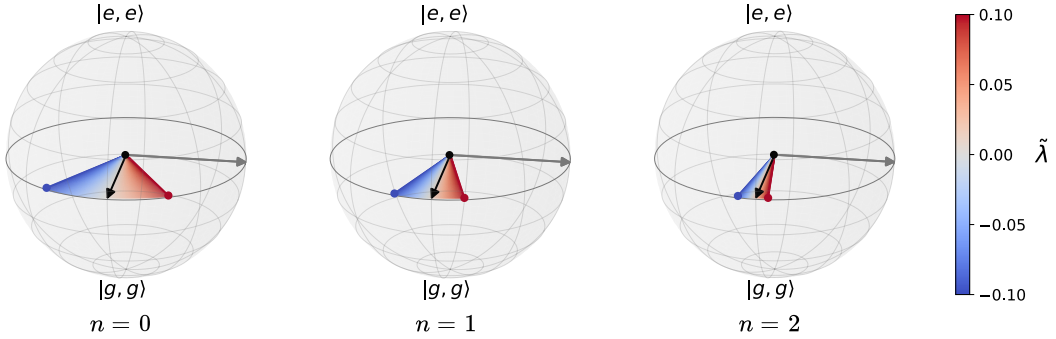

Figure 9.5: Representation of the final states obtained from first order Magnus expansion. Representation in the Bloch sphere spanned by $|g,g\rangle$ and $|e,e\rangle$ of the effect of applying the center line detuned gate on the initial state $|g,g,n\rangle$ obtained from first order Magnus expansion, shown in Eq. (9.49), for $n = 0, 1, 2$. The black arrow indicates the ideal final state $(|g,g\rangle - i\,|e,e\rangle)/\sqrt{2}$ and the grey arrow indicates the state $(|g,g\rangle + |e,e\rangle)/\sqrt{2}$. The colors shown in the legend are used to indicate the final state after the application of the MS gate as a function of the center line detuning. These states show a relative phase different from the ideal one, $(|g,g\rangle + \exp\left(i\phi^{(1)}_{g,g,n}(\tilde{\lambda})\right)|e,e\rangle)/\sqrt{2}$, given by Eq. (9.60) and Eq. (9.61) in Sec. 9.3.1. The error in the phase is larger for an initial Fock motional state of $n = 0$, and decreases for the cases $n = 1$ and $n = 2$. This can be understood by looking at the behaviour of the parameter a_n shown in Fig. 9.4, which one can use to predict, up to first order, the final relative phases for other values of the initial Fock state.

This shows that the predominant effect to first order, of the center line detuning is an error in the relative phase for the initial states $|e,e,n\rangle$ and $|g,g,n\rangle$ (see Fig. 9.5). Other relevant effects, e.g. in the final electronic and motional populations, quantum state fidelities or purity of the final qubit states appear in higher order, and thus require an expansion at least to second order in the center line detuning.

9.2.3 Second order Magnus expansion

In order to obtain the final states up to second order, we have to calculate the corresponding terms, as given by Eq. (9.37). These can be calculated (see Appendix A.4) and are given by

$$\left|\psi^{(2)}_{g,g,n}\right\rangle = \sum_{m\geq 0} J^n_{+,m}\,|g,g,m\rangle - J^n_{-,m}\,|e,e,m\rangle\,, \tag{9.57}$$

$$\left|\psi^{(2)}_{e,e,n}\right\rangle = \sum_{m\geq 0} -J^n_{-,m}\,|g,g,m\rangle + J^n_{+,m}\,|e,e,m\rangle\,, \tag{9.58}$$

$$\left|\psi^{(2)}_{g,e,n}\right\rangle = \left|\psi^{(2)}_{e,g,n}\right\rangle = \sum_{m\geq 0} \left(J^n_{1,m} - J^n_{2,m}\right)\Big(\,|g,e,m\rangle + |e,g,m\rangle\,\Big). \tag{9.59}$$

with $J^n_{+,m}$, $J^n_{-,m}$, $J^n_{1,m}$ and $J^n_{2,m}$ being numerical coefficients (see Appendix A.4) that, similarly as the I^n_m coefficients, do not depend on the center line detuning. While these coefficients depend on the pulse-shape, one only needs to calculate them once and then they can be used to calculate the final state up to second order, $\left|\Psi^{(2)}_{\sigma,\sigma',n}\right\rangle$, for any value of the center line detuning.

In this second order Magnus expansion, the effect of the gate can no longer be expressed as a unitary operator acting on the qubit states. This is because the states obtained from second (or higher) order have a residual entanglement between internal and motional states. As a consequence, the states obtained after tracing the phonons are no longer pure states. However, this second order expansion will allow us to obtain a better approximation of the final state, as we will see in the following section.

9.3 Predictions of the model

Having derived the final states after the application of the center line detuned gate by using a Magnus expansion, we are now in the position to estimate the effect that a center line detuning miscalibration has on the relative phase (Sec. 9.3.1), populations (Sec. 9.3.2), fidelities (Sec. 9.3.3), and purities (Sec. 9.3.4) of the final state with respect to the ideal one. While the following study can be performed for any initial state by using the results shown in Sec. 9.2, in the following we will focus on the case of $|g,g,n\rangle$ as initial state. We will also explain how these results can be generalised for the more experimentally relevant case where ions are in thermal motional states.

9.3.1 Relative phase

Following our perturbative approach, we can write the final relative phase of the state in Eq. (9.37) when considering the initial state $|\sigma,\sigma',n\rangle$ as the relative phase of the target state, $\phi^{(0)}_{\sigma,\sigma',n}$, plus the terms related to the k^{th} order correction, up to the considered K^{th} order:

$$\phi^{(K)}_{\sigma,\sigma',n}(\tilde{\lambda}) = \phi^{(0)}_{\sigma,\sigma',n} + \sum_{k=1}^{K} \tilde{\lambda}^k \delta\phi^{(k)}_{\sigma,\sigma',n} \tag{9.60}$$

Looking at the results from the first order Magnus expansion, we can see that the predominant effects of this miscalibration is over the relative phase of the final internal states. From Eq. (9.54) and Eq. (9.55) we can see that the initial states $|g,e,n\rangle$ and

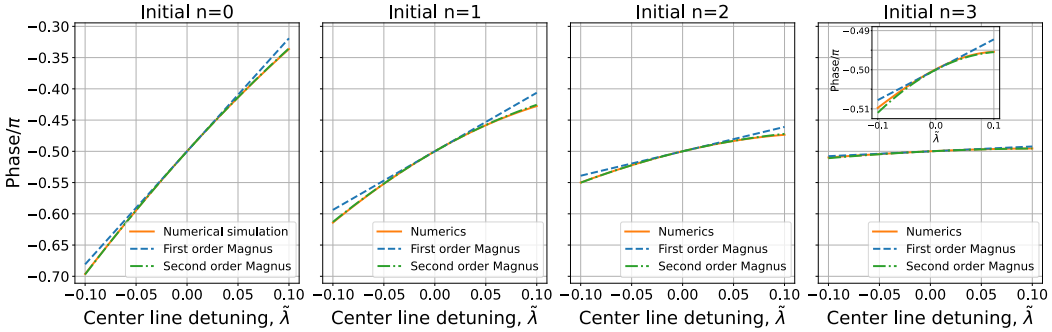

Figure 9.6: Relative phase predicted by the Magnus expansion model. Relative phases after the detuned MS gate with initial state $|g, g, n\rangle$ (in this example we consider initial COM phonon numbers $n = 0, 1, 2, 3$) for the numerical integration of the Hamiltonian in Eq. (9.27) and for the results from the first and second order Magnus expansion, $\phi^{(1)}_{g,g,n}$ and $\phi^{(2)}_{g,g,n}$, obtained by using Eq. (9.60). The ideal relative phase is $-\pi/2$ since the ideal final state is $(|g, g\rangle - i\,|e, e\rangle)/\sqrt{2}$. The second order terms improve the phase estimation as compared to the first order case. Very minor differences with respect to the numerics are expected and result from not accounting for higher order corrections. We note that for the cases shown, the dependence of the phase error on the center line detuning decreases as n increases, in accordance to what is shown in Fig. 9.5. An inset is included for the case with initial $n = 3$ for clarity.

$|e, g, n\rangle$ are not affected by a center line detuning in first order. As for the initial state $|g, g, n\rangle$, it has a first order correction given by (see Eq. (9.55))

$$\delta\phi^{(1)}_{g,g,n} = a_n. \tag{9.61}$$

This causes the final state to have an error in the final relative phase as compared to the target state in Eq. (9.49), of relative phase $\phi^{(0)}_{g,g,n} = -\pi/2$.

For the case of the initial state $|e, e, n\rangle$ one can obtain, after following the same derivation, that the relative phase introduced by the center line detuning is the same but of opposite sign. Therefore, the relative phase has a leading first order perturbative term dependent on the center line detuning. A visual representation of this effect is shown in Fig. 9.5.

Additionally, one can use the results from the second order Magnus expansion to improve the relative phase prediction. In order to do this, one can, for the initial state $|g, g, n\rangle$ case for example, calculate the coherence element between $|e, e\rangle$ and $|g, g\rangle$ of the traced final state:

$$\rho^{ee,gg\,(2)}_{g,g,n}(\tilde{\lambda}) = \frac{-i + \tilde{\lambda}a_n + \tilde{\lambda}^2 b_n}{2}. \tag{9.62}$$

where

$$b_n = -(1-i)\Big((J^n_{+,n})^* - J^n_{-,n}\Big) + \sum_{m\neq n}\Big(I^n_m - I^m_n\Big)\Big(I^n_m + I^m_n\Big)^* f^{\text{even}}_{n,m}. \tag{9.63}$$

Calculating the argument of this coherence term up to second order, we obtain

$$\delta\phi^{(2)}_{g,g,n} = \text{Re}(b_n), \tag{9.64}$$

which can be used with Eq. (9.60) to obtain the second order correction. A comparison between the relative phases predicted up to first and second order, $\phi^{(1)}_{g,g,n}$ and $\phi^{(2)}_{g,g,n}$, and the one obtained from the numerical integration of the Hamiltonian in Eq. (9.27), for different initial motional states is shown in Fig. 9.6.

This result can be generalised for the case where the initial motional state is in a mixed state defined by a thermal distribution with a mean number of phonons $\bar{n}$, $p_{\bar{n}}(n)$, as in Eq. (3.63). In this case, the relative phases in first, $\phi^{(1)}_{g,g,\bar{n}}$, and second order, $\phi^{(2)}_{g,g,\bar{n}}$, are given by

$$\phi^{(K)}_{g,g,\bar{n}} = \sum_{n=0} p_{\bar{n}}(n)\,\phi^{(K)}_{g,g,n}, \quad K = 1, 2. \tag{9.65}$$

Since each of the populations of the thermal state is affected by a different error in the final relative phase, one can expect that the center line detuning also introduces a dephasing of the final internal state superposition, causing decoherence in the quantum states.

9.3.2 Populations

Using the final states resulting from the first order Magnus expansion in Sec. 9.2.2, one can obtain that the center line detuning does not introduce a first order correction of the populations when considering the elements of the computational basis as initial states. Due to this, we have to consider the states obtained from the second order

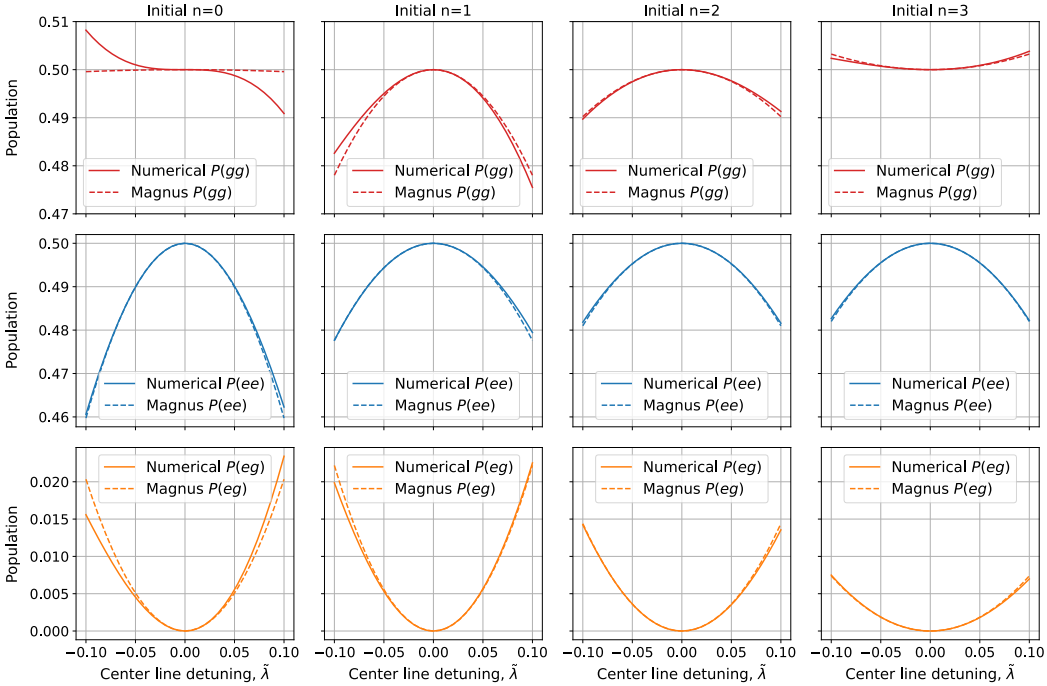

Figure 9.7: Populations predicted by the Magnus expansion model. Populations after the action of the detuned MS gate over the initial state $|g, g, n\rangle$ (in this example we consider the cases with $n = 0, 1, 2, 3$) obtained by numerical integration of the Hamiltonian in Eq. (9.27) and with the expressions for the second order Magnus expansion shown in Eq. (9.66)-(9.68). None of these populations have a linear dependence with the center line detuning, which justifies the use of the second order Magnus expansion for their study. While the quadratic terms captures the behaviour of the populations with the center line detuning, one can also see that the model has slight deviations from the numerics in higher order terms. This is specially the case for the behaviour of $P(gg)$ for the initial state $|g, g, 0\rangle$, in which the second order term has almost no importance, making the third order term (which is not considered in our calculations) dominant.

Magnus expansion. The populations obtained from $\left|\Psi^{(2)}_{g,g,n}\right\rangle$ are given by

$$P^{(2)}_{g,g,n}(gg, \tilde{\lambda}) = \frac{1}{2} + c_{g,g,n}\tilde{\lambda}^2, \tag{9.66}$$

$$P^{(2)}_{g,g,n}(ee, \tilde{\lambda}) = \frac{1}{2} + c_{e,e,n}\tilde{\lambda}^2, \tag{9.67}$$

$$P^{(2)}_{g,g,n}(ge, \tilde{\lambda}) = P_{g,g,n}(eg, \tilde{\lambda}) = c_{e,g,n}\tilde{\lambda}^2, \tag{9.68}$$

where the expressions for $c_{g,g,n}$, $c_{e,g,n}$ and $c_{e,e,n}$ can be found in Appendix A.4.

From these equations one can see that the center line does not only introduce an error in the populations of $|g, g\rangle$ and $|e, e\rangle$, but also populates states $|e, g\rangle$ and $|g, e\rangle$,

which are ideally unpopulated when considering the initial $|g,g,n\rangle$ state. A comparison between these predictions for the populations and the numerics is shown in Fig. 9.7. In this figure one can see that our model correctly predicts the behaviour obtained from the numerics, with differences arising from third-order terms, which we are not considering.

9.3.3 Fidelity

Here, we will study the fidelity $F_{g,g,n}(\tilde{\lambda})$ of the final internal state when applying a center line detuned MS gate to $|g,g,n\rangle$ compared to the ideal final internal state

$$\left|\psi^{tr}_{g,g,n}\right\rangle = \frac{1}{\sqrt{2}}\Big(\,|g,g\rangle - i\,|e,e\rangle\,\Big). \tag{9.69}$$

This fidelity will be given by (see Eq. (2.14))

$$F_{g,g,n}(\tilde{\lambda}) = \left\langle\psi^{tr}_{g,g,n}\right|\rho_{g,g,n}(\tilde{\lambda})\left|\psi^{tr}_{g,g,n}\right\rangle, \tag{9.70}$$

where $\rho_{g,g,n}(\tilde{\lambda})$ is the density matrix of the internal state after applying the center line detuned MS gate. In a similar way as for the populations studied in the previous section, this fidelity has no linear dependence with the center line detuning. Due to this, we consider the fidelity up to second order Magnus expansion, for which we will need to consider the second order density matrix, which has the form

$$\rho^{(2)}_{g,g,n}(\tilde{\lambda}) = \begin{pmatrix} P^{(2)}_{g,g,n}(gg,\tilde{\lambda}) & 0 & 0 & \rho^{ee,gg\,(2)}_{g,g,n}(\tilde{\lambda}) \\ 0 & P^{(2)}_{g,g,n}(eg,\tilde{\lambda}) & \rho^{ge,eg\,(2)}_{g,g,n}(\tilde{\lambda}) & 0 \\ 0 & \rho^{eg,ge\,(2)}_{g,g,n}(\tilde{\lambda}) & P^{(2)}_{g,g,n}(ge,\tilde{\lambda}) & 0 \\ \rho^{gg,ee\,(2)}_{g,g,n}(\tilde{\lambda}) & 0 & 0 & P^{(2)}_{g,g,n}(ee,\tilde{\lambda}) \end{pmatrix}, \tag{9.71}$$

where $\rho^{gg,ee\,(2)}_{g,g,n}(\tilde{\lambda})$ is the complex conjugate of $\rho^{ee,gg\,(2)}_{g,g,n}(\tilde{\lambda})$ in Eq. (9.62), and one can easily check that all the coherences of $|e,g\rangle$ and $|g,e\rangle$ with $|e,e\rangle$ and $|g,g\rangle$ are zero thanks to the appearance of products of $f^{\text{odd}}_{n,m}$ and $f^{\text{even}}_{n,m}$ defined in Eq. (9.46). Finally, the last element left, $\rho^{ge,eg\,(2)}_{g,g,n}(\tilde{\lambda})$, has the following form:

$$\rho^{ge,eg\,(2)}_{g,g,n}(\tilde{\lambda}) = \tilde{\lambda}^2 \sum_{m\geq 0} f^{\text{odd}}_{n,m}|I^m_n|^2, \tag{9.72}$$

although this element will not be needed to calculate the fidelity or the purity in Sec. 9.3.4 in second order approximation.

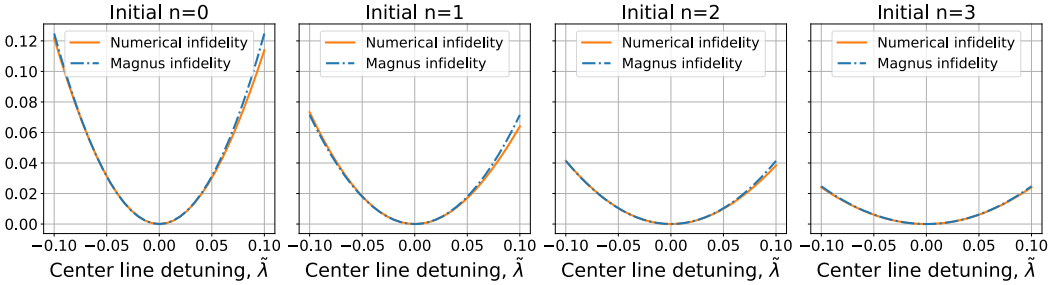

Figure 9.8: Infidelities predicted by the Magnus expansion model. Infidelity of the target internal state obtained for the ideal MS gate (no center line detuning) in Eq. (9.69) compared to the state obtained by numerically integrating the Hamiltonian in Eq. (9.27), and the fidelity estimation obtained from the second order Magnus expansion for initial motional states with $n = 0, 1, 2, 3$. The initial state used is $|g, g, n\rangle$, with the second order Magnus expansion prediction being Eq. (9.73).

Using this density matrix we can obtain the fidelity up to second order, which is given by

$$F^{(2)}_{g,g,n}(\tilde{\lambda}) = 1 + \frac{\tilde{\lambda}^2}{2}\left(c_{g,g,n} + c_{e,e,n} - \mathrm{Im}(b_n)\right), \tag{9.73}$$

We compare this result for the final state fidelities with the ones obtained numerically by integrating the Hamiltonian in Eq. (9.27) in Fig. 9.8.

Finally, we can generalise this result for the case of having an initial thermal state, for which we obtain

$$F^{(2)}_{g,g,\bar{n}}(\tilde{\lambda}) = \sum_n p_{\bar{n}}(n) F^{(2)}_{g,g,n}(\tilde{\lambda}). \tag{9.74}$$

9.3.4 Purity

Finally, we will study how much the center line detuned MS gate transforms the initial pure state $|g, g, n\rangle$ into a mixed state. In order to quantify this, we will consider again the density matrix of the final internal state, $\rho_{g,g,n}(\tilde{\lambda})$, which we will use to obtain its purity, $\gamma_{g,g,n}(\tilde{\lambda})$ (see Eq. (2.12)), given by

$$\chi_{g,g,n}(\tilde{\lambda}) = \mathrm{Tr}\left[\rho_{g,g,n}(\tilde{\lambda})^2\right]. \tag{9.75}$$

In a similar way as in the previous cases, the final purity does not show a first order dependence with the center line detuning. Therefore, we will consider the purity up to

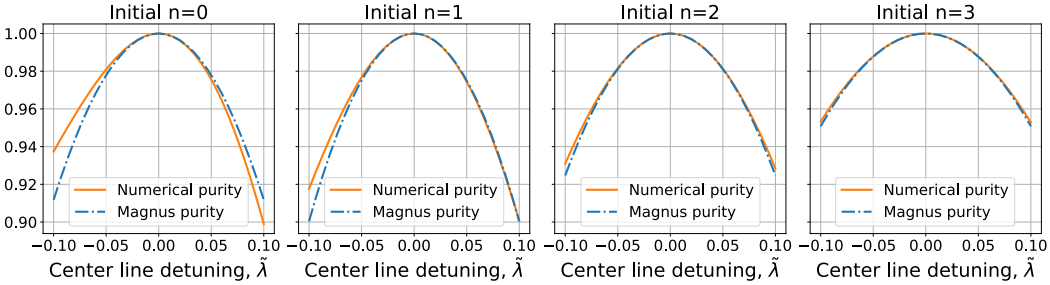

Figure 9.9: Purities predicted by the Magnus expansion model. Purity of the final state obtained numerically by taking $|g, g, n\rangle$ as the initial state compared to the purity obtained by using Eq. (9.76) derived from the second order Magnus expansion. The perturbative expression manages to capture the predominant second order effect of the center line detuning, with the differences from the numerics arising from terms of higher order not considered.

second order in the center line detuning, for which we obtain

$$\chi^{(2)}_{g,g,n}(\tilde{\lambda}) = \mathrm{Tr}\left[\left(\rho^{(2)}_{g,g,n}(\tilde{\lambda})\right)^2\right] = 1 - \tilde{\lambda}^2\left(\mathrm{Im}(b_n) - \frac{a_n^2}{2} - c_{g,g,n} - c_{e,e,n}\right). \tag{9.76}$$

From this result we can see that the phonon mixing introduced by the center line detuned MS gate affects the purity of the final state to second order in the center line detuning parameter. A comparison between the result in Eq. (9.76) and the numerics is shown in Fig. 9.9.

9.4 Experimental validation

In the previous section we compared the predictions of our model with the numerical simulation results. Now we will make a comparison of some of these model predictions with experimental results obtained by Lukas Gerster [2] at Innsbruck University.

To prepare the Fock states of the COM mode, the ions are initially Doppler cooled on the $4^2S_{1/2} \rightarrow 4^2P_{1/2}$ transition, followed by sideband cooling of the COM mode as explained in Sec. 4.3, to prepare the ground state $|g, g, 0\rangle$. We then apply a π-pulse to one of the ions to spectroscopically decouple it in an auxiliary level of the $D_{5/2}$ manifold [44]. We then apply alternating π-pulses on the blue and red sideband, where each pulse adds a single phonon. For odd phonon states, we apply a π-pulse on the carrier following the sideband pulses [188]. Finally, we retrieve the hidden ion from the auxiliary level. For the initial ground state cooling we find a mean phonon

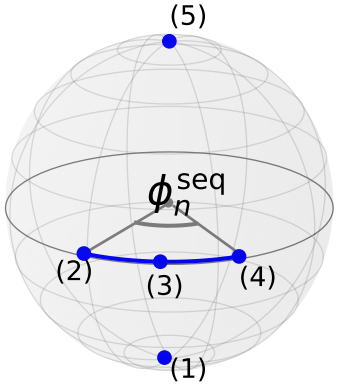

Figure 9.10: Cycle for the experimental phase measurement of the center line detuned MS gate. Representation of the effect of the MS gate sequence given by our model up to first order in the center line detuning. A center line detuned MS gate is applied to the initial state, $|g,g,n\rangle$ represented in (1). While the target state after a calibrated MS gate should be $1/\sqrt{2}(|g,g,n\rangle - i\,|e,e,n\rangle)$ in (2), the state after this first gate differs by a phase as given by Eq. (9.55), resulting in the state (3). The second detuned MS gate introduces a final phase, resulting in the state in (4), before applying the ideal entangling operation. The final state $|e,e,n\rangle$ in (5) after this sequence is obtained if the second MS gate has a relative phase with respect to the first one given by $\varphi_d = \phi_n^{\text{seq}}(\lambda)$.

number of $\bar{n} \approx 0.05$. After the preparation sequence for Fock states $n > 0$ we measure 5% population outside of the target electronic state, which decreases the signal-to-noise ratio of the measurement. We use an additional repumping step to return this population to the electronic ground state, but this leaves us with a corresponding error in the initial prepared Fock state.

After preparing the desired $|g,g,n\rangle$ state, we control the center line detuning of our MS gates. This center line detuning is introduced on purpose by changing the frequencies of the laser fields by λ from their ideal value. This causes the Hamiltonian of the MS gate to have the form

$$\hat{H}_{\text{exp}} = -\eta\Omega(a^\dagger e^{i\epsilon t} + a e^{-i\epsilon t})\left[S_y \cos(\varphi + \lambda\, t) + S_x \sin(\varphi + \lambda\, t)\right]. \tag{9.77}$$

This Hamiltonian can be obtained from the one that we considered in Eq. (9.25) with a time-independent value $\lambda(t) = \lambda$ by performing a picture change defined by $V(t) = R_z(2\,\lambda\, t)$. Therefore, after taking into account this picture change, all the results of our model can be used for this experiment. Although in the experiment the laser pulse is switched on and off adiabatically using a Blackman like shape [189], each of them requires only $\sim 4\%$ of the gate time. Due to this, we approximate the pulse-shape as a

constant one.

The evolution introduced by the MS gate in the experiment is, up to first order, given by

$$\hat{\mathcal{U}}^{(1),tr}_{n,\mathrm{exp},\varphi}(t_g,t_0) = R_z(2\lambda t_f)\hat{\mathcal{U}}^{(1),tr}_{n,\varphi}(t_g)R_z(-2\lambda t_0), \tag{9.78}$$

where t_0 is the time at the beginning of the gate, $t_f = t_0 + t_g$ is the time at the end, and we introduced φ to denote the phase of the MS gate. We perform a sequence of two center line detuned MS gates, where we consider that the second one has a relative phase of φ_d with respect to the first one. For this sequence, the resulting population predicted by our model, up to first order, is

$$\begin{aligned} P(ee,\lambda) &= \left|\langle e,e|\,\hat{\mathcal{U}}^{(1),tr}_{n,\mathrm{exp},\varphi_d}(2\,t_g,t_g)\hat{\mathcal{U}}^{(1),tr}_{n,\mathrm{exp},0}(t_g,0)\,|g,g\rangle\right|^2 \\ &= \left|\langle e,e|\,\mathrm{MS}_{\varphi_d}(\pi/2)R_z\left[-\phi_n^{\mathrm{seq}}(\lambda)\right]\mathrm{MS}_0(\pi/2)\,|g,g\rangle\right|^2 \\ &= \frac{1+\cos\left[2\,\varphi_d+\phi_n^{\mathrm{seq}}(\lambda)\right]}{2}, \end{aligned} \tag{9.79}$$

where

$$\phi_n^{\mathrm{seq}}(\lambda) = \frac{2\,\lambda\,a_n}{\epsilon} \tag{9.80}$$

represents the phase introduced by the center line detuning of the gates obtained from the first order terms of our model.

Using sequences of this type, we can measure the final population of $|e,e\rangle$ for a given center line detuning, while varying the value of φ_d. This data can then be used to experimentally obtain the values of $\phi_n^{\mathrm{seq}}(\lambda)$ for that center line detuning by fitting a cosine to the measurement outcomes, and compare them with the predicted values from our model. The fit includes amplitude and offset as free parameters, as higher order effects, dephasing, and SPAM errors will affect the amplitude of the observed oscillations. The comparison between the experimental results and the prediction from our model is shown in Fig. 9.11.

Using this setup, we can also study the behaviour of the populations after the application of a center line detuned gate in the experiment. In order to do this, we prepared $|g,g,n\rangle$ states with $n = 0,1,2,3$, to which we then applied a single MS gate while scanning over the center line detuning. A comparison between the experimental results and the populations predicted by our model up to second order is shown in Fig. 9.12.

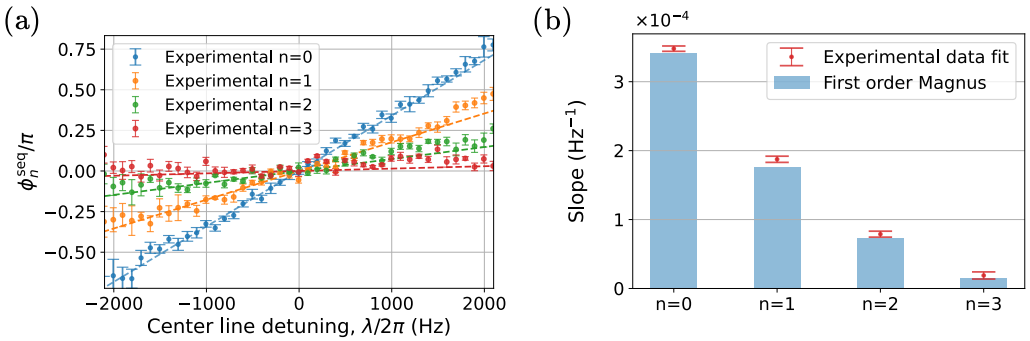

Figure 9.11: Experimental results for the phase error introduced by a center line detuned gate. (a) Experimental measurements of the phase $\phi_{\text{seq}}(\lambda)$ obtained by applying MS gates with $\epsilon = -2\pi \cdot 11\text{kHz}$ to initial states $|g, g, n\rangle$ with $n = 0, 1, 2, 3$. The dashed lines represent the corresponding estimated values of our model, obtained by using Eq. (9.80). The asymmetry of the error bars stems from the asymmetric behaviour of the $P(eg) + P(ge)$ outcomes observed in both the numerical simulations shown in Fig. 9.7 and the experimental results in Fig. 9.12, which causes an asymmetry on the contrast of the phase oscillation. (b) Comparison of the slope values obtained from first order Magnus expansion and from performing a linear fit using the experimental results.

9.5 Summary

In this chapter, we explained the results that we achieved in Ref. [2] for a semianalytical model to characterise the effects of a center line detuning on the implementation of a Mølmer-Sørensen gate. This model was obtained from a Magnus expansion where the center line detuning was considered as a perturbation to the ideal MS gate Hamiltonian. Using this approach, we have shown how to estimate the final states obtained after application of the miscalibrated MS gate, in our case up to first and second order on the center line detuning, by using a set of coefficients obtained from numerical integrations. Using these results it is then straightforward to understand the dependences of certain properties, such as relative phases, populations, fidelities, and purities, of the final states as polynomials characterised by the numerical coefficients mentioned before. We then compared the prediction of these properties obtained from our theoretical model to results from numerical integration, finding only minor differences arising for higher center line detuning values due to influence of higher than second order terms, which we do not consider in our work. However, this discrepancy between model and numerical predictions appears for values of the center line detuning higher than those appearing during an experimental calibration of the MS gate. The value of the center line detuning

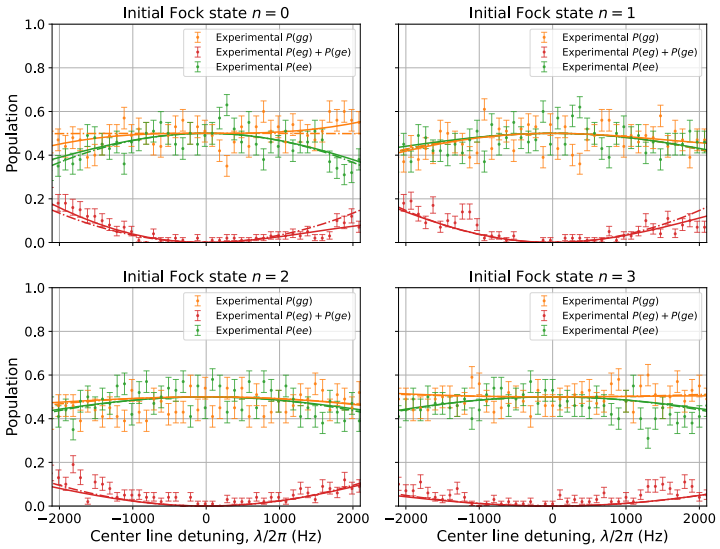

Figure 9.12: Experimental results for the populations after a center line detuned gate. Experimental measurements of the populations obtained by application of a MS gate with $\epsilon = -2\pi \cdot 11\text{kHz}$ to initial states $|g, g, n\rangle$ with $n = 0, 1, 2, 3$. The values obtained from the Magnus expansion are represented by the discontinuous lines, and the ones from numerical simulation by dashed-dotted lines.

miscalibration is typically only a fraction of the sideband detuning. Furthermore, we compared the predicted values of relative phases and populations from our model to values obtained from experimental measurements by systematically varying deliberately introduced center line detuning and find good agreement between the model predictions and the experimental results. These results further validated our model, and confirmed the utility of our model for studying and improving experimental implementations of the MS gate.

Our model was derived by assuming that the center line detuning was the only miscalibration, but this will not be the case in a real implementation of a MS gate, where other parameters will differ from their ideal values, with some of these examples and their consequences discussed in Sec. 9.1. However, in the cases where the center line detuning miscalibration is relatively larger than for the other parameters, it will be the predominant effect. In this case one can detect that the outcomes of the miscalibrated gate agree with the results expected from the analytical model, and this information can be used to compensate for the miscalibration of the center line detuning.

Overall, our model provides an in-depth understanding of the effects of a center line

detuning in an implementation of the MS gate, which before had only been assessed by performing numerical calculations [185]. This can then be used during the experimental calibration of the gate in order to identify and compensate the effect of center line detuning miscalibrations. Therefore, we believe that the method and the results presented here can help in designing and improving calibration routines for entangling gate operations. Indeed, with this in-depth understanding of the effects that the studied miscalibrations have on the MS gate, we are in a better position to explain in the next chapter the Bayesian protocol aimed at its calibration that we derived in Ref. [3].

Chapter 10

Bayesian calibration of the Mølmer–Sørensen gate

In Chapter 9 we introduced the Mølmer-Sørensen gate, used to create entanglement between trapped-ion qubits. We also explained some of the parameter miscalibrations that can appear during its implementation, as well as their effects on the performance of the gate. As we saw in that chapter, the implementation of the MS gate depends on a more complex physical model like the one shown in Sec. 4.3 for single-qubit gates. This higher complexity of the model increases the difficulty of properly calibrating the gate.

Several techniques have been developed over the years for the detection and characterisation of miscalibrated gates. In the experiment, one can perform quantum process tomography [190] to obtain a complete characterisation of a gate's action. However, as we saw in Sec. 2.5, this highly informative protocol has the drawback of scaling exponentially with the number of qubits involved in the gate [103]. Moreover, errors in the resulting characterisation can appear due to the existence of SPAM errors or systematic errors [191]. These problems motivate the use of alternative characterisation techniques such as randomised benchmarking [108, 192], cycle benchmarking [193, 194], gate set tomography [107, 108], machine-learning methods [195], and Bayesian inference protocols [196, 197]. Similarly as we did for other applications in this thesis, we will develop a Bayesian protocol for the detection and correction of the miscalibrations that can appear in the implementation of the MS gate.

Similar to the cases shown in Chapters 7 and 8, our Bayesian protocol benefits

from into account all the previous measurements when producing an estimate of the miscalibrations, even after changing the experimental settings. On top of this, our protocol will also enable a completely automated calibration process. However, we will find that the implementation of a Bayesian protocol for this gate has complications that did not appear in the calibration protocol for single-qubit gates shown in Chapter 8. Due to the higher complexity of the MS physical model, one needs to account for a higher number of parameters that can be miscalibrated in the experiment. This increases the difficulty of the calibration, not only due to higher dimensionality of the probability distributions involved but also because of correlations between experimental errors, which complicates the calibration of a single parameter at each time. Moreover, we also saw in Chapter 9 that there is no analytical derivation of the action of the gate for some of the parameters that we might consider to be miscalibrated. The lack of a likelihood function for the possible outcomes further complicates the implementation of a Bayesian protocol.

In this chapter, we address these difficulties and offer a Bayesian protocol for the calibration of the MS gate. This algorithm was developed in collaboration with the University of Innsbruck and implemented by the experimental collaborators, led by PhD student Lukas Gerster, in the joint work published in Ref. [3].

This chapter is organised as follows: In Sec. 10.1 we introduce the parameters in which we will focus our calibration process and explain their relevance. These parameters will be calibrated by using a set of control parameters and calibration rules that we describe in Sec. 10.2. In Sec. 10.3 we define our Bayesian protocol, with which we will obtain the estimates of the experimental parameters needed for their calibration, as well as all the components required for its implementation. Finally, in Sec. 10.4, we show the results obtained from this protocol.

10.1 Parameters of the calibration

In Chapter 9 we derived a MS gate Hamiltonian that included the contributions of the center line detuning, caused by an AC Stark shift of the qubit levels, $\lambda_{AC}(t)$, and a miscalibration of the frequencies of the bichromatic laser field, λ_l. We did this by considering the interaction picture defined by $W(t)$ in Eq. (9.24), which allowed us

to obtain the Hamiltonian in Eq. (9.25). In this chapter, we will consider a slightly different version of this interaction picture defined by $W_{AC}(t)$, given by

$$W_{AC}(t) = \exp\left[i \left(\sum_{j=1}^{N} \frac{\omega_{eg,0}\, t + \int_0^t \lambda_{AC}(t')dt'}{2} \sigma_{z,j} + \nu(a^\dagger a + 1/2)t \right) \right]. \tag{10.1}$$

Using this transformation and following a similar derivation as in the previous chapter, we obtain the Hamiltonian

$$\hat{H}(t) = -\eta\Omega(t)(a^\dagger e^{i\epsilon t} + a e^{-i\epsilon t}) \left[S_y \cos(\varphi + \Lambda(t)) + S_x \sin(\varphi + \Lambda(t)) \right], \tag{10.2}$$

which is the same that we obtained in Eq. (9.77), but including a time-dependent center line detuning. In Eq. (10.2) we used

$$\Lambda(t) \equiv \int_0^t \lambda(t')dt', \tag{10.3}$$

the integral of the total center line detuning $\lambda(t)$ as defined in Eq. (9.23).

In this chapter, we will use this new Hamiltonian, instead of the one in Eq. (9.25), to define the parameters that we want to calibrate in a more straightforward way. However, it is important to note that using one Hamiltonian or another is equivalent, since they only differ by a change of reference frame.

Now we are in the position of defining the parameters that we want to calibrate. First, in order to obtain the required entanglement between the qubits, we need to ensure that the rotation angle $\theta(t_g)$ at the end of the gate satisfies $\theta(t_g) = \pi/2$. Then, to avoid any residual entanglement between the internal states of the ions and their motional state at the end of the gate, the sideband detuning, ϵ, needs to be chosen such that the quantity $\Gamma(t)$, defined in Eq. (9.13), satisfies $\Gamma(t_g) = 0$. These first two conditions were derived and explained in more detail in Chapter 9, and they were found to be given, for the constant pulse-shape case, by $\theta(t_g) = (\eta\,\Omega)^2\, t_g/\epsilon = \pi/2$ and $\Gamma(t_g) = t_g|\epsilon| = 2\pi$. However, in the following we will consider that the laser pulse is switched on and off adiabatically using a Blackman-like shape [189], which is a better approximation of the pulse-shape used in the experiments. This pulse uses a small fraction of the gate time at the beginning of the pulse to increase the laser power to its maximum and, similarly, takes the same time to decrease the laser power to zero

at the end of the gate. The shape ensures adiabaticity during the switch-on and off of the laser, preventing unwanted excitation of the carrier transition [189]. Using this pulse-shape, we will redefine t_g as an effective gate time given by the duration of the laser pulse of the full width at half maximum.

The previous conditions were obtained for the case in which the laser frequencies are centered around the carrier at all times, that is, $\lambda(t) = 0$. When the AC Stark shift is time-dependent, this cannot be satisfied at all times using constant laser frequencies. In the following, we will consider that the center line detuning is time-independent, $\lambda(t) = \lambda$, even though this might not be the case, and we will aim to set it to zero. The error appearing from this approximation will be given by a non-zero integral $\Lambda(t_g)$. This error has the effect of accumulating an unwanted phase, $\Delta\varphi = \Lambda(t_g)$, for each application of each consecutive gate, as can be seen from Eq. (10.2). This cumulative phase can be detected by applying the MS gate more than once, and corrected by introducing a phase between consecutive gates.

Now that we know the conditions that we will be considering for a correct implementation of the MS gate, we will explain the control parameters that we can tune in order to realise a calibrated MS gate.

10.2 Experimental control parameters

In order to calibrate the MS gate we need to set the gate parameters

$$\boldsymbol{\Theta} = (\Omega,\, \lambda,\, \epsilon,\, \Delta\varphi), \tag{10.4}$$

as close as possible to their optimal values

$$\boldsymbol{\Theta}_{opt} = \left(\Omega_{\text{opt}} = \frac{\pi}{\eta t_g},\, \lambda_{opt} = 0,\, \epsilon_{opt} = \frac{2\pi}{t_g},\, \Delta\varphi_{opt} = 0\right), \tag{10.5}$$

where the condition for Ω_{opt} is obtained from setting $\theta(t_g) = (\eta\,\Omega)^2\, t_g/\epsilon = \pi/2$ and $\Gamma(t_g) = t_g|\epsilon| = 2\pi$. Since we do not have direct access to these experimental parameters, we rely on changing the control parameters of the gate $\boldsymbol{\Theta}_c = (t_g,\, f_{cl},\, f_{sb},\, \phi)$, i.e., the gate time t_g, the common frequency $f_{cl} = (f_r + f_b)/2$, which is the mean frequency between the red (f_r) and blue (f_b) tone of the laser, the frequency difference $2f_{sb} =$

$f_b - f_r$ of the bichromatic laser field, and the difference between the common phase between consecutive gates, ϕ.

These control parameters $\mathbf{\Theta}_c$ can be used to calibrate the gate in the following way: By performing measurements of the populations of the ions after the application of an MS gate sequence we obtain a set of estimates of the current experimental parameters, that we denote as

$$\overline{\mathbf{\Theta}} = (\overline{\Omega},\, \overline{\lambda},\, \overline{\epsilon},\, \overline{\Delta\varphi}). \tag{10.6}$$

These estimates can then be used to adjust the control parameters, $\mathbf{\Theta}_c$, to set $\mathbf{\Theta}$ equal to $\mathbf{\Theta}_{opt}$. This will be done in the following way: The time of the gate will be corrected as

$$t_g \to t_g \frac{\Omega_{\text{opt}}}{\overline{\Omega}}, \tag{10.7}$$

where we choose to change the gate time instead of the laser intensity since it is easier to control in the experiment, while producing an equivalent correction.

The other corrections are implemented by subtracting the difference between the estimated and the ideal parameter value from the control parameter. In the case of the sideband detuning this is given by

$$f_{sb} \to f_{sb} - \bar{\epsilon} + \epsilon_{opt}. \tag{10.8}$$

As for the correction of the center line detuning, this is described by

$$f_{cl} \to f_{cl} - \bar{\lambda} + \lambda_{opt}. \tag{10.9}$$

Finally, the phase between consecutive gates is changed as

$$\phi \to \phi - \overline{\Delta\varphi} + \Delta\varphi_{opt}. \tag{10.10}$$

With this set of rules, we will be able to update the parameters of the MS gate in order to iteratively bring the parameters $\mathbf{\Theta}$ closer to $\mathbf{\Theta}_{opt}$. In the following, we will consider an specific implementation of the MS gate with a Rabi frequency such as the ideal MS gate is achieved for a gate time of around $100\mu s$, which in turn corresponds to a target sideband detuning of around $\epsilon = 2\pi \cdot 10\text{kHz}$.

As we have seen, in order to calibrate the MS gate, we just need a way of obtaining the estimates $\overline{\mathbf{\Theta}}$. In the following, we will introduce a Bayesian protocol with which

we will be able to obtain and update our estimates after each set of measurements.

10.3 Bayesian inference protocol

While in Chapter 8 we implemented a Bayesian protocol that can be used for the calibration of single-qubit gates, we can already see some additional complications that will arise in the implementation of a Bayesian protocol for the calibration of the MS gate. First of all, for this case we do not have an analytical function for the likelihood function. While this is undesired, we will see how to solve this problem by using a numerical interpolator. The second problem that appears is that, since we have to estimate four parameters at the same time, the probability distributions involved will be four-dimensional, from which it might be inefficient to obtain the estimates and variances by using a naive approach. In order to solve this, we will particularise the particle filtering algorithm explained in Sec. 6.3. After solving these problems, we will then be able to define our Bayesian protocol.

10.3.1 Measurement settings

The measurements that we will be considering will consist in the application of MS gate sequences to an initial $|g, g\rangle$ state, and measuring the final populations of the qubits. The lengths of these sequences will be of $N_g = 1, ..., 7$ gates. The importance of performing sequences of more than one gate can be understood by considering that, for example, measurements of the populations after a single gate have no dependency on the phase difference miscalibration between MS gates, $\Delta\varphi$. Therefore, measuring the populations after a single gate yields no information about this parameter. Due to this, one needs to consider sequences of more than one gate. Furthermore, as the length of the gate sequence increases, so does the number of local maxima and minima of the corresponding likelihoods. This results in an enhanced sensitivity to miscalibrated gate parameters (see Fig. 10.1). However, this increased sensitivity by using longer gate sequences will be limited by errors not considered in our model, such as dephasing or amplitude damping of the qubits. Due to this, the longest gate sequences that we use consist in seven consecutive gates.

Additionally, one can introduce a phase difference between the gates, $\Delta\varphi_{\text{target}}$, on purpose. This can be done by changing the control parameter ϕ accordingly. In our

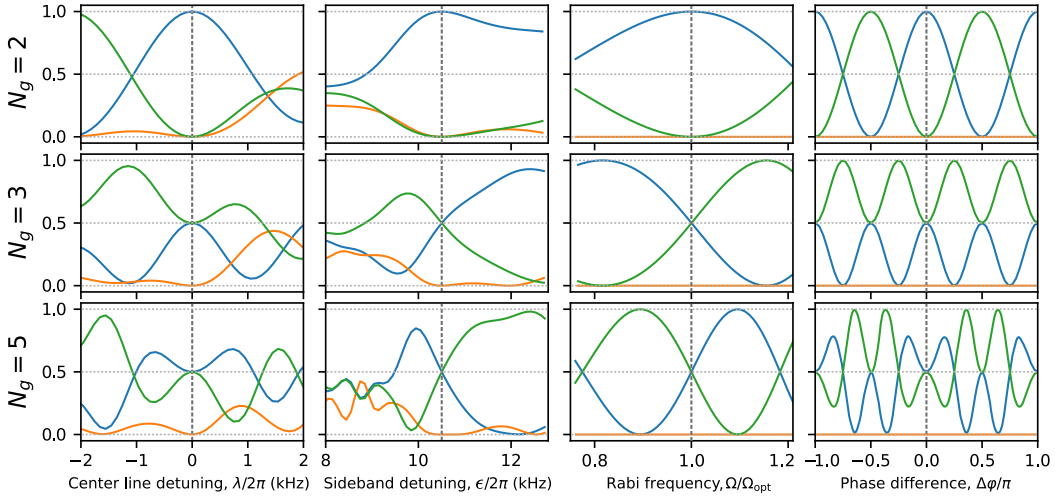

Figure 10.1: Scans of Mølmer-Sørensen gate sequences. Numerical simulations of scans of the populations of $|g,g\rangle$ (in green), $|e,e\rangle$ (in blue), and the sum of populations of $|e,g\rangle$ and $|g,e\rangle$ (in orange) of the final state obtained after sequences of $N_g = 2, 3$ and 5 gates. Each scan is performed by varying one of the parameters while keeping the others constant and equal to their optimal value for the MS gate. The vertical lines mark a set of optimal values for the parameters.

case, we will consider only the cases with $\Delta\varphi_{target} = 0$ or $\Delta\varphi_{target} = \pi/4$. The first case corresponds to sequences of MS gates without any relative phase introduced on purpose between each gate, while in the second case we introduce a relative phase of $\pi/4$ between each consecutive gate.

From this set of possible measurement settings, it is possible to obtain a criterion for the selection of optimal measurements, with some examples being discussed and compared in Ref. [3].

10.3.2 Interpolator

We have explained the different measurement settings that we will consider for the updates of our Bayesian protocol. However, we do not have analytical formulas for the likelihoods of each possible outcome given a measurement setting. These likelihoods could be obtained by numerical integration but, since we will be using a particle filter for our protocol, this integration should be performed for each particle of the particle filter at each iteration, which would make this approach prohibitively slow.

We will solve this problem by using an *interpolator*, which consists in a four-dimensional grid in the $\boldsymbol{\Theta}$ parameter space. Each of the points in the grid will have an

array composed by probabilities that the states $|e,e\rangle$, $|g,g\rangle$, $|e,g\rangle$ and $|g,e\rangle$ are measured after a gate sequence, given the values of $\mathbf{\Theta}$ associated to that point. These values are obtained from numerical integration of the Hamiltonian. To obtain the likelihoods for an arbitrary value in the parameter space we can then perform an interpolation with this discrete set of calculated likelihoods. For this we use a spline interpolator [198], which allows us to better approximate the outcome probabilities, without increasing the number of grid points required as compared to using linear interpolation. While the initial numerical calculations for all the points in the grid might be time consuming, these calculations must be done only once, before the actual experimental calibration. After obtaining these values, one can use them for approximating the likelihoods associated to a given gate sequence and point in parameter space. This can be done every time that a calibration of the gate is needed, without having to calculate the interpolator again. Since an interpolator depends on performing simple calculations to obtain the likelihoods, they are considerably faster than performing numerical integrations to obtain them. An interpolator is calculated for each of the previously mentioned gate sequences.

While there are other possible choices for an interpolator aside from the spline interpolator that we use, our choice produces faithful and fast enough results such that the interpolator is not a limiting factor of the calibration process. However, we note that for other calibration processes different from the MS gate calibration shown in this chapter, this might not be the case, which could require an in depth study of other types of interpolators with a potential to improve the efficiency.

10.3.3 Implementation of the particle filter

Now that we have an interpolator that gives us access to approximated values of the likelihoods, we are in the position to perform measurements in order to implement a Bayesian inference process. However, as we have seen, this inference process involves a four-dimensional probability distribution. This high dimensionality compromises the precision of the estimates and variances obtained from the inference process if one uses, for example, points in a fixed grid to evaluate the probability distributions. This occurs since, as the number of measurements increases, most of the fixed points used to sample the probability distribution would go to zero. This was the reason why we introduced in Sec. 6.3 the particle filtering algorithm, which updates the positions of the sampling

points to ensure that they are located in positions of the parameter space where the probability distribution is non-vanishing.

It is straightforward to particularise the particle filtering algorithm as described in Sec. 6.3 for the Bayesian inference estimation of the parameters $\mathbf{\Theta} = (\Omega, \lambda, \epsilon, \Delta\varphi)$. The inference protocol works as follows:

1. Sample a set of N_p particles from a simple initial probability distribution. In our case, we select our initial probability distribution to be a four-dimensional normal distribution with standard deviations of $\sigma_\Omega = 0.2 \cdot \Omega_{\text{opt}}$ for the Rabi frequency, $\sigma_\lambda = 2\pi \cdot 1\,\text{kHz}$ for the center line detuning, $\sigma_\epsilon = 2\pi \cdot 1\,\text{kHz}$ for the sideband detuning and $\sigma_{\Delta\varphi} = 0.33\pi$ for the phase, and we use $N_p = 10000$ particles. This value for N_p will be justified by the results shown in Sec. 10.4 and Fig. 10.4.

2. Select a measurement setting and perform a set of measurements.

3. Use the interpolator to obtain the likelihoods for the given measurement outcomes for each particle position and update their weights as given by Eq. (6.18).

4. Obtain the estimates, $\overline{\mathbf{\Theta}}_t$, and variances, $\text{Var}(\mathbf{\Theta}_t)$, at the current iteration, t, by using these updated particles as given by Eq. (6.19) and Eq. (6.20).

5. Resample the particles by using the SIR method as explained in Sec. 6.3.2 and displace them by introducing a small Gaussian noise to avoid stacking particles in the same positions.

6. Use the estimates obtained to update the control parameters as explained in Sec. 10.2, where the particles also have to be moved according to these corrections.

7. This completes an interation. Repeat the process starting from step 2 to perform the next iteration.

For a schematic of these steps, the reader is referred to Fig. 6.3.

10.3.4 Stopping criterion

Now that we have defined how to perform the Bayesian inference updates and, with it, the calibration protocol of the MS gate, we need a criterion to determine when to stop the protocol. In order to do this, we need to define a threshold that, when reached,

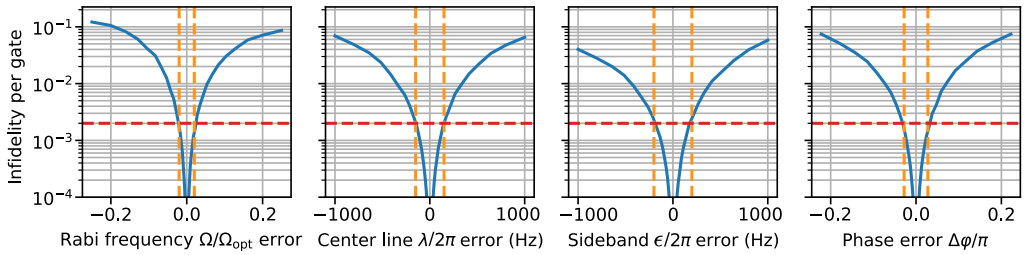

Figure 10.2: Randomised benchmarking stopping criterion. Expected infidelities per gate as a function of the individual parameter miscalibrations obtained from randomised benchmarking. The value $2 \cdot 10^{-3}$ (red dashed line) for each parameter has been chosen as an infidelity per gate threshold. These curves inform the choice of target thresholds for each experimental parameter (orange dashed lines) of values $T_\Omega = 0.02 \cdot \Omega_{\text{opt}}$, $T_\lambda = 2\pi \cdot 150\text{Hz}$, $T_\epsilon = 2\pi \cdot 200\text{Hz}$, $T_{\Delta\varphi} = 0.028\pi$.

informs us that the gate realised is good enough. In the Bayesian protocols explained in previous chapters, this was straightforward: In the case shown in Chapter 7, the uncertainty of the seven unwanted phases behaved equally, so it was enough to set a target uncertainty in the phases so that the algorithm could be stopped after reaching it. The case shown in Chapter 8 was similar, in which we would just need to define a target uncertainty in the laser frequency detuning with respect to the transition frequency under study. However, the current case is different. We have to calibrate four parameters, but we do not have any criterion yet for selecting the target uncertainties of each parameter. This is because we do not know how the performance of the gate depends on the errors of each parameter.

We solve this by simulating randomised benchmarking as explained in Sec. 2.5.3. We do this by keeping three of the parameters equal to their ideal values, while varying the fourth parameter. This process is repeated for each parameter. The results are four curves that tells us the behaviour of the fidelity per gate as a function of how far is each single parameter with respect to its ideal value (see Fig. 10.2).

Using these curves, we define a set of four thresholds, $T_{\boldsymbol{\Theta}} = (T_\Omega, T_\lambda, T_\epsilon, T_{\Delta\varphi})$, one for each experimental parameter, by obtaining the error for which these curves (shown in Fig. 10.2) start to have a bigger infidelity per gate than a selected threshold. The value of this infidelity per gate threshold is arbitrary, and in our case we chose $2 \cdot 10^{-3}$ since it is a value comparable to the achievable fidelity in the experimental system due to the presence of incoherent errors. This leads us to the following thresholds for each parameter: $T_\Omega = 0.02 \cdot \Omega_{\text{opt}}$, $T_\lambda = 2\pi \cdot 150\text{Hz}$, $T_\epsilon = 2\pi \cdot 200\text{Hz}$, $T_{\Delta\varphi} = 0.028\pi$.

We can then define our stopping criterion by using these thresholds. This will be done by stopping the protocol when the standard deviation of each parameter estimate is less than its corresponding threshold. However, it is important to note that reaching these thresholds for all the uncertainties does not mean that our infidelity per gate is smaller than the selected value of $2 \cdot 10^{-3}$. This is because the thresholds were obtained for the cases where only one of the parameters had a difference with respect to its ideal value. After the calibration, all the parameters will have slight deviations from their ideal values. Assuming the parameters are normally distributed with the standard deviation of the distributions equal to the thresholds we expect, from simulation, a median infidelity of $\approx 5 \cdot 10^{-3}$.

10.4 Results of the Bayesian calibration

In the previous section we have introduced all the components necessary for the implementation of a Bayesian inference protocol with the goal of obtaining the set of estimates, $\overline{\boldsymbol{\Theta}} = (\overline{\Omega}, \overline{\lambda}, \overline{\epsilon}, \overline{\Delta\varphi})$, of the parameters of the MS gate. The control parameters, $\boldsymbol{\Theta}_c = (t_g, f_{cl}, f_{sb}, \phi)$, can then be updated after each iteration of the Bayesian protocol by using the estimates obtained after that iteration. The calibration will then be finished after reaching the thresholds defined by the stopping criterion. A simulation of a run of this protocol, reaching the stopping criterion thresholds after eleven iterations (for a total of 1100 measurements), is shown in Fig. 10.3.

In order to study the performance of the algorithm, we define a distance of an initial set of experimental parameters to the target ones as

$$D^2_{\text{start}} = \sum_{\Theta} \frac{(\Theta_{\text{start}} - \Theta_{\text{opt}})^2}{\sigma^2_{\Theta}} \tag{10.11}$$

with σ^2_{Θ} being the variance of the prior distribution considered at the beginning of the calibration projected onto one of the experimental parameters, Θ, and Θ_{start} and Θ_{opt} being the corresponding starting value and optimal value, respectively, for that parameter. Using this definition of distance, we randomly generated sets of values of the experimental parameters at different distances, and performed Bayesian calibration on each of them. The phase was not varied since it is a periodic parameter, which limits how far the phase values can be from the optimal value. Using these results,

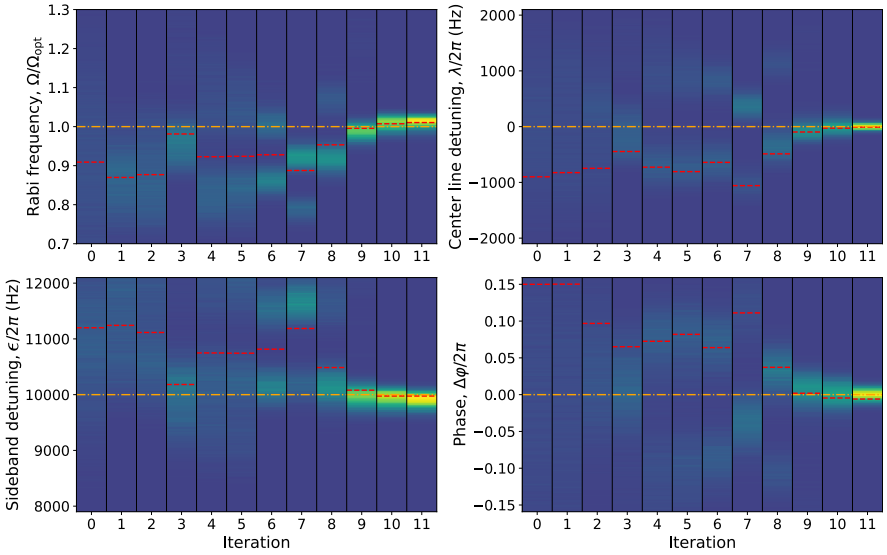

Figure 10.3: Example of a simulated MS gate Bayesian calibration. Projections of the particle densities of the particle filter for the experimental parameters, $\mathbf{\Theta} = (\Omega, \lambda, \epsilon, \Delta\varphi)$, at each iteration, t, of a single calibration run, with $t = 0$ representing the particles obtained from the prior four-dimensional normal distribution. The projections of the probability densities are normalised to their corresponding maximum values achieved during the calibration. The red lines represent the true value of each experimental parameter at a given iteration, and the orange lines represents the ideal target values to be achieved. For each iteration a measurement setting is used to obtain 100 measurement outcomes. The initial values of the experimental parameters used for this case are $\Omega_{\text{start}} = 0.91 \cdot \Omega_{\text{opt}}$, $\lambda_{\text{start}} = -2\pi \cdot 0.9\text{kHz}$, $\epsilon_{\text{start}} = 2\pi \cdot 11.2\text{kHz}$, and $\Delta\varphi_{\text{start}} = 0.3\pi$. The algorithm stops after eleven iterations, when it reaches the thresholds defined in Sec. 10.3.4 for the standard deviations of all the parameters, which have a value at the end of the calibration of $\sigma_{\Omega,\text{final}} = 0.007 \cdot \Omega_{\text{opt}}$, $\sigma_{\lambda,\text{final}} = 2\pi \cdot 51\text{Hz}$, $\sigma_{\epsilon,\text{final}} = 2\pi \cdot 117\text{Hz}$, and $\sigma_{\Delta\varphi,\text{final}} = 0.014\pi$. The true values of the experimental parameters achieved from this calibration are $\Omega_{\text{final}} = 1.009 \cdot \Omega_{\text{opt}}$, $\lambda_{\text{final}} = -2\pi \cdot 22\text{Hz}$, $\epsilon_{\text{final}} = 2\pi \cdot 9990\text{Hz}$, and $\Delta\varphi_{\text{final}} = 0.01\pi$.

we considered that, for each calibration process, the algorithm converged correctly if the experimental parameters obtained after the calibration were closer to their ideal values than twice the stopping thresholds. Following this procedure, we managed to obtain the convergence of the calibration protocol as a function of the initial distance of the experimental parameters. This process can also be done for different number of particles, N_p, which can be used to inform our decision on how many particles to use. The results are shown in Fig. 10.4.

Using this protocol, a calibration of the MS gate in the experiment was shown in Ref. [3]. In this implementation, a total of 100 measurements were performed for each

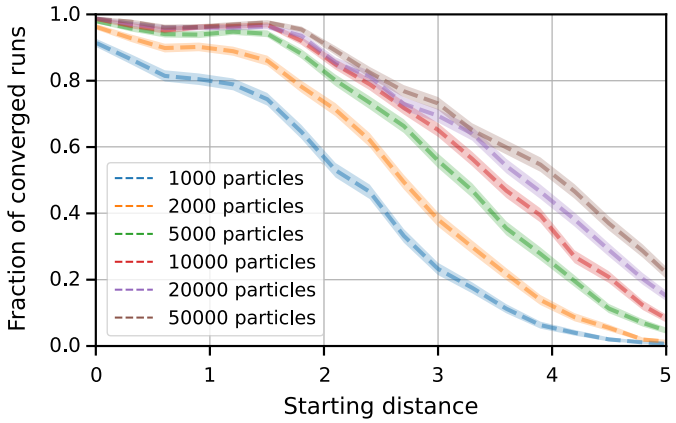

Figure 10.4: Capture range of the Bayesian protocol. The performance of our Bayesian protocol is analysed by simulating calibration rounds for initial sets of experimental parameters at different distances, as defined in Eq. (10.11), and obtaining the fraction of converged runs for each distance and number of particles used. A run is considered to have converged correctly if the distance of the experimental parameters obtained to the target values is less than two times the stopping thresholds. For each distance, 2000 tuneups were run. The initial normal prior distribution used was defined by the following standard deviations: $\sigma_\Omega = 0.2 \cdot \Omega_{\text{opt}}$, $\sigma_\epsilon = 2\pi \cdot 1\text{kHz}$, $\sigma_{\omega_{cl}} = 2\pi \cdot 1\text{kHz}$, and $\sigma_{\Delta\varphi} = 0.33\pi$.

iteration, requiring a total of 1200 ± 500 measurements to reach the target thresholds used for the stopping criterion. The time required for the complete calibration protocol was 41 ± 17s, achieving a median gate infidelity of $1.3(1) \cdot 10^{-3}$. The difference between this mean infidelity and the one of $5 \cdot 10^{-3}$ estimated in Sec. 10.3.4 was attributed to correlations appearing between the parameters partially compensating each other. We then compared in Ref. [3] our Bayesian protocol to another calibration protocol based on manual iterations over single parameter scans as defined in Ref. [199]. We found that the experimental results obtained using the Bayesian algorithm outperform the simulations of iterative single parameter scans both in terms of median gate infidelity achieved and measurements required. Examples of the efficiencies of these single parameter scans are a median gate infidelity of $4 \cdot 10^{-2}$ when performing 2000 measurements, which gets improved up to a median gate infidelity of $7 \cdot 10^{-3}$ when performing 5900 for the calibration. As can be seen, these results are considerable worse than the median gate infidelity obtained with our protocol, while also requiring a considerable higher number of measurements.

10.5 Summary

In this chapter we introduced a Bayesian inference protocol to estimate and calibrate the experimental parameters of an entangling two-qubit Mølmer-Sørensen gate. This process presented additional complications as compared to the other protocols explained in Chapter 7 and 8, such as the non-existence of an analytical likelihood function, or performing Bayesian inference with relatively high-dimensional probability distributions. In order to solve these problems, we introduced a numerical interpolator that allowed for fast numerical estimations of likelihoods at points in parameter space. This interpolator was then used with a particle filtering algorithm that allowed us to work with four-dimensional probability distributions efficiently. Using these tools, we obtained a completely automated Bayesian protocol that can be used for the calibration of the MS gate. A more advanced version of this protocol was then used in Ref. [3] to calibrate MS gates in the experiment, with improvements such as rules to optimise the measurement settings. This calibration of the MS gate in the experiment required 1200 ± 500 shots, and resulted in gates with a median residual infidelity of 0.13%.

While this protocol is particularised for the calibration of the MS gate, which in turn is a gate specific to trapped-ion architectures, it is possible to generalise it for other calibration problems. Due to this, similar Bayesian protocols can be studied and implemented for the calibration of other quantum gates in other physical platforms. This broad applicability of Bayesian protocols appears due to their only dependency on having access to a likelihood of the different possible experimental outcomes, which depends mainly on having a model of the Hamiltonian introduced by the gate. Finally, the tools that we used, such as the interpolators or the particle filtering algorithm, to avoid the difficulties arising during the derivation of our MS gate calibration protocol can be used in other Bayesian applications where these problems might appear.

Chapter 11

Conclusions and Outlook

The field of quantum information has been the subject of considerable work for the past years. The physical platforms that were theoretically proposed for the implementation of quantum information processing only a few decades ago led to the current experimental implementations of qubits and high-fidelity gates. Thanks to these developments, we are currently crossing the threshold from testing and improving quantum information processing implementations, to more complex and interesting experiments. Within these advanced implementations, one can think of two possible paths to follow: The first one is the development and experimental realisation of fault-tolerant QEC codes, which will be needed for a longer term implementation of an error free quantum computer. The second one consists in taking advantage of the currently available NISQ devices to run small quantum algorithms, with the goal of obtaining advantages with respect to classical computers. While these fields are seeing considerable and exciting advances, they still depend on further efforts to improve the current gates or increase the number of qubits available in a register.

The research presented in this thesis has been developed in this direction, with the main objective of designing protocols for the calibration of gates and quantum states. An objective when designing these protocols is to reduce the resources that they require, namely the amount of measurements required, and time invested by the laboratory personnel. The importance of this is clear: On the one hand, decreasing the number of measurements needed allows for a calibration that is faster than the time scales on which the to-be-calibrated parameters drift, leaving more time to perform other experiments with a calibrated setup. On the other hand, as the size of the quantum device achieved

in the experiment increases, so does the number of different calibrations that must be performed. This poses a scalability problem unless the calibration protocols are completely automated.

The protocols developed in this thesis make use of Bayesian inference to achieve the desired calibration. We have shown that these protocols have clear advantages, with respect to the aforementioned goals, as compared to other currently used calibration protocols based on frequentist approaches. The Bayesian inference process offers a clear criterion to obtain an estimate of the desired calibration parameters, which takes into account all the previous measurements. Furthermore, since these protocols work with probability distributions, they have direct access to not only the estimates, but also to their corresponding uncertainties, something that is, in general, more demanding for frequentist approaches. With respect to the number of measurements required, we have also shown that Bayesian protocols allow for a clear and intuitive interpretation on how to select measurement settings that optimise the information gained, effectively decreasing the amount of measurements needed. Finally, the simplicity of the Bayesian inference process, and the selection rules for the measurement settings, allow for a complete automation of the calibration protocols, which can be easily implemented by a computer program.

The protocols developed in this thesis were aimed at solving problems relevant in current quantum computers. In Chapter 7, we developed a protocol for the correction of unwanted phases appearing in the encoding of the logical states in the Steane code, which was the result of our work in Ref. [1]. This protocol uses a simple analytical rule for selecting optimal measurements and takes advantage of all the measurements. Due to these advantages, we demonstrated that our protocol requires 13 times less measurements than a frequentist approach that was implemented in the experiment in Ref. [52]. While, in the longer term, some parts of the error compensation achieved by our protocol might be taken care of by the QEC protocols themselves, in the near term it is a useful tool to compensate for the imperfections currently present on experimental preparations of the Steane code. In this direction, a possible generalisation of our protocol could be the improvement of other QEC codes of larger size, such as the recent experimental implementations of the surface code [200, 201]. Moreover, these protocols could also be used for the correction of stabiliser measurements. For this, a model of

the circuits used to perform stabiliser measurements, with possible error sources, could be developed. These errors could then be characterised by means of Bayesian inference, and taken into account for an improvement of the QEC code implementation in the experiment.

In Chapter 8, we developed a Bayesian protocol in a trapped-ion architecture to estimate the detuning of a laser frequency with respect to the qubit transition. Similarly as in the previous case, using this approach we obtained an analytical rule for selecting optimal measurement settings. This Bayesian protocol was then completely automated, and used to perform a dynamic calibration in the experiment. A possible continuation of this study could consist in the improvement of the protocol by introducing non-linear models for the drift. However, for us the most appealing generalisation was the study of this type of protocol for the calibration of entangling gates.

In Chapter 9, we introduced the Mølmer-Sørensen gate, used for creating entanglement between trapped-ion qubits. We developed a semianalytical model, based on a Magnus perturbative expansion, for understanding how the presence of a center line detuning affected the gate. The results from this line of research resulted in Ref. [2]. The predictions of our model were in agreement both with numerical simulations and experimental results. However, our proposed model could be further improved in different ways. For example, the predictions of our model for the populations are limited by the order of the Magnus expansion, but higher order terms could be calculated by using our systematic treatment to accurately predict higher order behaviours. Additionally, in the results shown, we considered that the pulse shape of the laser used to implement the MS gate was constant in time. However, one could consider a general time-dependent laser pulse to study the effect that the center line detuning has on a given pulse shape. This could be readily done by following a similar derivation as we did, and could be specially useful when considering implementations of fast gates [202–206], for which considering the laser pulse as constant might not be a valid approximation. Another interesting approach would consist in the incorporation of other miscalibrations on top of the center line detuning. A way to do this would consist in using the effects that were derived analytically for the other miscalibrations, and combine them with our model, since correlations between errors in these parameters should appear only from terms higher or equal to second order. The derivation of such a model could open the way for an analytical derivation of the interpolators, which we had to calculate numerically

for the Bayesian calibration of the MS gate. Finally, one could further generalise this model by considering open-system dynamics to account for additional sources of errors such as dephasing of the quantum states, or using a similar Magnus expansion approach to characterise the effects of miscalibrations in other quantum gates.

Equipped with a clear model of the MS gate and its parameters, we then introduced a Bayesian protocol aimed at its calibration in Chapter 10. An advanced version of this protocol, which included a criterion for the selection of optimal measurements, was then satisfactorily implemented in the experiment in Ref. [3]. For this case, we also obtained a completely automated protocol, for which we had to use auxiliary elements such as an interpolator, and a particle-filtering algorithm. Both of these auxiliary elements are not specific to this calibration protocol, and could be used for multi-parameter calibration of other quantum gates. Additionally, this protocol has been particularised for two-qubit entangling gates. This motivates the question of how this protocol could be extended for entangling gates of N qubits. Regarding this, an advantage of the MS gate is its simple generalisation for the entanglement of N qubits, which would allow the use of the same experimental parameters as the ones shown in this chapter. Due to this, our protocol would be generalisable to a higher number of qubits as long as the simulations performed to obtain the interpolator manage to describe other experimental imperfections such as magnetic field gradients or unequal Rabi frequencies on the individual ions. Another possible improvement would consist in using this protocol for performing a dynamical calibration of the four parameters involved, by modelling their evolution as a drift over time in a similar way as it was studied for the laser-locking case. Finally, another topic of research could consist in the study of the evolution of the qubits state by considering open-system dynamics. This would provide a more accurate physical model of the evolution introduced by the gate, and improve the quality of the interpolators, yielding an improvement of the estimates obtained with the protocol.

All of these Bayesian protocols were developed for specific calibrations, and some of them are even specific for trapped-ion architectures. However, an important outlook is that the parts that compose the Bayesian protocols as we implemented them are platform-agnostic, independent of the experiment that one wants to calibrate. That means that, as long as the likelihoods for all the possible outcomes in an experiment are available, one can develop and implement a Bayesian protocol. As a consequence,

the cases shown in this thesis can serve as a guide for generalising Bayesian protocols for the calibration of other quantum gates in other quantum computing architectures, or the improvement of QEC codes implemented in experiments.

Technical acknowledgement:

Numerical simulations have been performed on the Swansea SUNBIRD system. The Swansea SUNBIRD system is part of the Supercomputing Wales project, which is part-funded by the European Regional Development Fund (ERDF) via Welsh Government.

Appendix A

Appendices

A.1 Generalisation for the three-plaquette case

In this appendix, we provide details on the expressions appearing in the three-plaquette case. For the seven-qubit Steane code the logical 0 is given by

$$\begin{aligned}|0\rangle_L =&\frac{1}{2\sqrt{2}}(|0000000\rangle + |0110110\rangle + |1111000\rangle + |1001110\rangle \\ &+ |0011011\rangle + |0101101\rangle + |1100011\rangle + |1010101\rangle)\end{aligned} \tag{A.1}$$

Due to experimental errors, phases appear in the preparation of the $|0\rangle_L$ state. The state obtained will be then

$$\begin{aligned}|0'\rangle_L =&\frac{1}{2\sqrt{2}}(|0000000\rangle + e^{i\phi_1}|0110110\rangle + e^{i\phi_2}|1111000\rangle + e^{i\phi_3}|1001110\rangle \\ &+ e^{i\phi_4}|0011011\rangle + e^{i\phi_5}|0101101\rangle + e^{i\phi_6}|1100011\rangle + e^{i\phi_7}|1010101\rangle)\end{aligned} \tag{A.2}$$

Single-qubit Z rotations can be performed on the seven qubits of the code state $|0'\rangle_L$ to obtain the following state and likelihoods for each stabiliser combination

$$\begin{aligned}|0'\rangle_L \xrightarrow{\text{Rotations}} &\frac{1}{2\sqrt{2}}(|0000000\rangle + e^{i[\phi_1+2(\theta_2+\theta_3+\theta_5+\theta_6)]}|0110110\rangle \\ &+ e^{i[\phi_2+2(\theta_1+\theta_2+\theta_3+\theta_4)]}|1111000\rangle + e^{i[\phi_3+2(\theta_1+\theta_4+\theta_5+\theta_6)]}|1001110\rangle \\ &+ e^{i[\phi_4+2(\theta_3+\theta_4+\theta_6+\theta_7)]}|0011011\rangle + e^{i[\phi_5+2(\theta_2+\theta_4+\theta_5+\theta_7)]}|0101101\rangle \\ &+ e^{i[\phi_6+2(\theta_1+\theta_2+\theta_6+\theta_7)]}|1100011\rangle + e^{i[\phi_7+2(\theta_1+\theta_3+\theta_5+\theta_7)]}|1010101\rangle),\end{aligned} \tag{A.3}$$

$$P_1(\pm_{\boldsymbol{\theta}}|\boldsymbol{\phi}) = \frac{1}{8}\{4 \pm \cos[\phi_2 + 2(\theta_1+\theta_2+\theta_3+\theta_4)] \pm \cos[\phi_1 - \phi_3 + 2(-\theta_1+\theta_2+\theta_3-\theta_4)]$$

$$\pm \cos[\phi_4 - \phi_6 + 2(-\theta_1-\theta_2+\theta_3+\theta_4)] \pm \cos[\phi_5 - \phi_7 + 2(-\theta_1+\theta_2-\theta_3+\theta_4)]\}, \tag{A.4}$$

$$P_2(\pm_{\boldsymbol{\theta}}|\boldsymbol{\phi}) = \frac{1}{8}\{4 \pm \cos[\phi_1 + 2(\theta_2+\theta_3+\theta_5+\theta_6)] \pm \cos[\phi_2 - \phi_3 + 2(\theta_2+\theta_3-\theta_5-\theta_6)]$$

$$\pm \cos[\phi_4 - \phi_5 + 2(-\theta_2+\theta_3-\theta_5+\theta_6)] \pm \cos[\phi_6 - \phi_7 + 2(\theta_2-\theta_3-\theta_5+\theta_6)]\}, \tag{A.5}$$

$$P_3(\pm_{\boldsymbol{\theta}}|\boldsymbol{\phi}) = \frac{1}{8}\{4 \pm \cos[\phi_4 + 2(\theta_3+\theta_4+\theta_6+\theta_7)] \pm \cos[\phi_1 - \phi_5 + 2(\theta_3-\theta_4+\theta_6-\theta_7)]$$

$$\pm \cos[\phi_2 - \phi_6 + 2(\theta_3+\theta_4-\theta_6-\theta_7)] \pm \cos[\phi_3 - \phi_7 + 2(-\theta_3+\theta_4+\theta_6-\theta_7)]\}, \tag{A.6}$$

$$P_{12}(\pm_{\boldsymbol{\theta}}|\boldsymbol{\phi}) = \frac{1}{8}\{4 \pm \cos[\phi_3 + 2(\theta_1+\theta_4+\theta_5+\theta_6)] \pm \cos[\phi_1 - \phi_2 + 2(-\theta_1-\theta_4+\theta_5+\theta_6)]$$

$$\pm \cos[\phi_4 - \phi_7 + 2(-\theta_1+\theta_4-\theta_5+\theta_6)] \pm \cos[\phi_5 - \phi_6 + 2(-\theta_1+\theta_4+\theta_5-\theta_6)], \tag{A.7}$$

$$P_{13}(\pm_{\boldsymbol{\theta}}|\boldsymbol{\phi}) = \frac{1}{8}\{4 \pm \cos[\phi_6 + 2(\theta_1+\theta_2+\theta_6+\theta_7)] \pm \cos[\phi_1 - \phi_7 + 2(-\theta_1+\theta_2+\theta_6-\theta_7)]$$

$$\pm \cos[\phi_2 - \phi_4 + 2(\theta_1+\theta_2-\theta_6-\theta_7)] \pm \cos[\phi_3 - \phi_5 + 2(\theta_1-\theta_2+\theta_6-\theta_7)]\}, \tag{A.8}$$

$$P_{23}(\pm_{\boldsymbol{\theta}}|\boldsymbol{\phi}) = \frac{1}{8}\{4 \pm \cos[\phi_5 + 2(\theta_2+\theta_4+\theta_5+\theta_7)] \pm \cos[\phi_1 - \phi_4 + 2(\theta_2-\theta_4+\theta_5-\theta_7)]$$

$$\pm \cos[\phi_2 - \phi_7 + 2(\theta_2+\theta_4-\theta_5-\theta_7)] \pm \cos[\phi_3 - \phi_6 + 2(-\theta_2+\theta_4+\theta_5-\theta_7)]\}, \tag{A.9}$$

$$P_{123}(\pm_{\boldsymbol{\theta}}|\boldsymbol{\phi}) = \frac{1}{8}\{4 \pm \cos[\phi_7 + 2(\theta_1+\theta_3+\theta_5+\theta_7)] \pm \cos[\phi_1 - \phi_6 + 2(-\theta_1+\theta_3+\theta_5-\theta_7)]$$

$$\pm \cos[\phi_2 - \phi_5 + 2(\theta_1+\theta_3-\theta_5-\theta_7)] \pm \cos[\phi_3 - \phi_4 + 2(\theta_1-\theta_3+\theta_5-\theta_7)]\}. \tag{A.10}$$

The expected values of each plaquette can be easily obtained from these expressions.

For example, the first plaquette expected value is given by

$$\langle S_x^{(1)} \rangle = P_1(+_{\boldsymbol{\theta}}|\boldsymbol{\phi}) - P_1(-_{\boldsymbol{\theta}}|\boldsymbol{\phi}) \tag{A.11}$$

The expected values for the other plaquettes can be obtained from the corresponding likelihood in the same way. The marginal likelihoods are given by

$$P_1(\pm_{\boldsymbol{\theta}}|\phi_2) = \frac{4 \pm \cos[\phi_2 - \tilde{\theta}_2]}{8} \tag{A.12}$$

$$P_2(\pm_{\boldsymbol{\theta}}|\phi_1) = \frac{4 \pm \cos[\phi_1 - \tilde{\theta}_1]}{8} \tag{A.13}$$

$$P_3(\pm_{\boldsymbol{\theta}}|\phi_4) = \frac{4 \pm \cos[\phi_4 - \tilde{\theta}_4]}{8} \tag{A.14}$$

$$P_{12}(\pm_{\boldsymbol{\theta}}|\phi_3) = \frac{4 \pm \cos[\phi_3 - \tilde{\theta}_3]}{8} \tag{A.15}$$

$$P_{13}(\pm_{\boldsymbol{\theta}}|\phi_6) = \frac{4 \pm \cos[\phi_6 - \tilde{\theta}_6]}{8} \tag{A.16}$$

$$P_{23}(\pm_{\boldsymbol{\theta}}|\phi_5) = \frac{4 \pm \cos[\phi_5 - \tilde{\theta}_5]}{8} \tag{A.17}$$

$$P_{123}(\pm_{\boldsymbol{\theta}}|\phi_7) = \frac{4 \pm \cos[\phi_7 - \tilde{\theta}_7]}{8} \tag{A.18}$$

where

$$\tilde{\Theta} = \begin{cases} \tilde{\theta}_2 \equiv -2(\theta_1 + \theta_2 + \theta_3 + \theta_4) \\ \tilde{\theta}_1 \equiv -2(\theta_2 + \theta_3 + \theta_5 + \theta_6) \\ \tilde{\theta}_4 \equiv -2(\theta_3 + \theta_4 + \theta_6 + \theta_7) \\ \tilde{\theta}_3 \equiv -2(\theta_1 + \theta_4 + \theta_5 + \theta_6) \\ \tilde{\theta}_6 \equiv -2(\theta_1 + \theta_2 + \theta_6 + \theta_7) \\ \tilde{\theta}_5 \equiv -2(\theta_2 + \theta_4 + \theta_5 + \theta_7) \\ \tilde{\theta}_7 \equiv -2(\theta_1 + \theta_3 + \theta_5 + \theta_7) \end{cases} \tag{A.19}$$

As for the generalization of the pseudocode in Fig. 7.6, it is achieved by changing the previous definitions to the following ones

$$
\begin{aligned}
&J = 1, ..., 7, \\
&S = \{\, \tilde{\theta}_i = \phi_i + \beta_i \,\}, \\
&\mathcal{Q} = \{\, 1, 2, 3, 4, 5, 6, 7 \,\}, \\
&\mathcal{T} = \{\, \theta_1, \theta_2, \theta_3, \theta_4, \theta_5, \theta_6, \theta_7 \,\}, \\
&\boldsymbol{\phi} = \{\, \phi_1, \phi_2, \phi_3, \phi_4, \phi_5, \phi_6, \phi_7 \,\}, \\
&\mathcal{P} = \{\, P(\phi_1), P(\phi_2), P(\phi_3), P(\phi_4), P(\phi_5), P(\phi_6), P(\phi_7) \,\}, \\
&\mathcal{S} = \{S_x^{(2)}, S_x^{(1)}, S_x^{(1)}S_x^{(2)}, S_x^{(3)}, S_x^{(2)}S_x^{(3)}, S_x^{(1)}S_x^{(3)}, S_x^{(1)}S_x^{(2)}S_x^{(3)}\}, \\
&\Pi = \{P_2(\pm\boldsymbol{\theta}|\phi_1), P_1(\pm\boldsymbol{\theta}|\phi_2), P_{12}(\pm\boldsymbol{\theta}|\phi_3), P_3(\pm\boldsymbol{\theta}|\phi_4), P_{23}(\pm\boldsymbol{\theta}|\phi_5), P_{13}(\pm\boldsymbol{\theta}|\phi_6), P_{123}(\pm\boldsymbol{\theta}|\phi_7)\},
\end{aligned}
\tag{A.20}
$$

where the β_i in S are chosen randomly from the set $\{+\pi/2, -\pi/2\}$.

A.2 Analytical study of the variance scaling for the phase measurement case

In this appendix, we present some details on the scaling of the variance with the number of measurements when applying the Bayesian adaptive method to the single-qubit state of Eq. (7.3) in Chapter 7. The expressions obtained are easy to generalise to the two and three-plaquette cases, appearing also in that chapter.

Let us suppose that after n measurements the knowledge about the phase ϕ is given by a normal distribution with mean value $\overline{\phi}_n$ and variance σ_n^2

$$
P_n(\phi) = \frac{1}{\sqrt{2\pi\sigma_n^2}} e^{-\frac{(\phi-\overline{\phi}_n)^2}{2\sigma_n^2}}. \tag{A.21}
$$

After performing a measurement the updated probability distribution is given by

$$
P_{n+1}^{\pm}(\phi) = \frac{1}{p_{n+1}^{\pm}} \left(\frac{1 \pm \cos(\phi - \theta_{n+1})}{2} \right) P_n(\phi), \tag{A.22}
$$

where $p_{n+1}^{\pm}$ is the probability at step n of obtaining a $+$ or $-$ in the measurement $n+1$. Since at step n it is unknown what the measurement $n+1$ will yield, we consider the

expected value of the variance after the measurement $n+1$, $\overline{\sigma^2}_{n+1}$

$$\overline{\sigma^2}_{n+1} = p^+_{n+1}(\sigma^+_{n+1})^2 + p^-_{n+1}(\sigma^-_{n+1})^2, \tag{A.23}$$

where $(\sigma^\pm_{n+1})^2$ are the variances after obtaining a $+$ or $-$ for the measurement $n+1$ given by

$$(\sigma^\pm{}_{n+1})^2 = \int_{-\pi}^{\pi} \phi^2 P^\pm_{n+1}(\phi)d\phi - \left(\int_{-\pi}^{\pi} \phi P^\pm_{n+1}(\phi)d\phi\right)^2. \tag{A.24}$$

This yields

$$\begin{aligned} p^+_{n+1}(\sigma^+_{n+1})^2 = &\int_{-\pi}^{\pi} \phi^2 P_n(\phi)\frac{1+\cos(\phi-\theta_{n+1})}{2}d\phi \\ &- \frac{1}{p^+_{n+1}}\left(\int_{-\pi}^{\pi} \phi P_n(\phi)\frac{1+\cos(\phi-\theta_{n+1})}{2}d\phi\right)^2, \end{aligned} \tag{A.25}$$

$$\begin{aligned} p^-_{n+1}(\sigma^-_{n+1})^2 = &\int_{-\pi}^{\pi} \phi^2 P_n(\phi)\frac{1-\cos(\phi-\theta_{n+1})}{2}d\phi \\ &- \frac{1}{p^-_{n+1}}\left(\int_{-\pi}^{\pi} \phi P_n(\phi)\frac{1-\cos(\phi-\theta_{n+1})}{2}d\phi\right)^2. \end{aligned} \tag{A.26}$$

Introducing (A.25) and (A.26) into (A.23) yields

$$\begin{aligned} \overline{\sigma^2}_{n+1} = \sigma^2_n &- \frac{1}{4p^+_{n+1}p^-_{n+1}} \\ &\times \left(\int_{-\pi}^{\pi} \phi P_n(\phi)\cos(\phi-\theta_{n+1})d\phi\right)^2 + \frac{p^+_{n+1}-p^-_{n+1}}{2p^+_{n+1}p^-_{n+1}}\left(\int_{-\pi}^{\pi} \phi P_n(\phi)d\phi\right) \\ &\times \left(\int_{-\pi}^{\pi} \phi P_n(\phi)\cos(\phi-\theta_{n+1})d\phi\right) + \frac{4p^+_{n+1}p^-_{n+1}-1}{4p^+_{n+1}p^-_{n+1}}\left(\int_{-\pi}^{\pi} \phi P_n(\phi)d\phi\right)^2 \end{aligned} \tag{A.27}$$

where

$$4p^+_{n+1}p^-_{n+1} - 1 = -\left(\int_{-\pi}^{\pi} P_n(\phi)\cos(\phi-\theta_{n+1})d\phi\right)^2 \tag{A.28}$$

$$p^+_{n+1} - p^-_{n+1} = \left(\int_{-\pi}^{\pi} P_n(\phi)\cos(\phi-\theta_{n+1})d\phi\right) \tag{A.29}$$

Thus, we obtain

$$\overline{{\sigma^2}_{n+1} - {\sigma^2}_n} = -\frac{1}{p^+_{n+1}p^-_{n+1}}\left[\left(\int_{-\pi}^{\pi}\frac{P_n(\phi)\cos(\phi-\theta_{n+1})}{2}d\phi\right)\right.$$
$$\left.\times\left(\int_{-\pi}^{\pi}\phi P_n(\phi)d\phi\right) - \left(\int_{-\pi}^{\pi}\frac{\phi P_n(\phi)\cos(\phi-\theta_{n+1})}{2}d\phi\right)\right]^2 \tag{A.30}$$

If we consider $P_n(\phi)$ has a low enough standard deviation we can change the intervals of integration $[-\pi,\pi)$ with $(-\infty,\infty)$ to obtain

$$\int_{-\infty}^{\infty}\phi P_n(\phi)d\phi = \overline{\phi}_n,$$
$$\int_{-\infty}^{\infty}\frac{P_n(\phi)\cos(\phi-\theta_{n+1})}{2}d\phi = \frac{e^{-\sigma_n^2/2}}{2}\cos\big(\overline{\phi}_n-\theta_{n+1}\big),$$
$$\int_{-\infty}^{\infty}\frac{\phi P_n(\phi)\cos(\phi-\theta_{n+1})}{2}d\phi = -\frac{e^{-\sigma_n^2/2}\sigma_n^2}{2}\sin\big(\overline{\phi}_n-\theta_{n+1}\big) + \frac{e^{-\sigma_n^2/2}\bar{\phi}_n}{2}\cos\big(\overline{\phi}_n-\theta_{n+1}\big),$$
$$p^{\pm}_{n+1} = \frac{1}{2}\left(1 \pm e^{-\sigma_n^2/2}\cos\big(\overline{\phi}_n-\theta_{n+1}\big)\right). \tag{A.31}$$

Replacing the values of these integrals in (A.30) we obtain

$$\overline{{\sigma^2}_{n+1} - {\sigma^2}_n} = -\frac{e^{-\sigma_n^2}\sigma_n^4\sin^2(\overline{\phi}_n-\theta_{n+1})}{1-e^{-\sigma_n^2}\cos^2(\overline{\phi}_n-\theta_{n+1})}. \tag{A.32}$$

Similar calculations can be performed for the two and three plaquette case likelihoods, the only difference being the cosine appearing in the likelihood having amplitude 1/4 and 1/8 respectively and the angle $\tilde{\theta}_{i,n+1}$ being a linear combination of the rotations performed on different qubits for measurement $n+1$. Taking this into account, for the two-plaquette case the decrease in the variance for each ϕ_i is

$$\overline{{\sigma^2}_{i,n+1} - {\sigma^2}_{i,n}} = -\frac{e^{-\sigma_{i,n}^2}\sigma_{i,n}^4\sin^2(\overline{\phi}_{i,n}-\theta_{i,n+1})}{4-e^{-\sigma_{i,n}^2}\cos^2(\overline{\phi}_{i,n}-\theta_{i,n+1})} \tag{A.33}$$

and for the three-plaquette case

$$\overline{{\sigma^2}_{i,n+1} - {\sigma^2}_{i,n}} = -\frac{e^{-\sigma_{i,n}^2}\sigma_{i,n}^4\sin^2(\overline{\phi}_{i,n}-\theta_{i,n+1})}{16-e^{-\sigma_{i,n}^2}\cos^2(\overline{\phi}_{i,n}-\theta_{i,n+1})}. \tag{A.34}$$

A.3 Analytical study of the variance scaling for the Ramsey cycle case

In this appendix, we present the scaling of the variance with the number of measurements when applying the Bayesian adaptive method to the Ramsey spectroscopy in Chapter 8.

Let us suppose that after n measurements the knowledge about the detuning Δ is given by a normal distribution with mean value $\overline{\Delta}_n$ and variance σ_n^2

$$P_n(\Delta) = \frac{1}{\sqrt{2\pi\sigma_n^2}} e^{-\frac{(\Delta-\overline{\Delta}_n)^2}{2\sigma_n^2}}. \tag{A.35}$$

We can follow the same procedure as we did in Appendix A.2, but using the likelihood in Eq. (8.15). With this, we obtain the following integrals

$$\begin{aligned}
&\int_{-\infty}^{\infty} \Delta P_n(\Delta) d\Delta = \overline{\Delta}_n, \\
&\int_{-\infty}^{\infty} \frac{P_n(\Delta)\cos(\Delta+\phi_{n+1})}{2} d\Delta = \frac{e^{-\sigma_n^2\tau_{R,n+1}^2/2}}{2}\cos\big(\overline{\Delta}_n\tau_{R,n+1}+\phi_{n+1}\big), \\
&\int_{-\infty}^{\infty} \frac{\Delta P_n(\Delta)\cos(\Delta+\phi_{n+1})}{2} d\Delta \\
&= \frac{e^{-\sigma_n^2\tau_{R,n+1}^2/2}}{2}\Big[\overline{\Delta}_n\cos\big(\overline{\Delta}_n\tau_{R,n+1}+\phi_{n+1}\big) - \sigma_n^2\tau_{R,n+1}\sin\big(\overline{\Delta}_n\tau_{R,n+1}+\phi_{n+1}\big)\Big], \\
&p_{n+1}^{\pm} = \frac{1}{2}\left[1 \pm e^{-\sigma_n^2\tau_{R,n+1}^2/2}\cos\big(\overline{\Delta}_n\tau_{R,n+1}+\phi_{n+1}\big)\right],
\end{aligned} \tag{A.36}$$

where we use $+$ and $-$ in $p_{n+1}^{\pm}$ to denote a $|1\rangle$ and $|0\rangle$ measurement, respectively. Using these results and (A.30), we obtain

$$\overline{{\sigma^2}_{n+1} - {\sigma^2}_n} = -\frac{e^{-\sigma_n^2\tau_{R,n+1}^2}\sigma_n^4\tau_{R,n+1}^2\sin^2(\overline{\Delta}_n\tau_{R,n+1}+\phi_{n+1})}{1-e^{-\sigma_n^2\tau_{R,n+1}^2}\cos^2(\overline{\Delta}_n\tau_{R,n+1}+\phi_{n+1})}. \tag{A.37}$$

Assuming that $\overline{\Delta}_n$, which is always possible if after each measurement we correct the detuning so that the normal distribution in Eq. (A.35) is centered around zero, we obtain

$$\overline{{\sigma^2}_{n+1} - {\sigma^2}_n} = -\frac{e^{-\sigma_n^2\tau_{R,n+1}^2}\sigma_n^4\tau_{R,n+1}^2\sin^2(\phi_{n+1})}{1-e^{-\sigma_n^2\tau_{R,n+1}^2}\cos^2(\phi_{n+1})}. \tag{A.38}$$

This expected decrease in the variance is maximised when the measurement settings of

the $n+1$ measurement are selected to be $\phi_{n+1} = \pi/2$ and $\tau_{R,n+1} = 1/\sigma_n$.

A.4 Numerical coefficients

In this appendix, we derive the form of the numerical coefficients that were used in Chapter 9. In the basis defined by the eigenstates of S_y, $|+,+\rangle$, $|+,-\rangle$, $|-,+\rangle$ and $|-,-\rangle$, where

$$|\pm\rangle = \frac{1}{\sqrt{2}}(|g\rangle \pm i\,|e\rangle), \tag{A.39}$$

the evolution operator of the ideal MS gate can be written as

$$\hat{U}_0(\tau) = \begin{pmatrix} D[F(\tau)]e^{iG(\tau)} & 0 & 0 & 0 \\ 0 & 1 & 0 & 0 \\ 0 & 0 & 1 & 0 \\ 0 & 0 & 0 & D[-F(\tau)]e^{iG(\tau)} \end{pmatrix}, \tag{A.40}$$

where $F(\tau) = \tilde{\Omega}(e^{i\tau} - 1)$ and $G(\tau) = \tilde{\Omega}^2(\tau - \sin\tau)$. From Eq. (9.33) and Eq. (9.36) we obtain

$$\hat{U}_{1,M}(\tau_g) \equiv \hat{U}_0(\tau_g)M_1(\tau_g) = -i\tilde{\lambda}\int_0^{\tau_g} \hat{U}_0^\dagger(\tau' - \tau_g)\, S_z\, \hat{U}_0(\tau')d\tau'. \tag{A.41}$$

Analysing the form of the integrand shows that its application couples a $|+,+,n\rangle$ state with $|+,-,m\rangle$ and $|-,+,m\rangle$, with corresponding coefficients $I^{++,n}_{+-,m}$ and $I^{++,n}_{+-,m}$, that is

$$\hat{U}_{1,M}(\tau_g)\,|+,+,n\rangle = -\tilde{\lambda}\sum_{m=0} I^{++,n}_{+-,m}\,|+,-,m\rangle + I^{++,n}_{-+,m}\,|-,+,m\rangle\,. \tag{A.42}$$

Similarly, for the action on other S_y basis states we obtain

$$\hat{U}_{1,M}(\tau_g)\,|-,-,n\rangle = -\tilde{\lambda}\sum_{m=0} I^{--,n}_{+-,m}\,|+,-,m\rangle + I^{--,n}_{-+,m}\,|-,+,m\rangle\,, \tag{A.43}$$

$$\hat{U}_{1,M}(\tau_g)\,|+,-,n\rangle = -\tilde{\lambda}\sum_{m=0} I^{+-,n}_{++,m}\,|+,+,m\rangle + I^{+-,n}_{--,m}\,|-,-,m\rangle\,, \tag{A.44}$$

$$\hat{U}_{1,M}(\tau_g)\,|-,+,n\rangle = -\tilde{\lambda}\sum_{m=0} I^{-+,n}_{++,m}\,|+,+,m\rangle + I^{-+,n}_{--,m}\,|-,-,m\rangle\,. \tag{A.45}$$

These coefficients are obtained from numerical integration of matrix elements as described in Eq. (A.41), and they can all be described in terms of $I_m^n \equiv I_{+-,m}^{++,n}$,

$$I_{+-,m}^{++,n} = I_{-+,m}^{++,n} = I_{++,n}^{+-,m} = I_{++,n}^{-+,m} = I_m^n, \tag{A.46}$$

$$I_{+-,m}^{--,n} = I_{-+,m}^{--,n} = I_{--,n}^{+-,m} = I_{--,n}^{-+,m} = (-1)^{n-m} I_m^n. \tag{A.47}$$

Therefore, it is enough to calculate the coefficients I_m^n, which have the form

$$I_m^n = \frac{i}{2} \int_0^{\tau_g} e^{iG(\tau)} \langle m| D[F(\tau)] |n\rangle \, d\tau, \tag{A.48}$$

where for $m \geq n$

$$\langle m| D(\alpha) |n\rangle = \sqrt{\frac{m!}{n!}} \alpha^{m-n} e^{-|\alpha|^2/2} \sum_{k=0}^{n} (-1)^k \binom{n}{k} \frac{|\alpha|^{2k}}{(m-n+k)!}, \tag{A.49}$$

and for $m < n$

$$\langle m| D(\alpha) |n\rangle = \sqrt{\frac{m!}{n!}} (\alpha^*)^{n-m} e^{-|\alpha|^2/2} \sum_{k=0}^{m} (-1)^{n-k} \binom{n}{k} \frac{|\alpha|^{2(m-k)}}{(m-k)!}. \tag{A.50}$$

By using these expressions, one can numerically calculate the I_m^n coefficients for the first order Magnus expansion.

As for the second order coefficients, we have to work with Eq. (9.34) and the second order terms of Eq. (9.36) to obtain them. This requires to calculate the action of the following operators

$$\hat{U}_0(\tau_g) M_2(\tau_g) = -\frac{\tilde{\lambda}^2}{2} \hat{U}_0(\tau_g) \int_0^{\tau_g} \int_0^{\tau_1} \left[\hat{U}_0^\dagger(\tau_1) \, S_z \, \hat{U}_0(\tau_1), \hat{U}_0^\dagger(\tau_2) \, S_z \, \hat{U}_0(\tau_2) \right] d\tau_2 d\tau_1, \tag{A.51}$$

$$\hat{U}_0(\tau_g) M_1(\tau_g)^2 = -\tilde{\lambda}^2 \int_0^{\tau_g} \int_0^{\tau_g} \hat{U}_0^\dagger(\tau_1 - \tau_g) \, S_z \, \hat{U}_0(\tau_1) \hat{U}_0^\dagger(\tau_2) \, S_z \, \hat{U}_0(\tau_2) d\tau_2 d\tau_1, \tag{A.52}$$

where for convenience we define the combination of these operators as

$$\hat{U}_{2,M}(\tau_g) = \hat{U}_0(\tau_g) \left(M_2(\tau_g) + \frac{M_1(\tau_g)^2}{2} \right) \tag{A.53}$$

By close inspection of the previous integrands, one can see that they couple $|+,+,n\rangle$

and $|-,-,n\rangle$ to states of the form $|+,+,m\rangle$ and $|-,-,m\rangle$

$$\hat{U}_{2,M}(\tau_g)\,|+,+,n\rangle = -\tilde{\lambda}^2 \sum_{m=0} J^n_{1,m}\,|+,+,m\rangle + J^n_{2,m}\,|-,-,m\rangle\,, \tag{A.54}$$

$$\hat{U}_{2,M}(\tau_g)\,|-,-,n\rangle = -\tilde{\lambda}^2 \sum_{m=0} J^n_{2,m}\,|+,+,m\rangle + J^n_{1,m}\,|-,-,m\rangle\,. \tag{A.55}$$

Similarly, they couple $|+,-,n\rangle$ and $|-,+,n\rangle$ to $|+,-,m\rangle$ and $|-,+,m\rangle$

$$\hat{U}_{2,M}(\tau_g)\,|+,-,n\rangle = -\tilde{\lambda}^2 \sum_{m=0} J^n_{3,m}(|+,-,m\rangle + |-,+,m\rangle), \tag{A.56}$$

$$\hat{U}_{2,M}(\tau_g)\,|-,+,n\rangle = -\tilde{\lambda}^2 \sum_{m=0} J^n_{3,m}(|+,-,m\rangle + |-,+,m\rangle), \tag{A.57}$$

where the coefficients, $J^n_{1,m}$, $J^n_{2,m}$, and $J^n_{3,m}$, can be calculated by numerically integrating Eq. (A.51) and Eq. (A.52) using Eq. (A.49) and Eq. (A.50). Their expressions are

$$\begin{aligned} J^n_{1,m} = {} & \frac{1}{4}\int_0^{\tau_g}\int_0^{\tau_1} e^{-i(G(\tau_1)-G(\tau_2)-G(\tau_g))}\,\langle m|\,D(F(\tau_g))D^\dagger(F(\tau_1))D(F(\tau_2))\,|n\rangle\,d\tau_2 d\tau_1 \\ & - \frac{1}{4}\int_0^{\tau_g}\int_0^{\tau_1} e^{i(G(\tau_1)-G(\tau_2)+G(\tau_g))}\,\langle m|\,D(F(\tau_g))D^\dagger(F(\tau_2))D(F(\tau_1))\,|n\rangle\,d\tau_2 d\tau_1 \\ & + \frac{1}{4}\int_0^{\tau_g}\int_0^{\tau_g} e^{i(G(\tau_2)-G(\tau_1-\tau_g))}\,\langle m|\,|D^\dagger(F(\tau_1-\tau_g))D(F(\tau_2))\,|n\rangle\,d\tau_2 d\tau_1 \end{aligned} \tag{A.58}$$

$$\begin{aligned} J^n_{2,m} = {} & \frac{1}{4}\int_0^{\tau_g}\int_0^{\tau_1} e^{-i(G(\tau_1)-G(\tau_2)-G(\tau_g))}\,\langle m|\,D^\dagger(F(\tau_g))D(F(\tau_1))D(F(\tau_2))\,|n\rangle\,d\tau_2 d\tau_1 \\ & - \frac{1}{4}\int_0^{\tau_g}\int_0^{\tau_1} e^{i(G(\tau_1)-G(\tau_2)+G(\tau_g))}\,\langle m|\,D^\dagger(F(\tau_g))D(F(\tau_2))D(F(\tau_1))\,|n\rangle\,d\tau_2 d\tau_1 \\ & + \frac{1}{4}\int_0^{\tau_g}\int_0^{\tau_g} e^{i(G(\tau_2)-G(\tau_1-\tau_g))}\,\langle m|\,D(F(\tau_1-\tau_g))D(F(\tau_2))\,|n\rangle\,d\tau_2 d\tau_1 \end{aligned} \tag{A.59}$$

$$\begin{aligned} J^n_{3,m} = {} & \frac{1}{8}\int_0^{\tau_g}\int_0^{\tau_1} e^{i(G(\tau_1)-G(\tau_2))}\,\langle m|\,D^\dagger(F(\tau_1))D(F(\tau_2)) + D(F(\tau_1))D^\dagger(F(\tau_2))\,|n\rangle\,d\tau_2 d\tau_1 \\ & - \frac{1}{8}\int_0^{\tau_g}\int_0^{\tau_1} e^{i(G(\tau_2)-G(\tau_1))}\,\langle m|\,D^\dagger(F(\tau_2))D(F(\tau_1)) - D(F(\tau_2))D^\dagger(F(\tau_1))\,|n\rangle\,d\tau_2 d\tau_1 \\ & + \frac{1}{8}\int_0^{\tau_g}\int_0^{\tau_g} e^{i(G(\tau_1)-G(\tau_2))}\,\langle m|\,D^\dagger(F(\tau_1))D(F(\tau_2)) + D(F(\tau_1))D^\dagger(F(\tau_2))\,|n\rangle\,d\tau_2 d\tau_1 \end{aligned} \tag{A.60}$$

After obtaining the numerical coefficients I_m^n, $J_{1,m}^n$, $J_{2,m}^n$, and $J_{3,m}^n$, we can write the action of the center line detuned gate over the states $|+,+,n\rangle$, $|+,-,n\rangle$, $|-,+,n\rangle$ and $|-,-,n\rangle$. To consider the action over the states $|g,g,n\rangle$, $|g,e,n\rangle$, $|e,g,n\rangle$ and $|e,e,n\rangle$ it is enough to use

$$|g,g,n\rangle = \frac{1}{2}\Big(|+,+,n\rangle + |+,-,n\rangle + |-,+,n\rangle + |-,-,n\rangle \Big), \tag{A.61}$$

$$|g,e,n\rangle = \frac{-i}{2}\Big(|+,+,n\rangle - |+,-,n\rangle + |-,+,n\rangle - |-,-,n\rangle \Big), \tag{A.62}$$

$$|e,g,n\rangle = \frac{-i}{2}\Big(|+,+,n\rangle + |+,-,n\rangle - |-,+,n\rangle - |-,-,n\rangle \Big), \tag{A.63}$$

$$|e,e,n\rangle = \frac{1}{2}\Big(- |+,+,n\rangle + |+,-,n\rangle + |-,+,n\rangle - |-,-,n\rangle \Big). \tag{A.64}$$

Using the previous relations and Eq. (A.42)-(A.45), we obtain the first order correction to the states, $\left|\psi^{(1)}_{\sigma,\sigma',n}\right\rangle$, defined in Eq. (9.43)-(9.45). Similarly, Using Eq. (A.54)-(A.57), we obtain the second order correction to the states, $\left|\psi^{(2)}_{\sigma,\sigma',n}\right\rangle$, defined in Eq. (9.57)-(9.59), where we introduced the following coefficients

$$J_{+,m}^n = \frac{J_{1,m}^n + J_{2,m}^n + 2J_{3,m}^n}{2}, \tag{A.65}$$

$$J_{-,m}^n = \frac{J_{1,m}^n + J_{2,m}^n - 2J_{3,m}^n}{2}. \tag{A.66}$$

Finally, from the form of the final state corrected up to second order when using the initial state $|g,g,n\rangle$, $\left|\Psi^{(2)}_{g,g,n}\right\rangle$, we can calculate the coefficients that are used in Sec. 9.3.2 and Sec. 9.3.4:

$$c_{g,g,n} = -\mathrm{Re}\Big(J_{+,n}^n\Big) - \mathrm{Im}\Big(J_{+,n}^n\Big) + \sum_{m\geq 0} |I_m^n + I_n^m|^2 f_{n,m}^{\mathrm{even}}, \tag{A.67}$$

$$c_{e,e,n} = \mathrm{Re}\Big(J_{-,n}^n\Big) - \mathrm{Im}\Big(J_{-,n}^n\Big) + \sum_{m\neq n} |I_m^n - I_n^m|^2 f_{n,m}^{\mathrm{even}}, \tag{A.68}$$

$$c_{e,g,n} = \sum_{m\neq n} |I_n^m|^2 f_{n,m}^{\mathrm{odd}}. \tag{A.69}$$

The corresponding coefficients when the initial state is in a different state of the computational basis can be calculated in a similar way.

References

[1] F. Martínez-García, D. Vodola, and M. Müller, "Adaptive Bayesian phase estimation for quantum error correcting codes," *New Journal of Physics* **21** no. 12, (2019) 123027. 7, 77, 89, 162

[2] F. Martínez-García, L. Gerster, D. Vodola, P. Hrmo, T. Monz, P. Schindler, and M. Müller, "Analytical and experimental study of center-line miscalibrations in Mølmer-Sørensen gates," *Physical Review A* **105** no. 3, (2022) 032437. 8, 120, 141, 144, 163

[3] L. Gerster, F. Martínez-García, P. Hrmo, M. van Mourik, B. Wilhelm, D. Vodola, M. Müller, R. Blatt, P. Schindler, and T. Monz, "Experimental Bayesian calibration of trapped-ion entangling operations," *PRX Quantum* **3** no. 2, (2022) 020350. 9, 146, 148, 153, 158, 159, 160, 164

[4] A. M. Turing, "On computable numbers, with an application to the Entscheidungsproblem," *Proceedings of the London mathematical society* **2** no. 1, (1937) 230–265. 1

[5] G. E. Moore *et al.*, "Cramming more components onto integrated circuits," 1965. 1

[6] J. Schmidhuber, "Deep learning in neural networks: An overview," *Neural networks* **61** (2015) 85–117. 1

[7] R. P. Feynman, "Simulating physics with computers," *International Journal of Theoretical Physics* **21** no. 6-7, (1982) 467–488. 1

[8] P. W. Shor, "Polynomial-time algorithms for prime factorization and discrete logarithms on a quantum computer," *SIAM review* **41** no. 2, (1999) 303–332. 2

[9] L. K. Grover, "A fast quantum mechanical algorithm for database search," in *Proceedings of the twenty-eighth annual ACM symposium on Theory of computing*, pp. 212–219. 1996. 2

[10] R. L. Rivest, A. Shamir, and L. Adleman, "A method for obtaining digital signatures and public-key cryptosystems," *Communications of the ACM* **21** no. 2, (1978) 120–126. 2

[11] C. H. Bennett and G. Brassard, "Quantum cryptography: Public key distribution and coin tossing," in *Proceedings of the International Conference on Computers, Systems and Signal Processing*, pp. 175–179. 1984. 2

[12] N. Gisin, G. Ribordy, W. Tittel, and H. Zbinden, "Quantum cryptography," *Reviews of Modern Physics* **74** no. 1, (2002) 145.

[13] G. Cariolaro, *Quantum communications*. Springer, 2015. 2

[14] W. K. Wootters and W. H. Zurek, "A single quantum cannot be cloned," *Nature* **299** no. 5886, (1982) 802–803. 2, 57

[15] C. L. Degen, F. Reinhard, and P. Cappellaro, "Quantum sensing," *Reviews of Modern Physics* **89** no. 3, (2017) 035002. 2

[16] B. Bauer, S. Bravyi, M. Motta, and G. K.-L. Chan, "Quantum algorithms for quantum chemistry and quantum materials science," *Chemical Reviews* **120** no. 22, (2020) 12685–12717. 2

[17] S. McArdle, S. Endo, A. Aspuru-Guzik, S. C. Benjamin, and X. Yuan, "Quantum computational chemistry," *Reviews of Modern Physics* **92** no. 1, (2020) 015003. 2

[18] M. A. Nielsen and I. L. Chuang, *Quantum computation and quantum information*. Cambridge University Press, 2002. 2, 13, 19, 23, 59

[19] J. I. Cirac and P. Zoller, "Quantum computations with cold trapped ions," *Physical Review Letters* **74** no. 20, (1995) 4091. 2, 3, 43, 54

[20] H. Häffner, C. F. Roos, and R. Blatt, "Quantum computing with trapped ions," *Physics Reports* **469** no. 4, (2008) 155–203.

[21] K. R. Brown, J. Kim, and C. Monroe, "Co-designing a scalable quantum computer with trapped atomic ions," *npj Quantum Information* **2** no. 1, (2016) 1–10.

[22] R. Blatt and D. Wineland, "Entangled states of trapped atomic ions," *Nature* **453** no. 7198, (2008) 1008–1015.

[23] B. B. Blinov, D. Leibfried, C. Monroe, and D. J. Wineland, "Quantum computing with trapped ion hyperfine qubits," *Quantum Information Processing* **3** no. 1, (2004) 45–59.

[24] T. Harty, D. Allcock, C. J. Ballance, L. Guidoni, H. Janacek, N. Linke, D. Stacey, and D. Lucas, "High-fidelity preparation, gates, memory, and readout of a trapped-ion quantum bit," *Physical Review Letters* **113** no. 22, (2014) 220501.

[25] T. Sriarunothai, S. Wölk, G. S. Giri, N. Friis, V. Dunjko, H. J. Briegel, and C. Wunderlich, "Speeding-up the decision making of a learning agent using an ion trap quantum processor," *Quantum Science and Technology* **4** no. 1, (2018) 015014.

[26] M. Johanning, A. F. Varón, and C. Wunderlich, "Quantum simulations with cold trapped ions," *Journal of Physics B: Atomic, Molecular and Optical Physics* **42** no. 15, (2009) 154009.

[27] D. Leibfried, R. Blatt, C. Monroe, and D. Wineland, "Quantum dynamics of single trapped ions," *Reviews of Modern Physics* **75** no. 1, (2003) 281. 2, 43, 44, 51

[28] Y. Nakamura, Y. A. Pashkin, and J. S. Tsai, "Coherent control of macroscopic quantum states in a single-Cooper-pair box," *Nature* **398** no. 6730, (1999) 786–788. 2, 43

[29] J. Clarke and F. K. Wilhelm, "Superconducting quantum bits," *Nature* **453** no. 7198, (2008) 1031–1042. 43

[30] M. Kjaergaard, M. E. Schwartz, J. Braumüller, P. Krantz, J. I.-J. Wang, S. Gustavsson, and W. D. Oliver, "Superconducting qubits: Current state of play," *Annual Review of Condensed Matter Physics* **11** (2020) 369–395. 2

[31] D. Loss and D. P. DiVincenzo, "Quantum computation with quantum dots," *Physical Review A* **57** no. 1, (1998) 120. 2, 43

[32] R. Hanson, L. P. Kouwenhoven, J. R. Petta, S. Tarucha, and L. M. Vandersypen, "Spins in few-electron quantum dots," *Reviews of Modern Physics* **79** no. 4, (2007) 1217. 2, 43

[33] S. Barz, "Quantum computing with photons: introduction to the circuit model, the one-way quantum computer, and the fundamental principles of photonic experiments," *Journal of Physics B: Atomic, Molecular and Optical Physics* **48** no. 8, (2015) 083001. 2

[34] D. Jaksch, J. Cirac, P. Zoller, S. Rolston, R. Côté, and M. Lukin, "Fast quantum gates for neutral atoms," *Physical Review Letters* **85** no. 10, (2000) 2208. 2, 43

[35] M. Saffman, T. G. Walker, and K. Mølmer, "Quantum information with rydberg atoms," *Reviews of Modern Physics* **82** no. 3, (2010) 2313.

[36] D. Crow, R. Joynt, and M. Saffman, "Improved error thresholds for measurement-free error correction," *Physical Review Letters* **117** no. 13, (2016) 130503. 43

[37] I. S. Madjarov, J. P. Covey, A. L. Shaw, J. Choi, A. Kale, A. Cooper, H. Pichler, V. Schkolnik, J. R. Williams, and M. Endres, "High-fidelity entanglement and detection of alkaline-earth rydberg atoms," *Nature Physics* **16** no. 8, (2020) 857–861. 2

[38] S. E. Anderson, K. Younge, and G. Raithel, "Trapping rydberg atoms in an optical lattice," *Physical Review Letters* **107** no. 26, (2011) 263001. 2, 43

[39] M. Viteau, M. Bason, J. Radogostowicz, N. Malossi, D. Ciampini, O. Morsch, and E. Arimondo, "Rydberg excitations in bose-einstein condensates in

quasi-one-dimensional potentials and optical lattices," *Physical Review Letters* **107** no. 6, (2011) 060402.

[40] P. Schauß, M. Cheneau, M. Endres, T. Fukuhara, S. Hild, A. Omran, T. Pohl, C. Gross, S. Kuhr, and I. Bloch, "Observation of spatially ordered structures in a two-dimensional rydberg gas," *Nature* **491** no. 7422, (2012) 87–91. 2, 43

[41] F. Nogrette, H. Labuhn, S. Ravets, D. Barredo, L. Béguin, A. Vernier, T. Lahaye, and A. Browaeys, "Single-atom trapping in holographic 2d arrays of microtraps with arbitrary geometries," *Physical Review X* **4** no. 2, (2014) 021034. 2, 43

[42] T. Xia, M. Lichtman, K. Maller, A. Carr, M. Piotrowicz, L. Isenhower, and M. Saffman, "Randomized benchmarking of single-qubit gates in a 2d array of neutral-atom qubits," *Physical Review Letters* **114** no. 10, (2015) 100503. 2, 43

[43] D. P. DiVincenzo, "The physical implementation of quantum computation," *Fortschritte der Physik: Progress of Physics* **48** no. 9-11, (2000) 771–783. 2

[44] P. Schindler, D. Nigg, T. Monz, J. T. Barreiro, E. Martinez, S. X. Wang, S. Quint, M. F. Brandl, V. Nebendahl, C. F. Roos, *et al.*, "A quantum information processor with trapped ions," *New Journal of Physics* **15** no. 12, (2013) 123012. 3, 47, 48, 104, 141

[45] C. Gidney and M. Ekerå, "How to factor 2048 bit RSA integers in 8 hours using 20 million noisy qubits," *Quantum* **5** (2021) 433. 3, 4

[46] P. W. Shor, "Fault-tolerant quantum computation," in *Proceedings of 37th Conference on Foundations of Computer Science*, pp. 56–65, IEEE. 1996. 3, 58

[47] E. Knill, R. Laflamme, and W. H. Zurek, "Resilient quantum computation: error models and thresholds," *Proceedings of the Royal Society of London. Series A: Mathematical, Physical and Engineering Sciences* **454** no. 1969, (1998) 365–384. 3, 58

[48] P. Schindler, J. T. Barreiro, T. Monz, V. Nebendahl, D. Nigg, M. Chwalla, M. Hennrich, and R. Blatt, "Experimental repetitive quantum error correction," *Science* **332** no. 6033, (2011) 1059–1061. 3, 43

[49] J. Chiaverini, D. Leibfried, T. Schaetz, M. D. Barrett, R. Blakestad, J. Britton, W. M. Itano, J. D. Jost, E. Knill, C. Langer, *et al.*, "Realization of quantum error correction," *Nature* **432** no. 7017, (2004) 602–605. 43

[50] J. Zhang, R. Laflamme, and D. Suter, "Experimental implementation of encoded logical qubit operations in a perfect quantum error correcting code," *Physical Review Letters* **109** no. 10, (2012) 100503.

[51] D. Nigg, M. Mueller, E. A. Martinez, P. Schindler, M. Hennrich, T. Monz, M. A. Martin-Delgado, and R. Blatt, "Quantum computations on a topologically encoded qubit," *Science* **345** no. 6194, (2014) 302–305. 43, 59, 78, 79, 101

[52] M. Müller, A. Rivas, E. Martínez, D. Nigg, P. Schindler, T. Monz, R. Blatt, and M. Martin-Delgado, "Iterative phase optimization of elementary quantum error correcting codes," *Physical Review X* **6** no. 3, (2016) 031030. 77, 79, 88, 162

[53] M. Takita, A. D. Córcoles, E. Magesan, B. Abdo, M. Brink, A. Cross, J. M. Chow, and J. M. Gambetta, "Demonstration of weight-four parity measurements in the surface code architecture," *Physical Review Letters* **117** no. 21, (2016) 210505.

[54] G. Waldherr, Y. Wang, S. Zaiser, M. Jamali, T. Schulte-Herbrüggen, H. Abe, T. Ohshima, J. Isoya, J. Du, P. Neumann, *et al.*, "Quantum error correction in a solid-state hybrid spin register," *Nature* **506** no. 7487, (2014) 204–207.

[55] J. Kelly, R. Barends, A. G. Fowler, A. Megrant, E. Jeffrey, T. C. White, D. Sank, J. Y. Mutus, B. Campbell, Y. Chen, *et al.*, "State preservation by repetitive error detection in a superconducting quantum circuit," *Nature* **519** no. 7541, (2015) 66–69.

[56] J. M. Gambetta, J. M. Chow, and M. Steffen, "Building logical qubits in a superconducting quantum computing system," *npj Quantum Information* **3** no. 1, (2017) 1–7. 3, 59

[57] M. Saffman, "Quantum computing with atomic qubits and Rydberg interactions: progress and challenges," *Journal of Physics B: Atomic, Molecular and Optical Physics* **49** no. 20, (2016) 202001. 3

[58] G. Wendin, "Quantum information processing with superconducting circuits: a review," *Reports on Progress in Physics* **80** no. 10, (2017) 106001.

[59] H.-L. Huang, D. Wu, D. Fan, and X. Zhu, "Superconducting quantum computing: a review," *Science China Information Sciences* **63** no. 8, (2020) 180501.

[60] S. Slussarenko and G. J. Pryde, "Photonic quantum information processing: A concise review," *Applied Physics Reviews* **6** no. 4, (2019) 041303.

[61] C. D. Bruzewicz, J. Chiaverini, R. McConnell, and J. M. Sage, "Trapped-ion quantum computing: Progress and challenges," *Applied Physics Reviews* **6** no. 2, (2019) 021314. 3

[62] D. Gottesman, "An introduction to quantum error correction and fault-tolerant quantum computation," in *Quantum information science and its contributions to mathematics, Proceedings of Symposia in Applied Mathematics*, vol. 68, pp. 13–58. 2010. 3

[63] D. Aharonov and M. Ben-Or, "Fault-tolerant quantum computation with constant error rate," *SIAM Journal on Computing* (2008) . 58

[64] A. Y. Kitaev, "Quantum error correction with imperfect gates," in *Quantum communication, computing, and measurement*, pp. 181–188. Springer, 1997. 3

[65] M. Abobeih, Y. Wang, J. Randall, S. Loenen, C. Bradley, M. Markham, D. Twitchen, B. Terhal, and T. Taminiau, "Fault-tolerant operation of a logical qubit in a diamond quantum processor," *arXiv:2108.01646* (2021) . 4, 59

[66] L. Postler, S. Heußen, I. Pogorelov, M. Rispler, T. Feldker, M. Meth, C. D. Marciniak, R. Stricker, M. Ringbauer, R. Blatt, *et al.*, "Demonstration of fault-tolerant universal quantum gate operations," *arXiv:2111.12654* (2021) .

[67] C. Ryan-Anderson, J. Bohnet, K. Lee, D. Gresh, A. Hankin, J. Gaebler, D. Francois, A. Chernoguzov, D. Lucchetti, N. Brown, *et al.*, "Realization of real-time fault-tolerant quantum error correction," *arXiv:2107.07505* (2021) . 59

[68] S. Krinner, N. Lacroix, A. Remm, A. Di Paolo, E. Genois, C. Leroux, C. Hellings, S. Lazar, F. Swiadek, J. Herrmann, *et al.*, "Realizing Repeated Quantum Error Correction in a Distance-Three Surface Code," *arXiv:2112.03708* (2021) . 4, 59

[69] J. Preskill, "Quantum Computing in the NISQ era and beyond," *Quantum* **2** (2018) 79. 4

[70] K. Bharti, A. Cervera-Lierta, T. H. Kyaw, T. Haug, S. Alperin-Lea, A. Anand, M. Degroote, H. Heimonen, J. S. Kottmann, T. Menke, *et al.*, "Noisy intermediate-scale quantum (NISQ) algorithms," *arXiv:2101.08448* (2021) . 4

[71] F. Arute, K. Arya, R. Babbush, D. Bacon, J. C. Bardin, R. Barends, R. Biswas, S. Boixo, F. G. Brandao, D. A. Buell, *et al.*, "Quantum supremacy using a programmable superconducting processor," *Nature* **574** no. 7779, (2019) 505–510. 4

[72] "IBM Eagle quantum processor." `https://newsroom.ibm.com/2021-11-16-IBM-Unveils-Breakthrough-127-Qubit-Quantum-Processor`. Accessed: 2021-11-27. 4

[73] "IBM Quantum Experience." `https://quantum-computing.ibm.com/`. Accessed: 2021-11-27. 4

[74] "Quantum in the Cloud." `http://www.bristol.ac.uk/physics/research/quantum/engagement/qcloud/`. Accessed: 2021-09-08.

[75] "Rigetti quantum computing systems." `https://www.rigetti.com/systems`. Accessed: 2021-09-08. 4

[76] M. Benedetti, E. Lloyd, S. Sack, and M. Fiorentini, "Parameterized quantum circuits as machine learning models," *Quantum Science and Technology* **4** no. 4, (2019) 043001. 4

[77] A. Peruzzo, J. McClean, P. Shadbolt, M.-H. Yung, X.-Q. Zhou, P. J. Love, A. Aspuru-Guzik, and J. L. O'brien, "A variational eigenvalue solver on a photonic quantum processor," *Nature communications* **5** no. 1, (2014) 1–7. 4

[78] E. Farhi, J. Goldstone, and S. Gutmann, "A quantum approximate optimization algorithm," *arXiv:1411.4028* (2014) . 4

[79] R. Harper and S. T. Flammia, "Fault-tolerant logical gates in the IBM Quantum Experience," *Physical Review Letters* **122** no. 8, (2019) 080504. 4

[80] R. Li, U. Alvarez-Rodriguez, L. Lamata, and E. Solano, "Approximate quantum adders with genetic algorithms: an ibm quantum experience," *Quantum Measurements and Quantum Metrology* **4** no. 1, (2017) 1–7.

[81] S. Mahanti, S. Das, B. K. Behera, and P. K. Panigrahi, "Quantum robots can fly; play games: an IBM quantum experience," *Quantum Information Processing* **18** no. 7, (2019) 1–10.

[82] K. Srinivasan, S. Satyajit, B. K. Behera, and P. K. Panigrahi, "Efficient quantum algorithm for solving travelling salesman problem: An IBM Quantum Experience," *arXiv:1805.10928* (2018) .

[83] Y. Lee, J. Joo, and S. Lee, "Hybrid quantum linear equation algorithm and its experimental test on ibm quantum experience," *Scientific reports* **9** no. 1, (2019) 1–12.

[84] S. I. Doronin, E. Fel'dman, and A. I. Zenchuk, "Solving systems of linear algebraic equations via unitary transformations on quantum processor of ibm quantum experience," *Quantum Information Processing* **19** no. 2, (2020) 1–20. 4

[85] "Quantum computing report." `https://quantumcomputingreport.com/privatestartup/`. Accessed: 2021-12-16. 4

[86] J. Otterbach, R. Manenti, N. Alidoust, A. Bestwick, M. Block, B. Bloom, S. Caldwell, N. Didier, E. S. Fried, S. Hong, *et al.*, "Unsupervised machine learning on a hybrid quantum computer," *arXiv:1712.05771* (2017) . 4

[87] S. Fernández-Lorenzo, D. Porras, and J. J. García-Ripoll, "Hybrid quantum–classical optimization with cardinality constraints and applications to finance," *Quantum Science and Technology* **6** no. 3, (2021) 034010.

[88] D. Amaro, C. Modica, M. Rosenkranz, M. Fiorentini, M. Benedetti, and M. Lubasch, "Filtering variational quantum algorithms for combinatorial optimization," *arXiv:2106.10055* (2021) .

[89] D. Amaro, M. Rosenkranz, N. Fitzpatrick, K. Hirano, and M. Fiorentini, "A case study of variational quantum algorithms for a job shop scheduling problem," *arXiv:2109.03745* (2021) .

[90] S. Palmer, S. Sahin, R. Hernandez, S. Mugel, and R. Orus, "Quantum Portfolio Optimization with Investment Bands and Target Volatility," *arXiv:2106.06735* (2021) .

[91] M. P. Harrigan, K. J. Sung, M. Neeley, K. J. Satzinger, F. Arute, K. Arya, J. Atalaya, J. C. Bardin, R. Barends, S. Boixo, *et al.*, "Quantum approximate optimization of non-planar graph problems on a planar superconducting processor," *Nature Physics* **17** no. 3, (2021) 332–336.

[92] M. Benedetti, M. Fiorentini, and M. Lubasch, "Hardware-efficient variational quantum algorithms for time evolution," *Physical Review Research* **3** no. 3, (2021) 033083.

[93] A. Perdomo-Ortiz, A. Feldman, A. Ozaeta, S. V. Isakov, Z. Zhu, B. O'Gorman, H. G. Katzgraber, A. Diedrich, H. Neven, J. de Kleer, and et al., "Readiness of Quantum Optimization Machines for Industrial Applications," *Physical Review Applied* **12** no. 1, (Jul, 2019) .

[94] M. Streif, S. Yarkoni, A. Skolik, F. Neukart, and M. Leib, "Beating classical heuristics for the binary paint shop problem with the quantum approximate optimization algorithm," *Physical Review A* **104** no. 1, (2021) 012403. 4

[95] A. Gelman, J. B. Carlin, H. S. Stern, and D. B. Rubin, *Bayesian data analysis.* Chapman and Hall/CRC, 1995. 5

[96] G. A. Young, T. A. Severini, G. A. Young, R. Smith, R. L. Smith, *et al.*, *Essentials of statistical inference*, vol. 16. Cambridge University Press, 2005.

[97] P. Lee, *Bayesian statistics: an introduction.* Wiley, Chichester, West Sussex Hoboken, N.J, 2012. 5

[98] T. Bayes, "An essay towards solving a problem in the doctrine of chances," *Philosophical transactions of the Royal Society of London* no. 53, (1763) 370–418. 5

[99] R. Jozsa, "Fidelity for mixed quantum states," *Journal of Modern Optics* **41** no. 12, (1994) 2315–2323. 16

[100] M. Kafatos, *Bell's theorem, quantum theory and conceptions of the universe*, vol. 37. Springer Science & Business Media, 2013. 17

[101] D. M. Greenberger, M. A. Horne, and A. Zeilinger, "Going beyond Bell's theorem," in *Bell's theorem, quantum theory and conceptions of the universe*, pp. 69–72. Springer, 1989. 17

[102] K. Kraus, A. Böhm, J. D. Dollard, and W. Wootters, "States, effects, and operations: fundamental notions of quantum theory. Lectures in mathematical physics at the University of Texas at Austin," *Lecture notes in physics* **190** (1983) . 20

[103] I. L. Chuang and M. A. Nielsen, "Prescription for experimental determination of the dynamics of a quantum black box," *Journal of Modern Optics* **44** no. 11-12, (1997) 2455–2467. 24, 147

[104] J. Emerson, R. Alicki, and K. Życzkowski, "Scalable noise estimation with random unitary operators," *Journal of Optics B: Quantum and Semiclassical Optics* **7** no. 10, (2005) S347. 26

[105] E. Magesan, J. M. Gambetta, and J. Emerson, "Characterizing quantum gates via randomized benchmarking," *Physical Review A* **85** no. 4, (2012) 042311.

[106] J. P. Gaebler, A. M. Meier, T. R. Tan, R. Bowler, Y. Lin, D. Hanneke, J. D. Jost, J. Home, E. Knill, D. Leibfried, *et al.*, "Randomized benchmarking of multiqubit gates," *Physical Review Letters* **108** no. 26, (2012) 260503. 26

[107] R. Blume-Kohout, J. K. Gamble, E. Nielsen, K. Rudinger, J. Mizrahi, K. Fortier, and P. Maunz, "Demonstration of qubit operations below a rigorous fault tolerance threshold with gate set tomography," *Nature Communications* **8** no. 1, (2017) 14485. 26, 147

[108] S. Mavadia, C. L. Edmunds, C. Hempel, H. Ball, F. Roy, T. M. Stace, and M. J. Biercuk, "Experimental quantum verification in the presence of temporally correlated noise," *npj Quantum Information* **4** no. 1, (2017) . 26, 147

[109] D. Gottesman, "Theory of fault-tolerant quantum computation," *Physical Review A* **57** no. 1, (1998) 127. 26

[110] C. Cohen-Tannoudji, B. Diu, and F. Laloë, *Quantum Mechanics, Volume 1: Basic Concepts, Tools, and Applications*. John Wiley & Sons, 2019. 31, 41

[111] M. Abramowitz and I. A. Stegun, *Handbook of mathematical functions with formulas, graphs, and mathematical tables*, vol. 55. US Government printing office, 1948. 33

[112] K. R. Brown, A. C. Wilson, Y. Colombe, C. Ospelkaus, A. M. Meier, E. Knill, D. Leibfried, and D. J. Wineland, "Single-qubit-gate error below 10- 4 in a trapped ion," *Physical Review A* **84** no. 3, (2011) 030303. 43

[113] A. Myerson, D. Szwer, S. Webster, D. Allcock, M. Curtis, G. Imreh, J. Sherman, D. Stacey, A. Steane, and D. Lucas, "High-fidelity readout of trapped-ion qubits," *Physical Review Letters* **100** no. 20, (2008) 200502. 43

[114] J. Benhelm, G. Kirchmair, C. F. Roos, and R. Blatt, "Towards fault-tolerant quantum computing with trapped ions," *Nature Physics* **4** no. 6, (2008) 463–466. 43

[115] S. Stahl, F. Galve, J. Alonso, S. Djekic, W. Quint, T. Valenzuela, J. Verdú, M. Vogel, and G. Werth, "A planar Penning trap," *The European Physical Journal D-Atomic, Molecular, Optical and Plasma Physics* **32** no. 1, (2005) 139–146. 44

[116] M. Hellwig, A. Bautista-Salvador, K. Singer, G. Werth, and F. Schmidt-Kaler, "Fabrication of a planar micro Penning trap and numerical investigations of versatile ion positioning protocols," *New Journal of Physics* **12** no. 6, (2010) 065019.

[117] J. Goldman and G. Gabrielse, "Optimized planar penning traps for quantum-information studies," *Physical Review A* **81** no. 5, (2010) 052335. 44

[118] W. Paul, "Electromagnetic traps for charged and neutral particles," *Reviews of Modern Physics* **62** no. 3, (1990) 531. 44

[119] M. M. Chwalla, *Precision spectroscopy with $^{40}Ca^{+}$ ions in a Paul trap*. PhD thesis, PhD thesis, Universität Innsbruck, 2009. 45, 106

[120] F. M. Arscott, *Periodic differential equations: an introduction to Mathieu, Lamé, and allied functions*, vol. 66. Elsevier, 2014. 45

[121] D. James, "Quantum dynamics of cold trapped ions with application to quantum computation," *Applied Physics B* **66** (1998) 181–190. 47, 120

[122] K. A. Landsman, Y. Wu, P. H. Leung, D. Zhu, N. M. Linke, K. R. Brown, L. Duan, and C. Monroe, "Two-qubit entangling gates within arbitrarily long chains of trapped ions," *Physical Review A* **100** no. 2, (2019) 022332. 48

[123] S. Kim, *Acousto-optic devices for optical signal processing and quantum computing*. PhD thesis, University of Colorado at Boulder, 2008.

[124] P. Parrado-Rodríguez, C. Ryan-Anderson, A. Bermudez, and M. Müller, "Crosstalk suppression for fault-tolerant quantum error correction with trapped ions," *Quantum* **5** (2021) 487. 48

[125] D. Kielpinski, C. Monroe, and D. J. Wineland, "Architecture for a large-scale ion-trap quantum computer," *Nature* **417** no. 6890, (2002) 709–711. 48

[126] V. Kaushal, B. Lekitsch, A. Stahl, J. Hilder, D. Pijn, C. Schmiegelow, A. Bermudez, M. Müller, F. Schmidt-Kaler, and U. Poschinger, "Shuttling-based trapped-ion quantum information processing," *AVS Quantum Science* **2** no. 1, (2020) 014101.

[127] J. M. Pino, J. M. Dreiling, C. Figgatt, J. P. Gaebler, S. A. Moses, M. Allman, C. Baldwin, M. Foss-Feig, D. Hayes, K. Mayer, *et al.*, "Demonstration of the trapped-ion quantum CCD computer architecture," *Nature* **592** no. 7853, (2021) 209–213.

[128] H. Kaufmann, T. Ruster, C. T. Schmiegelow, M. A. Luda, V. Kaushal, J. Schulz, D. Von Lindenfels, F. Schmidt-Kaler, and U. Poschinger, "Scalable

creation of long-lived multipartite entanglement," *Physical Review Letters* **119** no. 15, (2017) 150503.

[129] Y. Wan, D. Kienzler, S. D. Erickson, K. H. Mayer, T. R. Tan, J. J. Wu, H. M. Vasconcelos, S. Glancy, E. Knill, D. J. Wineland, *et al.*, "Quantum gate teleportation between separated qubits in a trapped-ion processor," *Science* **364** no. 6443, (2019) 875–878. 48

[130] F. Schmidt-Kaler, H. Häffner, M. Riebe, S. Gulde, G. P. Lancaster, T. Deuschle, C. Becher, C. F. Roos, J. Eschner, and R. Blatt, "Realization of the Cirac-Zoller controlled-NOT quantum gate," *Nature* **422** no. 6930, (2003) 408–411. 54

[131] A. Sørensen and K. Mølmer, "Quantum Computation with Ions in Thermal Motion," *Physical Review Letters* **82** no. 9, (1999) 1971–1974. 55, 121

[132] A. Sørensen and K. Mølmer, "Entanglement and quantum computation with ions in thermal motion," *Physical Review A* **62** no. 2, (2000) 022311. 55, 121, 123

[133] K. Fujii, *Quantum Computation with Topological Codes: from qubit to topological fault-tolerance*, vol. 8. Springer, 2015. 58

[134] E. Dennis, A. Kitaev, A. Landahl, and J. Preskill, "Topological quantum memory," *Journal of Mathematical Physics* **43** no. 9, (2002) 4452–4505. 59

[135] S. B. Bravyi and A. Y. Kitaev, "Quantum codes on a lattice with boundary," *arXiv:9811052* (1998) . 59

[136] H. Bombin and M. A. Martin-Delgado, "Topological quantum distillation," *Physical Review Letters* **97** no. 18, (2006) 180501. 59, 60, 62

[137] A. M. Stephens, "Fault-tolerant thresholds for quantum error correction with the surface code," *Physical Review A* **89** no. 2, (2014) 022321. 59

[138] R. Raussendorf and J. Harrington, "Fault-tolerant quantum computation with high threshold in two dimensions," *Physical Review Letters* **98** no. 19, (2007) 190504.

[139] E. T. Campbell, B. M. Terhal, and C. Vuillot, "Roads towards fault-tolerant universal quantum computation," *Nature* **549** no. 7671, (2017) 172–179. 59

[140] A. J. Landahl, J. T. Anderson, and P. R. Rice, "Fault-tolerant quantum computing with color codes," *arXiv:1108.5738* (2011) . 59

[141] C. Chamberland, A. Kubica, T. J. Yoder, and G. Zhu, "Triangular color codes on trivalent graphs with flag qubits," *New Journal of Physics* **22** no. 2, (2020) 023019.

[142] M. E. Beverland, A. Kubica, and K. M. Svore, "Cost of Universality: A Comparative Study of the Overhead of State Distillation and Code Switching with Color Codes," *PRX Quantum* **2** no. 2, (2021) 020341. 59

[143] B. Eastin and E. Knill, "Restrictions on transversal encoded quantum gate sets," *Physical Review Letters* **102** no. 11, (2009) 110502. 59

[144] R. Versluis, S. Poletto, N. Khammassi, B. Tarasinski, N. Haider, D. J. Michalak, A. Bruno, K. Bertels, and L. DiCarlo, "Scalable quantum circuit and control for a superconducting surface code," *Physical Review Applied* **8** no. 3, (2017) 034021. 59

[145] T. J. Yoder and I. H. Kim, "The surface code with a twist," *Quantum* **1** (2017) 2.

[146] R. Chao and B. W. Reichardt, "Quantum error correction with only two extra qubits," *Physical Review Letters* **121** no. 5, (2018) 050502.

[147] B. W. Reichardt, "Fault-tolerant quantum error correction for steane's seven-qubit color code with few or no extra qubits," *Quantum Science and Technology* **6** no. 1, (2020) 015007. 59

[148] S. J. Devitt, W. J. Munro, and K. Nemoto, "Quantum error correction for beginners," *Reports on Progress in Physics* **76** no. 7, (2013) 076001. 59

[149] J. Roffe, "Quantum error correction: an introductory guide," *Contemporary Physics* **60** no. 3, (2019) 226–245. 59

[150] D. Gottesman, *Stabilizer codes and quantum error correction*. California Institute of Technology, 1997. 59

[151] B. M. Terhal, "Quantum error correction for quantum memories," *Reviews of Modern Physics* **87** no. 2, (2015) 307. 59

[152] A. M. Steane, "Error correcting codes in quantum theory," *Physical Review Letters* **77** no. 5, (1996) 793. 60

[153] D. Sivia and J. Skilling, *Data analysis: a Bayesian tutorial*. OUP Oxford, 2006. 64, 65, 67

[154] T. M. Cover, *Elements of information theory*. John Wiley & Sons, 1999. 65

[155] C. E. Shannon, "A mathematical theory of communication," *The Bell system technical journal* **27** no. 3, (1948) 379–423. 65

[156] S. Kullback and R. A. Leibler, "On information and sufficiency," *The annals of mathematical statistics* **22** no. 1, (1951) 79–86. 67

[157] M. Nica, "Optimal strategy in "guess who?": Beyond binary search," *Probability in the Engineering and Informational Sciences* **30** no. 4, (2016) 576–592. 67

[158] A. Y. Khinchin, *Mathematical foundations of information theory*. Courier Corporation, 2013. 67

[159] M. Patra, "Quantum state determination: estimates for information gain and some exact calculations," *Journal of Physics A: Mathematical and Theoretical* **40** no. 35, (2007) 10887. 67

[160] N. J. Gordon, D. J. Salmond, and A. F. Smith, "Novel approach to nonlinear/non-Gaussian Bayesian state estimation," in *IEE proceedings F (radar and signal processing)*, vol. 140, pp. 107–113, IET. 1993. 68

[161] J. S. Liu and R. Chen, "Sequential Monte Carlo methods for dynamic systems," *Journal of the American statistical association* **93** no. 443, (1998) 1032–1044.

[162] A. Tulsyan, R. B. Gopaluni, and S. R. Khare, "Particle filtering without tears: A primer for beginners," *Computers & Chemical Engineering* **95** (2016) 130–145.

[163] D. Q. Mayne, "A solution of the smoothing problem for linear dynamic systems," *Automatica* **4** no. 2, (1966) 73–92.

[164] J. E. Handschin and D. Q. Mayne, "Monte Carlo techniques to estimate the conditional expectation in multi-stage non-linear filtering," *International Journal of Control* **9** no. 5, (1969) 547–559. 68

[165] I. Nagrath, *Control systems engineering*. New Age International, 2006. 70

[166] N. F. Ramsey, "A molecular beam resonance method with separated oscillating fields," *Physical Review* **78** no. 6, (1950) 695. 77

[167] R. F. Werner, "Quantum states with Einstein-Podolsky-Rosen correlations admitting a hidden-variable model," *Physical Review A* **40** no. 8, (1989) 4277. 79

[168] W. H. Press, H. William, S. A. Teukolsky, A. Saul, W. T. Vetterling, and B. P. Flannery, *Numerical recipes 3rd edition: The art of scientific computing*. Cambridge university press, 2007. 81

[169] F. Huszár and N. M. Houlsby, "Adaptive Bayesian quantum tomography," *Physical Review A* **85** no. 5, (2012) 052120. 85

[170] K. S. Kravtsov, S. S. Straupe, I. V. Radchenko, N. M. Houlsby, F. Huszár, and S. P. Kulik, "Experimental adaptive Bayesian tomography," *Physical Review A* **87** no. 6, (2013) 062122.

[171] V. Negnevitsky, *Feedback-stabilised quantum states in a mixed-species ion system*. PhD thesis, ETH Zurich, 2018. 85

[172] N. Wiebe and C. Granade, "Efficient Bayesian phase estimation," *Physical Review Letters* **117** no. 1, (2016) 010503. 101

[173] B. L. Higgins, D. W. Berry, S. D. Bartlett, H. M. Wiseman, and G. J. Pryde, "Entanglement-free Heisenberg-limited phase estimation," *Nature* **450** no. 7168, (2007) 393–396.

[174] V. Giovannetti, S. Lloyd, and L. Maccone, "Quantum-enhanced measurements: beating the standard quantum limit," *Science* **306** no. 5700, (2004) 1330–1336.

[175] S. Paesani, A. A. Gentile, R. Santagati, J. Wang, N. Wiebe, D. P. Tew, J. L. O'Brien, and M. G. Thompson, "Experimental Bayesian quantum phase estimation on a silicon photonic chip," *Physical Review Letters* **118** no. 10, (2017) 100503. 101

[176] R. Drever, J. L. Hall, F. Kowalski, J. Hough, G. Ford, A. Munley, and H. Ward, "Laser phase and frequency stabilization using an optical resonator," *Applied Physics B* **31** no. 2, (1983) 97–105. 103

[177] J. Bernard, L. Marmet, and A. Madej, "A laser frequency lock referenced to a single trapped ion," *Optics Communications* **150** no. 1-6, (1998) 170–174. 103

[178] M. Bußjäger, "Automated Frequency Locking via Spectroscopy on trapped $^{40}Ca^{+}$ Ions," Master's thesis, Universität Innsbruck, 2020. 104, 115, 117

[179] I. I. Rabi, "Space quantization in a gyrating magnetic field," *Physical Review* **51** no. 8, (1937) 652. 104

[180] V. Nebendahl, H. Häffner, and C. Roos, "Optimal control of entangling operations for trapped-ion quantum computing," *Physical Review A* **79** no. 1, (2009) 012312. 119

[181] W. Magnus, "On the exponential solution of differential equations for a linear operator," *Communications on Pure and Applied Mathematics* **7** no. 4, (1954) 649–673. 120, 128, 129

[182] C. F. Roos, "Ion trap quantum gates with amplitude-modulated laser beams," *New Journal of Physics* **10** no. 1, (2008) 013002. 123

[183] W. Rossmann, *Lie groups: an introduction through linear groups*, vol. 5. Oxford University Press on Demand, 2006. 123

[184] H. Häffner, S. Gulde, M. Riebe, G. Lancaster, C. Becher, J. Eschner, F. Schmidt-Kaler, and R. Blatt, "Precision measurement and compensation of optical stark shifts for an ion-trap quantum processor," *Physical Review Letters* **90** no. 14, (2003) 143602. 126

[185] G. Kirchmair, J. Benhelm, F. Zähringer, R. Gerritsma, C. F. Roos, and R. Blatt, "Deterministic entanglement of ions in thermal states of motion," *New Journal of Physics* **11** no. 2, (2009) 023002. 126, 146

[186] S. Blanes, F. Casas, J. A. Oteo, and J. Ros, "A pedagogical approach to the Magnus expansion," *European Journal of Physics* **31** no. 4, (2010) 907–918. 128, 129

[187] F. Martinez-Garcia, "Coefficients Magnus MS gate center line modelling." `https://github.com/FernandoMartinezG/Coefficients-Magnus-MS-gate-center-line-modelling`, 2021. 132

[188] D. J. Wineland, C. Monroe, W. M. Itano, D. Leibfried, B. E. King, and D. M. Meekhof, "Experimental issues in coherent quantum-state manipulation of trapped atomic ions," *Journal of research of the National Institute of Standards and Technology* **103** no. 3, (1998) 259. 141

[189] P. Schindler, "Frequency synthesis and pulse shaping for quantum information processing with trapped ions," Master's thesis, University of Innsbruck, 2008. 142, 149, 150

[190] M. Riebe, K. Kim, P. Schindler, T. Monz, P. O. Schmidt, T. K. Körber, W. Hänsel, H. Häffner, C. F. Roos, and R. Blatt, "Process Tomography of Ion Trap Quantum Gates," *Physical Review Letters* **97** no. 22, (2006) 220407. 147

[191] S. T. Merkel, J. M. Gambetta, J. A. Smolin, S. Poletto, A. D. Córcoles, B. R. Johnson, C. A. Ryan, and M. Steffen, "Self-consistent quantum process tomography," *Physical Review A* **87** no. 6, (2013) 1–9. 147

[192] E. Knill, D. Leibfried, R. Reichle, J. Britton, R. B. Blakestad, J. D. Jost, C. Langer, R. Ozeri, S. Seidelin, and D. J. Wineland, "Randomized benchmarking of quantum gates," *Physical Review A* **77** no. 1, (2008) 012307. 147

[193] A. Erhard, J. J. Wallman, L. Postler, M. Meth, R. Stricker, E. A. Martinez, P. Schindler, T. Monz, J. Emerson, and R. Blatt, "Characterizing large-scale quantum computers via cycle benchmarking," *Nature Communications* **10** no. 1, (2019) 5347. 147

[194] J. J. Wallman and J. Emerson, "Noise tailoring for scalable quantum computation via randomized compiling," *Physical Review A* **94** no. 5, (2016) 052325. 147

[195] E. Greplova, C. K. Andersen, and K. Mølmer, "Quantum parameter estimation with a neural network," *arXiv:1711.05238* (2017) 1–8. 147

[196] I. Pogorelov, G. Struchalin, S. Straupe, I. Radchenko, K. Kravtsov, and S. Kulik, "Experimental adaptive process tomography," *Physical Review A* **95** no. 1, (2017) 012302. 147

[197] C. Granade, C. Ferrie, and S. T. Flammia, "Practical adaptive quantum tomography," *New Journal of Physics* **19** no. 11, (2017) . 147

[198] P. A. Walker, "Quadcubic interpolation: a four-dimensional spline method," *arXiv:1904.09869* (2019) . 154

[199] N. Akerman, N. Navon, S. Kotler, Y. Glickman, and R. Ozeri, "Universal gate-set for trapped-ion qubits using a narrow linewidth diode laser," *New Journal of Physics* **17** no. 11, (2015) . 159

[200] G. Q. AI, "Exponential suppression of bit or phase errors with cyclic error correction," *Nature* **595** no. 7867, (2021) 383. 162

[201] K. Satzinger, Y. Liu, A. Smith, C. Knapp, M. Newman, C. Jones, Z. Chen, C. Quintana, X. Mi, A. Dunsworth, *et al.*, "Realizing topologically ordered states on a quantum processor," *arXiv:2104.01180* (2021) . 162

[202] J. J. García-Ripoll, P. Zoller, and J. I. Cirac, "Speed optimized two-qubit gates with laser coherent control techniques for ion trap quantum computing," *Physical Review Letters* **91** no. 15, (2003) 157901. 163

[203] J. P. Gaebler, T. R. Tan, Y. Lin, Y. Wan, R. Bowler, A. C. Keith, S. Glancy, K. Coakley, E. Knill, D. Leibfried, and D. J. Wineland, "High-Fidelity Universal Gate Set for $^{9}Be^{+}$ Ion Qubits," *Physical Review Letters* **117** no. 6, (2016) 1–5.

[204] V. M. Schäfer, C. J. Ballance, K. Thirumalai, L. J. Stephenson, T. G. Ballance, A. M. Steane, and D. M. Lucas, "Fast quantum logic gates with trapped-ion qubits," *Nature* **555** no. 7694, (2018) 75–78.

[205] A. M. Steane, G. Imreh, J. P. Home, and D. Leibfried, "Pulsed force sequences for fast phase-insensitive quantum gates in trapped ions," *New Journal of Physics* **16** no. 5, (2014) 053049.

[206] Z. Mehdi, A. K. Ratcliffe, and J. J. Hope, "Fast entangling gates in long ion chains," *Physical Review Research* **3** no. 1, (2021) 013026. 163